



2017

ANNUAL REPORT
JAHRESBERICHT

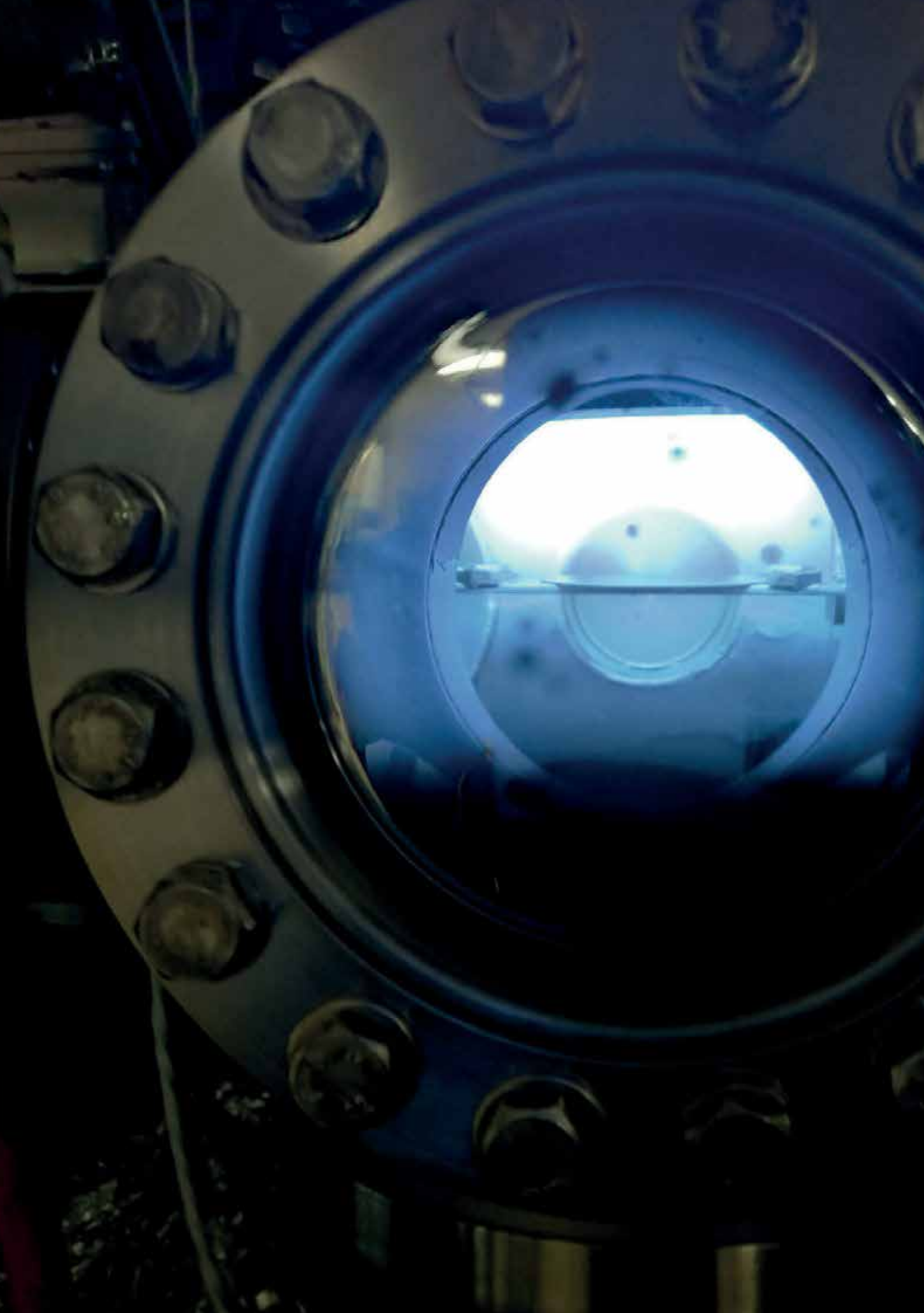


Paul-Drude-Institut
für Festkörperelektronik
Leibniz-Institut im Forschungsverbund Berlin e.V.

Table of Contents

Inhaltsverzeichnis

Preface	
Vorwort	5
Director's Column	
Kolumne des Direktors	11
Scientific Advisory Board	
Wissenschaftlicher Beirat	15
Research Highlights	
Forschungshighlights	17
Core Research Areas	
Forschungsschwerpunkte	41
Brief Reports	
Kurzberichte	65
Departments	
Abteilungen	131
Facts & Figures	
Zahlen & Fakten	153
Contact	
Kontakt	175
Imprint	
Impressum	180



Preface

Vorwort

We are pleased to present to you the annual report of PDI. It covers the period between the two meetings of our Scientific Advisory Board in October 2016 and October 2017.

As we have done for a number of years now, we take this opportunity to inform not only colleagues from our field, but also to provide the interested public with an insight into our research. The contributions include easy-to-read introductions to our Core Research Areas, they present our departments' expertise and also discuss some aspects of science policy.

A few selected scientific success stories are presented as highlights. These longer contributions are complemented by a selection of shorter reports about projects that have yielded significant progress during the year.

The first highlight comes from the Core Research Area Nanofabrication, where we work on the fabrication of novel materials in the form of thin films or nanostructures with utmost crystalline perfection. Here, one of our activities deals with the synthesis of two-dimensionally bonded materials, where, as in graphite, atoms within one plane are strongly bonded to each other, while these individual planes are kept together only by weak electrostatic forces. Many such materials are presently finding great attention in research, not only because of their novel properties, but also because they can be stacked on top of each other in a simple way even if the inter-atomic distances are widely different. For a number of years we have successfully worked on the fabrication of layers of graphene, which consist of single layers of carbon atoms. Such graphene layers now serve as a substrate for the growth

Der vor Ihnen liegende Jahresbericht unseres Instituts stellt wissenschaftliche Ergebnisse und Erfolge vor, die wir im Zeitraum zwischen den Treffen unseres wissenschaftlichen Beirats vom Oktober 2016 und Oktober 2017 erarbeitet haben.

Wie wir es seit mittlerweile etlichen Jahren praktizieren, wollen wir mit unserem Jahresbericht nicht nur die Fachkollegen unseres Arbeitsgebietes informieren, sondern auch der wissenschaftlich interessierten Öffentlichkeit einen Eindruck von unserer Arbeit vermitteln. Die Beiträge umfassen daher allgemeinverständliche Einführungen in unsere zentralen Forschungsgebiete (Core Research Areas), sie stellen die Expertise unserer Abteilungen dar und berichten auch über unser wissenschaftspolitisches Umfeld.

Einige ausgewählte wissenschaftliche Erfolge präsentieren wir in ausführlicher Form als Highlights. Sie werden ergänzt durch eine Selektion von Kurzbeiträgen.

Das erste Highlight zeigt exemplarisch, wie wir daran arbeiten, neuartige Materialien als dünne Schichten oder in Form von Nanostrukturen in möglichst perfekter kristalliner Qualität herzustellen. Wir beschäftigen uns hier mit der Herstellung von zweidimensional gebunden Materialien, bei denen ähnlich wie in Graphit die Atome innerhalb einer Ebene stark aneinander gebunden sind, wobei aber diese Ebenen nur durch sehr schwache elektrostatische Kräfte zusammengehalten werden. Diese Materialien, die derzeit starke Beachtung finden, versprechen nicht nur neuartige Eigenschaften, sondern auch die Möglichkeit, verschiedene Materialien mit stark unterschiedlichen Atomabständen auf einfache Weise aufeinander zu stapeln. Seit

of hexagonal boron nitride, a material with a similar two-dimensional structure but with totally different electrical properties. As can be easily imagined, the detection and the detailed investigation of such layers which are only one or a few atoms thick is quite a challenge. The presented results elucidate how the initial phases of the growth of crystalline boron nitride proceed and thereby provide important understanding on the way towards producing large area layers in a controlled fashion.

An important part of our work deals with the production of semiconductor nanostructures in different geometries, where we place great emphasis in understanding and quantitatively modeling the underlying principles. In the past years we have intensively studied the growth of so-called nanowires, where structural features below 100 nm can be realized only by using the specifics of crystal growth, i.e. without any externally provided structuring. These growth processes critically depend on the surface energy [a microscopic analogon of surface tension as it is observed on droplets of water]. This can be altered by the presence of certain chemical elements. Our study of such effects have shown that the coverage of the surface with bismuth atoms allows to switch on and off the formation of three-dimensional nanostructures. This effect also works on surfaces where the formation of such nanostructures was impossible up to now, and which due to their symmetry are of special interest, both from fundamental physical aspects as well as with regard to application as sources of single photons.

The third highlight in this annual review presents a good example how PDI, along with the realization of nanostructures and nanoscale devices, always investigates their physical properties in great depth. Here we use sophisticated spectroscopic methods to study the elementary processes of generating light in the meanwhile ubiquitous light-emitting diodes based on indium-gallium nitride/gal-

einigen Jahren arbeiten wir erfolgreich daran, Schichten aus Graphen, also einzelnen Lagen von Kohlenstoff-Atomen, großflächig herzustellen. Diese Graphenschichten nutzen wir jetzt als Unterlage für die Herstellung von hexagonalem Bornitrid, das eine ähnliche zweidimensionale Struktur, aber ganz andere elektrische Eigenschaften besitzt. Wie sich leicht vorstellen lässt, sind der Nachweis und die detaillierte Untersuchung solcher Schichten, die nur eine oder wenige Atomlagen dick sind, sehr anspruchsvoll. Mit den dargestellten Ergebnissen zeigen wir, wie der Beginn des Wachstums von kristallinem Bornitrid abläuft und bieten damit wichtiges Verständnis auf dem Weg zu einem kontrollierten und großflächigen Kristallwachstum dieser Materialklasse.

Ein wichtiger Teil der Arbeiten unseres Instituts beschäftigt sich damit, Halbleiternanostrukturen in verschiedenen Geometrien herzustellen und die dabei zugrunde liegenden Prinzipien zu verstehen und quantitativ zu beschreiben. Hierzu haben wir in den letzten Jahren intensiv das Wachstum sogenannter Nanodrähte studiert, bei dem alleine durch den Prozess des Kristallwachstums Durchmesser von unter 100 nm erzeugt werden können. Der Ablauf dieser Wachstumsprozesse wird entscheidend durch die Oberflächenenergie (ein mikroskopisches Äquivalent der Oberflächenspannung, wie man sie zum Beispiel von Wassertropfen kennt) bestimmt. Diese kann durch Zugabe bestimmter chemischer Elemente verändert werden. Beim Studium derartiger Effekte konnten wir zeigen, dass sich durch kontrollierte Bedeckung der Oberfläche mit Wismutatomen die Ausbildung von dreidimensionalen Nanostrukturen quasi ein- und ausschalten lässt. Dieser Effekt funktioniert auch auf Oberflächen, bei denen die Ausbildung solcher Nanostrukturen bislang nicht möglich war, die aber aufgrund ihrer atomaren Symmetrie von besonderem Interesse sind, sowohl aus grundlegender physikalischer Sicht, als auch hinsichtlich der Anwendung als Quellen von einzelnen Photonen.

lum nitride. This topic is obviously of enormous commercial interest and has consequently received large scientific attention. Still it was not entirely clear which routes electrons and holes take in the LED before they recombine either by emitting a photon or by a so-called non-radiative process, that only produces heat. Previous works typically centered either around the role of the inherent fluctuations in chemical composition in indium gallium nitride—as associated with the localization of electrons and holes—or on the role of internal electric fields. Our experiments, which also employ samples from industry, allowed to observe light emission under an additional external electric field. By varying this applied field, we could show that localization in fact always plays a large role. The magnitude of the combined external and internal fields, however decides if electrons and holes are localized separately or if they can localize in one place, forming a strongly bound exciton. Thus, the two distinct characteristic situations can be induced in one and the same sample. In parallel to this, the efficiency of light emission was quantitatively determined in all experiments. Our results have thereby significantly contributed to the physical understanding of gallium nitride LEDs, at the same time providing guidance for their further optimization.

It is a great pleasure to remark that the two last mentioned highlights have not only yielded highly visible research results for PDI, but also supported the further careers of two more young colleagues who obtained outstanding positions in the academic world and in industrial R&D.

I would like to take this occasion to thank all members of our Institute for their highly creative and committed work, which continuously advances our research. I also thank the numerous colleagues who have helped keeping our annual report interesting and attractive.

Das dritte Highlight dieses Berichts gibt ein sehr schönes Beispiel dafür, dass am PDI neben der Herstellung von Nanostrukturen und nanoskaligen Bauelementen immer auch deren physikalische Eigenschaften mit großem Tiefgang untersucht werden. Mit ausgeklügelten spektroskopischen Methoden wird in diesem Highlight untersucht, wie die elementaren Prozesse der Lichterzeugung in den mittlerweile weit verbreiteten Leuchtdioden auf der Basis von Indium-Galliumnitrid/Galliumnitrid ablaufen. Obwohl dieses Thema von enormer kommerzieller Bedeutung ist und dementsprechend umfangreiche wissenschaftliche Aufmerksamkeit erhalten hat, war bis jetzt immer noch nicht völlig klar, welche Wege Elektronen und Löcher in der Leuchtdiode nehmen, bevor sie entweder unter Emission eines Lichtquants rekombinieren oder über einen sogenannten nicht-strahlenden Prozess nur Wärme erzeugen. Bisherige Arbeiten konzentrierten sich entweder auf die Rolle von inhärenter Fluktuation der chemischen Zusammensetzung – und damit die Lokalisierung von Elektronen und Löchern – in Indium-Galliumnitrid, oder auf die Rolle von internen elektrischen Feldern. Durch geschickte Experimente, bei denen auch Proben aus der Halbleiterindustrie verwendet wurden, gelang es, die Lichtemission unter einem zusätzlich von außen angelegten elektrischen Feld zu beobachten. Dabei konnten wir zeigen, dass die Lokalisierung in der Tat immer eine große Rolle spielt. Je nach der Höhe des insgesamt wirkenden Feldes rekombinieren Elektronen und Löcher entweder aus getrennt lokalisierten Positionen oder sie sind beide an einer Stelle lokalisiert und rekombinieren als stark gebundenes Exciton. Somit konnten beide charakteristischen Situationen in ein und derselben Probe induziert werden. In allen Experimenten wurde gleichzeitig der Wirkungsgrad der Lichterzeugung quantitativ bestimmt. Unsere Ergebnisse vervollständigen damit das physikalische Verständnis von Galliumnitrid-Leuchtdioden und zeigen gleichzeitig Wege zu deren weiteren Optimierung auf.

Furthermore I would like to thank all our partners from academic and industrial research for numerous fruitful collaborations. As always, I express my special gratitude to the members of our Scientific Advisory Board and to our funding agencies for their continuous support.

Looking forward to further fruitful collaborations, I wish you enjoyable and inspiring reading,

An dieser Stelle sei angemerkt, dass die Arbeiten der beiden letztgenannten Highlights erfreulicherweise – neben den für das PDI hervorragenden Forschungsergebnissen – auch dazu geführt haben, dass mit den beiden Erstautoren zwei weitere junge Kollegen ausgezeichnete Positionen in der akademischen Welt und in industrieller Forschung und Entwicklung erhalten haben.

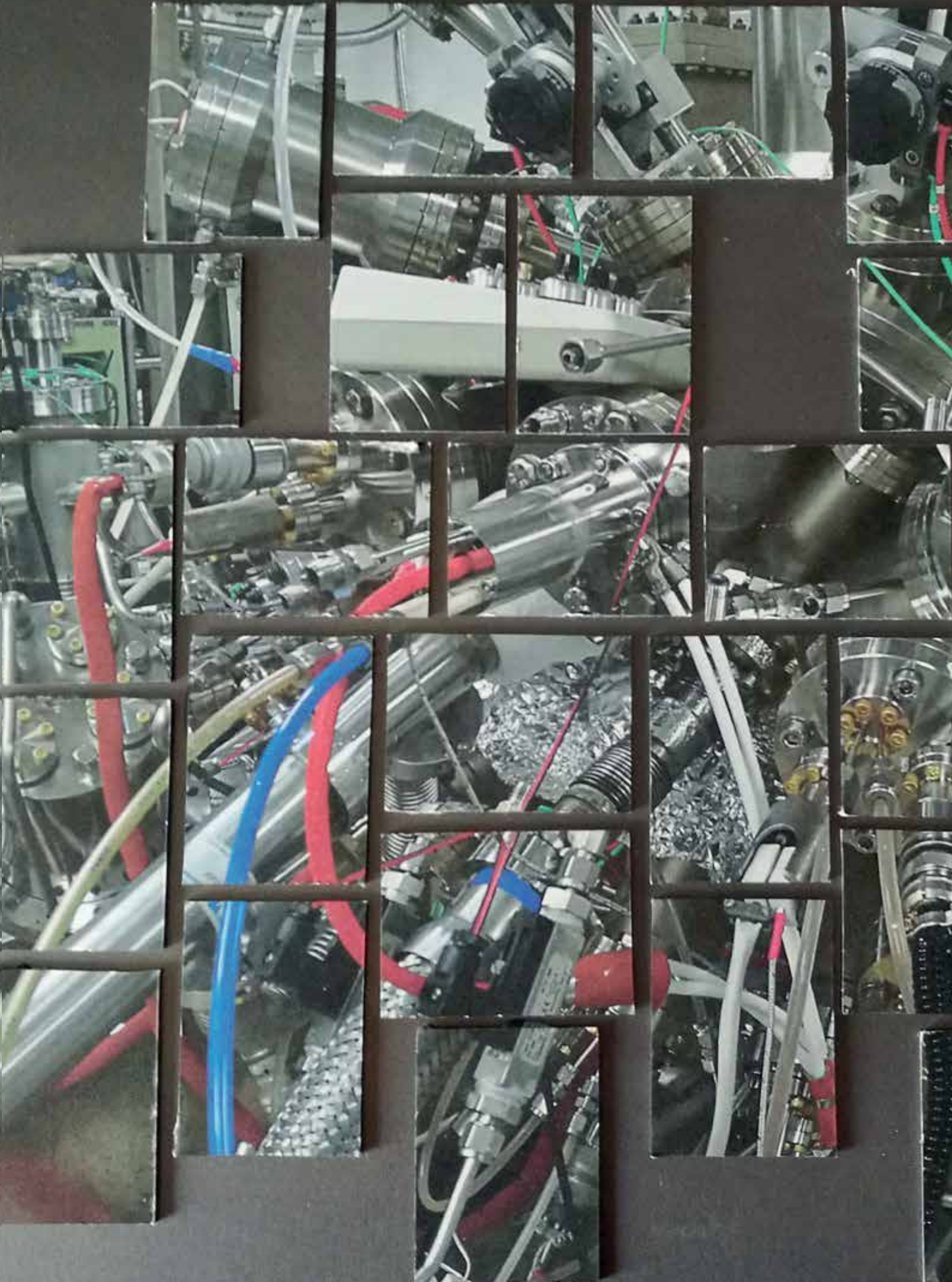
Ich möchte an dieser Stelle allen Mitarbeiterinnen und Mitarbeitern des Instituts meinen ungeteilten Dank dafür aussprechen, dass sie durch ihre kreative und engagierte Arbeit unsere Forschungen beständig vorantreiben. Auch danke ich den zahlreichen Mitarbeiterinnen und Mitarbeitern, die unseren Jahresbericht aktuell und attraktiv gestaltet haben.

Letztlich möchte ich diesen Jahresbericht wiederum nutzen, um allen wissenschaftlichen Kooperationspartnern in unserem akademischen und industriellen Umfeld für die zahlreichen fruchtbaren Zusammenarbeiten zu danken. Herzlich bedanken möchte ich mich ebenso bei den Mitgliedern unseres wissenschaftlichen Beirats für die engagiert kritische Begleitung unserer Arbeit, sowie bei unseren Fördergebern beim Bund und beim Land Berlin.

Ich wünsche Ihnen viel Freude bei der Lektüre und freue mich auf weitere fruchtbare Zusammenarbeit,



Henning Riechert



CSW 2017

Compound Semiconductor Week 2017



PDI between basic research and application

Das PDI zwischen Grundlagenforschung und Anwendung

In recent discussions with the supervisory board of the Forschungsverbund Berlin concerning PDI's concept and likewise in meetings with political representatives in the framework of "Leibniz in Parliament", we were faced with the question how our institute should position its work between fundamental research and application. Obviously, funding agencies expect that we rapidly and visibly provide solutions to today's technological and societal challenges. This is as well the premise of all institutions of the Leibniz Association: research for the benefit of society. How can we respond to this—or asked in a different way, how much basic research is necessary at PDI, how much application can be feasible?

The central mission to which we agreed with our scientific advisory board and which we laid out in the framework of the last evaluation, encompasses pushing the outermost borders of materials and nanoscale devices for solid-state electronics and photonics. The evaluation has confirmed our approach to use our outstanding expertise in molecular beam epitaxy with its extreme control and accuracy on an atomic scale to realize novel nanostructures.

Obviously our topics, which are driven by novel materials, innovative nanostructures and their physics, are at the forefront of research for semiconductor technology. New ideas and concepts, such as the employment of III-V nanostructures in silicon technology or in silicon photonics typically take more than 10 years to find their way into marketable devices. In this process many approaches need to be tested, stringent comparisons with existing technologies have to be drawn and ever so many new routes need to be explored.

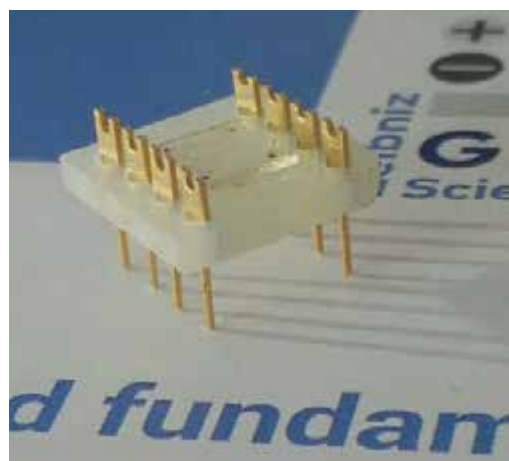
In der jüngsten Diskussion mit dem Kuratorium des Forschungsverbund Berlin e.V. über das Institutskonzept des PDI und auch in Gesprächen mit Abgeordneten im Rahmen von „Leibniz im Bundestag“ kam immer wieder die Frage auf, wie sich unser Institut mit seiner Arbeit im Spannungsfeld zwischen grundlegender Forschung und Anwendung positionieren sollte. Verständlicherweise erwarten die Fördergeber, dass wir möglichst sichtbar und auch schnell Beiträge zu Lösungen von aktuellen technischen und gesellschaftlichen Fragestellungen liefern sollen. Dies ist ja auch der Ansatz aller Einrichtungen der Leibniz-Gemeinschaft: Forschung zum Wohl der Gesellschaft. Wie können wir dem nachkommen – oder anders gefragt, wieviel Grundlagenforschung ist am PDI nötig, wieviel Anwendung ist möglich?

Die zentrale Mission, die wir uns im Rahmen der letzten Evaluierung und mit unserem wissenschaftlichen Beirat gesetzt haben, besteht darin, die äußersten Grenzen von Materialien und nanoskaligen Bauelementen für die Festkörperferelektronik und Photonik weiter herauszuschieben. Die Evaluierung hat uns darin bestärkt, uns weiterhin auf unsere herausragende Expertise in der Molekularstrahlepitaxie zu stützen und ihre außergewöhnliche Kontrolle und Genauigkeit auf atomarer Skala für die Realisierung neuartiger Nanostrukturen konsequent zu nutzen.

Offensichtlich liegen unsere Themen, die durch neue Materialien, neue Nanostrukturen und deren Physik getrieben werden, weit im Vorfeld der halbleitertechnologischen Forschung. Neue Ideen und Konzepte wie z.B. der Einsatz von III-V-Nanostrukturen in der Si-Technologie oder der Si-Photo-

In my opinion, the most important motivation for our work is based on the fact that true innovation arises only on the basis of fundamental research. Incremental development is not sufficient. True innovation requires that novel approaches are envisioned and experimentally proven—which is our expertise and therefore defines our research tasks. It by the way involves the duty of protecting intellectual property, which at this fundamental level is usually most valuable.

In order to make our specific role in the chain of innovations understood and appreciated, we obviously have to elucidate which research tasks need to be fulfilled and how their character changes in the process of turning a new idea into a realistic device. While research in the later phase is rather evolutionary, device-driven and characterized by engineering, the required expertise in the early phase of developments needs to be much more exploratory and built on fundamental research. Typically, this whole chain of development cannot be covered by a single institution—also because the mentality in the approach necessarily changes from being curiosity driven ("which new effect can be envisioned, how can I understand this, what can I do with it") to application driven ("how can I do this better, faster, more cost efficiently ..., where else can I apply this"). There is typically a division of tasks in our broad field of research which has largely proven to be successful.



nik benötigen typischerweise mehr als zehn Jahre, um ihren Weg in die Anwendung zu finden. Dabei müssen viele Ansätze getestet, harte Vergleiche mit bestehenden Technologien ausgestanden und auch immer wieder neue Wege gesucht werden.

Die entscheidende Motivation für unsere Arbeiten liegt nach meiner Ansicht darin, dass echte Innovation nur auf der Basis von grundlegender Forschung zustande kommt. Inkrementelle Weiterentwicklung reicht nicht aus, sondern neue Ansätze müssen erdacht und experimentell erprobt werden – hier liegt unsere Expertise und hieraus definiert sich unsere Aufgabe. Sie beinhaltet im Übrigen auch die Verpflichtung zum Schutz von intellectual property, das auf grundlagen-naher Ebene meist besonders wertvoll ist.

Damit unsere spezifische Rolle in dieser Innovationskette verstanden und geschätzt werden kann, müssen wir offensichtlich erläutern, welche Forschungsaufgaben zu erfüllen sind und wie sich deren Charakter im Laufe der Umsetzung einer neuen Idee verändert. Während in der späteren Phase eher bauelementgetriebene, evolutionäre und ingenieurwissenschaftlich geprägte Aktivitäten dominieren, ist die benötigte Expertise in der frühen Phase entsprechender Entwicklungen sehr viel explorativer, wissenschaftlicher und grundlagenorientierter geprägt. In der Regel ist die gesamte Kette der Entwicklung nicht in einer Institution allein abzudecken – auch weil die Mentalität der Herangehensweise sich von Neugierde-getrieben („was geht da, wie kann ich das verstehen, was kann ich damit machen“) zu Anwendungs-getrieben („wie geht das besser, schneller, kostengünstiger ... wo kann ich das noch anwenden“) ändern muss. Diese Art der Arbeitsteilung ist in unserem breit aufgestellten Arbeitsgebiet etabliert und hat sich im Großen und Ganzen bewährt.

Konkret bedeutet dies für unser Institut, dass wir uns auf den grundlagennahen Teil

Specifically for PDI this means that we concentrate on the more fundamental part in the spectrum of tasks. We carry out this work all the way to the realization of meaningful demonstrator structures or device prototypes and publish our results such that they offer a basis for decision in the more application oriented research. To put it more briefly, we are the scouts who point out the most promising ways towards application in the multitude of emerging novel materials and physical effects.

So what does it mean for PDI to be oriented towards application? This target of our research is manifested in our "Institutskonzept" where we pledge to take up explicitly and only projects which exhibit a clear potential for device applications. Consequently, we characterize our work by the term "device-inspiring research".

des Aufgabenspektrums konzentrieren. Diese Arbeiten treiben wir dann bis zur Realisierung aussagekräftigen Demonstrator-Strukturen oder Bauelement-Prototypen und publizieren unsere Ergebnisse so, dass wir eine richtungsweisende Entscheidungsbasis für anwendungsnähere Forschung bieten. Kurz gesagt sind wir die Pfadfinder, die in der Fülle vielversprechender neuer Materialien und physikalischer Effekte die tragfähigsten Wege zur Anwendung hin aufzeigen.

Was bedeutet unter diesen Umständen für das PDI „Anwendungsorientierung“? Dieses Ziel unserer Forschung manifestiert sich dadurch, dass wir uns in unserem Institutskonzept dazu verpflichten, gerade solche und auch nur solche Projekte neu aufzunehmen, die das Potenzial für neue Bauelementanwendungen haben. Nicht zuletzt aufgrund dieses Anspruches charakterisieren wir unsere Arbeit durch den Begriff „device-inspiring research“ (Bauelemente-inspirierende Forschung).

Prof. Dr. Manfred Bayer
Fakultät Physik, Experimentelle Physik 2, TU Dortmund,
44221 Dortmund, Deutschland

Prof. Oscar Dubon
UC Berkeley 210 Hearst Memorial Mining Building
#1760 Berkeley, CA 94720 USA

Dr. Steven C. Erwin
Center for Computational Materials Science, Naval Research Laboratory,
Washington, DC 20375, U.S.A.

Prof. Dr. José Manuel Calleja Pardo
Departamento de Física de Materiales, Universidad Autónoma de Madrid,
Cantoblanco, 28049 Madrid, Spain

Dr. Heike Riel
IBM Research – Zurich
Säumerstr. 4 CH-8803 Rüschlikon Schweiz

Dr. Matthias Sabathil
Osram Opto Semiconductors GmbH, OSCTO ACE
Leibnizstr. 4
93055 Regensburg, Deutschland

Prof. Dr. James S. Speck
Materials Department, University of California,
Santa Barbara, CA 93106-5050, U.S.A.

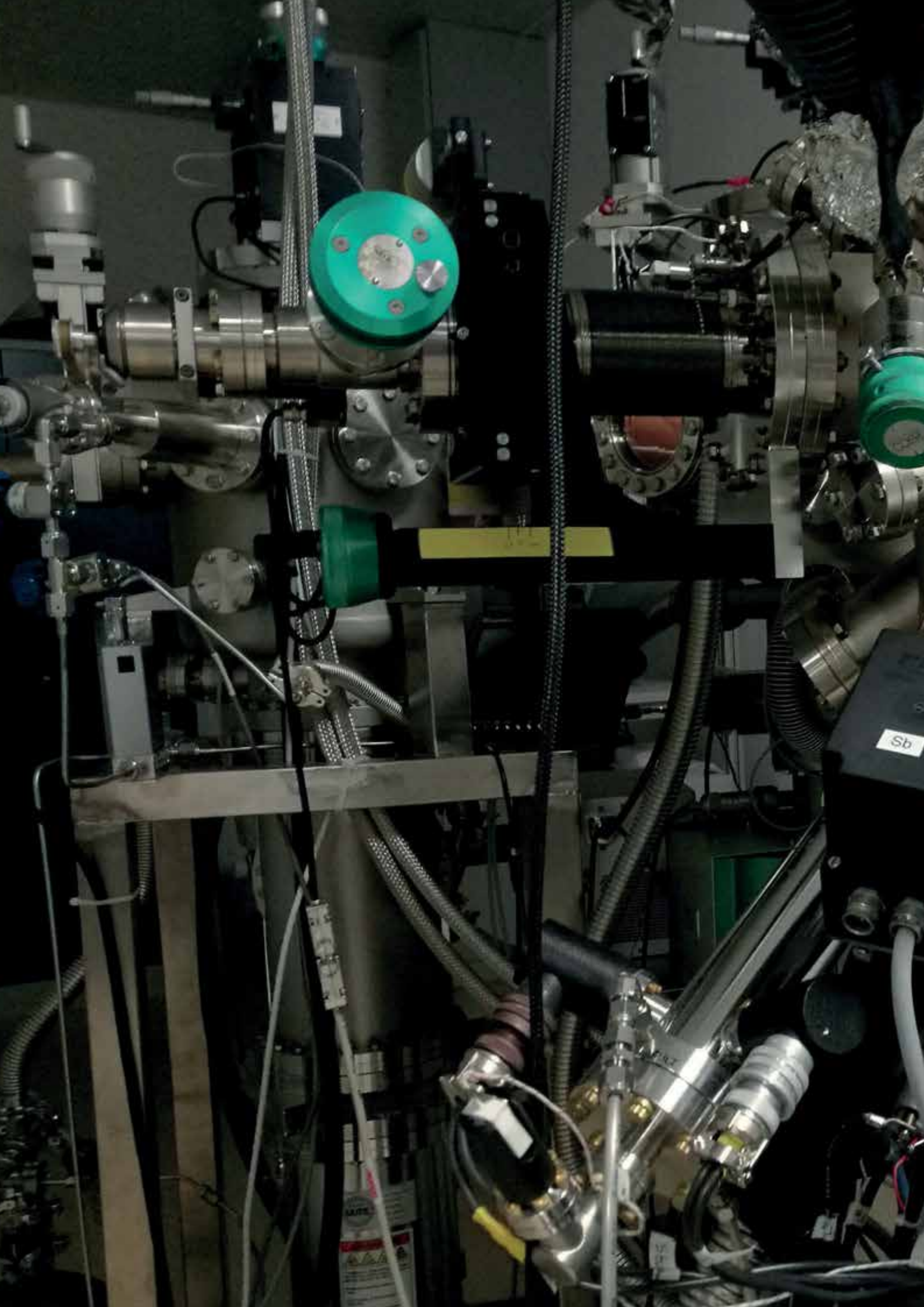
Prof. Werner Wegscheider
Advanced Semiconductor Quantum Materials Laboratory
for Solid State Physics ETH Zürich
Otto-Stern-Weg 1 CH-8093 Zürich

Prof. Dr. Matthias Wuttig
I. Physikalisches Institut (IA), RWTH Aachen,
Sommerfeldstraße 14, 52074 Aachen, Germany

Dr. Hiroshi Yamaguchi
NTT Basic Research Laboratories,
Nippon Telegraph and Telephone Corporation, 3-1, Morinosato Wakamiya,
Atsugi-shi, Kanagawa 243-0198, Japan

A photograph showing a group of people in what appears to be a meeting or conference room. In the foreground, a man with grey hair and a suit is looking down thoughtfully with his hand near his chin. Behind him, another man wearing glasses and a dark jacket is also looking down. The background shows other people and a whiteboard or screen. A large white rectangular box is overlaid on the upper portion of the image, containing the text.

Scientific Advisory Board Wissenschaftlicher Beirat





Research Highlights

Forschungshighlights

Van-der-Waals-Wachstum von zweidimensionalem, hexagonalem Bornitrid auf Graphen	18
Van der Waals growth of two-dimensional hexagonal boron nitride on graphene	19
Selbstorganisiertes Wachstum von Quantenpunkten auf GaAs(110)-Oberflächen in der Form von planaren Schichten und Nanodraht-Facetten, getrieben durch eine Surfactant-induzierte morphologische Instabilität	26
Quantum Dot Self-Assembly on GaAs(110) Planar Layers and Nanowire Facets Driven by a Surfactant-Induced Morphological Instability	27
Einfluss eines externen reverse bias auf den Rekombinationsmechanismus in Ga-polar (In, Ga)N/GaN Leuchtdioden	32
Influence of an external reverse bias on the recombination mechanism in Ga-polar (In,Ga)N/GaN light-emitting diodes	33

Van-der-Waals-Wachstum von zweidimensionalem, hexagonalem Bornitrid auf Graphen

Angeführt von der Entdeckung von Graphen – einer zweidimensionalen (2D) Modifikation des Kohlenstoffs – wuchs im letzten Jahrzehnt das Interesse an einer ganzen Klasse von planaren Materialien, die aus einzelnen Atomlagen besteht. Seither wurden weitere dieser Materialien mit metallischen, halbleitenden oder isolierenden Eigenschaften identifiziert, die durch vertikales Stapeln zu einer Vielzahl neuartiger Heterostrukturen kombiniert werden können. Dies gestattet neue Gestaltungsmöglichkeiten für elektronische Bauelemente, die aus nur noch wenigen Atomlagen bestehen, was in Zukunft etwa flexible und transparente elektronische Anwendungen ermöglichen könnte. Hexagonales Bornitrid (hBN), eine dem Graphen ähnliche Anordnung von Bor- und Stickstoffatomen, ist zum Beispiel wegen seiner großen Bandlücke (~ 5.2 eV) als Dielektrikum für den Einsatz in 2D Transistoren oder in Kondensatoren von Interesse. Des Weiteren werden andere 2D Materialien meist mit mehreren Lagen elektrisch isolierendem hBN umschlossen, um sie so vor negativen externen Einflüssen abzuschirmen.

Momentan werden für die Herstellung von 2D Heterostrukturen die einzelnen 2D Materialien von ihrem dreidimensionalen, kristallinen Pendant „abgeschält“ (zum Beispiel Graphen von Graphit) und aufeinander gestapelt. Obwohl so erste funktionsfähige 2D Heterostrukturen hergestellt werden konnten, ist dies doch ein langwieriger Prozess, der grundsätzlich nicht skalierbar ist. Zudem führen die Transferschritte der unterschiedlichen 2D Materialien häufig zu Verunreinigungen der Oberflächen, was deren Eigenschaften wiederum negativ beeinflusst.

Um nun die Herstellung von 2D Heterostrukturen weiterzuentwickeln, untersuchen wir in diesem Beitrag das direkte Wachstum von hBN auf Graphen mittels Molekularstrahlepitaxie. Als Substrat wurde epitaktisches Graphen auf SiC verwendet. Dieses zeichnet sich durch seine hohe kristalline Güte und die Möglichkeit, es direkt auf einem dielektrischen Substrat abzuscheiden, aus. 2D Materialien besitzen im Prinzip keine Bindungen außerhalb ihrer Ebene, wodurch sich bei ihrem Wachstum anstelle von stabilen kovalenten Bindungen zwischen ihren Schichten van-der-Waals-Wechselwirkungen ausbilden. Die unterschiedlich lange und bei unterschiedlichen Temperaturen gewachsenen 2D Heterostrukturen wurden mittels rasterkraftmikroskopischer Methoden sowie Raman- und Röntgenphotoelektronenspektroskopie untersucht. Hierbei zeigte sich eine Keimbildung des hBN an Defekten im Graphen, von welchen dann eine 2D Schicht hBN in der Ebene wächst. Der isolierende Charakter dieser hBN Schichten konnte mittels elektrischer Messungen mit einem Rasterkraftmikroskop aufgezeigt werden. Zudem wurde ersichtlich, dass an den Kristallisationskeimen zusätzliche hBN Schichten in vertikaler Richtung aufeinander wachsen. Die Ergebnisse in diesem Beitrag dienen damit dem Verständnis der Keimbildung während des van-der-Waals-Wachstums von 2D Materialien, was einen ersten Schritt hin zu einem kontrollierten und skalierbaren Kristallwachstum von 2D Heterostrukturen darstellt.

Van der Waals growth of two-dimensional hexagonal boron nitride on graphene

M. Heilmann, M. Bashouti¹, H. Riechert, and J. M. J. Lopes

Hexagonal boron nitride (hBN), an insulating isomorph of graphene, is a promising building block as a dielectric layer in novel, atomically thin and flexible two-dimensional (2D) electronic devices such as graphene-based capacitors or field-effect transistors. It is also preferentially used as a substrate or as a van der Waals (vdW) bonded encapsulating layer for other 2D materials as it improves their electronic properties by shielding them from environmental influences.

So far such 2D heterostructures have been demonstrated by mechanically stacking hBN and graphene sheets which were exfoliated from their bulk counterparts. However, this approach is time-consuming, inherently non-scalable and the interfaces may suffer from impurities introduced during transfer processes. To advance 2D heterostructures with clean interfaces and to process them on large area, a heteroepitaxial growth within a controlled environment will be crucial.

In this work, we perform a direct growth of insulating hBN on graphene by molecular beam epitaxy (MBE). Hexagonal BN was grown for varying durations and at different temperatures to study its evolution from nucleation to coalesced layers during the vdW epitaxy. For a comprehensive growth study a reliable and reproducible fabrication of graphene substrates is indispensable. Consequently, we fabricated high quality epitaxial graphene (EG) via controlled sublimation of Si from SiC(0001), which could be used as a substrate without any transfer processes.

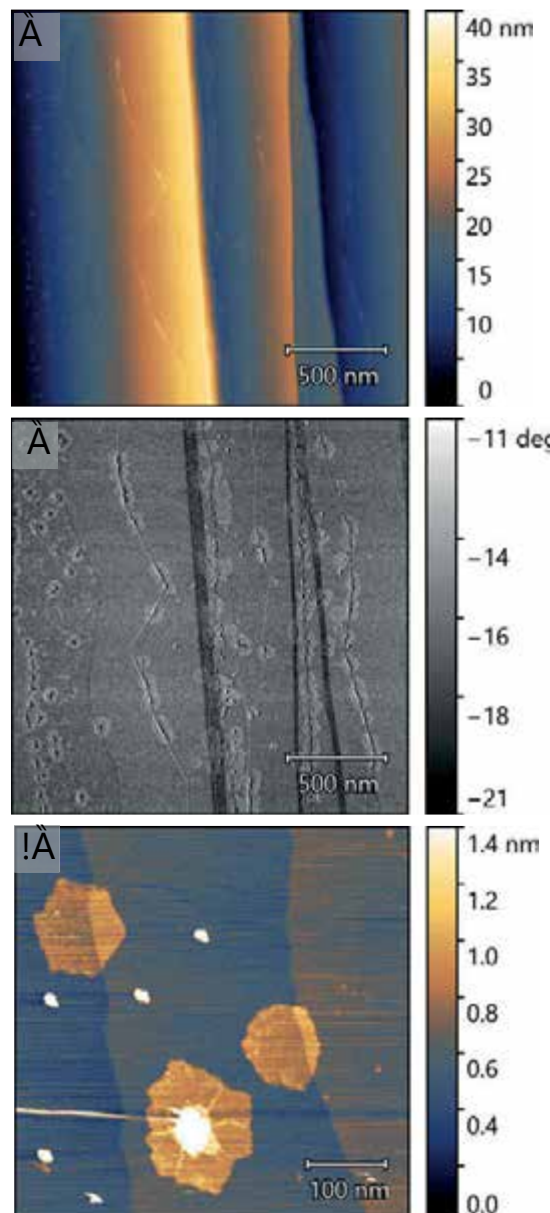


Fig. 1. (a) AFM and (b) corresponding phase contrast image of hBN grown on EG for 300 min at 850 °C. (c) Detailed AFM image of hBN islands.

¹ Jacob Blaustein Institute for Desert Research, Seder Boqer Campus, Ben-Gurion University of the Negev, Sede Boqer, Israel

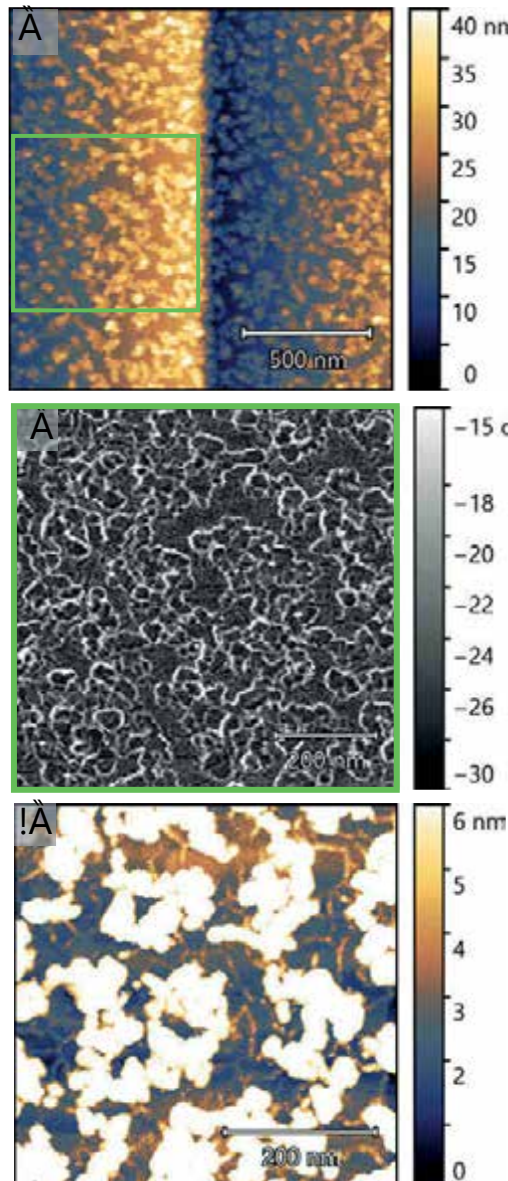


Fig. 2. (a) AFM image of hBN grown for 600 min at 850°C. (b) Phase contrast image of the area marked with a green frame in (a). (c) Detailed AFM image of wrinkled hBN ML and NPs from another sample area. The height scale was adjusted to the hBN ML, hence the NPs are out of scale.

Figure 1(a) shows an atomic force microscopy (AFM) image of a representative sample area after 300 min growth of hBN at 850°C on EG. The most pronounced surface features are the step edges of EG with heights up to 25 nm and terraces (width up to 1 μm) of SiC with graphene on top. The

EG contains wrinkles of 2 to 3 nm height, which formed during its fabrication procedure. Nanoparticles (NPs) with heights of about 4 nm formed along morphological defects on EG (e.g. step edges and wrinkles). The phase contrast image in Fig. 1(b) reveals hexagonally shaped areas of brighter contrast around these NPs, with a diameter of about 100 nm. The different phase contrast of these areas suggests a different composition of the scanned material, which we assume to be hBN.

The detailed AFM image in Fig. 1(c) shows two different hBN islands, one has a smooth surface and a hexagonal shape and the other nucleated at a wrinkle with a cluster of NPs in its center and is slightly distorted. From the NPs, line shaped features spread radially on the island, which we assume to be lines of coalescence between differently in-plane oriented hBN domains. The hBN islands have a height of about 0.33 nm, which is consistent with the vdW separation between graphene and hBN monolayers (MLs).

Prolonging the growth time to 600 min led to the surface being completely covered by NPs with heights up to 12 nm [see Fig. 2(a)]. The phase contrast image in Fig. 2(b) shows no difference between their flat top facets and the lower areas between them. This indicates that the entire surface is covered by hBN, and that the NPs consist of the same material. In the detailed AFM image in Fig. 2(c) line shaped features are visible in between the NPs. These can be wrinkles forming in hBN due to a different thermal expansion coefficient as compared to EG. The higher density of NPs after 600 min is attributed to the formation of additional nucleation sites at defective lines of coalescence between differently in-plane oriented hBN domains.

Observing the growth behavior of hBN over time leads us to the conclusion that NPs initially nucleate at wrinkles and step edg-

es in EG. At these morphological defects additional hBN MLs grow on top of each other forming NPs. As the first ML coalesces, the defective lines between differently oriented hBN ML islands allow the formation of additional NPs. In a second growth series, hBN samples were grown at temperatures of 630°C and 1000°C for 300 min. For the lower growth temperature, the surface got completely covered with hBN [see AFM image in Fig. 3(a)]. The continuous hBN ML contains wrinkles similar to the ones observed in Fig. 2(c). However, the clustered NPs have a height of only about 3.5 nm, which is rather similar to the NPs formed after 300 min of growth at 850°C. The AFM and phase contrast images of the sample grown at 1000°C are shown in Figs. 3(b) and 3(c). Compared to the sample grown at 850°C for 300 min, the diameter of the ML islands is reduced to about 75 nm, while the height of the NPs is similar. Increasing the growth temperature also increases the desorption rate of B and N adatoms from the surface, thus leading to a lower growth rate of hBN. The height of the NPs remains mostly independent of the growth temperature, while their density is strongly increased at a growth temperature of 630°C. The latter point can be related to a lower desorption rate of B and N and thus to a higher nucleation density on EG, as well as to a higher surface coverage of hBN with additional nucleation sites at lines of coalescence in the first ML, similar to Fig. 2.

Comparing the hBN ML islands grown at 850°C (see Fig. 1) and 1000°C [see Figs. 3(b) and 3(c)] shows a larger size of the extended ML islands at lower temperatures at a constant time and a constant supply of material. This indicates that the in-plane growth of hBN MLs is governed by the desorption of the adatoms. This conclusion was supported by growing a sample under similar conditions as used for the sample shown in Fig. 1, but at a reduced flux form the B source (not shown here), which resulted in the formation of NPs with

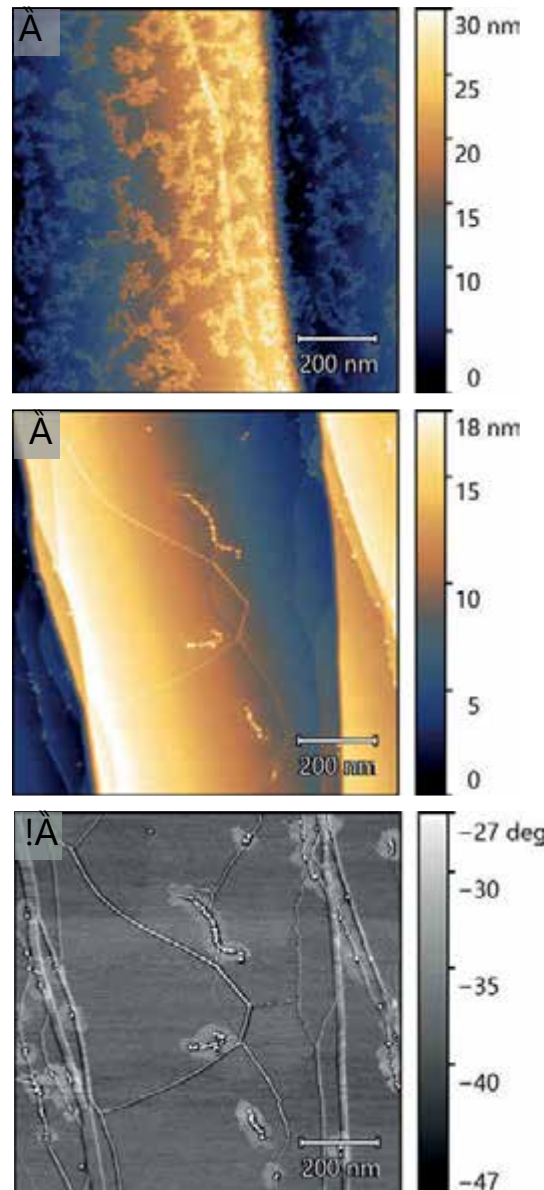


Fig. 3. (a) AFM image of hBN grown on EG for 300 min at 630°C. (b) AFM and (c) corresponding phase contrast image of hBN grown for 300 min at 1000°C.

a mean height of 2.5 nm without extended hBN MLs.

The chemical bonds in the sample grown for 600 min at 850°C were investigated by X-ray photoelectron spectroscopy (XPS). Figure 4(a) shows the XPS core level spectra around the B1s region with a peak at 190 eV, which is attributed to B bonded to N. Consequently, there is also a peak of N

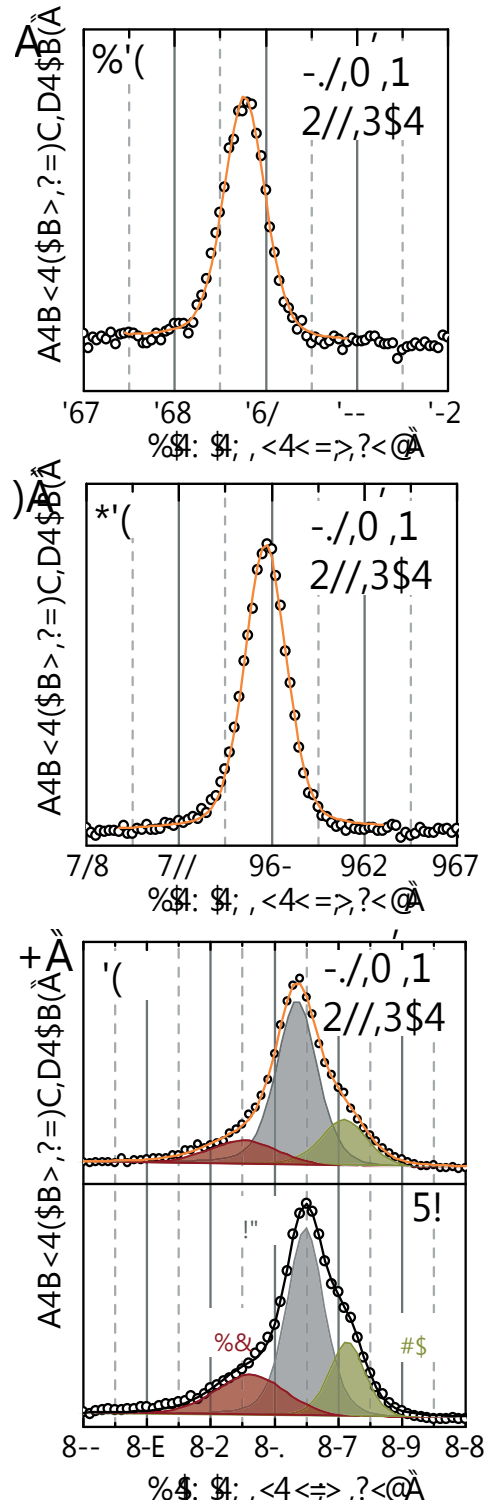


Fig. 4. XPS core level spectra of (a) the B1s, (b) the N1s and (c) C1s region for the sample grown at 850 °C for 600 min. In addition, (c) shows a comparison with bare EG.

bonded to B detected in the N1s region at 398.1 eV [see Fig. 4(b)]. A comparison of the corrected areas of these two peaks yields a ratio between B and N of about 1, as it would be expected for hBN with one B and one N atom per unit cell. The measurement points (black circles) from both peaks can be well fitted with a single Lorentzian (orange lines), demonstrating the purity of the hBN samples with no pronounced intermixing with C. Figure 4(c) shows the spectral region around the C1s peak from the hBN sample (upper panel) and compares it to bare EG (lower panel). The spectra appear similar with a peak at 284.5 eV attributed to the sp^2 bonded C in graphene (C_{GR}). Shoulders at the higher and lower energetic flank are attributed to sp^3 bonded C in the buffer layer (BL) at the interface between EG and SiC (C_{BL}) and to bulk SiC (C_{SiC}), respectively, demonstrating no pronounced influence of the hBN growth on the EG. The latter point was supported by Raman measurements (not shown here), which demonstrated no increase in defect density in EG after the growth of hBN.

The same area of the sample grown at 850 °C for 300 min [see Fig. 5(a)] was investigated by tunneling current AFM (TUNA) and Kelvin probe force microscopy (KPFM) using a Pt/Ir coated tip. A constant tunneling current of about 1 nA was measured on bare EG at a bias of 250 mV [see Fig. 5(b)], which was reduced around the hBN NPs and ML islands. As defect-free hBN with a large band gap of 5.2 eV is an insulator there should be no occupied states from where the electrons could tunnel to the tip. Figure 5(c) shows the contact potential difference (CPD) between tip and sample of the same area as in Fig. 5(a). The CPD at the step edges (marked by white lines) is attributed to fewlayer graphene (FLG), as there is no influence of the BL. On the terraces three discrete CPD values -of 0 mV (purple), 100 mV (cyan) and 150 mV (green) are apparent and attributed to FLG, BLG and single-layer graphene (SLG). There is

a stronger charge transfer from the BL to the SLG, which decreases for additional layers due to screening effects. Hexagonal BN NPs and ML islands elevate the CPD, which is attributed to the different dielectric constant of hBN or to interface dipoles. A higher nucleation density of hBN is visible on SLG, probably due to a higher defect density or attractive forces from the BL.

A detailed AFM image of the same sample is displayed in Fig. 6(a) with the corresponding TUNA image at higher sensitivity in Fig. 6(b). A small tunneling current was detected in bare ML islands, either in the center (marked by the magenta dotted circle) or at their border (magenta arrow). These currents are attributed to defects in the insulating 2D layer, where hBN nucleated via covalent bonds at point defects in EG. Furthermore, higher tunneling currents are detected at the periphery of the NPs (marked by the transparent green circles). These measurements confirmed that hBN nucleates preferentially at defects in EG, from where ML islands may extend laterally, while additional hBN MLs form NPs. Even though defects can pass through to upper hBN MLs in the NPs they are eventually terminated and leave additional MLs on the top free from defects. Furthermore, these data show that in addition to morphological defects, point defects can induce nucleation. The same measurements were conducted on a completely covered sample where hBN was grown at 850°C for 600 min. The AFM and TUNA images of this sample can be seen in Figs. 6(c) and 6(d), respectively. Nearly the complete surface appears insulating, with small tunneling currents only detected at wrinkles in EG, which shows that defective hBN at NPs gets covered over time by additional defect-free MLs.

In summary, our comprehensive growth study revealed the evolution of 2D hBN during the growth on EG by MBE from nucleation to coalescence. The integrity of EG

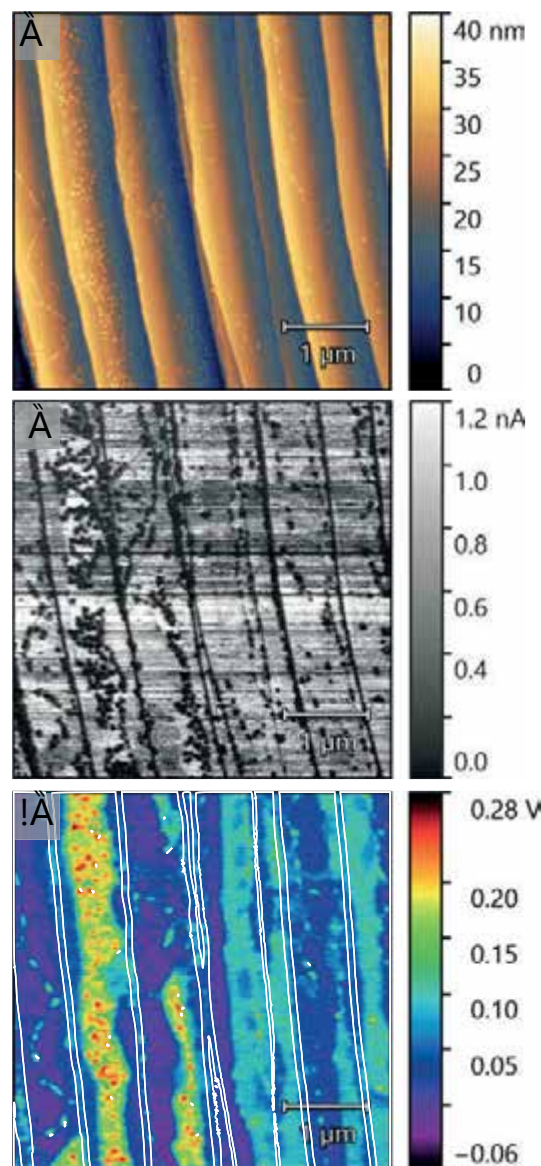


Fig. 5. (a) AFM image from hBN grown for 300 min at 850°C with (b) corresponding TUNA and (c) KPFM image (white solid lines represent locations of the step edges).

against the growth of hBN on top and the absence of intermixing have been shown via XPS measurements. A defect-mediated nucleation has been observed (either at point or morphological defects) using a novel combination of TUNA and KPFM. From defects in EG, mobile adatoms on the surface form extended hexagonally shaped hBN islands with a diameter dependent on the

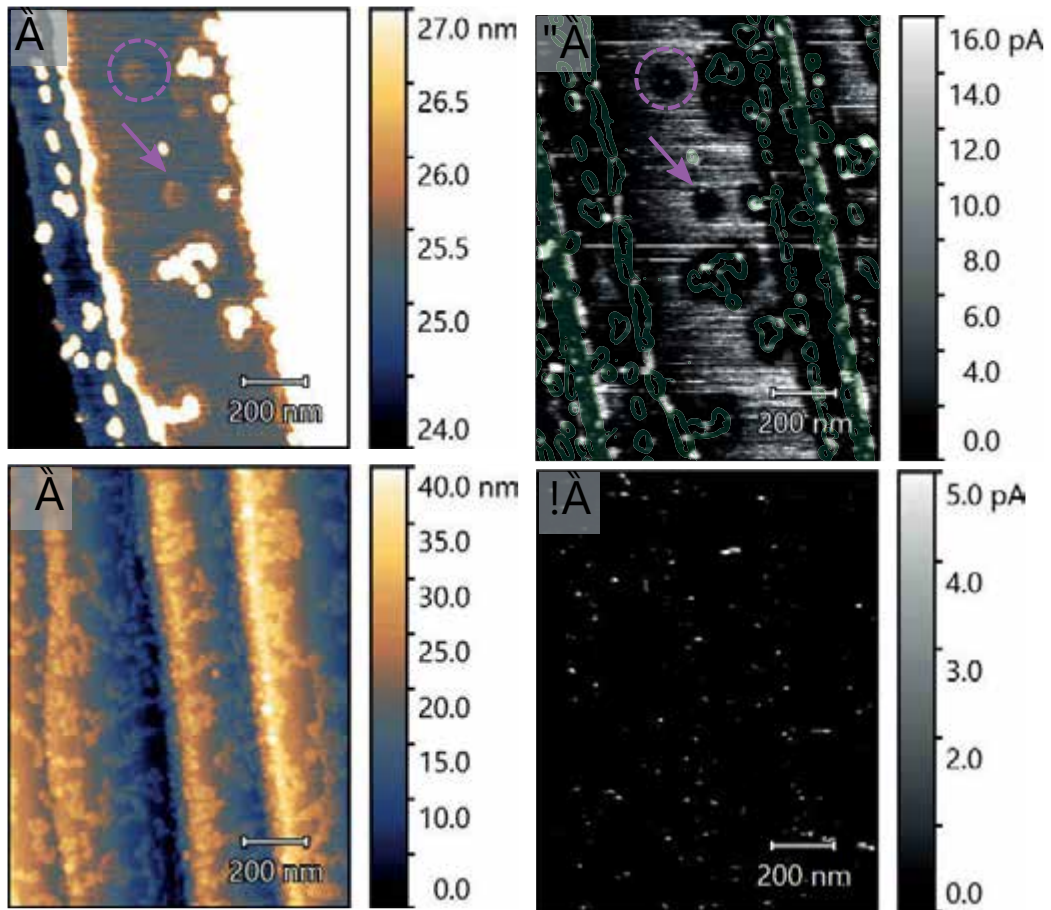
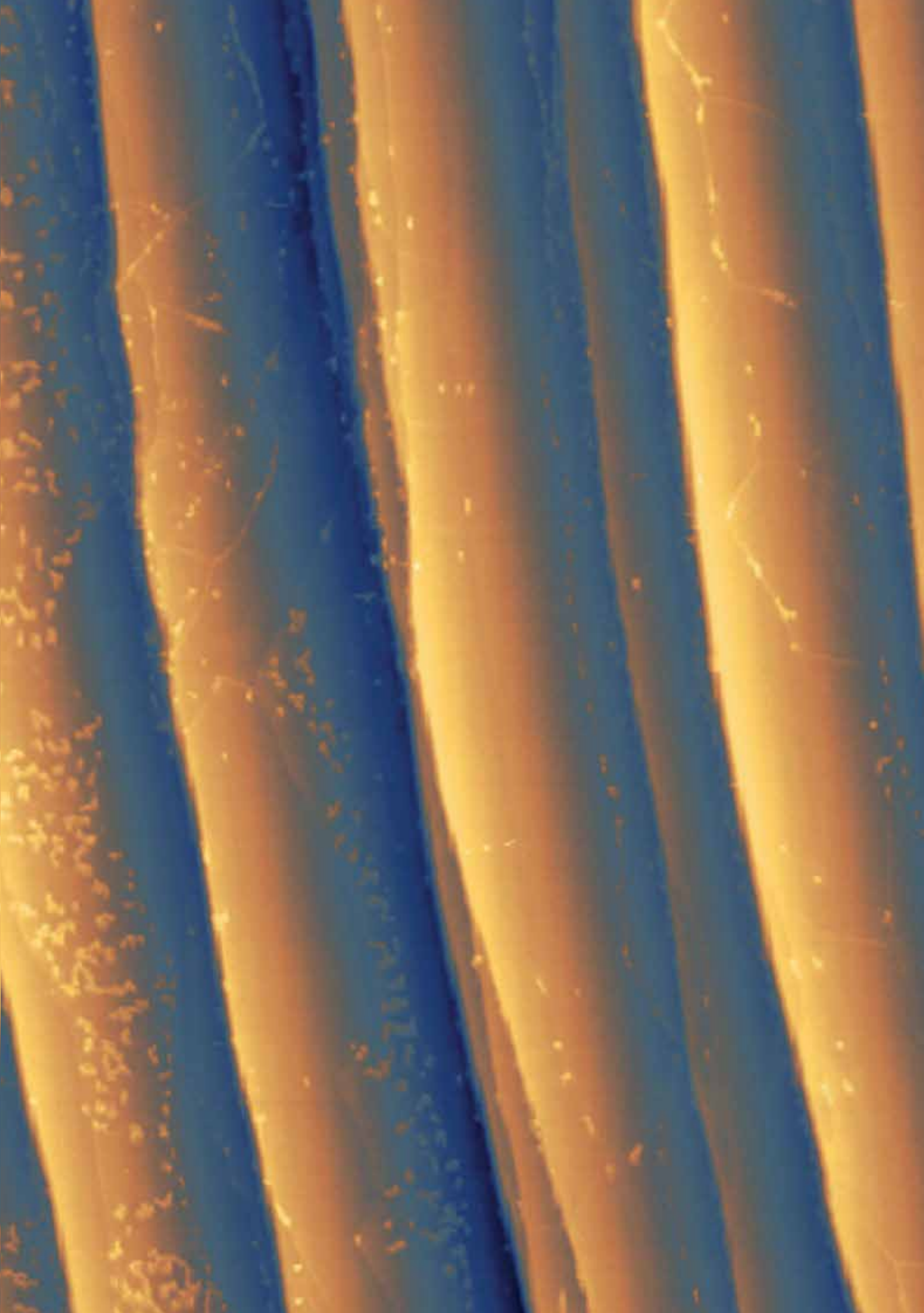


Fig. 6. (a) Detailed AFM image and (b) corresponding TUNA image of the same sample at higher sensitivity superimposed with the local slope in green. The magenta dotted circle and arrow indicate the positions of hBN ML islands. (c) Detailed AFM image and (d) corresponding TUNA image of hBN grown for 600 min at 850°C on EG.

growth time and temperature. Additional hBN layers form NPs over time and cover electronic defects in the first layers. The presented results provide a deeper understanding of nucleation during heteroepitaxy of 2D materials in general and point out a route for a scalable production of 2D heterostructures.



Selbstorganisiertes Wachstum von Quantenpunkten auf GaAs(110)-Oberflächen in der Form von planaren Schichten und Nanodraht-Facetten, getrieben durch eine Surfactant-induzierte morphologische Instabilität

Dreidimensionale (3D) Inseln, die als Quantenpunkte fungieren, werden gewöhnlich durch einen selbstorganisierten Prozess synthetisiert, der Stranski-Krastanov (SK) Wachstum genannt wird – einem von drei fundamentalen Moden des epitaktischen Wachstums. Normalerweise wird der bevorzugte Wachstumsmodus durch energetische Faktoren (Oberfläche, Grenzfläche, Verzerrung) bestimmt, die durch die Wahl des Adsorbats und Substrats festgelegt werden. In Maßen können diese thermodynamischen Einschränkungen kinetisch überwunden werden, so dass 3D-Inselwachstum kinetisch unterdrückt und dadurch zweidimensionales Frank-van der Merwe Wachstum möglich wird. Dazu werden entweder die Abscheidebedingungen entsprechend angepasst, oder die Oberflächenchemie wird durch den Einsatz segregierender Elemente verändert. Nichtsdestotrotz bleibt dabei der energetisch bevorzugte Wachstumsmodus unkontrollierbar. Insbesondere ist es auf diesem Wege nicht möglich, 3D-Inselwachstum zu erzwingen, wenn 2D-Wachstum energetisch bevorzugt ist. Dies hat zur Folge, dass die Präparation von Quantenpunkten in Bezug auf Materialkombinationen und Substratorientierungen Einschränkungen unterliegt.

In diesem Beitrag zeigen wir nun, dass der Einsatz von oberflächenaktiven Substanzen (Surfactants) morphologische Phasenübergänge in verzerrten Schichtsystemen induzieren kann und so das Entstehen von 3D-Inseln „auf Knopfdruck“ möglich wird.

Quantum dot self-assembly on GaAs(110) planar layers and nanowire facets driven by a surfactant-induced morphological instability

R. B. Lewis, P. Corfdir, H. Li, J. Herranz, H. Küpers, C. Pfüller, U. Jahn, O. Brandt, and L. Geelhaar

Three-dimensional (3D) islands that act as quantum dots (QDs) are typically synthesized by a self-assembly process known as Stranski-Krastanov (SK) growth, one of the three fundamental modes of epitaxy. In general, the preferred growth mode of a system is determined by energetic considerations (surface, interface, strain), which are fixed by the choice of adsorbate and substrate. To some extent these thermodynamic constraints can be overcome kinetically, either by adjusting deposition conditions or by changing the surface chemistry using surface segregating elements, allowing 3D island formation to be kinetically suppressed in favor of two-dimensional (2D) Frank-van-der-Merwe (FM) growth. However, control over the energetically preferred growth mode, as well as inducing 3D island formation when 2D growth is favored, has remained elusive. And as a result, QD synthesis has been restricted in terms of materials and substrate orientations.

(In,Ga)As on GaAs(001) is considered the model SK system, with 3D island formation occurring for a wide range of compositions and deposition conditions. In contrast, for (In,Ga)As growth on the low index (110) and (111) GaAs surfaces, the 3D SK mode is not observed and deposition always results in a 2D layer with strain relaxing by the formation of dislocations. This is unfortunate since these surfaces have symmetries which differ from (001), and owing to their low energy they are often present in nanowires (NWs).

Here we show that surfactants can provoke morphological phase transitions in strained layers, inducing the formation of 3D islands "on-demand". We explore Bi as a surfactant in the growth of InAs on GaAs(110) by

molecular beam epitaxy, and find that the presence of surface Bi induces SK growth of 3D islands, while growth without Bi always favors 2D layer formation. Density functional theory (DFT) calculations reveal that surface Bi reduces the energetic cost of 3D island formation by altering the surface energy of the GaAs and InAs surfaces. We exploit this effect to induce the formation of InAs 3D nanostructures directly on the $\{1\bar{1}0\}$ sidewalls of GaAs NWs. With increasing InAs deposition, the 3D islands elongate along $\langle 110 \rangle$ directions in the plane of the NW sidewalls, which we exploit to realize a series of novel nanostructures ranging from InAs 3D islands to zig-zag shaped nanorings. The small 3D islands behave as optically active QDs, demonstrating their perspective for quantum optics embedded in GaAs NWs. This work illustrates how modifying surface energies with surfactants can allow for unprecedented control over nanostructure self-assembly and open the door to new possibilities for hierarchical nanostructures.

Figure 1(a)–1(b) shows atomic force microscopy (AFM) topographs after deposition of 2.1 monolayers (MLs) of InAs on GaAs(110), without and with the presence of a 0.4 ML/s Bi flux during the InAs deposition at 420°C. In the absence of Bi [Fig. 1(a)], InAs forms a 2D layer with atomic terraces on the surface. The addition of a Bi flux [Fig. 1(b)] results in a drastically different surface morphology, showing an array of 3D islands with an average height of 4.3 ± 0.5 nm. The presence of 3D islands is in striking contrast to the expectation that InAs deposition on GaAs(110) always proceeds by a 2D FM mode. The islands in Fig. 1(b) are elongated in the $[1\bar{1}0]$ direction, likely a result of the higher adatom

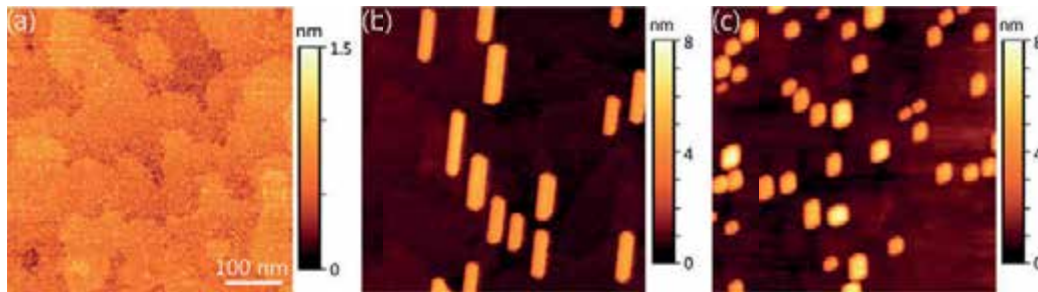


Fig. 1. Surface topographs of 2.1 ML of InAs on GaAs(110) deposited (a) in the absence of Bi, (b) with a simultaneous Bi flux, and (c) with subsequent exposure of a static InAs layer to Bi. In the absence of Bi the surface is atomically smooth, while both growth with the Bi flux and subsequently exposing the 2D InAs layer to Bi result in 3D islands. The presence of Bi on the surface could not be detected with energy-dispersive X-ray spectroscopy, consistent with the assumption that excess Bi desorbed. The horizontal scale is the same for all images and the [1̄10] direction is approximately upward.

diffusion along [1̄10]. During the growth of this sample, the reflection high energy electron diffraction (RHEED) pattern showed a streaky-to-spotty (2D-to-3D) transition at a thickness of about 1.9 ML. The observation of a critical thickness for 3D island nucleation is consistent with SK growth.

The above results demonstrate that the presence of surface Bi can alter the fundamental growth mode of InAs on GaAs(110) from 2D to 3D. In the absence of Bi, 3D islands never form because the critical thickness for their formation is larger than the critical thickness for plastic relaxation (reported to be 2–3 MLs). With the presence of surface Bi, the situation is reversed. To further explore the effect of surface Bi on the morphological stability of InAs, we expose a 2.1 ML thick 2D InAs layer grown without Bi [Fig. 1(a)] to a subsequent Bi flux for 30 s. Figure 1 (c) shows the resulting surface topography. Remarkably, exposing the 2D InAs layer to Bi results in a rearrangement of the InAs into 3D islands. Compared to the sample grown with codeposition of Bi and InAs [Fig. 1(b)], the island density is about three times higher and the dots are more symmetric, suggesting that island nucleation occurs more rapidly. The initiation of the Bi exposure produces an abrupt transition of the RHEED pattern from 2D streaks to 3D spots. Therefore, surface Bi can provoke a morphological

phase transition in static InAs layers, indicating that the effect of surface Bi goes beyond modifying adatom kinetics. In the absence of Bi, the 2.1 ML InAs thickness is below the critical thicknesses for both 3D island formation and plastic relaxation, but in the presence of Bi the layer is thicker than the critical thickness for 3D island formation. Therefore, the morphological stability of the layer can be controlled externally through the Bi coverage, allowing a morphological phase transition to be induced on-demand. This unprecedented external control opens up new possibilities for 3D nanostructure self-assembly.

To elucidate the effect of surface Bi on the surface energy, we carried out DFT calculations. We consider various surface configurations and compare the surface formation energies relative to the energy of the relaxed bulk-truncated 1×1 GaAs(110) surface. The relative surface formation energy is defined as

$$(1) \quad \Delta\gamma = [E_{\text{surf}} - E_{\text{ref}} - \sum n_i \mu_i]/A$$

where E_{surf} and E_{ref} are the total energies calculated for the surface structure and the reference 1×1 GaAs(110) structure, n_i and μ_i are the excess number of atoms (compared to the reference structure) and the chemical potential of element i , respectively, and A is the surface area.

The relative surface energy includes contributions from the strain energy, as well as energy changes due to the surface and interfaces. We find that the most stable configuration for bulk GaAs(110) and InAs(110) surfaces is a single Bi adlayer covering the 1×1 surface. Therefore, for calculations involving InAs epilayers on GaAs(110) we consider only $1\times$ surfaces and a single Bi adlayer. We note that growth of InAs on top of a Bi monolayer is highly energetically unfavorable. Therefore, during InAs growth the Bi layer is expected to remain on the surface. Figure 2 displays the relative surface energy as a function of InAs thickness on GaAs(110) with and without Bi adlayer coverage. In the absence of Bi, $\Delta\gamma$ is negative for an InAs coverage of 1 ML due to the lower InAs surface energy, but positive for higher coverages as a result of strain. Therefore, it is energetically preferable for InAs to wet the GaAs(110) surface. However, beyond 1 ML coverage, the coherent layer is metastable. With the addition of a Bi adlayer, the situation is strikingly different. In this case, the Bi terminated GaAs(110) surface (0 ML InAs) shows a large negative $\Delta\gamma$ of -7.4 meV/ \AA^2 . Thus, Bi behaves as a surfactant on GaAs, reducing the surface energy. With increasing InAs wetting layer thickness $\Delta\gamma$ increases monotonically, due to the increasing strain energy. In contrast to the case without Bi, the lowest energy surface does not contain an InAs wetting layer.

The DFT results indicate that the Bi adlayer reduces the relative surface energies of bulk GaAs(110) and InAs(110). Furthermore, surface Bi reduces the thermodynamic driving force for InAs wetting on GaAs(110), as the lowest energy state is Bi-terminated GaAs(110). In other words, 2D InAs layers under the Bi adlayer always have an energy greater than Bi-terminated GaAs(110) plus bulk InAs. These effects will favor 3D island formation compared to the case without Bi.

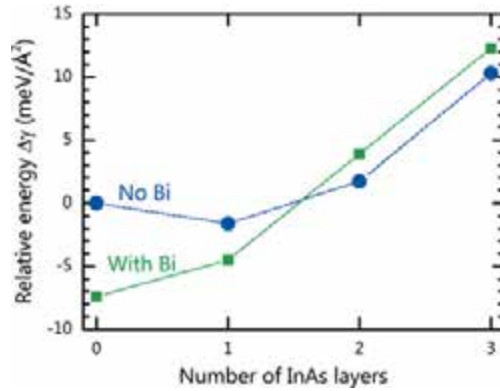


Fig. 2. Relative surface formation energies of InAs/GaAs(110) surfaces with varying InAs coverage for Bi terminated and bare surfaces assuming the 1×1 epitaxial continued layer structure. The in-plane lattice parameter is fixed to that of bulk GaAs.

We now explore the deposition of thin InAs shells around GaAs NWs under the presence of a Bi flux. The sidewall morphologies of 60-nm-diameter NWs with varying nominal InAs shell thicknesses are shown in Fig. 3. For 0.8 MLs of InAs [Fig. 3(a)], the NW sidewalls show no sign of 3D islands, consistent with the existence of a critical thickness for 3D island formation. After 1.4 ML of InAs deposition [Fig. 3(b)], 3D islands become visible on the NW sidewalls. For this sample, individual islands are found to mostly occupy only single sidewall facets. As the InAs thickness is further increased to 2.1 MLs, individual nanostructures elongate and begin occupying multiple facets of the NWs [Fig. 3(c)]. Consistent with growth on planar GaAs(110), the elongation direction is along $\langle 110 \rangle$ directions in the plane of the nanowire sidewalls. As a result, when a 3D island crosses to an adjacent $\{1\bar{1}0\}$ facet, the axial component of the elongation direction reverses. This peculiar growth process results in V-shaped 3D islands when a single nanostructure occupies two adjacent $\{1\bar{1}0\}$ facets. Finally, for the largest deposition thickness of 3.5 MLs [Fig. 3(d)], many structures completely encircle the NW core, producing well defined zig-zag shaped nanostructures. We note that in the absence of Bi, 3D growth of InAs is not

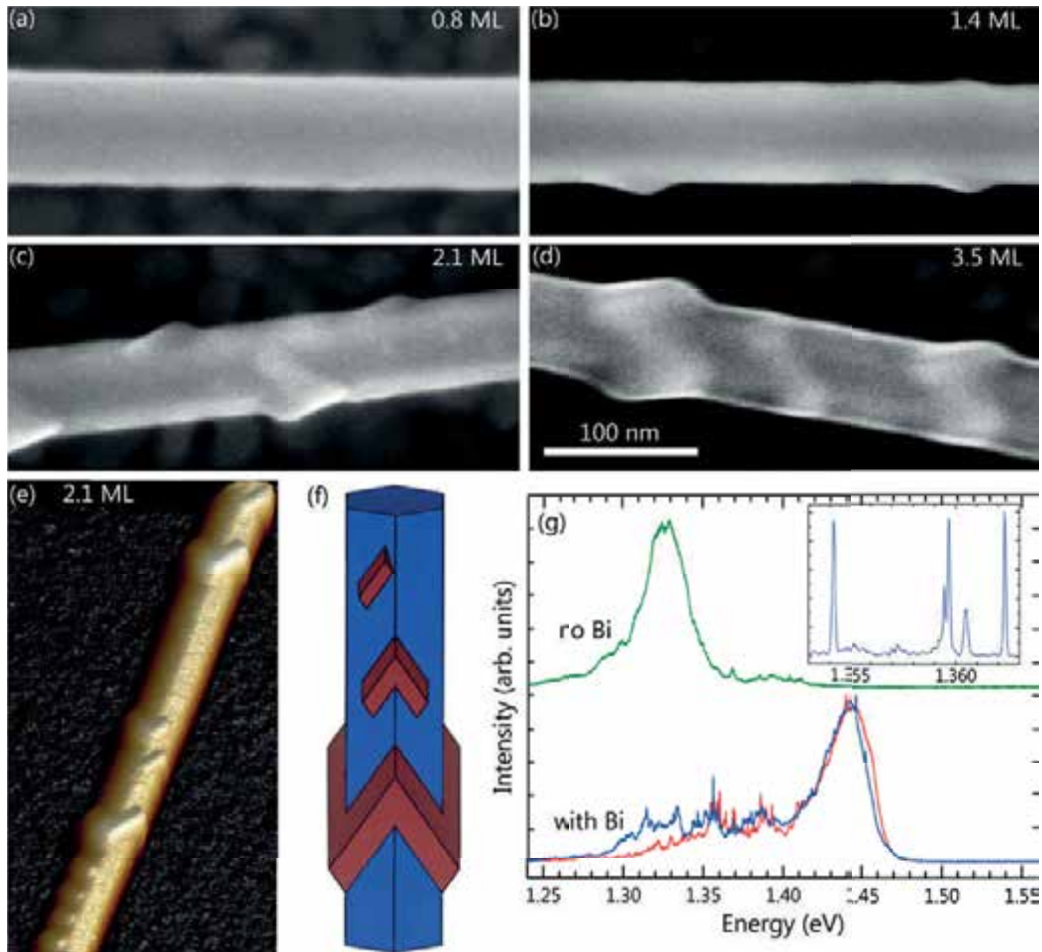


Fig. 3. (a)–(d) SEM images of 60-nm-diameter dispersed NWs after depositing InAs with nominal thicknesses indicated in the figure under a Bi flux of 0.4 ML/s. The viewing direction is normal to the NW axis. (a) No indication of 3D growth is observed after 0.8 MLs of InAs. (b) After 1.4 MLs of InAs, 3D objects appear on the NW sidewalls. (c) With 2.1 MLs of deposition, the 3D nanostructures are observed to occupy multiple sidewall facets, forming V-shaped nanostructures as they cross the facet edges. (d) At 3.5 MLs InAs deposition, zig-zag nanorings completely encircling the NW core are observed. (e) An AFM topograph of a dispersed NW after 2.1 ML of InAs showing an assortment of 3D nanostructures composed of {111} facets and covering both single and multiple facets. (f) Illustration of the observed nanostructures composed of {111} facets on a NW composed of six {1-10} sidewall facets. (g) PL spectra taken at 9 K from as-grown capped NW samples containing 1.4 MLs of InAs grown with and without the presence of a Bi flux. Scans from two regions of the sample grown with Bi show a series of narrow transitions in the 1.3–1.4 eV energy range, and the wetting layer emission is blue-shifted compared to the sample grown without Bi. The inset shows transitions with FWHMs of about 120 eV (resolution limited) from the sample grown with Bi.

observed and a discontinuous shell results (not shown). An AFM topograph of a single NW after 2.1 MLs of InAs deposition is shown in Fig. 3(e), revealing an assortment of nanostructures covering both single and multiple facets. These features have typical heights of 5–9 nm, and are found to exhibit a pair of {111} facets on each {1-10} NW sidewall facet. Figure 3(f) illustrates the family of nanostructures composed of {111} facets. For zig-zag shaped nanorings encircling the GaAs core, the nanostructure

is completely defined by six {111} facets and the NW core. These findings illustrate that Bi not only provokes the self-assembly of InAs 3D islands on the {1-10} sidewalls of GaAs NWs, but the well defined elongation of these islands allows for an array of novel hierarchical nanostructures to be realized.

We have shown that the presence of a Bi flux can provoke the formation of InAs 3D islands directly on the {1-10} sidewalls of GaAs NWs, while the absence of Bi results

in a discontinuous InAs shell. To explore the impact of these morphological changes on the NW optical properties, as-grown NWs of 60 nm core diameter containing 1.4 MLs of InAs deposited with and without the presence of Bi and capped with GaAs/AlAs/GaAs shells were investigated by photoluminescence (PL) and cathodoluminescence (CL) spectroscopy. Figure 3(g) presents PL spectra from these samples. The PL spectrum for the sample grown without Bi is dominated by a band at about 1.33 eV, which we associate with emission from the thin InAs shell. This spectrum exhibits some narrow features with a full width at half maximum (FWHM) of at least 1 meV, which we attribute to local fluctuations in shell width and possibly In content (due to intermixing), as well as the fact that the shell is polytypic. Two spectra are presented for the sample grown with Bi, which are dominated by a band centered at 1.44 eV. On the lower energy side of this band, additional sharp transitions are detected. As shown in the inset of Fig. 3(g), the FWHM for the transitions in the 1.3–1.4 eV energy range is about 120 eV, which corresponds to the spectral resolution of our setup system. We attribute these changes in the PL properties to the fact that when grown using the Bi surfactant, the InAs shell consists of a thin wetting layer covered by 3D islands, giving rise to the broad transition at 1.44 eV and to the narrow lines in the 1.3–1.4 eV energy range, respectively. Cathodoluminescence spectral line scans on individual nanowires confirm that the 1.44 eV emission is delocalized along the NW length while the sharp emission features are spatially localized (not shown). We note that

we also observe transitions of comparable linewidths in the same energy range in the PL spectra of InAs 3D islands of 10 nm diameter and 1–2 nm height grown on planar GaAs(110) substrates using Bi (not shown). We therefore conclude that the transitions observed in the 1.3–1.4 eV energy range in Fig. 3(g) result from recombination of excitons in InAs islands of similar size present on the NW sidewalls. Finally, we note that luminescence from the GaAs NW core could not be detected, as carriers generated in the core are captured by the InAs shell, which is beneficial for increasing the luminescence intensity of the InAs QDs. These results indicate that Bi can induce the formation of optically active InAs QDs directly on the {110} sidewalls of GaAs NWs.

In conclusion, morphological phase transitions in strained films can be induced by externally modifying surface energies with surfactants. We have used this approach to synthesize optically active quantum dots on the {110} sidewalls of GaAs nanowires, surfaces on which 3D growth is otherwise inhibited. These structures are promising for optoelectronic devices operating at telecommunications wavelengths, as well as optomechanical applications. We also realize novel zig-zag nanoring structures encircling the nanowire core. Given the crucial role of surface effects for nanostructure self-assembly, this work illustrates that surfactants can provide an unprecedented level of external control over the synthesis of these structures, paving the way to realizing quantum dots with new materials and on new substrates.

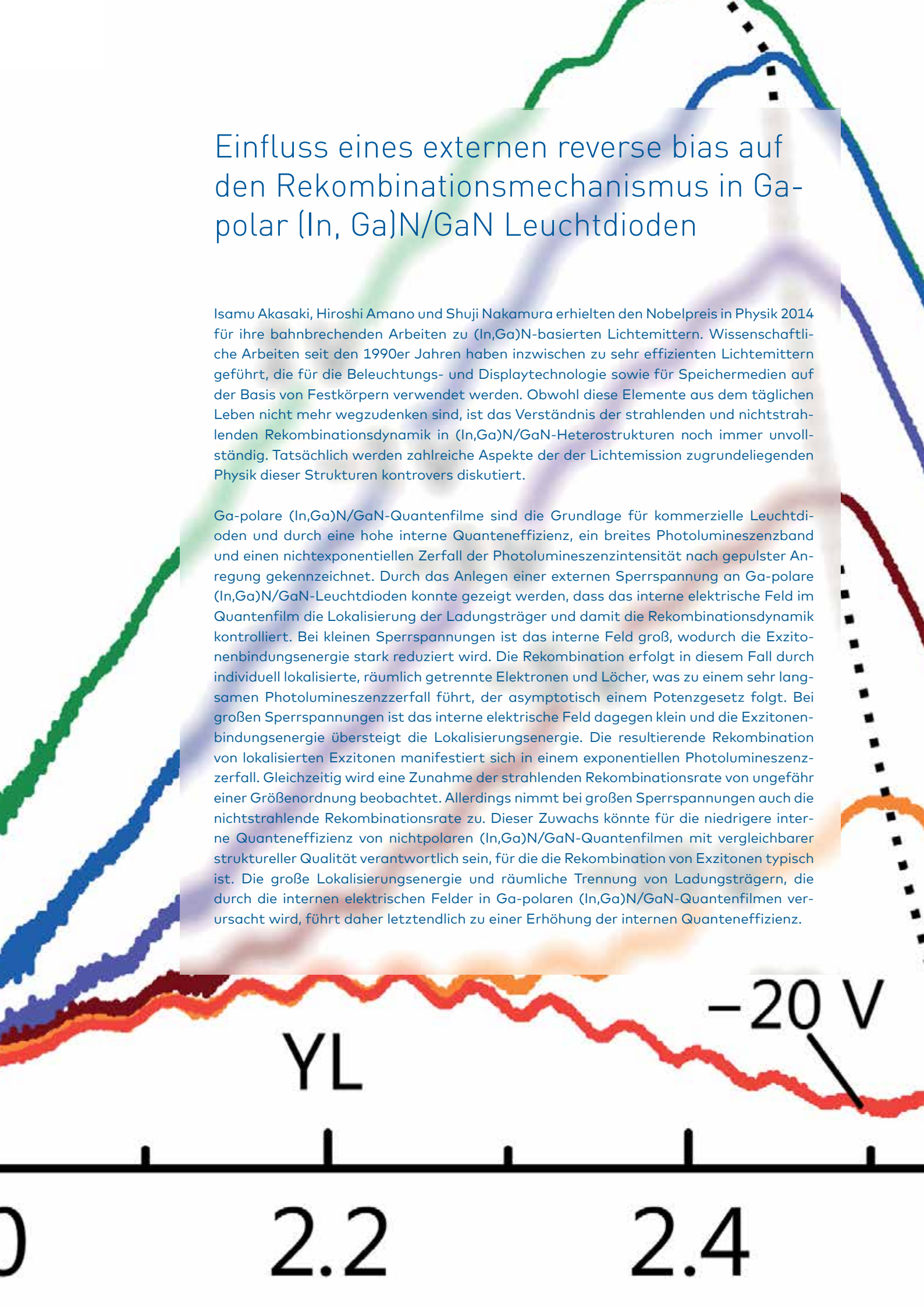
R. B. Lewis, P. Corfdir, H. Li, J. Herranz, C. Pfüller, O. Brandt, and L. Geelhaar,
Quantum dot self-assembly driven by a surfactant-induced morphological instability,
Phys. Rev. Lett. **119**, 086101 (2017).

R. B. Lewis, P. Corfdir, J. Herranz, H. Küpers, U. Jahn, O. Brandt, and L. Geelhaar,
Self-assembly of InAs nanostructures on the sidewalls of GaAs nanowires directed by a Bi surfactant,
Nano Lett. **17**, 4255 (2017).

Einfluss eines externen reverse bias auf den Rekombinationsmechanismus in Ga-polaren (In, Ga)N/GaN Leuchtdioden

Isamu Akasaki, Hiroshi Amano und Shuji Nakamura erhielten den Nobelpreis in Physik 2014 für ihre bahnbrechenden Arbeiten zu (In,Ga)N-basierten Lichtemittern. Wissenschaftliche Arbeiten seit den 1990er Jahren haben inzwischen zu sehr effizienten Lichtemittern geführt, die für die Beleuchtungs- und Displaytechnologie sowie für Speichermedien auf der Basis von Festkörpern verwendet werden. Obwohl diese Elemente aus dem täglichen Leben nicht mehr wegzudenken sind, ist das Verständnis der strahlenden und nichtstrahlenden Rekombinationsdynamik in (In,Ga)N/GaN-Heterostrukturen noch immer unvollständig. Tatsächlich werden zahlreiche Aspekte der der Lichtemission zugrundeliegenden Physik dieser Strukturen kontrovers diskutiert.

Ga-polare (In,Ga)N/GaN-Quantenfilme sind die Grundlage für kommerzielle Leuchtdioden und durch eine hohe interne Quanteneffizienz, ein breites Photolumineszenzband und einen nichtexponentiellen Zerfall der Photolumineszenzintensität nach gepulster Anregung gekennzeichnet. Durch das Anlegen einer externen Sperrspannung an Ga-polare (In,Ga)N/GaN-Leuchtdioden konnte gezeigt werden, dass das interne elektrische Feld im Quantenfilm die Lokalisierung der Ladungsträger und damit die Rekombinationsdynamik kontrolliert. Bei kleinen Sperrspannungen ist das interne Feld groß, wodurch die Exzitonenbindungsenergie stark reduziert wird. Die Rekombination erfolgt in diesem Fall durch individuell lokalisierte, räumlich getrennte Elektronen und Löcher, was zu einem sehr langsamem Photolumineszenzzerfall führt, der asymptotisch einem Potenzgesetz folgt. Bei großen Sperrspannungen ist das interne elektrische Feld dagegen klein und die Exzitonenbindungsenergie übersteigt die Lokalisierungsenergie. Die resultierende Rekombination von lokalisierten Exzitonen manifestiert sich in einem exponentiellen Photolumineszenzzerfall. Gleichzeitig wird eine Zunahme der strahlenden Rekombinationsrate von ungefähr einer Größenordnung beobachtet. Allerdings nimmt bei großen Sperrspannungen auch die nichtstrahlende Rekombinationsrate zu. Dieser Zuwachs könnte für die niedrigere interne Quanteneffizienz von nichtpolaren (In,Ga)N/GaN-Quantenfilmen mit vergleichbarer struktureller Qualität verantwortlich sein, für die die Rekombination von Exzitonen typisch ist. Die große Lokalisierungsenergie und räumliche Trennung von Ladungsträgern, die durch die internen elektrischen Felder in Ga-polaren (In,Ga)N/GaN-Quantenfilmen verursacht wird, führt daher letztendlich zu einer Erhöhung der internen Quanteneffizienz.



Influence of an external reverse bias on the recombination mechanism in Ga-polar (In,Ga)N/GaN light-emitting diodes

F. Feix, T. Flissikowski, P. Corfdir, O. Marquardt, A. Gomez-Iglesias¹, L. Geelhaar, H. T. Grahn, and O. Brandt

For their pioneering achievements concerning (In,Ga)N-based light emitters, Isamu Akasaki, Hiroshi Amano, and Shuji Nakamura received the Nobel Prize in Physics in 2014. World-wide research activities since the 1990s have resulted in highly efficient light emitters used for solid-state lighting, display, and storage technology. However, the understanding of the radiative and nonradiative recombination dynamics in (In,Ga)N/GaN heterostructures is still far from complete, despite the everyday presence of these devices. In fact, many aspects of the physics underlying the light emission from these structures are discussed controversially.

Ga-polar (In,Ga)N/GaN(0001) quantum well (QW) heterostructures are the basis of commercial light-emitting diodes (LEDs) and are characterized by a high internal quantum efficiency (IQE), a broad photoluminescence (PL) band, and a nonexponential decay of the PL intensity after pulsed excitation. In the late 1990s, it was generally accepted that all these features are linked to excitons localized at In-rich clusters. However, recent microscopic investigations revealed that the In atoms in high-quality (In,Ga)N/GaN(0001) QWs are actually randomly distributed. In the early 2000s, the absence of clustering led to a widespread belief that localization effects should not be important in these structures. Phenomena such as the nonexponential PL decay were consequently interpreted as being a sole consequence of the internal electrostatic fields in these polar QWs. In fact, the slow PL decay (on the order of μs) of the polar QWs differs drastically from the fast single exponential transients (on the

order of a ns) observed in nonpolar (In,Ga)N/GaN(1100) QWs. However, recent theoretical and experimental work has demonstrated the significance of localization even in a perfectly random (In,Ga)N alloy and thus initiated a renaissance of the investigation of localization effects in (In,Ga)N.

In Fig. 1(a), we show low-temperature PL spectra of a Ga-polar (In,Ga)N/GaN QW structure, a nonpolar (In,Ga)N shell QW formed around a GaN micro-rod, and a 40-nm-thick Ga-polar (In,Ga)N layer. These samples are representative for their respective type and exhibit a comparable In content. The polar QW emits at lower energy as compared to the bulk-like layer due to the quantum-confined Stark effect induced by the internal electrostatic field. In contrast, the emission of the nonpolar QW is blueshifted because of quantum confinement and the absence of such fields. The linewidth of the PL bands is clearly different, which does not necessarily reflect a different degree of compositional uniformity. In particular, well width fluctuations contribute to the broadening of the PL bands for the QWs, but may also induce localized states not present in the layer. Furthermore, a significant contribution to the linewidth observed for the nonpolar QWs originates from a macroscopic gradient of the In content along the axis of the (In,Ga)N/GaN micro-rod as confirmed by cathodoluminescence measurements. Because of the different contributions to the broadening of the emission bands, it is difficult to ascertain that the samples truly have a comparable compositional uniformity.

¹ OSRAM Opto Semiconductors GmbH, Regensburg, Germany

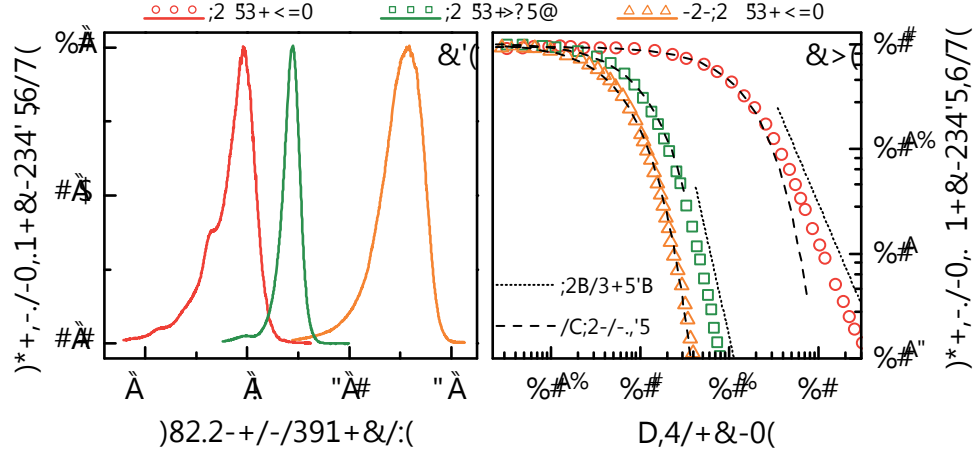


Fig. 1. Normalized low-temperature (a) steady-state PL spectra and (b) PL transients of polar and nonpolar (In,Ga)N/GaN QWs as well as a Ga-polar (In,Ga)N layer. In (b), the dotted lines indicate the power law asymptote, while the dashed lines represent single exponential fits to the data.

Despite this uncertainty, it is instructive to examine the temporal characteristic of the emission of these samples. In Fig. 1(b), we present normalized PL transients of the three samples under investigation recorded at 10 K. The transients were acquired with a low excitation density to ensure that no dynamic screening of the internal fields occurs in the polar QWs. The overall shape of the transient does not change up to room temperature. For the polar QWs, we observe a very slow decay, which asymptotically approaches a power law. In contrast, the nonpolar QWs exhibit a single exponential decay over three orders of magnitude with a lifetime of 530 ps. For the thick layer, we observe an initial exponential decay followed by a power law asymptote. These distinctly different decay types cannot be attributed solely to the presence or absence of internal fields. In fact, in the absence of localization, we would expect to see a slow but single exponential decay also for the Ga-polar QW. A power law decay instead reflects the recombination of spatially separated, individually localized electrons and holes [cf. the related report entitled *N-polar (In,Ga)N quantum disks in GaN nanowires vs. Ga-polar (In,Ga)N/GaN quantum wells*]. In contrast, the single exponential decay observed for the nonpolar

QW and its temperature dependence (not shown here) is consistent with the recombination of localized excitons.

Assuming that the samples are in fact comparable in terms of compositional uniformity, we suggest that the recombination mechanism is determined by a competition between the exciton binding energy (E_x) and the localization energy (E_{loc}) of the individual particles. For the (In,Ga)N layer, the PL transient depicted in Fig. 1(b) indicates a coexistence of localized excitons and individually localized electrons and holes, suggesting that $E_{loc} \approx 25$ meV, which corresponds to E_x in GaN. This value is exclusively due to the localization of holes by random compositional fluctuations as shown in recent calculations ($E_{loc} = E_{loc,h}$) [Schulz *et al.*, Phys. Rev. B **91**, 035439 (2015)]. For QWs, this study furthermore revealed that electrons tend to be localized at monolayer fluctuations at the interface, giving rise to an additional contribution $E_{loc,e}$. Schrödinger-Poisson simulations (not shown) yield values for $E_{loc,e}$ of 40 meV (5 meV) for polar (nonpolar) QWs. These values are to be compared to that of E_x , which variational calculations show to be as high as 50 meV in 3-nm-thick nonpolar $\text{In}_{0.1}\text{Ga}_{0.9}\text{N}/\text{GaN}$ QWs, but only 30 meV for otherwise identical

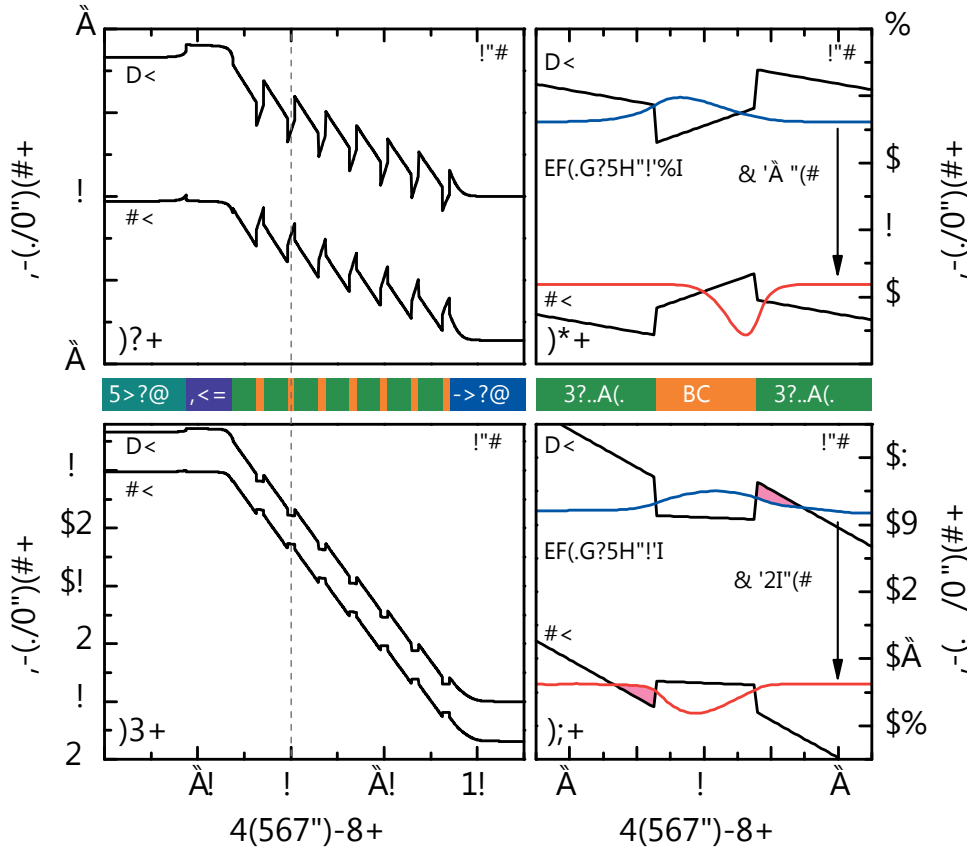


Fig. 2. Valence (VB) and conduction (CB) band profile of an $\text{In}_{0.24}\text{Ga}_{0.76}\text{N}/\text{GaN}$ LED simulated with an applied voltage of (a) 0 V and (b) -20 V. The simulated layer sequence with the electron blocking layer (EBL) is schematically depicted between the corresponding graphs. The dashed line marks the QW which is magnified in (c) and (d) for the indicated voltages. The electron (blue) and hole (red) wave functions of the ground state, the overlap of the wave functions, and the transition energy E are shown for the selected QW. Additionally, the reduced effective potential barrier (pink area) for electrons and holes at a bias of -20 V is indicated in (d).

Ga-polar QWs. Hence, for the Ga-polar QW, $E_x \approx 30 \text{ meV} < E_{\text{loc}} \approx 70 \text{ meV}$, while for the nonpolar QW $E_x \approx 50 \text{ meV} > E_{\text{loc}} \approx 35 \text{ meV}$. In other words, the combination of a low exciton binding energy and a high localization energy of electrons in the polar QWs, both caused by the large internal electrostatic fields, leads to the dissociation of excitons and to the recombination of spatially separated electrons and holes. In contrast, excitons remain stable in the field-free nonpolar ($\text{In},\text{Ga}\text{N}/\text{GaN}$ QWs and thus localize as a whole.

This simple interpretation relies on the assumption that the samples under investigation are structurally comparable, par-

ticularly with respect to the compositional and interfacial fluctuations responsible for localization. Because of the inequivalence of the crystallographic planes defining the growth front as well as the different growth conditions, this assumption is not necessarily valid. For this reason, it would be desirable to study the impact of the internal field on the recombination mechanism in one and the same sample. For this purpose, we apply a reverse bias to a research and development Ga-polar ($\text{In},\text{Ga}\text{N}$)-based LED, emitting in the green spectral range, to tune the internal field over a wide range. Figures 2(a) and 2(b) show the band edge profiles of this green LED at 0 and -20 V obtained by self-consistent

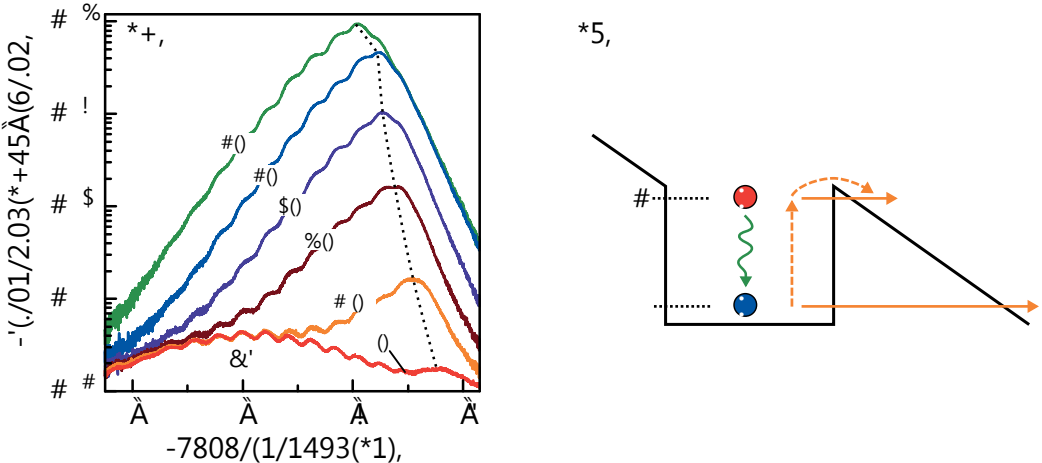


Fig. 3. (a) Room temperature steady-state PL spectra of a biased green LED excited with 70 W/cm^2 at 3.08 eV . The PL band blueshifts as indicated by the dashed line. The broad band centered at 2.2 eV is caused by the yellow luminescence in GaN. The spectra are modulated by thickness interference fringes of the GaN buffer. (b) Schematic of the tunneling (solid arrows) and the thermionic (dashed arrows) escape of charge carriers either from the excited state (1) or the ground state (0) of a Ga-polar QW at a large reverse bias.

Schrödinger-Poisson calculations. For the latter large reverse bias, the potential drop over the intrinsic region counteracts the internal electrostatic fields in the QWs such that the total field is almost zero. These reduced fields are expected to result in a blueshift of the PL band and a larger overlap of the electron and hole wave functions as shown in the magnified view of a selected QW in Figs. 2(c) and 2(d).

Figure 3(a) shows room temperature steady-state PL spectra of the green LED at various biases and an excitation density of 70 W/cm^2 . At 1 V , the PL band is centered at 2.42 eV . At a four orders of magnitude higher excitation density, the band exhibits a blueshift of 100 meV (not shown) due to the screening of the internal fields. With increasing reverse bias, the PL band blueshifts as expected from the result of the corresponding simulation in Fig. 2. At -20 V , the PL band peaks at 2.57 eV both for low and high excitation densities. This result implies that the residual internal field at -20 V is close to zero as predicted by the simulations shown in Fig. 2(d).

Concomitant with the detected reduction of the PL intensity over several orders of

magnitude [see Fig. 3(a)], we measure an increasing photocurrent with increasing reverse bias (not shown), revealing that an increasing fraction of the charge carriers photoexcited in the QWs escape from the active region. The origin of this carrier leakage lies in the reduced effective barrier height for the charge carriers in the QWs at large reverse biases, which enhances the probability of tunneling escape or thermionic emission [see pink area marked in Fig. 2(d)]. It is important to consider the consequences of these processes for time-resolved experiments.

In Fig. 3(b), the escape of charge carriers from an excited state (1) or the ground state (0) of a QW at a large reverse bias is depicted schematically. The escape time associated with the combined thermionic emission and tunneling of charge carriers at the energy of the excited state (red) is obviously much shorter (due to the smaller effective potential barrier) than that of carriers that have relaxed to the ground state (blue). If these processes are also faster than the relaxation process (curved arrow), the photoexcited carriers will be simply extracted immediately after their excitation and will not be able to relax to

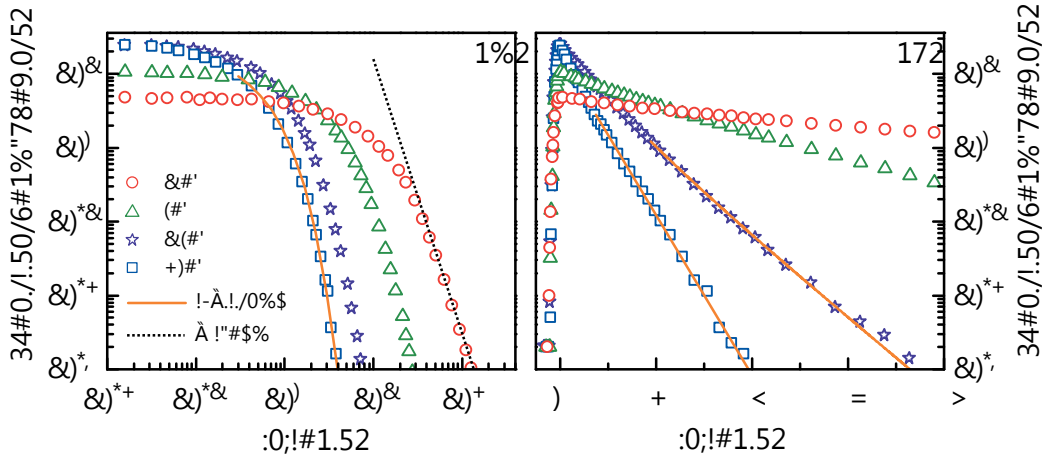


Fig. 4. (a) Double- and (b) semilogarithmic representations of PL transients of the green LED at various reverse biases. The QWs of the green LED were excited at 2.79 eV with an energy fluence per pulse of about 85 J/cm^2 . Panel (a) shows most clearly the power law asymptote at small reverse bias (dotted line), while panel (b) demonstrates the exponential nature of the decay at -15 and -20 V (solid lines).

the ground state. These extracted charge carriers contribute to the photocurrent and reduce the number of carriers captured by the QW, but this process does not influence the recombination dynamics of carriers in the ground state.

A quantitative consideration of the competing relaxation, recombination, and escape processes shows that this scenario should prevail up to at least -15 V . For larger reverse biases, carrier escape from the ground state of the QW is expected to set in. This process will result in an exponentially decreasing effective lifetime, which would thus eventually become much shorter than the lifetime of excitons in $(\text{In},\text{Ga})\text{N}/\text{GaN}$ QWs at room temperature (typically on the order of 500 ps). As we will see below, we do not encounter these conditions in our experiments.

Figure 4 shows PL transients of the green LED acquired with time-correlated single-photon counting at room temperature for various reverse biases. The transients are intentionally shown in both double-[Fig. 4(a)] and semilogarithmic [Fig. 4(b)] representations. As indicated by the dotted line in Fig. 4(a), the asymptote of the decay

at -1 V obeys a power law, as universally observed for polar QWs [cf. Fig. 1(b)]. For increasing reverse biases, both the initial decay and the power law asymptote become faster. For reverse biases above -15 V , the entire transient approaches a single exponential decay [see Fig. 4(b)], suggesting that recombination is excitonic at this and larger reverse biases. In fact, the lifetime of 400 ps observed at -20 V basically coincides with the values reported for the lifetimes of excitons in (unbiased) nonpolar $(\text{In},\text{Ga})\text{N}/\text{GaN}$ QWs (cf. room temperature lifetime of 490 ps for the shell QW investigated above at 10 K).

Concurrently with the transition from a power law to an exponential decay, we observe that the peak intensity of the transient increases with increasing reverse bias. Note that, for fs excitation as in our experiments, the peak intensity is not affected by nonradiative processes such as the escape of carriers from the QW by tunneling or thermionic emission, but is given by the instantaneous excitation density and the initial radiative rate. In the present case, the nominal excitation density is constant, but the actual one is decreased by the extraction of carriers as described above. As

we have measured the photocurrent also for pulsed excitation simultaneously with the PL transients, we can correct for the effectively decreasing excitation density and calculate the actual increase of the radiative rate. Considering carrier losses, we estimate that the initial radiative rate increases by more than an order of magnitude between -1 and -20 V. This increase is much stronger than expected from the overlap of the electron and hole wave functions as shown in Figs. 2(c) and 2(d) and thus reflects the transition from the slow recombination of spatially separated electrons and holes to the much faster radiative decay of localized excitons.

The drastic increase of the radiative rate in the absence of the internal field seems to imply that the IQE of nonpolar (In,Ga)N/GaN QWs should be higher than that of their polar counterparts. However, nonradiative processes also slow down when electrons and holes are spatially separated [cf. the related report entitled *N-polar (In,Ga)N quantum disks in GaN nanowires vs. Ga-polar (In,Ga)N/GaN quantum wells*] and speed up when delocalization sets in and excitons form. Whether exciton formation leads to an increase or a decrease of the IQE cannot be predicted in general, but depends on the recombination and capture coefficients of the respective recombination events. The results of the present study tend to support the counterintuitive view that the electron-hole separation increases the IQE, but dedicated studies are necessary to establish a firm quantitative understanding of the impact of carrier vs. exciton localization on the IQE.

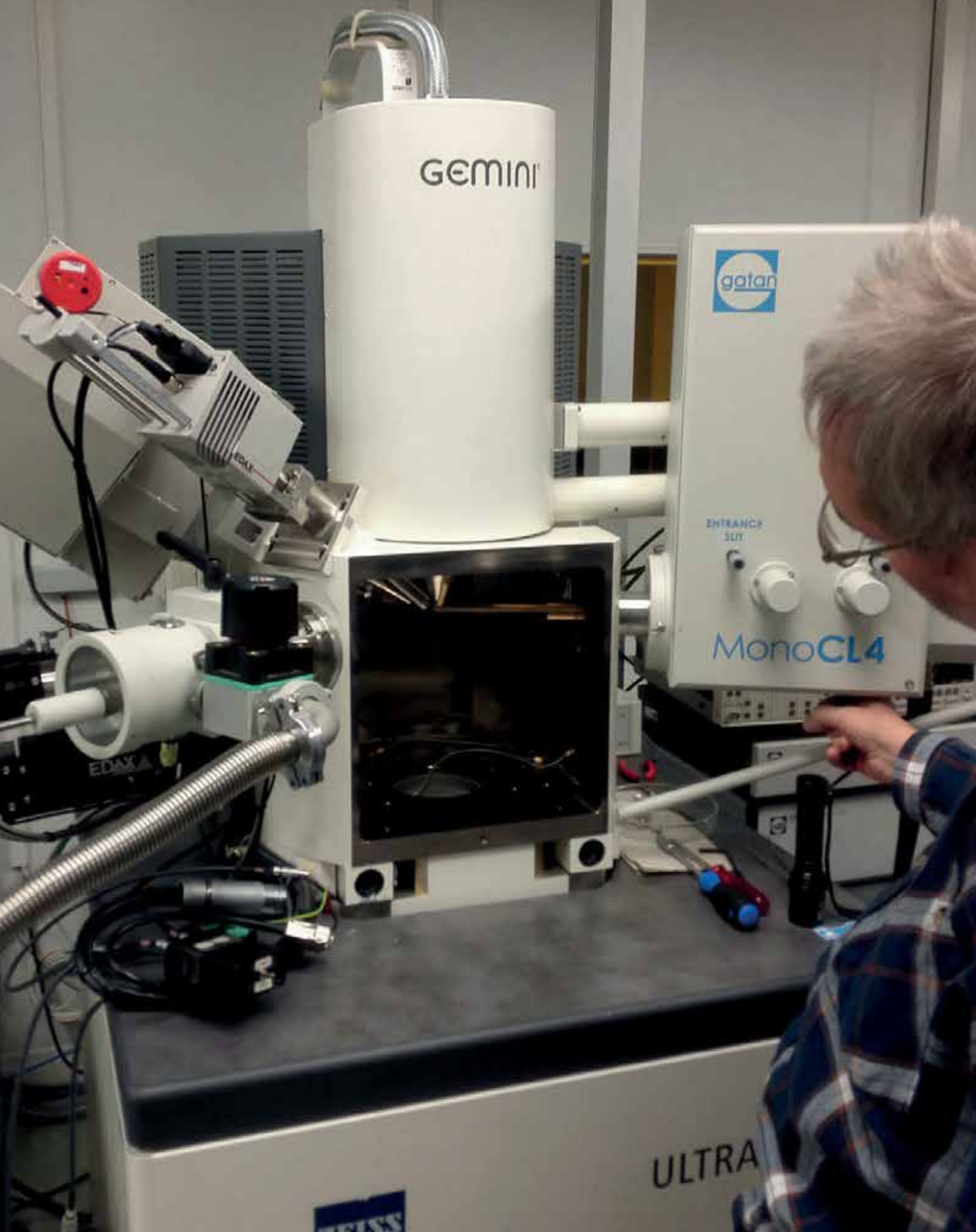
GEMINI



ENTRANCE SLIT

MonoCL4

ULTRA





Core Research Areas

Forschungsschwerpunkte

Nanofabrication Nanofabrikation	43
Nanoanalytics Nanoanalytik	49
Control of Elementary Excitations by Acoustic Fields Die Kontrolle von elektrischen Anregungen in Halbleiter-Nanostrukturen	53
III-V Nanowires for Optoelectronics III-V-Nanodrähte und deren Anwendung in der Optoelektronik	57
Intersubband Emitters: GaAs-based Quantum-Cascade Lasers Intersubbandemitter: GaAs-basierte Quantenkaskadenlaser	61

Nanofabrication

Nanofabrikation

Contact:

[Dr. Lutz Geelhaar](#)

[Dr. Klaus Biermann – Group-III arsenides](#)

[Dr. Oliver Bierwagen – Oxides](#)

[Dr. Raffaella Calarco – Group-III nitrides,
GeTe-Sb₂Te₃ phase-change materials](#)

[Dr. Joao Marcelo Lopes – Graphene,
hexagonal BN](#)

The subject of this core research area is the fabrication of novel types of nanostructured crystals and the investigation of fundamental growth mechanisms. The perspective of such samples is to enable the investigation of exciting physical phenomena or to offer new tailored functionalities that may inspire innovative devices. In general, we fabricate our samples in the bottom-up approach, i.e. in a process of adding material by growth in contrast to removing material by etching. Thus, for the desirable high level of control over fabrication it is mandatory to understand the underlying growth mechanisms. Moreover, these mechanisms are often highly fascinating by themselves.

The standard technique for the fabrication of samples at PDI is molecular beam epitaxy (MBE). Hence, our samples are usually grown as epitaxial thin films on crystalline substrates, and different materials may be stacked on top of each other to form heterostructures of considerable complexity. In addition, we also grow on substrates whose surface has been pre-patterned by lithography to induce lateral variations in growth, and self-organization phenomena can be employed for the deliberate formation of three-dimensional structures like nanowires instead of two-dimensional planar films.

The samples that we aim to fabricate are novel in at least one of the following aspects:

Das Thema dieses Forschungsschwerpunktes ist die Herstellung neuartiger nanostrukturierter Kristalle und die Untersuchung fundamentaler Wachstumsmechanismen. Solche Proben dienen dazu, spannende physikalische Phänomene zu untersuchen oder aber neue, maßgeschneiderte Funktionalitäten zu ermöglichen, die innovative Anwendungen inspirieren können. Generell werden die Proben in einem sogenannten ‚bottom-up‘-Ansatz (englisch für ‚von unten nach oben‘) hergestellt. Dies bedeutet, dass während des Herstellungsprozesses Material durch Wachstum hinzugefügt wird – im Unterschied zu Verfahren, bei denen aus einer größeren Probe Material durch Ätzprozesse abgetragen wird. Daher ist es für das angestrebte hohe Maß an Kontrolle bei der Probenherstellung unabdingbar, die zugrundeliegenden Wachstumsmechanismen genau zu verstehen – ganz abgesehen davon, dass diese Mechanismen per se faszinierend sind.

Die Standardmethode, die wir am PDI für die Probenherstellung verwenden, ist die Molekularstrahlepitaxie (englisch molecular beam epitaxy, MBE). Infolgedessen werden unsere Proben gewöhnlich als epitaktische dünne Schichten auf kristallinen Substraten gezüchtet. Hierbei können unterschiedliche Materialien als Schichtsystem übereinander gewachsen werden und bilden dann Heterostrukturen von hoher Komplexität. Darüber hinaus wird auf Substraten gewachsen, deren Oberflächen mittels lithographischer Techniken vorstrukturiert sind. Somit können laterale Änderungen im Wachstum induziert werden. Außerdem werden Phänomene der Selbstorganisation aus-

- A material of this chemical composition has not been synthesized before, or at least not in this crystalline quality and/or chemical purity.
- Different materials are monolithically integrated to form an unprecedented hybrid structure.
- A known material or combination of materials is structured on the nanoscale in a new way, i.e. the sample is shaped in at least one dimension to a new type of geometry, or a heterostructure of exceptional complexity or precision is created.

Typical examples are extending the range of compositions over which films can be grown in high quality, the use of novel substrates, and the heteroepitaxy of dissimilar materials.

In general, all growth mechanisms are governed by the interplay between thermodynamics and kinetics. At the nanoscale, the role of surface and interface effects is often crucial. In heterostructures, differences between the crystal lattices induce strain which affects crystal growth and is often accommodated by the formation of defects. Hence, the elucidation of growth mechanisms is inextricably linked to the investigation of surface structure, interface formation, and in general the microstructure of the sample. Therefore, the close collaboration with the core research area *Nanoanalytcs* is indispensable for the understanding of growth mechanisms and the successful fabrication of nanostructures. Where needed, experiments are complemented by theoretical calculations. In this context we collaborate with the group of C. Draxl at Humboldt University in Berlin.

Our research is based on the long-standing expertise of PDI in the MBE of III-As and III-N compound semiconductors, but more and more we study the growth of other materials. One general objective is the

genutzt, um die Ausbildung dreidimensionaler Strukturen – wie zum Beispiel Nano-drähten – anstelle von planaren Schichten zu ermöglichen.

Die Proben, deren Herstellung wir anstreben, sind unter mindestens einem der folgenden Gesichtspunkte neuartig:

- Ein Material dieser chemischen Zusammensetzung wurde zuvor noch nicht synthetisiert – zumindest nicht in dieser kristallinen Qualität oder chemischen Reinheit.
- Unterschiedliche Materialien werden monolithisch integriert, um eine bislang nicht existierende Hybrid-Struktur zu erzeugen.
- Ein bekanntes Material oder eine Materialkombination wird auf der Nanoskala auf neuartige Weise strukturiert – d.h. die Probe wird entlang zumindest einer Raumrichtung zu einer neuartigen Geometrie geformt, oder eine Heterostruktur von außergewöhnlicher Komplexität oder Präzision wird erschaffen.

Typische Beispiele sind die Verwendung neuartiger Substrate, die Erweiterung des Zusammensetzungsbereichs, in dem Schichten in hoher Qualität gezüchtet werden können, und die Heteroepitaxie von sich stark unterscheidenden Materialien.

monolithic integration of various materials on silicon. In the following, the material systems that are currently under investigation will be presented.

The epitaxial growth of group-III-arsenide heterostructures serves as the backbone of various internal and external research projects, due to the unique structural quality of the (Al,Ga)As material system and its very abrupt interfaces even in complex heterostructures—like quantum cascade lasers (QCLs) for the THz emission frequency range, which consist of up to some thousands of single thin layers with nominal thicknesses down to one monolayer. Typically, such a THz-QCL contains a 10 µm thick active region and its growth takes about 25 hours. Microcavity structures for exciton-polaritons are similarly complex structures with the cavity layers sandwiched between two highly reflective distributed Bragg reflectors. By means of a growth – ex-situ patterning – regrowth procedure, such exciton-polariton microcavities were realized with lateral 1D and 2D optically confining potentials and also with lateral arrays of interacting traps. The corresponding quantized exciton-polariton states could be clearly mapped by spatially resolved photoluminescence measurements. These experiments revealed that the anisotropy of the overgrowth process sets for the used (001) substrates a lower limit to the size of the exciton traps of about 1 µm. Further work is needed to obtain the desired size of about 0.5 µm. Additionally, we continued our studies on regrowth of patterned templates on (113)A and (001) substrates to form channels for transport of charge carriers, excitons or spins by means of surface acoustic waves. In the past, we used exclusively photolithography and wet chemical etching to fabricate the patterned templates but achieved recently successful overgrowth of a sample patterned by electron beam lithography. Another approach to achieve lateral structuring with high resolution that we pursue is patterning of GaAs templates by local

anodic oxidation using the biased tip of an atomic force microscope.

Other sample structures for internal and external partners include heterostructures grown on GaAs(111) and GaAs(110) substrates that were designed for various experiments like studying the electric amplification of phonons in superlattices, electron spin dynamics and electrical spin injection, and symmetry evaluation of quantum dots grown by droplet epitaxy. Investigations based on samples that were deposited on the more common GaAs(001) substrates comprise subjects like X-ray diffractometry of misfit dislocations, bias dependence of dipolariton test structures, indirect exciton molecules in stacked double quantum wells, and waveguide structures for acoustically driven multiplexers.

In the field of group-III nitride epitaxy, our focus is on In-rich (In,Ga)N layers. This material is important for the development of efficient light emitting and laser diodes in the green spectral range. Yet, the growth of (In,Ga)N alloys with high In content as required to access the higher wavelength range of the emission spectrum is still challenging. In this context, short period superlattices (SPSLs) made of alternating binary InN and GaN layers, have been proposed as an ordered alternative to (In,Ga)N layers. However, the fabrication of such SPSLs on Ga-polar GaN was not achieved, (In,Ga)N/GaN SPSLs with an In content of 25% at maximum were obtained instead. Theoretical calculations predicted the absence of any growth window for the coherent growth of InN on GaN as In incorporation in (In,Ga)N may be limited by strain induced by the substrate. To overcome this limitation, we investigate the growth on ZnO, which is isomorphic to InN and lattice-matched to $\text{In}_{0.18}\text{Ga}_{0.82}\text{N}$. However, the growth on ZnO of a small amount of Ga, even as little as 5%, induces high defect densities and a severe degradation of the interface between (In,Ga)N and ZnO(0001̄) due to a high chemical reactivity of Ga with ZnO. There-

fore, we developed a protocol to protect the ZnO surface from Ga by depositing a very thin coherent InN buffer layer on ZnO prior to the GaN growth.

The fabrication of ferromagnet semiconductor hybrid structures in high crystal perfection is a prerequisite for the investigation of spin transport phenomena relevant for spintronic device concepts. Our focus is on the growth of half-metallic Heusler alloys on GaAs-related structures. The preparation of fully crystalline thin film stacks consisting of a semiconducting channel sandwiched between two ferromagnetic layers offers new possibilities for the engineering of vertical devices. In order to overcome the challenges associated with the growth of a semiconductor on a ferromagnetic metal, we continued to develop solid-phase epitaxy as an approach where an amorphous film of Ge is deposited on Fe₃Si and then crystallized slowly by thermal annealing. We found that a sufficiently thin Ge layer incorporates Fe and Si atoms to spontaneously form an ordered super lattice, with two-dimensional planes of Fe atoms interposed between tetragonal Ge formations. This crystal structure is understood as Ge₂Fe (the Si atoms replacing some Ge lattice sites), a new compound that is not energetically stable as a bulk material. Semiconducting Ge₂Fe thin films are ferromagnetic below 150 K and show strong magneto-crystalline anisotropy, with thickness dependent coercivity on the order of a few hundred Oe along the easy magnetization axis.

MgO interlayers at the Co₂FeSi/GaAs interface have the potential to prevent the Fe and Co diffusion and to act as spin-filtering barriers. We studied Co₂FeSi /MgO/ GaAs hybrid structures with different MgO layer thicknesses (0 to 2.1 nm) grown by MBE. Spin valve and Hanle measurements revealed an enhanced spin generation efficiency and an increased spin diffusion length in the GaAs transport channel with

respect to Co₂FeSi /GaAs reference structures. These results demonstrate the benefit of MgO interlayers for the performance of lateral spin valves with Co₂FeSi contacts.

Transparent (semi)conducting oxides are widely used in devices. For example, n-type In₂O₃, Ga₂O₃, SnO₂, and NiO traditionally serve as active material in conductometric gas sensors and—highly doped—as transparent contact layers in solar cells, displays, and LEDs. The requirements on material quality for these traditional applications are low, and usually met by polycrystalline, sputtered material. During the last decade, however, transparent semiconducting oxides have been re-discovered as true wideband-gap semiconductors by virtue of their synthesis to semiconductor standards (single crystalline, highly pure with well-defined doping). This development enables the investigation of the underlying physics of these materials and their applications. It further opens up the possibility for novel and improved conventional oxide-semiconductor-based devices by rational design. For example, based on its large band gap of Eg = 4.5 eV, single crystalline Ga₂O₃ is a promising material for next generation power electronics as well as solar-blind ultra violet sensors. Combined with In₂O₃ (Eg = 2.7 eV) and Al₂O₃ (Eg = 8.8 eV), band-gap engineering and heterostructures with large band offsets are foreseeable. Compared to traditional compound semiconductors, semiconducting oxides are at an early stage of development with many open fundamental questions. Our efforts to answer these questions are embedded in the Leibniz ScienceCampus GraFOx, lead by PDI. The main contribution of our core research area in this context is the growth of semiconducting oxides by MBE, a proven tool to synthesize high-quality semiconductor thin films, and to investigate their properties.

This year, investigations of the MBE growth of the alloy (In,Ga)₂O₃ uncovered a catalytic

effect on the growth of Ga_2O_3 : Adding the element In drastically increased the growth rate of Ga_2O_3 during MBE without being incorporated into the film. As a consequence, the presence of In allows to grow Ga_2O_3 at higher growth temperatures than before, which is foreseen to enable films of higher crystalline quality. Moreover, on the chosen substrate Ga_2O_3 formed a special crystalline structure that is uniquely suitable for developing heterostructures with In_2O_3 . Given the simple reaction chemistry of MBE, the observed catalytic effect is generally valid and thus applicable to all materials possessing similar properties. The focus of our investigations at the PHARAO experiment, run jointly with the core research area Nanoanalytics, shifted to the homoepitaxy of the β -phase of Ga_2O_3 . On exactly (100) oriented substrates the films were found to form in a layer-by-layer growth as evidenced by oscillations in reflection high-energy electron diffraction.

Phase change materials (PCM) are unique compounds employed in non-volatile random access memory thanks to the rapid and reversible transformation between the amorphous and crystalline state that display large differences in electrical and optical properties. Our unique approach in this field is the use of MBE for the fabrication of epitaxial PCM, which makes possible advanced studies on the properties of these materials. The epitaxial growth of GeSbTe alloys is quite demanding as an interplay between composition, phase and ordering occurs. Control over those three parameters is mandatory to obtain material with well defined physical properties. Thus, this year we established the use of Raman spectroscopy as the basis for a correlation between growth parameters and structural properties. Raman scattering is perfectly suited for the investigation of changes in bonding as well as symmetry of GeSbTe. The inelastic interaction between optical laser radiation and electron orbitals is used to probe the bonding of atoms in the short

range and thus can be applied indiscriminately to amorphous and crystalline material.

Graphene is promising for several applications, and is thus anticipated to play a major role in future technologies. The practical utilization of this material in nanoelectronics will require the development of scalable processes enabling its controlled synthesis on various substrates. For this purpose we have systematically studied MBE large-area synthesis (up to two-inch wafers) of graphene on different metallic and insulating substrates. While on metals such as Ni state-of-the-art graphene could be realized, achieving the same degree of crystalline perfection for graphene grown on insulators (e.g. Al_2O_3) has proven challenging. Hence, we continue to work on the improvement of the growth protocols aiming at reaching a level of quality comparable to that of graphene on metals. Furthermore, MBE of atomically thin hexagonal boron nitride (h-BN) films has also been investigated. This is also a layered material that has been intensively studied due to its great technological potential, in particular when combined with graphene to form the so-called van der Waals (vdW) heterostructures. Following our previous work on h-BN/graphene heterostacks prepared on Ni templates, we investigated the formation of similar vdW systems by performing direct MBE growth of h-BN on epitaxial graphene (on SiC). This study permitted to gain an in-depth understanding of the defect-mediated vdW epitaxy of h-BN on graphene. Additionally, it pointed out a route for a scalable and technologically relevant fabrication of h-BN/graphene heterostructures.

Parallel to MBE, we operate a furnace in which Si is desorbed from SiC to induce epitaxial graphene formation. This is an established method which enables us to fabricate continuous graphene films (single layer to multi-layer thick) on SiC of state-

of-the-art quality. We have employed this type of samples as templates to perform fundamental growth studies of different materials on graphene such as h-BN (as mentioned above) and GaN nanowires. The high crystalline quality, inertness, and atomic flatness of epitaxial graphene on SiC makes it an ideal substrate for the development of growth protocols for vdW epitaxy.

Nanoanalytics

Nanoanalytik

Contact:

Dr. Achim Trampert

Dr. Stefan Fölsch – Scanning tunneling microscopy and spectroscopy

Dr. Michael Hanke – Synchrotron studies

The ongoing miniaturization in semiconductor technology increases the demand for precise information on the structural and compositional quality of low-dimensional systems and nanomaterials. The mission of this Core Research Area is the development and combination of sophisticated experimental and theoretical tools for materials analysis on the nanometer scale. For this purpose synchrotron X-ray diffraction is carried out to investigate surfaces and interfaces in epitaxial layers and three-dimensional nanostructures during growth. The structural and optical properties of as-grown materials are investigated by various electron microscopy techniques including imaging, diffraction and spectroscopy with high spatial resolution. Low-temperature scanning tunneling microscopy is applied to build and analyze individual nanostructures.

The research addresses the following topics:

- Interfaces in low-dimensional heterostructures and nanosystems
- Order-disorder phenomena and phase transitions in alloys and oxides
- Structure, chemistry and mechanical properties of metastable and nanostructured systems
- Manipulation and spectroscopy of materials at the single-atom scale

Die stetige Miniaturisierung in der Halbleitertechnologie erhöht den Bedarf an präziser Information über die strukturelle Qualität und chemische Zusammensetzung niedrig-dimensionaler Halbleiterstrukturen und Nanomaterialien. Das Ziel dieser Core Research Area ist die Entwicklung und Kombination ausfeilter experimenteller und theoretischer Untersuchungswerzeuge zur Materialanalyse auf der Nanometerskala. Hier wird Synchrotron-Röntgenbeugung für die Untersuchung von Oberflächen und Grenzschichten in epitaktisch gewachsenen Schichtsystemen und dreidimensionalen Nanostrukturen während des Wachstums eingesetzt. Nach der Schichtaufbringung werden die strukturellen und optischen Eigenschaften des gewachsenen Materials mit unterschiedlichen elektronenmikroskopischen Abbildungstechniken – einschließlich der Elektronenbeugung, der energiedispersiven Röntgenspektroskopie und der Elektronenenergieverlustspektroskopie – mit höchster räumlicher Auflösung untersucht. Darüber hinaus erlaubt die Tieftemperatur-Rastertunnelmikroskopie individuelle Nanostrukturen gezielt herzustellen und strukturell und spektroskopisch zu analysieren.

Die Forschung der Core Research Area *Nanoanalytik* behandelt folgende Themen:

- Grenzflächen in niedrig-dimensionalen Heterostrukturen und Nano-Systemen
- Ordnungs-Unordnungsphänomene und Phasenübergänge in Legierungen und Oxiden
- Struktur, Chemie und mechanische Eigenschaften von metastabilen und nanostrukturierten Systemen
- Manipulation und Spektroskopie von Materialien auf der Skala von Einzelatomen

A central goal in preparing modern artificial heterostructures and nanomaterials is the control of **interfaces** and the understanding of their building principles. Interfaces have a crucial effect on both, physical properties and device performance, in particular as structure sizes become smaller. Epitaxial hetero-interfaces are generally classified as coherent or semi-coherent, depending on the epitaxial strain. We are studying the character of epitaxial strain and strain relieving defects as well as the atomic configuration and translation state of coherent interfaces between dissimilar materials. In addition, interfaces in III-V semiconductor heterostructures are quantitatively analyzed with respect to structural roughness and chemical intermixing as defined by compositional profiles. We found that the experimentally determined concentration dependence at III-V interfaces follows a sigmoidal law for the transition region of two-dimensionally (2D) grown layers or quantum wells.

For some time, we have improved our understanding of interfaces in axial and radial III-V nanowires, two-dimensional layered materials, and, especially in dilute Ga(As, Bi)/GaAs heterostructures and quantum wells. Nanometer-sized lateral composition modulations form in Ga(As,Bi)/GaAs quantum wells spontaneously. Our interface analysis between the Bi-rich units and the matrix revealed that the modulation process is assisted by a complex Bi segregation mechanism implying both, lateral and vertical mass transport. Currently, our interest is focused on Ga(Sb,Bi), another novel dilute bismide compound semiconductor. Although Ga(Sb,Bi) is a highly-mismatched alloy as well, epilayers and quantum wells reveal a remarkable structural perfection, even up to 11–14 %, the maximum Bi concentration incorporated into GaSb so far. No composition modulations are detectable in the pseudomorphic layers. In fact, the mismatch in atomic radius and electronegativity between Sb and Bi is smaller than between As and Bi and, thus, a

higher solubility of Bi into GaSb is expected compared to that of Bi into GaAs. In addition, the quantum wells exhibit regular and homogeneous morphologies including smooth and stable interfaces with a chemical width of the same order as in other high-quality III-V hetero-interfaces. The results may give reasons for the astonishing room temperature laser operation based on the very same quantum well structures.

The physical properties of ferromagnetic Heusler alloys as well as semiconducting oxide layers depend on their structural **order** and **phase stability**. The stability limitations and phase transformation processes are studied in dependence on internal parameters like chemical composition and strain state as well as external parameters given by temperature and growth kinetics. The degree of order/disorder and their spatial distribution in thin films are determined quantitatively by X-ray diffraction and electron microscopy.

We have continued our work on Schottky-Barrier-Tunneling-Transistors based on Fe₃Si/Ge/Fe₃Si thin film stacks. Usually, the development of such devices is limited by the difficulty of growing epitaxial semiconductors over metallic surfaces while preventing chemical reactions—a requirement to obtain abrupt interfaces. We have used a solid-phase-epitaxy approach to realize Ge crystalline thin films on the MBE grown Fe₃Si on GaAs(001). The crystallized Ge layer forms superlattice regions, which are caused by interdiffusion of Fe and Si atoms. X-ray diffraction measurements in combination with local transmission electron microscopy studies indicate that the layers are fully crystalline, lattice-matched and exhibit atomically sharp interfaces over extended areas.

Apart from that, we continued our studies on phase stability and evolution in semiconducting oxides, a work which is embedded into the Leibniz ScienceCampus GraFOx. Ga₂O₃ is a wide-bandgap trans-

parent semiconducting oxide with optical and electrical properties predestined for various applications, as e.g. photodetectors in the deep UV, field effect transistors and high temperature gas sensors. On the way to commercial applications there are, however, still several tasks that need to be addressed, in particular the formation of heterostructures with further group-III sesquioxides as e.g. In_2O_3 . On that way a well-controlled homoepitaxial process on bulk substrates becomes an essential prerequisite. We focussed on the homoepitaxy of Ga_2O_3 on (100)-oriented substrates during MBE. To study the growth mode a combination of various in-situ and ex-situ tools has been applied at PDI's PHARAO facility (beamline U125/2-KMC at BESSYII, Helmholtz-Zentrum Berlin). In-situ X-ray diffraction data, taken during growth, and reflection high-energy electron diffraction (RHEED) data indicate a layer-by-layer mode accompanied by (1×1) surface reconstruction. Surprisingly the specular RHEED intensity shows remarkable periodicity with two discrete time scales. Such a complex oscillating behavior proves sequential, clearly distinguishable nucleation steps, suggesting that the deposition can be characterized as a 2D growth mode. The homoepitaxial layers are grown pseudomorphic with the substrate without in-plane strain as probed by in-plane azimuthal RHEED and out-of-plane synchrotron-based high resolution X-ray diffraction. In contrast to the substrate, stacking faults and twin domains are present in the layer without affecting the 2D growth front.

The functionality of low-dimensional and/or metastable ternary and quaternary semiconductor compounds is controlled by the microstructure and the compositional homogeneity on the atomic as well as mesoscopic length scale. Many systems are characterized by a large thermodynamic miscibility gap, which affects the alloy stability and leads to phase separation with compositional fluctuations or

with stress-induced structural instabilities. In-situ X-ray diffraction is applied in combination with ex-situ transmission electron microscopy techniques to obtain detailed structural information in correlation with growth, dimensionality and optical properties.

In the last years, nanofocus synchrotron radiation has developed into a powerful technique for characterizing the local strain field and chemical composition as well as morphological properties of, e.g. quantum dots and nanowires. Hereby, the characterization of ensembles as well as individual members has been demonstrated by, e.g. scanning nanofocus X-ray diffraction. Along with the steady improvement of nanofocusing optics, X-ray beam sizes below 100 nm FWHM with high photon flux (10^{10} photons/sec) at hard X-ray energies (10–30 keV) are nowadays available at third-generation synchrotrons like PETRAIII at DESY in Hamburg, Germany, or the European Synchrotron Radiation Facility (ESRF) in Grenoble, France. In recent studies, we investigated the local strain field of an isolated micro-rod, induced by $(\text{In},\text{Ga})\text{N}/\text{GaN}$ multi quantum wells embedded in a core-shell geometry. Due to the high spatial resolution of $150 \times 150 \text{ nm}^2$ provided at the synchrotron beamlines at ESRF, we were able to probe the local strain field within one individual facet. These studies are accompanied by a numerical treatment of local deformation fields by the finite element method, which serves as input for kinematical X-ray scattering simulations.

The complete three-dimensional knowledge of the microstructure is essential for the quality improvement of monolithically integrated optoelectronic components. In this light, electron tomography has been applied to analyze the spatial distribution of crystal defects in III-Sb based laser structures epitaxially grown on Si(001). In particular, the origin of threading dislocations at the highly mismatched interface between the AlSb wetting layer and the Si

substrate is explored. The buried AlSb islands of the initial wetting layer are reconstructed so that the locations of island coalescence can be clearly established from the tomogram. Complementary scanning transmission electron microscopy reveals the location of threading dislocations and anti-phase boundaries. The number density of threading dislocations emanating from the interface and their distribution are not simply correlated to sizes of AlSb-island coalescence or to the film closure during transition from 2D to 3D growth—as been commonly assumed. Consequently, new concepts of dislocations formation during heteroepitaxy of highly mismatched systems have been elaborated based on our electron tomography results.

We employ **atom manipulation** by low-temperature scanning tunneling microscopy (LTSTM) to investigate the quantum properties of nanostructures on III-V semiconductor surfaces. Understanding and controlling these properties is essential for future device concepts based on quantum effects. State-of-the-art LTSTM is used to create individual nanostructures atom-by-atom and subsequently analyze their electronic structure and elementary excitations by local tunneling spectroscopy. We found that +1 charged adatoms on an InAs surface can be positioned with atomic precision to form perfectly defined quantum dots and coupled dot assemblies. This approach is now extended to explore artificial two-dimensional lattices with tunable electronic properties. In addition, we started a new STM research track focused on epitaxial transition metal dichalcogenide (TMD) layers with an emphasis on vertical and lateral TMD heterostructures.

Control of Elementary Excitations by Acoustic Fields

Die Kontrolle von elektrischen Anregungen in Halbleiter-Nanostrukturen

Contact:

[Dr. Paulo V. Santos](#)

This core research area explores the dynamic fields of surface acoustic waves (SAWs) for the control of electronic excitations in semiconductor nanostructures. SAWs are elastic vibrations propagating on a solid surface, which resemble seismic waves created during earthquakes. SAWs can be electrically generated on a piezoelectric substrate using interdigital transducers (IDTs)—this standard technique is widely used in signal processing, sensors, and acousto-optical modulation. In recent years, there has been a growing interest to apply SAW fields to control and manipulate electronic effects in semiconductors. Here, one takes advantage of the fact that these fields are composed of a dynamic strain component and, in piezoelectric semiconductors, of a piezoelectric component. Both components induce a time- and spatially dependent modulation of the materials band structure, which produces moving potentials for the confinement and transport of electronic excitations. Interestingly, the fields produced by high-frequency SAWs (GHz range) have wavelengths on the order of one micrometer, thus being comparable to the dimensions of semiconductor components. The acoustic and acoustoelectric effects are furthermore investigated for novel device functionalities. Quite naturally the studies also include the development of piezoelectric materials compatible with semiconductors as well as efficient processes for the electrical excitation of SAWs in non-piezoelectric materials (such as, e.g. Si).

The activities carried out in 2017 included (i) investigations of SAW generation in doped semiconductors, (ii) the efficient acoustic transport in GaAs quantum wells (QWs) and epitaxial graphene, (iii) the interaction

Diese Core Research Area untersucht die dynamischen Felder, die von akustischen Oberflächenwellen erzeugt werden, um sie für die Kontrolle von elektronischen Anregungen in Halbleiter-Nanostrukturen zu nutzen. SAWs sind elastische Schwingungen, die sich auf einer festen Oberfläche ausbreiten. Sie sind ähnlich wie seismische Wellen, die während Erdbeben entstehen. Diese Wellen können auf piezoelektrischen Substraten durch sogenannte Interdigital Transducer (Finger-Wandler) elektrisch erzeugt werden. Diese Technik ist in der Signal-Verarbeitung, bei Sensoren und akusto-optischen Modulatoren weit verbreitet.

Seit einiger Zeit wächst das Interesse, SAW-Felder für die Kontrolle und Veränderung von elektronischen Effekten in Halbleitern einzusetzen. Hierfür nutzt man die Tatsache, dass die Felder auf piezoelektrischen Halbleitern aus dynamischen elastischen und piezoelektrischen Komponenten zusammengesetzt sind. Beide Komponenten bewirken eine zeitlich und räumlich abhängige Modulation der Bandstruktur, was wiederum propagierende Potentiale für das Einschließen und den Transport von Elektronischen Anregungen erzeugt. Interessanterweise haben die Felder, die hochfrequente SAWs (im GHz-Bereich) begleiten, Wellenlängen in der Größenordnung einiger Mikrometer und sind somit mit den Größen von Halbleiterkomponenten vergleichbar. Die akustischen und akustoelektrischen Effekte werden darüber hinaus für ihre Eignung für neue Bauelementfunktionalitäten untersucht.

Sowohl die Entwicklung von piezoelektrischen Materialien, die mit Halbleitern kompatibel sind, als auch die Entwicklung von effizienten Prozessen zur elektrischen

of SAWs with magnetic excitations, and (iv) the control of excitonic structures in the form of indirect excitons (IXs) and microcavity polaritons in (Al,Ga)As structures. This report highlights two of the activities related to the last topic. The first (by C. Hubert and co-workers) relates to the interaction between excitonic dipoles in double quantum well structures. The dipolar interaction depends on the separation between the dipoles as well as on the angle between their dipole moment. For collinear dipoles arranged in different layers, this interaction turns from repulsive for large inter-layer separations to attractive for short separations. We experimentally demonstrate that the attractive component of this interaction binds excitonic dipoles consisting of IXs in stacked double quantum well structures. By using spatially resolved photoluminescence spectroscopy we show that the presence of a dipolar cloud in one layer increases the binding energy and changes the spatial distribution of excitonic dipoles in a remote layer. The increase in binding energy far exceeds the one expected for a molecule consisting of two aligned dipoles. The results demonstrate the feasibility of dipolar control gates and open the way for the realization of interacting dipolar lattices in semiconductor systems. These studies were carried out within a collaboration project with the Hebrew University of Jerusalem financed by the German-Israeli foundation (GIF). The investigations are now being carried out using IX lattices created by SAWs.

The second report (by A. Kuznetsov and co-workers) addresses the development of efficient potential traps for microcavity polaritons (MPs). These are required to explore quantum functionalities, where one needs the control of the energy and wave functions of single polariton states using μm -sized potentials with controlled shape. We have demonstrated the confinement of microcavity polaritons in traps with an effective potential width down to one micrometer produced by patterning the MC

Anregung von SAW sind Teil dieser Studien. Wir beschreiben knapp unsere Kern-Aktivitäten in diesem Jahr im Bereich der Kontrolle indirekter Exzitonen und Exziton Polaritonen. Die Untersuchungen zu Spin-Kontrolle in (111) GaAs Quantum Wells, die ein grosartiger Kandidat für Spin Transport durch SAWs sind, werden im Highlight-Beitrag „Acoustically driven Photon anti-bunching in nanowires“ beschrieben.

in between two growth runs by molecular beam epitaxy (MBE). The correlation between spectroscopic and structural data demonstrate that the growth dynamics induces a graded confinement potential characterized by lateral interface widths of approximately 1 μm . This structuring method is suitable for the fabrication of polariton lattices with negligible site disorder and supporting hybridization between adjacent lattice sites. The later will be combined with acoustic field to create lattices with tunable potential amplitudes.

III-V Nanowires for Optoelectronics

III-V-Nanodrähte und deren Anwendung in der Optoelektronik

Contact:

Dr. Lutz Geelhaar

Dr. Oliver Brandt

Semiconductor nanowires are structures with an extremely high aspect ratio and a diameter typically smaller than 100 nm that can be created in a bottom-up approach, i.e. in a process of adding material by growth. Feature sizes down to 10 nm can be achieved without any lithography in many material systems. The quasi-one-dimensional shape, the nanometric size, and the comparably simple fabrication make nanowires an exciting subject for fundamental studies and offer many conceptual advantages for various applications. We investigate how the specific properties of nanowires can be employed to improve optoelectronic devices or enable new functionalities and applications in this field. Since the emission of light is the realm of compound semiconductors made from elements of the third and fifth group in the periodic system (III-V semiconductors in short), we work mostly with nanowires consisting of these materials. In particular, we grow both group-III-nitride and group-III-arsenide nanowires by molecular beam epitaxy. By combining various experimental characterization techniques, we investigate fundamental properties of nanowires that crucially influence optoelectronic applications. In order to do so, our work includes the fabrication of demonstrator devices.

In the following, we highlight some of the most prominent conceptual advantages of III-V nanowires for optoelectronic applications. The fabrication of devices typically in-

Halbleiter-Nanodrähte sind Strukturen mit extrem hohem Aspektverhältnis und Durchmessern von typischerweise weniger als 100 nm, die im sogenannten ‚bottom-up‘-Ansatz (englisch für ‚von unten nach oben‘) hergestellt werden können. Dies bedeutet, dass während des Herstellungsprozesses Material durch Wachstum hinzugefügt wird – im Unterschied zu Verfahren, bei denen aus einer größeren Probe Material durch Ätzprozesse abgetragen wird („top-down“ für englisch ‚von oben nach unten‘). In vielen Materialsystemen können auf diese Weise Strukturgrößen bis hinunter zu 10 nm ohne lithographische Prozesse erzielt werden. Die quasi eindimensionale Struktur, die Größe im Bereich von Nanometern und die vergleichsweise einfache Herstellung machen Nanodrähte zu einem spannenden Objekt für grundlegende Untersuchungen und bieten zahlreiche konzeptionelle Vorteile für unterschiedliche Anwendungen.

Wir untersuchen, wie die spezifischen Eigenschaften von Nanodrähten eingesetzt werden können, um optoelektronische Bauelemente zu verbessern oder neue Funktionalitäten und Anwendungen in diesem Gebiet zu ermöglichen. Da die Emission von Licht die Domäne von Verbindungshalbleitern bestehend aus Elementen der dritten und der fünften Gruppe des Periodensystems darstellt, arbeiten wir überwiegend mit Nanodrähten aus diesen Materialien. Insbesondere züchten wir Gruppe-III-Arsenid und -Nitrid-Nanodrähte mittels Molekularstrahlepitaxie. Zur Untersuchung der fundamentalen Nanodrahteigenschaften kombinieren wir unterschiedliche experimentelle Charakterisierungsmethoden. Zusätzlich umfassen unsere Arbeiten auch die Herstellung von Demonstratorbauelementen.

volves the growth of heterostructures that are composed of several materials, and the most important part of these heterostructures—e.g., where the actual generation of light takes place—is called the active region. In the nanowire geometry, such heterostructures can be created in the radial direction resulting in simple core-shell or complex multilayers resembling onion skins. As a direct consequence of the high surface-to-volume ratio, the area of the active region is drastically enlarged with respect to a planar geometry.

In general, heterostructures in devices have to be created by epitaxial growth, i.e. ideally all the constituting materials form a single perfect crystal. However, differences in the crystal lattices of these materials lead to the accumulation of strain, and above a certain threshold this strain is released by the formation of defects in the crystal lattice. Such dislocations usually spread throughout the entire device structure and severely degrade device performance. The geometry of free-standing nanowires grown vertically on a substrate is characterized by the small footprint and the high aspect ratio. Thus, the nanowire is free to relax laterally, and the formation of dislocations is avoided. Even if dislocations develop at the interface, they are either confined there or quickly bend to the sidewalls of the nanowire. Dislocations propagating along the nanowire axis are, in comparison, energetically highly unfavorable. By the same token, nanowire segments of different materials can be combined to axial heterostructures along the nanowire length that are unattainable in the conventional planar geometry.

From these considerations, two advantages arise for the fabrication of optoelectronic devices in the form of nanowires. First, the composition of the material in the active region can be varied by a larger degree, which would enable, e.g., the emission of light in other colors than for planar devices. Second, the use of substrates that dif-

fer significantly in crystal structure from the actual device part is much less harmful for device performance. This advantage is particularly relevant for GaN and related materials for which bulk substrates are not readily available. Moreover, a greater freedom in the choice of substrates might lead to substantial cost reductions and new functionalities. In particular, the growth of III-V semiconductor nanowires in high crystal quality on Si substrates holds the promise for the monolithic integration of light emitters with the mature Si technology that is employed for all modern computer processors. This integration could enable faster data transfer between processors.

Many of the advantages listed above only be achieved if the nanowires are synthesized by growth, although in principle similar structures can also be fabricated in a top-down approach by patterning a large crystal. There are several ways to induce the growth of nanowires, but in general they all require that crystal growth is enhanced in one direction and suppressed in all others. One very popular method is the vapor-liquid-solid growth in which the formation of a solid nanowire from the vapor phase is mediated by a tiny liquid metal droplet. In that case, growth is locally enhanced below the droplet, and that is why the droplet is often called catalyst, seed, or collector. Most of our growth experiments with group-III-arsenide nanowires are based on this approach. As an alternative, one can employ the pronounced tendency of some materials to form nanowires under suitable growth conditions spontaneously, i.e. without any external guidance. As a prerequisite, the crystal structure must exhibit a marked anisotropy in one property that leads to uniaxial growth, although often it is very difficult to identify this property. Our group-III-nitride nanowires are typically grown by such self-assembly processes. While such self-organization phenomena provide a fairly easy way to fabricate nanowires, applications often require a level of control, reproducibility, and homogeneity

within the nanowire ensemble that calls for the prepatterning of the substrates. Thus, position and size of the nanowires are determined by a combination of lithography and growth mechanisms. Along this line, we cover substrates with mask layers, etch small holes into the latter, and identify conditions under which nanowires grow only in the holes.

This year, we have discovered a novel way to synthesize optically active InAs quantum dots on the sidewalls of GaAs nanowires. Typically, quantum dots are grown by the so-called Stranski-Krastanov mechanism, one of the three fundamental modes of epitaxy. However, for some material systems it is energetically favorable to form dislocations in the planar adlayer instead of three-dimensional quantum dots. This holds in particular for InAs on GaAs(110), the type of surface that builds the sidewalls of GaAs nanowires induced by Ga droplets. Now, we have demonstrated that the presence of Bi as a surfactant drastically changes the energetics of this material system and thus enables the Stranski-Krastanov transition. We have evidenced this effect both for planar substrates and for nanowires. In the planar case, we have even found that an already deposited planar InAs layer breaks up into three-dimensional islands by exposure to Bi, i.e., on demand. On the nanowire sidewalls, increased InAs deposition leads to novel nanostructures like zig-zag shaped nanorings. Control over the preferred epitaxial mode by tailoring thermodynamic constraints is a very fundamental result that paves the way to realizing quantum dots with new materials and on new substrates. Furthermore, quantum dots on the sidewalls of GaAs nanowires are promising for optoelectronic devices operating at telecommunications wavelengths, as well as optomechanical applications.

During the self-assisted vapor-liquid-solid growth of nanowires, any imbalance in the material fluxes reaching the droplet changes its volume, which in turn results in a

change in the nanowire diameter. This effect is particularly immanent during the Ga-assisted growth of GaAs nanowires on prepatterned Si(111). Locally Ga-rich conditions are needed for a high yield of vertical nanowires, but these conditions lead to droplet enlargement and thus inverse tapering. In contrast, we have shown that decreasing the Ga flux after nanowire formation enables the growth of untapered thin nanowires. Beyond this practical achievement, we have systematically investigated and successfully modeled the factors influencing the diameter evolution. We have found that in addition to the droplet dynamics, direct vapor-solid growth on the sidewalls is significant. In particular, the untapered morphology we obtained is the consequence of these two factors compensating each other.

In 2016, we demonstrated the fabrication of vertically oriented GaN nanowires on flexible Ti foils. As an attractive alternative to these conventional metal foils, we have investigated this year the synthesis of GaN nanowires on epitaxial graphene layer structures. We have found that the exposure of graphene to the N plasma used for the growth of GaN results in its progressive removal from the substrate. Despite this effect, we have succeeded in the direct growth of GaN nanowires on multilayer graphene. A detailed structural analysis has shown the presence of graphene underneath as well as in between nanowires, as desired for the use of this material as contact layer in nanowire-based devices. The nanowires nucleate preferentially at step edges, are vertical, well aligned, epitaxial, and of comparable structural quality as similar structures fabricated on conventional substrates such as Si or TiN.

One general challenge for the self-assembled growth of GaN nanowires is that it typically results in a very high number density, such that massive coalescence between nanowires is inevitable and imposes limitations on their structural quality. Now, we have identified for crystalline TiN films nanowire growth conditions leading to

number densities that prevent coalescence up to nanowire lengths exceeding 1 μm . A detailed analysis of the nearest neighbor distribution reveals that the low number density is enabled by considerable adatom diffusion on the substrate. These nanowire ensembles are promising templates for the growth of core-shell heterostructures. To obtain GaN nanowire ensembles with even lower number densities, we have developed a conceptually novel approach that allows us to achieve selective area epitaxy without the need of an ex situ prepatternning step. This approach is based on the fact that GaN nanowires do not form in plasma-assisted molecular beam epitaxy on structurally and chemically uniform cation-polar substrates. However, we have found that the in situ deposition and nitridation of Si on a Ga-polar GaN film induces a local polarity reversal that results in the selective area epitaxy of N-polar GaN nanowires. By accurately controlling the amount of predeposited Si, we have obtained ensembles of single-crystalline and uncoalesced nanowires with diameters as small as 20 nm and a number density well below 10^8 cm^{-2} . Hence, this growth approach allows us to gain control over the nanowire number density while preserving the small diameters and the high structural perfection of self-assembled GaN NWs.

External quantum efficiencies for light emitting diodes based on axial (In,Ga)N/GaN nanowire heterostructures have only rarely been reported, and have invariably been found to be disappointingly low. To elucidate the origin of this finding, we have performed a comparative analysis of carrier recombination in a planar device-grade Ga-polar (In,Ga)N/GaN quantum well structure and a representative N-polar GaN nanowire ensemble containing (In,Ga)N quantum disks. For both samples, the temporal decay of the photoluminescence intensity obeys a power law, reflecting the fact that recombination occurs between individual electrons and holes with varying spatial separation. For a quantitative understanding of these transients, we have developed

a model based on a coupled system of stochastic integro-differential equations taking into account both radiative and nonradiative Shockley-Read-Hall recombination of spatially separate electrons and holes as well as their diffusion. The transients of the nanowire sample can only be reproduced by a dominant nonradiative process assuming capture coefficients that are more than two orders of magnitude larger than those of the planar sample, resulting in an internal quantum efficiency of only 0.2% at 300 K as compared to 40% for the planar sample. This low efficiency seems to be inherent to N-polar (In,Ga)N/GaN quantum structures, questioning their suitability for future long-wavelength emitters.

To examine whether this phenomenon also affects N-polar (Al,Ga)N/GaN nanowire heterostructures, we have investigated the carrier recombination in ensembles of (Al,Ga)N nanowires with a single embedded GaN quantum disk of different thicknesses. For all samples, intense photoluminescence emission is observed at an energy above the band gap of GaN, shifting only weakly with disk thickness. This finding is in contrast to the strong quantum-confined Stark effect expected for these structures. Utilizing energy dispersive x-ray spectroscopy and atom probe tomography, we found that complex axial and radial compositional gradients had spontaneously formed during growth in the nominally uniform (Al,Ga)N nanowires. The unintended axial gradient results in a high electron density in the embedded GaN quantum disk due to polarization doping, an effect arising from the spontaneous polarization of the group-III nitrides. This two-dimensional electron gas screens the internal electrostatic fields in the disks to such an extent that the quantum-confined Stark effect is essentially absent. The metallic nature of the electron system furthermore results in a fast and only weakly temperature-dependent recombination between photoexcited holes and the degenerate electron gas in the quantum disk.

Intersubband Emitters: GaAs-based Quantum-Cascade Lasers

Intersubbandemitter: GaAs-basierte Quantenkaskadenlaser

Contact:

Prof. Dr. Holger T. Grahn

Dr. Lutz Schrottke

The excellent state of semiconductor science and technology allows for the development and application of sophisticated devices such as quantum-cascade lasers (QCLs). These devices rely on the comprehensive understanding and the high-quality growth of complex planar heterostructures. For the terahertz spectral region, which typically ranges from 0.1 to 10 THz bridging the electronics-based microwave region with the optics-based infrared region, GaAs/(Al,Ga)As-based heterostructures are the material of choice. The terahertz region is of great current interest for spectroscopic applications, since rotational states of many molecules, impurity transitions in semiconductors, and fine-structure transitions of atoms as well as ions can result in terahertz absorption or emission. The advantages of terahertz QCLs, covering at present the emission frequency range of 1 to 5 THz, are their compactness, narrow emission lines, and optical output powers typically between several mW and several tens of mW. Therefore, terahertz QCLs are already used as local oscillators in heterodyne receivers and are promising sources for high-resolution absorption spectroscopy, for instance for the precise determination of the absolute density of atoms and ions in technologically relevant plasma processes. In particular, QCLs for local oscillators at 4.75 THz are currently unrivaled for heterodyne detection of atomic oxygen, which is important in planetary and interstellar science.

Der hervorragende Stand der Halbleiterforschung und -technologie erlaubt die Entwicklung und Anwendung von anspruchsvollen Bauelementen wie Quantenkaskadenlasern (QCLs). Diese Bauelemente erfordern ein umfassendes Verständnis und das Wachstum komplexer planarer Heterostrukturen von hoher Qualität. Für den Terahertz-Spektralbereich, der typischerweise von 0,1 bis 10 THz reicht und den Bereich der elektronisch erzeugten Mikrowellenstrahlung mit dem der optisch erzeugten Infrarotstrahlung verbindet, sind GaAs/(Al,-Ga)As-Halbleiterheterostrukturen das bevorzugte Materialsystem. Terahertz-Strahlung ist derzeit von großem Interesse für spektroskopische Untersuchungen, da Rotationszustände vieler Moleküle, Übergänge in Fremdatomen in Halbleitern sowie Feinstrukturübergänge in Atomen und Ionen zu Absorption oder Emission in diesem Spektralbereich führen können. Die Vorteile von QCLs, deren Frequenzbereich sich derzeit von 1 bis 5 THz erstreckt, bestehen in ihrer Kompaktheit, schmalen Emissionslinien und Ausgangsleistungen von typischerweise einigen mW bis zu einigen 10 mW. Diese Laser werden bereits als Lokaloszillatoren in Heterodyn-Empfängern für astronomische Untersuchungen verwendet und sind vielversprechende Quellen für die hochauflösende Terahertz-Spektroskopie, unter anderem für die genaue Bestimmung der absoluten Dichte von Atomen und Ionen in technologisch relevanten Plasmen. Insbesondere sind QCLs als Lokaloszillatoren bei 4,75 THz gegenwärtig konkurrenzlos.

Im Gegensatz zu konventionellen Intersubband-Halbleiterlasern sind QCLs Intersubbandemitter, da der Laserübergang inner-

In contrast to conventional interband semiconductor lasers, QCLs are so-called intersubband emitters, since the lasing transition takes place within the conduction band rather than across the energy gap. Therefore, they are unipolar lasers, i.e., only one type of carrier, typically electrons, is injected into the laser structure. In order to obtain population inversion between subbands of the conduction band, a rather complex semiconductor heterostructure with typically 6 to 20 layers with thicknesses in the range of a few to about 20 nanometers has to be realized, which is repeated about 100 times forming a semiconductor superlattice with a complex unit cell. The total thickness of the complete structure typically amounts to about 10 µm. The realization of such a structure requires both, an appropriate modeling as well as design strategy and a highly accurate growth technique such as molecular beam epitaxy with a very good stability of the growth parameters over up to 20 hours. This growth expertise is one of the core competences of our institute. After growth, the wafers are processed using wet chemical or dry etching to form edge-emitting Fabry-Pérot ridge lasers. For single-mode operation, distributed-feedback lasers using lateral gratings of different order or two-section cavity lasers are realized. Typical dimensions of the laser ridges are widths of 15 to 200 µm and lengths of 0.5 to 7.5 mm.

Our activities in the field of terahertz QCLs cover the design, the growth, the fabrication, and the determination of the operating parameters of these lasers. Since 2014, QCLs developed in our institute have been used as local oscillators in the German REceiver for Astronomy at Terahertz frequencies (GREAT) on board of the Stratospheric Observatory For Infrared Astronomy (SOFIA) for the detection of the fine-structure transition of interstellar neutral atomic oxygen (OI) at 4.7448 THz. Recently, an improved laser has been operated in the

halb des Leitungsbands und nicht über die Energielücke erfolgt. Deshalb sind QCLs unipolare Halbleiterlaser, d.h. nur eine Ladungsträgerart, typischerweise Elektronen, wird in die Laserstruktur injiziert. Um Besetzungsinversion zwischen den Subbändern des Leitungsbandes zu erreichen, wird eine komplexe Heterostruktur mit etwa 100 Perioden, die typischerweise 6 bis 20 Schichten innerhalb einer Periode mit Dicken zwischen etwa 1 und 20 nm enthalten und die insgesamt etwa 10 µm dick ist, realisiert. Die Entwicklung von Terahertz-QCLs erfordert sowohl das Design und die Modellierung der Laser als auch die Herstellung komplexer Heterostrukturen. Dafür wird eine sehr präzise Wachstumsmethode wie die Molekularstrahl-Epitaxie mit einer guten Stabilität der Wachstumsparameter über bis zu 20 Stunden benötigt. Das Wachstum mittels Molekularstrahl-Epitaxie ist eine der Kernkompetenzen unseres Instituts. Die Laser werden anschließend mittels nass-chemischer Verfahren oder Trockenätzten als kantenemittierende Fabry-Pérot-Laserstreifen hergestellt. Für den Einzelmodenbetrieb werden Resonatoren mit verteilter Rückkopplung unter Verwendung von lateralen Gittern verschiedener Ordnungen oder Zweisektionslaser verwendet. Typische Abmessungen der Laserstreifen sind Breiten von 15 bis 200 µm und Längen von 0,5 bis 7,5 mm.

Unsere Aktivitäten auf dem Gebiet der Terahertz-QCLs beinhalten das Design, das Wachstum, die Herstellung und die Bestimmung der Betriebsparameter dieser Laser. Seit 2014 wurden ein von uns entwickelter Laser im German REceiver for Astronomy at Terahertz frequencies (GREAT) und ein weiterer, verbesserter Laser im neuen upGREAT-Instrument während der Beobachtungsflüge des Stratospheric Observatory for Infrared Astronomy (SOFIA) für den Nachweis eines Feinstrukturübergangs in interstellarem Sauerstoff bei 4,7448 THz eingesetzt.

next generation of terahertz astronomical receivers based on multichannel detection (upGREAT).

QCLs for the terahertz spectral region are usually based on GaAs/Al_xGa_{1-x}As heterostructures with 0.1 ≤ x ≤ 0.25. Since 2016, we have been able to realize GaAs/AlAs QCLs operating at 4.75 THz, which exhibit an about three times higher wall plug efficiency than GaAs/Al_{0.25}Ga_{0.75}As QCLs with an almost identical design. Substituting AlAs for the Al_{0.25}Ga_{0.75}As barriers leads to a larger energy separation between the subbands so that the probability for leakage currents through parasitic states and the reabsorption of the laser radiation can be reduced. Based on this new materials system, we have realized an improved QCL emitting at 4.75 THz with operating parameters adequate for spaceborne applications. Furthermore, we have successfully enlarged the frequency range of terahertz QCLs by shifting the upper frequency limit to above 5.6 THz.

For high-resolution spectroscopy, single-mode operation in conjunction with a sufficient tuning range is necessary. In 2017, we have realized single-mode QCLs using already functioning lasers by preparing a two-section cavity laser with a focused ion beam. In this case, the single-mode emission occurs at a frequency, where a mode is present in both cavities. Since the frequencies of these modes are not exactly the same, this type of laser can be tuned by external illumination of the back facet. Due to a local change of the refractive index and therefore of a reduction of the effective resonator length, a tuning of the laser modes can be observed. For a 3-THz QCL, we achieved tuning ranges of about 5 and 12 GHz for continuous-wave and pulsed operation, respectively. In contrast, distributed-feedback lasers cannot be tuned by this method, since the grating period selects the frequency for single-mode emission.

Terahertz-QCLs beruhen üblicherweise auf GaAs/Al_xGa_{1-x}As-Heterostrukturen mit 0,1 ≤ x ≤ 0,25. Seit 2016 können wir GaAs/AlAs-Laser für 4,75 THz mit einem mehr als dreifachen Gesamtwirkungsgrad im Vergleich zu GaAs/Al_{0,25}Ga_{0,75}As-Lasern herstellen. Der Ersatz der Al_{0,25}Ga_{0,75}As-Barrieren durch AlAs-Schichten führt zu einem größeren Energieabstand der Subbänder, so dass die Wahrscheinlichkeit von Leckströmen durch parasitäre Zustände reduziert wird. Auf Grundlage dieses neuen Materialsystems haben wir verbesserte 4,75-THz-Laser, die für weltraumgestützte Beobachtungsmissionen geeignet sein können, entwickelt. Weiterhin haben wir erfolgreich den zur Verfügung stehenden Frequenzbereich von Terahertz-QCLs durch eine Verschiebung der Höchstgrenze auf oberhalb von 5,6 THz vergrößert.

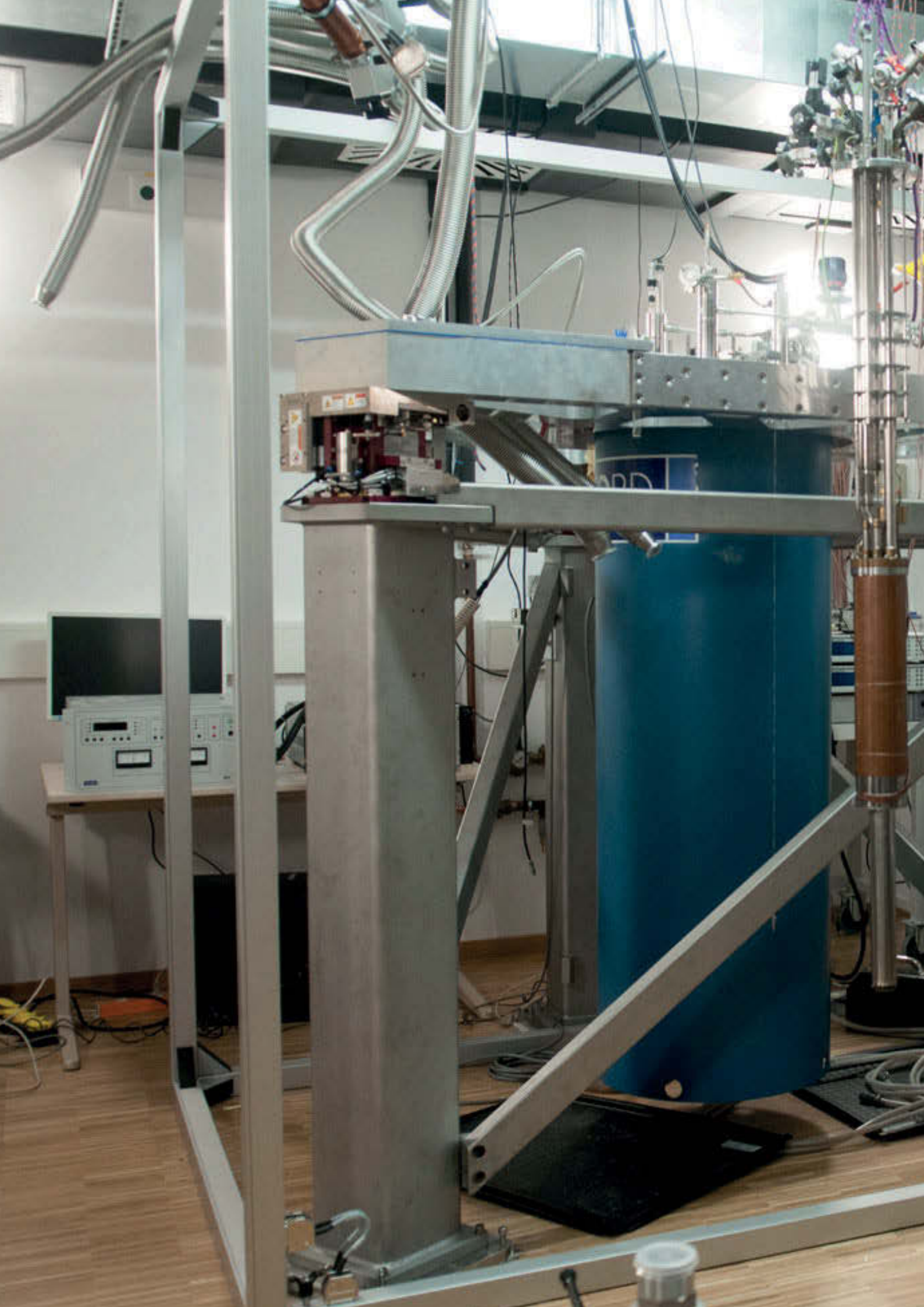
Für hochauflösende Spektroskopie müssen die Lasermoden im Einzelmodenbetrieb über die Absorptionslinien abstimmbar sein. Im Jahr 2017 haben wir unter Verwendung funktionierender Laser Einzelmodenbetrieb durch die Präparation von Zwei-sektionslasern mittels fokussierter Ionenstrahlen realisiert. Hierbei entsteht der Einzelmodenbetrieb bei einer Frequenz, für die Moden in beiden Teilresonatoren existieren. Da beide Modenfrequenzen nicht ganz genau übereinstimmen, kann dieser Lasertyp durch die Beleuchtung der Rückfacette mit nahinfraroter Strahlung durchgestimmt werden. Die erzeugten Ladungsträger führen zu einer lokalen Änderung des Brechungsindeks und dadurch zu einer Verringerung der effektiven Resonatorlänge. Für einen 3-THz-Laser haben wir Abstimmbereiche von etwa 5 und 12 GHz für Dauerstrich- bzw. gepulsten Betrieb erreicht. Im Gegensatz dazu können Laser mit verteilter Rückkopplung nicht mit dieser Methode durchgestimmt werden, da die Gitterperiode die Frequenz des Einzelmodenbetriebs bestimmt.

The intrinsic frequency tuning of multi-mode terahertz QCLs allows for a spectrally quasi-continuous terahertz radiation source based on a novel operation principle, the gapless, time-averaged wideband operation, if the tuning range due to current and temperature changes during the ramping of the applied current covers the mode spacing for a Fabry-Pérot resonator. For this operation mode, the ramping time has to be much shorter than the time constant of the detector. Applying a terahertz QCL in gapless, time-averaged wideband operation to a Fourier-transform infrared spectrometer, we have achieved a gapless spectrum over 72 GHz for a 4.7-THz QCL. Compared to a conventional thermal source based on a heated SiC rod, the available radiation powers of the QCL are larger by two orders of magnitude and the signal-to-noise ratios still by about one order of magnitude. As an example, we demonstrated the superiority of the QCL over the thermal source by detecting a water absorption line in humid air.

Since terahertz QCLs can be conveniently operated in liquid-coolant-free mechanical coolers, new paths have been opened toward various applications. Based on terahertz QCLs developed at the PDI, the group of Prof. Dr. Heinz-Wilhelm Hübers (Institute for Optical Sensor Systems at the Deutsches Zentrum für Luft und Raumfahrt in Berlin) has demonstrated real-time gas sensing based on optical feedback in a terahertz QCL and Lamb-dip spectroscopy with a terahertz QCL in 2017. Finally, the high level of design and growth of terahertz QCLs is demonstrated by several requests for commercial applications of our QCLs in table-top terahertz systems.

Das intrinsische Verstimmen der Laserfrequenz von Mehrmodenlasern mittels Strom- und Temperaturänderung erlaubt ein neues Betriebskonzept, die lückenlose, zeitgemittelte Emission von Laserstrahlung, wenn der Durchstimmbarkeitsbereich der Moden größer als der Modenabstand und die Durchstimmzeit viel kürzer als die Zeitkonstante des Detektors sind. Die Verwendung eines 4,7-THz-Lasers in diesem Betriebsmodus in einem Fourier-transform-Infrarotspektrometer führte zu einem lückenlosen Spektrum über 72 GHz. Im Vergleich zu einer konventionellen thermischen Quelle auf der Grundlage eines geheizten SiC-Stabes erreichten wir eine um zwei Größenordnungen höhere verfügbare optische Leistung und ein um etwa eine Größenordnung besseres Signal-zu-Rausch-Verhältnis. Als Nachweis des Vorteils dieser neuen Methode haben wir eine Wasserabsorptionslinie in feuchter Luft detektiert.

Da die Terahertz-QCLs problemlos in mechanischen Kühlern ohne kryogene Flüssigkeiten betrieben werden können, eröffnet sich eine Reihe von neuen Anwendungsmöglichkeiten. Unter Verwendung von Lasern, die im PDI entwickelt wurden, hat die Gruppe von Prof. Dr. Heinz-Wilhelm Hübers (Institut für Optische Sensorsysteme, Deutsches Zentrum für Luft und Raumfahrt in Berlin) im Jahre 2017 Echtzeit-Gas-Detektion auf der Basis von optischer Rückkopplung und Lamb-dip-Spektroskopie mit einem Terahertz-QCL demonstriert. Schließlich zeigt sich das hohe Niveau des Designs und des Wachstums von Terahertz-QCLs im PDI durch mehrere Anfragen für kommerzielle Anwendungen unserer Laser in kompakten Table-top-Terahertz-Systemen.





Brief Reports

Kurzberichte

Growth of $(\text{Ga},\text{In})\text{N}/\text{GaN}$ monolayers and short period superlattices on $\text{ZnO}(0001)$	67
Metal-exchange catalysis in the growth of sesquioxides: Towards heterostructures of transparent oxide semiconductors.....	71
Investigation of the bonding nature and symmetry of the crystalline phases of GeSbTe-based alloys and heterostructures	75
Transition metal dichalcogenides studied with low-temperature scanning tunneling microscopy	77
Challenges in transmission electron microscopy of emerging $\text{Ga}(\text{Sb},\text{Bi})$ epilayers and quantum wells for optoelectronic applications	81
In-situ growth mode analysis of homoepitaxial grown (100)-oriented $\beta\text{-}\text{Ga}_2\text{O}_3$	85
Gaussian beam electron optics with quantum point contacts	89
Coupled dipolar excitons in $(\text{Al},\text{Ga})\text{As}$ multilayers.....	93
Quantum confinement of exciton-polaritons by microscopic potentials in a patterned $(\text{Al},\text{Ga})\text{As}$ microcavity.....	95
Diameter evolution of selective area grown Ga-assisted GaAs nanowires	99
Polarity-induced selective area epitaxy of GaN nanowires.....	103
Molecular beam epitaxy of GaN nanowires on epitaxial graphene	107
Self-assembled formation of long, thin, and uncoalesced GaN nanowires on crystalline TiN films.....	111
N-polar $(\text{In},\text{Ga})\text{N}$ quantum disks in GaN nanowires vs. Ga-polar $(\text{In},\text{Ga})\text{N}/\text{GaN}$ quantum wells: Comparative analysis of carrier recombination, diffusion, and radiative efficiency.....	115
Absence of quantum-confined Stark effect in $\text{GaN}/(\text{Al},\text{Ga})\text{N}$ nanowires grown by molecular beam epitaxy.....	119
Continuous tuning of two-section, single-mode terahertz quantum-cascade lasers by fiber-coupled, near-infrared illumination.....	123
Terahertz quantum-cascade lasers as high-power and wideband, gapless sources for spectroscopy.....	127

Growth of (Ga,In)N/GaN monolayers and short period superlattices on ZnO(0001)

C. Chèze, T. Ernst, R. Calarco

ZnO is an attractive substrate for (Ga,In)N alloys as it is isomorphic to GaN and InN, and lattice-matched to $\text{In}_{0.18}\text{Ga}_{0.82}\text{N}$. Although the fabrication of InN films with high structural quality on O-polar ZnO(0001) by plasma-assisted molecular beam epitaxy is feasible [Cho *et al.* Appl. Phys. Lett. **100**, 152105 (2012)], for (Ga,In)N the strong chemical reaction of Ga with ZnO induces high defect densities [Cho *et al.* Appl. Phys. Lett. **101**, 052103 (2012)]. Here, we intend to protect the surface by depositing an intermediate InN layer coherent to ZnO. We therefore investigate the growth of InN, and InN/GaN heterostructures on ZnO of both the O-(O-ZnO) and the Zn-(Zn-ZnO) polarities by reflection

high-energy electron diffraction (RHEED) in the $\langle\bar{1}\bar{1}00\rangle$ azimuth.

We fabricated two sets of samples at 450°C on both ZnO polar surfaces in separate experiments. Prior to growth we monitored a streaky RHEED pattern for all ZnO substrates. Post-growth, no metal droplets were found on the surface, indicating that nearly all supplied In and Ga amounts were incorporated into the layers as the metal desorption was negligible at such a low growth temperature.

The first set of samples consists of InN layers of thickness between 1 monolayer (ML) and 10 MLs. For this set, we measured a

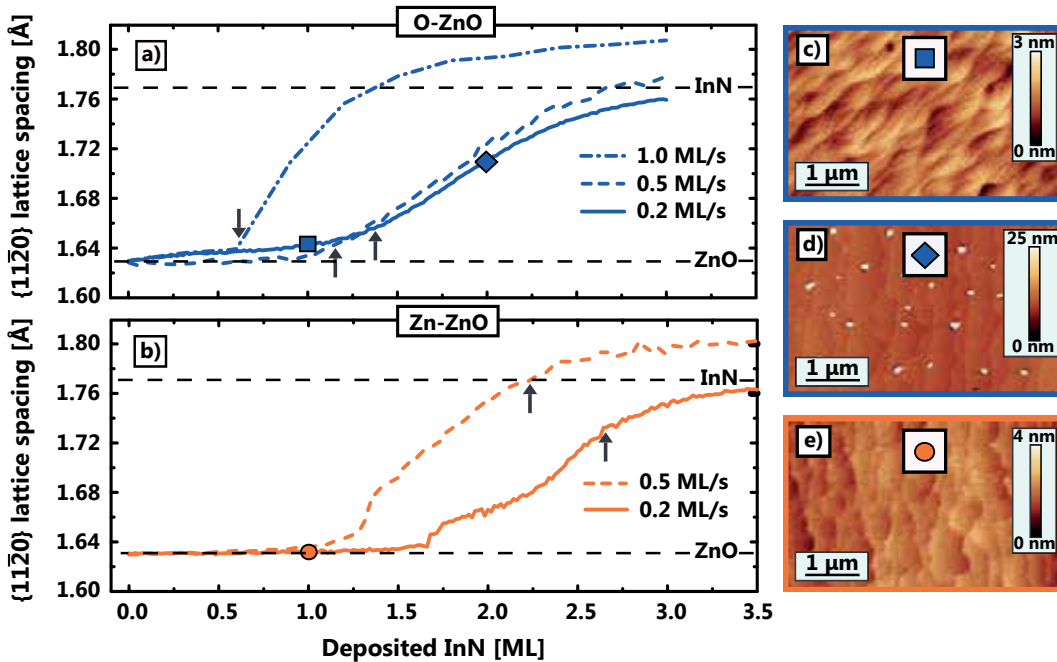


Fig. 1. (a), (b) $\{11\bar{2}0\}$ lattice spacing evolution measured by RHEED during the growth of InN on O-ZnO and Zn-ZnO for different growth rates, respectively. The grey arrows highlight the transition from streaky to spotty RHEED patterns, while the dashed black lines indicate the unstrained $\{11\bar{2}0\}$ lattice constants of InN and ZnO. (c), (d) AFM images of 1ML and 2MLs of InN on O-ZnO, and (e) 1ML of InN on Zn-ZnO. In (a)–(e) the color code indicates the growth on O-ZnO (blue) and Zn-ZnO (orange). Symbols in (a) (square, diamond) and (b) (circle) refer to the samples measured in (c)–(e). 1

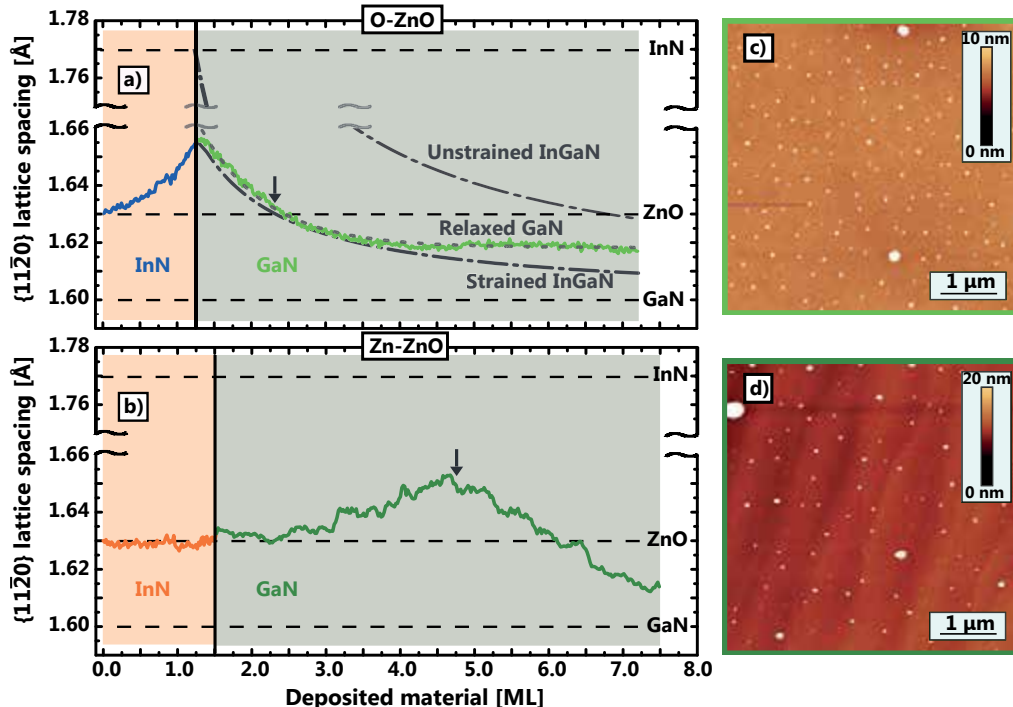


Fig. 2. (a), (b) $\{11\bar{2}0\}$ lattice spacing evolution measured by RHEED during the growth of 6MLs of GaN on 1.2 MLs and 1.5 MLs of InN on O-ZnO and Zn-ZnO, respectively. The grey arrows highlight the transition from streaky to spotty RHEED patterns, while the dashed black lines indicate the unstrained $\{11\bar{2}0\}$ lattice constants of InN, GaN, and ZnO. (c), (d) AFM images of the samples corresponding to (a) and (b), respectively. In (a)–(d) the color code indicates the growth on O-ZnO (blue) and Zn-ZnO (orange). In (a)–(d) we also plotted the lattice spacing evolution of $(\text{Ga},\text{In})\text{N}$ following Vegard's law (dashed-dotted lines) for the unstrained and strained cases, as well as the one of GaN relaxing following an exponential law (dotted line).

similar evolution of the $\{11\bar{2}0\}$ lattice spacing during InN growth on O-ZnO [Fig. 1(a)] and on Zn-ZnO [Fig. 1(b)]. As growth starts, the streak spacing corresponds to the unstrained ZnO lattice spacing, i.e. InN grows at first pseudomorphic to ZnO. Beyond a critical thickness, the lattice spacing increases and relaxation sets in. The critical layer thickness increases up to 1.4–1.6 MLs with the decrease of the growth rate down to 0.2 ML/s and is comparable on both polarities at identical growth rate. In contrast, the roughening of the surface revealed by the emergence of the spotty patterns in RHEED [see grey arrows in Fig. 1(a), (b)] occurs at different stages of the relaxation depending on the ZnO polarity. For O-ZnO it approximately coincides with the beginning of the relaxation process, i.e. at the onset of the increase of the lattice spacing, while for Zn-ZnO it occurs towards the end

of the relaxation. This finding is also confirmed by the surface morphology of three dedicated samples investigated by atomic force microscopy (AFM) [Fig. 1(c)–(e)]. In brief, coherent and smooth InN layers can be grown on ZnO only if their thickness is less than 1.6 MLs.

For the second set of samples, we deposited 6 MLs of GaN on top of 1.2 MLs of InN on O-ZnO and 1.5 MLs of InN on Zn-ZnO. After the deposition of the InN layers, we obtained a streaky RHEED pattern on both surfaces in agreement with the above results. Nonetheless, the monitoring of the $\{11\bar{2}0\}$ lattice spacing in dependence of the thickness of InN and GaN revealed this time a very different evolution for growth on O-ZnO and on Zn-ZnO. On O-ZnO [Fig. 2(a)] the lattice spacing gradually decreases at the start of GaN deposition.

Beyond the thickness of 1ML, the lattice spacing even decreases further below the lattice spacing of ZnO and the pattern becomes spotty. Considering the possible alloying into (Ga,In)N, the evolution of the lattice spacing calculated by Vegard's law provides a satisfactory agreement only when setting the InN $\{11\bar{2}0\}$ lattice spacing equal to the experimental value attained just before the start of GaN deposition. Moreover, beyond a total layer thickness of 3.5MLs (1.2MLs InN + 2.3MLs GaN), the experimental and calculated data diverge. A much better agreement is obtained when considering a gradual relaxation of GaN following an exponential law, also supported by the spotty pattern. Thus, we attribute the changes in the GaN lattice spacing rather to relaxation than to intermixing.

In striking contrast, on Zn-ZnO [Fig. 2(b)] the $\{11\bar{2}0\}$ lattice spacing remains constant up to a total layer thickness of 3.2MLs (1.5MLs InN + 1.7MLs GaN). Thus, the thickness of 1.7MLs can be assigned to the critical thickness of GaN on InN fully strained to ZnO. Beyond 3.2MLs, the $\{11\bar{2}0\}$ lattice spacing increases slightly, possibly due to the formation of partially relaxed (Ga,In)N or to the relaxation of the InN intermediate layer. Beyond 4.7MLs (1.5MLs InN + 3.2MLs GaN) the $\{11\bar{2}0\}$ lattice spacing inverts its evolution and decreases concomitantly to the appearance of the spotty pattern in RHEED, that points to further relaxation. After growth the investigation by AFM revealed the formation of three-dimensional features on both sample surfaces [Fig. 2(c), (d)], which further confirmed the RHEED observations. The surface between these features appears in both cases still smooth and atomic steps are observed.

To summarize and conclude, we monitored the growth of InN and InN/GaN layers on ZnO{0001} by RHEED. For InN, we measured for the onset of relaxation critical thickness values of 1.4–1.6MLs. With this

information, we utilized coherently grown and smooth InN layers as intermediate layers for the growth of GaN to prevent the chemical reaction of Ga with ZnO. We further probed the critical thickness of GaN on such layers, which is clearly below 1.0ML on O-ZnO and 1.7MLs on Zn-ZnO. Thereby, we identified the characteristics of a starting layer protective against chemical reactions with Ga to be utilized for further growth of (Ga,In)N heterostructures pseudomorphic to ZnO.

Metal-exchange catalysis in the growth of sesquioxides: Towards heterostructures of transparent oxide semiconductors

P. Vogt, O. Brandt, H. Riechert, J. Lähnemann, and O. Bierwagen

The possibility of band gap engineering by fabricating group III-V semiconductor alloys and heterostructures has enabled the development of key technologies such as optoelectronics, telecommunication, and solid-state lighting. The sesquioxides In_2O_3 , Ga_2O_3 and Al_2O_3 are an emerging class of materials with unique physical properties, and promising candidates for the next generation of opto- and powerelectronic devices. However, the synthesis of these oxides is much more complex as compared to III-V semiconductors. Particularly, the growth rate of the binary sesquioxides is limited by volatile suboxide formation and its subsequent desorption. This restricts their growth conditions to rather low growth temperatures T_G and mainly to the O-rich regime, with detrimental consequences for the crystal quality.

In this report, we present a novel mechanism which circumvents suboxide formation and lifts the rigid constraints on the conditions under which the synthesis of Ga_2O_3 films is possible. Using an additional flux of In (Φ_{In}) during the O plasma-assisted molecular beam epitaxy (PAMBE) of Ga_2O_3 , we observe that its growth rate $\Gamma_{\text{Ga}_2\text{O}_3}$ is drastically enhanced. It remains high even for T_G for which Ga_2O_3 does not form at all in the absence of In. We show that this phenomenon is caused by the rapid formation of In_2O_3 followed by an exchange of In in In_2O_3 by Ga adatoms. In adatoms released by this reaction can be reoxidized, and In_2O_3 hence acts as a catalyst for the growth of Ga_2O_3 .

Figure 1 shows the flux of Ga_2O ($\Phi_{\text{Ga}_2\text{O}}^{\text{des}}$) and In ($\Phi_{\text{In}}^{\text{des}}$) desorbing from a monoclinic $\beta\text{-Ga}_2\text{O}_3$ template as measured by line-of-sight quadrupole mass spectrometry

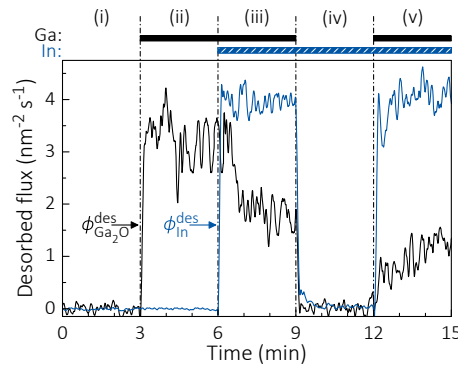


Fig. 1. Desorption of Ga_2O and In from a $\beta\text{-Ga}_2\text{O}_3(\bar{2}01)$ surface. The metals supplied in the time intervals (i)–(v) are indicated by the bars on top.

(QMS). During the initial time interval (i), the surface was only exposed to an active O flux (Φ_O), and no desorption of metal species takes place. In the time interval (ii), a Ga flux (Φ_{Ga}) was additionally supplied to the surface. At this $T_G = 700^\circ$, no Ga_2O_3 growth takes place as evidenced *in situ* by laser reflectometry (LR, not shown). Instead, Ga reacts with O forming the volatile suboxide Ga_2O . The desorption flux of Ga_2O indeed accounts for the total Φ_{Ga} supplied. In the time interval (iii), Φ_{In} is supplied in addition to Φ_{Ga} and Φ_O . After a short delay, the Ga_2O desorption flux decreases, and LR evidences the growth of Ga_2O_3 (not shown). At this T_G , all In supplied to the surface desorbs in agreement with the absence of In in the Ga_2O_3 film as measured by *ex situ* energy dispersive x-ray spectroscopy (EDX). When the Ga shutter is closed in the time interval (iv), In desorption ceases as In_2O_3 nucleates immediately, and in combination with LR, complete In incorporation is observed and the growth rate of In_2O_3 corresponds to Φ_{In} . Once the Ga shutter is opened again in the time interval (v), Ga_2O_3 growth sets in

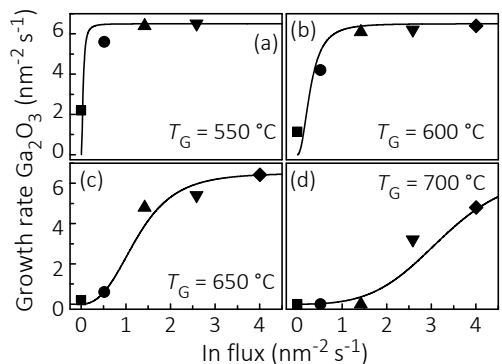


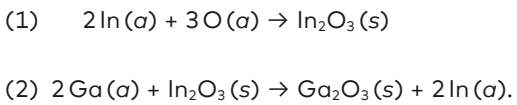
Fig. 2. Dependence of $\Gamma_{\text{Ga}_2\text{O}_3}$ on Φ_{In} for different T_G as indicated in the figures. Symbols represent experimental data and solid lines are predictions of a rate-equation model.

again with $\Gamma_{\text{Ga}_2\text{O}_3} = 4.4 \text{ nm}^{-2}\text{s}^{-1}$ on In_2O_3 , and In desorbs simultaneously. This sequence of experiments shows most clearly that the additional In has a catalytic effect on the formation of Ga_2O_3 : It enables the growth of Ga_2O_3 under conditions where Ga_2O_3 will not form at all in the absence of In.

Figure 2 plots the measured growth rate $\Gamma_{\text{Ga}_2\text{O}_3}$ of Ga_2O_3 as a function of Φ_{In} at different T_G . *Ex-situ* EDX measurements confirm that no In was incorporated in the entire parameter space. The data points depicted at $\Phi_{\text{In}} = 0$ correspond to the values of $\Gamma_{\text{Ga}_2\text{O}_3}$ in the absence of In at otherwise identical growth conditions. Evidently, additional Φ_{In} enhances $\Gamma_{\text{Ga}_2\text{O}_3}$ significantly even at low T_G , and enables the growth at higher T_G . This effect is the stronger the higher Φ_{In} : with increasing Φ_{In} , $\Gamma_{\text{Ga}_2\text{O}_3}$ monotonically increases until it saturates at Φ_{Ga} , corresponding to complete Ga incorporation. Note that $\Gamma_{\text{Ga}_2\text{O}_3}$ can exceed Φ_{In} , demonstrating that a fraction of In atoms released by the In-Ga exchange process is reoxidized.

Based on the understanding of the factors governing the growth of Ga_2O_3 acquired in our previous studies, we explain this observation by a two-step reaction. Due to the higher oxidation efficiency of In compared to Ga, the formation of In_2O_3 is kinetically

favored, i.e., In adatoms are faster to react with the impinging Φ_{O} compared to Ga adatoms. Hence, In_2O_3 is formed predominantly in this first step of the reaction. However, In_2O_3 is unstable in the presence of Ga as it is energetically favorable to replace In by Ga in the In-O bonds. Ga exchanges In, using the O reacted to In_2O_3 as a reservoir, while transferring the exchanged In to the oxide surface. In this way, the formation of the volatile suboxide Ga_2O is bypassed, allowing Ga_2O_3 to be grown at elevated T_G and nominally Ga-rich conditions. Depending on the surface lifetime of In adatoms, they can be reoxidized to In_2O_3 , and subsequently exchanged by other Ga adatoms. This reoxidation step principally enables $\Gamma_{\text{Ga}_2\text{O}_3}$ to exceed Φ_{In} , as indeed experimentally observed. The consecutive catalytic reaction including the initial formation of In_2O_3 and the subsequent In-Ga exchange, constituting the metal-exchange oxide growth, thus reads as:



The adsorbate and solid phases are denoted as α and s , respectively. Based on this two-step reaction we have set up a rate-equation model which takes into account the most likely reaction mechanisms governing the formation of In_2O_3 and Ga_2O_3 (not presented here).

As a unique benefit of the observed metal-exchange catalysis, we are able to explore PAMBE growth regimes for the synthesis of Ga_2O_3 films which were previously inaccessible. These regimes allow to form the metastable hexagonal modification $\epsilon\text{-Ga}_2\text{O}_3$, whose x-ray diffraction (XRD) pattern in the growth direction is depicted in Fig. 3. This ϵ -phase, synthesized at high T_G and high Φ_{Ga} by virtue of the metal-exchange catalysis, is of considerable interest for the realization of $\epsilon\text{-Ga}_2\text{O}_3(0001)/\text{In}_2\text{O}_3(111)$ heterostructures since the sur-

face symmetry of these phases matches. In addition, the structural similarity between the hexagonal modification of Ga_2O_3 and the bixbyite structure of In_2O_3 may facilitate the synthesis of homogeneous $(\text{In}_x\text{Ga}_{1-x})_2\text{O}_3$ alloys with a significant In content, where In incorporation is promoted by a sufficiently high Φ_0 .

Finally, we point out that the metal-exchange catalysis discovered in the present work should apply to all ternary materials whose binary constituents exhibit analogous kinetic and thermodynamic properties as those discussed above for In_2O_3 and Ga_2O_3 . We expect catalytic effects for a wide range of ternary oxide alloys, but also for various other multicomponent oxides fabricated by MBE. If successful, these developments will open a new path for the band gap engineering and heterostructural synthesis of transparent semiconducting oxides.

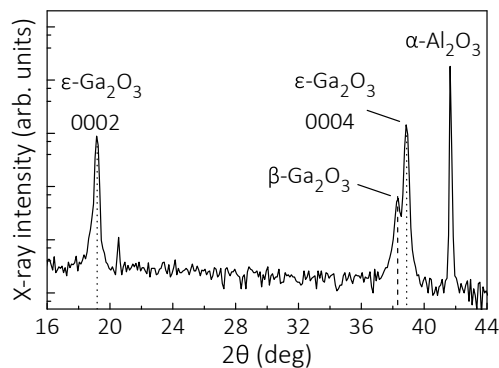


Fig. 3. Longitudinal XRD scan of an $\varepsilon\text{-Ga}_2\text{O}_3(0001)$ film on a $\beta\text{-Ga}_2\text{O}_3(201)$ / $\alpha\text{-Al}_2\text{O}_3(0001)$ template.

Investigation of the bonding nature and symmetry of the crystalline phases of GeSbTe-based alloys and heterostructures

E. Zallo, V. Bragaglia, R. Wang, and R. Calarco

GeSbTe-based (GST) alloys can be switched reversibly between the amorphous (a-) and the crystalline (x-)phase. Due to the difference in the bonding nature and atomic arrangement, a striking change in the optical and electrical properties occurs between the a-phase (low reflectivity and high resistance), and the x-phase (high reflectivity and low resistance). Thus, information storage can be accomplished by associating a binary code to the different values of optical reflectivity or electrical resistivity of the one or the other phase.

GST alloys present two x-phases: A metastable cubic one (c-GST), which is the one technologically relevant, and a stable trigonal one (t-GST). The two x-phases, however, are rather similar: They fundamentally consist of alternately stacked Te and Ge/Sb layers along the [111] direction. Differences arise from the vacancies configuration, being randomly distributed in the Ge/Sb layers for c-GST and organized in periodic van der Waals (vdW) gaps in between two adjacent Te layers for t-GST. Thermal annealing allows to transform the crystal-symmetry from disordered c-GST into ordered t-GST.

The growth of GST alloys is quite demanding as an interplay between composition, phase and ordering occurs. Control over those three parameters is mandatory to obtain material with well defined physical properties. Thus, we establish here the use of Raman spectroscopy as the basis for a correlation between growth parameters and structural properties. Raman scattering is perfectly suited for the investigation of changes in bonding as well as symmetry of GST. The inelastic interaction between optical laser radiation and electron orbitals is used to probe the bonding of atoms

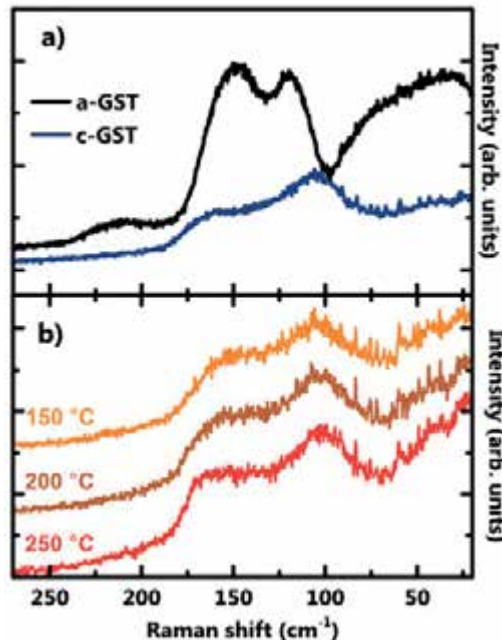


Fig. 1. (a) Comparison of Raman spectra for as-grown a-GST (black) and c-GST (blue). (b) Raman spectra of crystallizing a-GST for three different temperatures. Upon increasing the temperature new modes appear, indication of the transition from c- to t-GST.

in the short range and thus can be applied indiscriminately to amorphous and crystalline material.

In Fig. 1(a) Raman spectra of as-grown a- and c-GST samples are presented. The a-GST spectrum is characterized by the boson peak ($30\text{--}100\text{ cm}^{-1}$), two modes centered at 120 and 148 cm^{-1} and a broad feature at 210 cm^{-1} . In the c-GST spectrum two strong broad modes centered at 105 cm^{-1} (symmetry type E_g) and 160 cm^{-1} (A_g) are present. Such modes are characteristic of the metastable cubic c-GST phase (point group $m3m$). According to the $Fm\bar{3}m$ space group expected for metastable c-GST, no Raman active modes should be allowed. The fact that such vibrations are observed and are broad, is attributed

to the presence of vacancies and defects that are responsible for the local symmetry breaking.

In order to study the temperature dependence of the vibrational modes, annealing of a-GST was performed during Raman data acquisition. At $T=150^{\circ}\text{C}$ [orange curve in Fig. 1 (b)] the characteristic modes of the cubic phase compare well with those reported in Fig. 1 (a) for the as-grown c-GST. At $T=250^{\circ}\text{C}$ the film transforms into t-GST [red curve in Fig. 1 (b)], for which two evident modes are identified: One at 170 cm^{-1} (A) and a second one at 100 cm^{-1} (E). A third faint mode at 45 cm^{-1} is also detected. The mode at 170 cm^{-1} starts to be visible in the spectra at $T=200^{\circ}\text{C}$, and is associated to vacancies ordering into layers which breaks locally the cubic symmetry, and this ordering transforms into vdW gaps once the t-GST phase is achieved (red curve).

These results laid the groundwork for the investigation of crystalline GST based superlattices (SL), which resemble the ordered t-GST structure due to the presence of periodic vdW gaps in between building blocks of alternating Te, Sb and Ge layers. SLs are particularly interesting as they display reduced switching energies, improved write-erase cycle lifetimes, and faster switching speeds. Furthermore, for SLs exists possibly a non-thermal route in the optical switching process, so that the excitation process induces a negligible temperature change, differently from the case of melting needed for the switching of GST alloys. In particular, a combination of electrical and optical studies on similar SLs highlighted the influence of the electric field on the switching properties, although the laser light still altered the temperature of the sample.

In Fig. 2, Raman spectra of a 112 nm thick SL {stack [GeTe (4.4 nm)/ Sb_2Te_3 (6.8 nm)] \times 10} acquired at different laser illumination powers are presented. The spectra at low laser powers resembles the

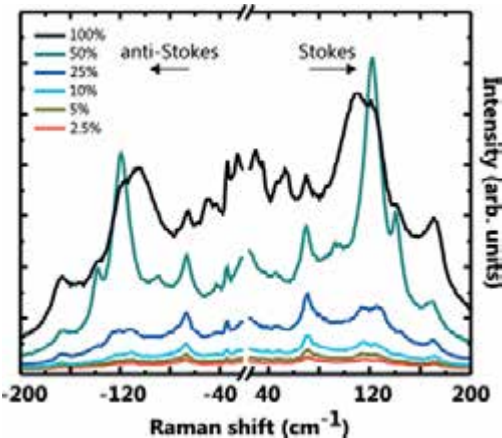


Fig. 2. Raman spectra of a $\text{GeTe}/\text{Sb}_2\text{Te}_3$ SL recorded at room temperature with different laser illumination powers as indicated in the legend. Due to Rayleigh scattering the central portion of the spectra is removed for the sake of clarity.

typical vibrational modes of Sb_2Te_3 with symmetry type A_{1g} (1) at 69 cm^{-1} , E_g (2) at 114 cm^{-1} , A_{1g} (2) at 171 cm^{-1} and a weak E_g (1) mode at 45 cm^{-1} . A high-frequency shoulder of the A_{1g} (1) mode is located at the position of the E mode of GeTe at 78.5 cm^{-1} .

By analyzing the intensity ratio of anti-Stokes and Stokes scattering, we are able to estimate the heat transfer to the sample during illumination. We find that at high laser power (100% corresponding to a power density of 10^5 W/cm^2) the spectrum changes irreversibly with the formation of an ordered GST phase: During the spectrum acquisition the local sample temperature rises up to 177°C . Such a GST structure is not observed after annealing of the same sample up to 300°C . Hence, we conclude that the observed transition results from the interaction of the electric field with the crystal bonds, thus providing the additional energy budget necessary for the transformation. We therefore envision that the application of ultra short laser pulses at an optimized fluence on such as-grown SLs might pave the way to controlling the structural phase of chalcogenide SLs at a temperature lower than the melting point.

Transition metal dichalcogenides studied with low-temperature scanning tunneling microscopy

Y. Pan, Y.-C. Lin, B. Jariwala, J. Robinson, R. M. Feenstra, and S. Fölsch

Transition metal dichalcogenide (TMD) monolayers are currently of great fundamental and technological interest because they represent atomically thin semiconductors. In general, the electrical properties of TMD layers are highly sensitive to microscopic details like atomic-scale defects or interfacial effects in the case of TMD heterostructures. Here, we employ a scanning tunneling microscope (STM) operated at 5 K to probe the microscopic structure and electronic states of these two-dimensionally (2D) layered materials.

In the TMD monolayer, a layer of transition metal atoms is sandwiched between two layers of chalcogen atoms. The in-plane hexagonal bonding geometry is illustrated in Fig. 1(a). The TMD layers studied here were grown by metal-organic chemical vapor deposition (WSe_2) and powder vaporization (MoS_2) on epitaxial graphene (EG)

which was formed on SiC substrates. Figure 1(b) shows an STM topography image of a WSe_2 single layer at atomic resolution, visualizing the hexagonal atomic arrangement within the topmost Se layer. In addition, the image shows a total of eight point defects that fall into three different categories regarding their STM appearance. We attribute these point defects to single Se vacancies (either in the topmost or the lower layer) and double Se vacancies (in the topmost and lower layer). Point defects in terms of chalcogen vacancies were previously observed by others with transmission electron microscopy. For the WSe_2 layers under study, we find an average point defect density of $2 \times 10^{12} \text{ cm}^{-2}$ as deduced from a large number of wide-area STM images.

Figure 1(c) shows dI/dV spectra (as a measure of the electronic density of

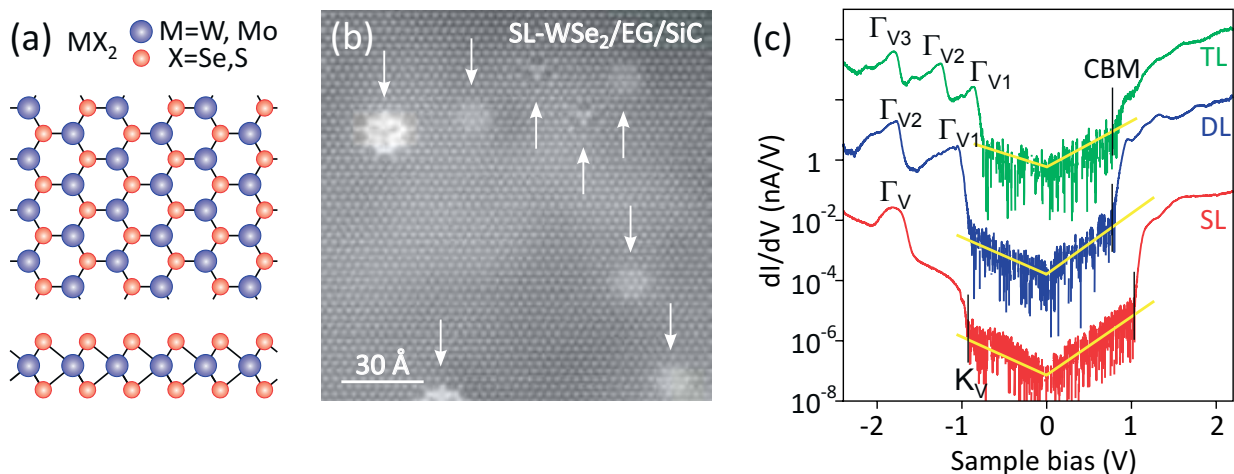


Fig. 1. (a) Stick-and-ball model of the transition metal dichalcogenide monolayer in top view (upper panel) and side view (lower panel) with blue balls being the transition metal and red balls the chalcogen. (b) STM topography image (100 pA, 1.3 V, 140 Å × 140 Å) of a WSe_2 single layer grown on epitaxial graphene (EG) showing the arrangement of Se atoms in the surface layer; three different types of point defects are marked by arrows. (c) dI/dV spectra recorded with the STM tip located on top of a single (SL), double (DL), and triple WSe_2 layer (TL). The dI/dV peak observed at -1.81 V for the SL (red curve) is associated with the valence band (VB) maximum at the Γ point. Due to interlayer coupling, this band splits into two and three bands for the DL (blue curve) and TL (green curve), respectively.

states) recorded by probing a single (SL), double (DL), and triple WSe₂ layer (TL) with the STM tip. The yellow lines indicate the noise level in each measurement. For the single layer (red curve), the absolute valence band (VB) maximum at the K point of the surface Brillouin zone is observed at -0.95 V, whereas the relative VB maximum at the Γ point occurs at -1.81 V. For the double layer (blue curve), on the other hand, the absolute VB maximum is at the Γ point and the interlayer coupling leads to a band splitting as obvious from the emergence of two dI/dV peaks in the VB regime. Finally, for the triple layer (green curve) a splitting into three bands and thus the occurrence of three dI/dV peaks is observed in the VB regime. The data in Figure 1(c) also show that the band gap of SL WSe₂ amounts to $E_g = 1.97$ eV. While SL WSe₂ has a direct band gap at the K point, thicker layers are known to be indirect band-gap semiconductors. Our measurements show that the gap width decreases as the layer thickness increases, yielding values of $E_g = 1.69$ eV (DL) and $E_g = 1.56$ eV (TL), respectively. These observations are consistent with previous predictions and findings regarding the electronic structure of WSe₂ layers.

We also investigate vertical TMD heterostructures grown on EG. As an example, Fig. 2(a) shows an STM image of a SL MoS₂ island grown on top of an extended SL WSe₂ terrace documenting the formation of regular triangular islands. Clearly, the island edges are decorated by irregular clusters pointing to local step-edge oxidation as a result of air exposure during sample transfer between growth setup and STM. This known effect arises from the presence of dangling bonds and thus enhanced reactivity at the step edges. On the other hand, bare terraces of MoS₂ and WSe₂ are chemically inert and can be readily cleaned after air exposure by annealing at 280°C in ultra-high vacuum. Figure 2(a) also reveals a hexagonal corrugation of the MoS₂ surface with a characteristic length of about 85 Å

indicating moire pattern formation due to the lattice mismatch between the two weakly coupled TMD layers (the hexagonal lattice constants at room temperature are 3.16 Å for MoS₂ and 3.30 Å for WSe₂, respectively).

Scanning tunneling spectroscopy (STS) measurements of the differential tunneling conductance were performed also to explore the electronic properties of the vertical MoS₂-WSe₂ heterostructure. The dI/dV spectra in Fig. 2(b) show that the band gap of SL MoS₂ is $E_g = 1.52$ eV, i.e., significantly smaller than that of SL WSe₂. The band edges of the MoS₂ layer are shifted to lower energies relative to the band edges of the WSe₂ layer, leading to the type II staggered-gap alignment schematically shown in Fig. 2(c). In addition, we found that the oxidized step edges are associated with electronic gap states, resulting in a quasi-semimetallic character in contrast to the semiconducting character of the homogeneous layer.

Our results demonstrate that single-crystalline TMD layers and vertical heterostructures of low defect density can be epitaxially grown on EG and their microscopic properties can be probed in detail by STM and STS at low temperature. This provides a basis for future TMD-related research in which we plan to focus on, e.g., the electronic properties of intrinsic point defects, lateral heterojunctions induced by the graphene substrate, and the atomically precise manipulation of adatoms and point defects with the STM tip.

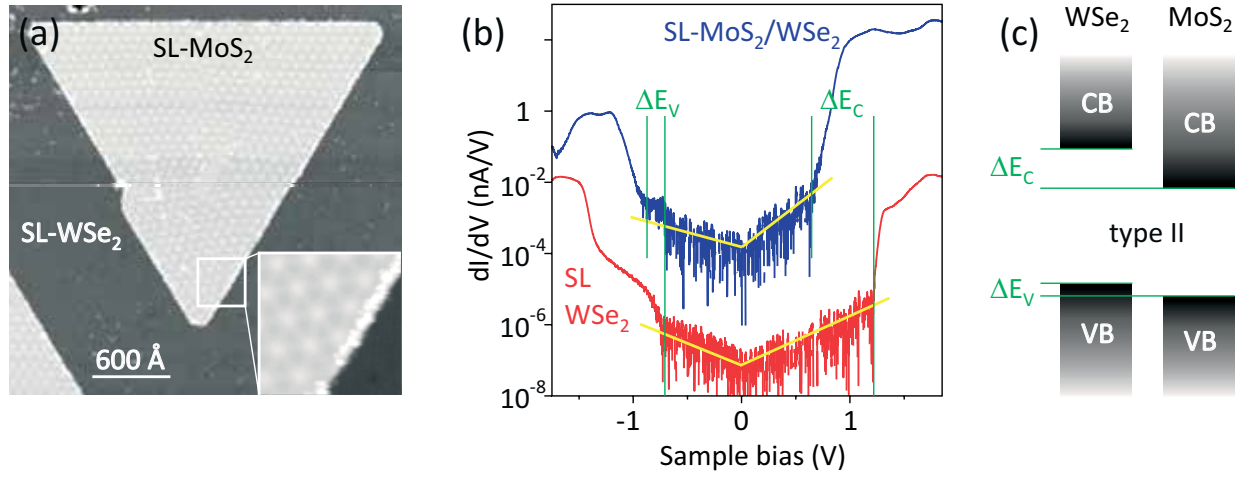


Fig. 2. (a) STM topography image (10 pA, 2.5 V, 3020 Å × 3020 Å) of a SL MoS₂ island grown on an extended SL WSe₂ terrace, revealing oxidized step edges and a moire pattern due to the mismatch between the two TMD lattices; the close-up inset shows the step edge structure and the moire pattern in more detail. (b) dI/dV spectra recorded on the bare SL WSe₂ terrace (red) and the SL MoS₂ grown on top of it (blue), the respective band edge positions reveal a type II staggered-gap alignment as marked by the vertical green lines. (c) Scheme of the type II staggered-gap alignment with the energy offsets ΔE_V and ΔE_C at the valence and conduction band edges, respectively, indicated in green.

Challenges in transmission electron microscopy of emerging Ga(Sb,Bi) epilayers and quantum wells for optoelectronic applications

E. Luna, O. Delorme^{1,2}, L. Cerutti^{1,2}, E. Tournié^{1,2}, J.-B. Rodriguez^{1,2}, and A. Trampert

The development of III-V-Bi compounds has recently emerged as a strong research field in semiconductor science and technology. This is mainly due to the unique properties of dilute bismides, such as the large band gap reduction and spin-orbit splitting energy increase upon the incorporation of a few percent Bi. Among Bi-containing III-V semiconductors, Ga(As,Bi) is with some limitations the most investigated material. On the contrary, GaSb compounds alloyed with Bi have been far less studied. Most of the few published works on Ga(Sb,Bi) focus on growth to explore the parameters controlling Bi incorporation. The assessment of the quality of the samples is commonly based on X-ray diffraction (XRD), atomic force microscopy, scanning electron microscopy and optical measurements. The Bi composition is mainly determined using Rutherford backscattering spectroscopy (RBS). Surprisingly, there is an apparent lack of information on the samples' microstructure determined using transmission electron microscopy (TEM), otherwise a powerful tool to get experimental evidence of the structural quality of the epilayers, interface abruptness and estimations of the local chemical composition.

As discussed here, the TEM investigation of Ga(Sb,Bi) poses several difficulties. We found out that one of the very first limitations concerns the delicate TEM specimen preparation on its own, which requires the development of specific preparation techniques and steps to assure high-quality TEM specimens free of artifacts introduced during preparation. Furthermore, we encounter the challenge of chemically sensitive \mathbf{g}_{002} dark-field (DF)TEM imaging of Ga(Sb,Bi), characterized by an extremely low contrast. In this report, we present the analysis by scanning (S)TEM of a series of

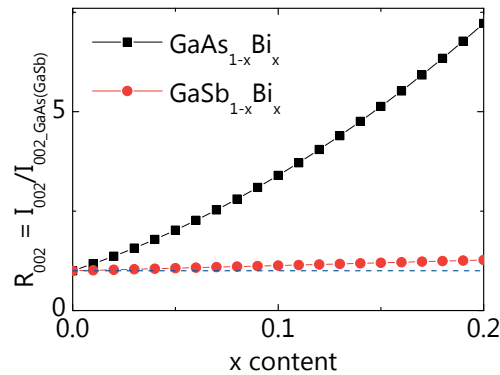


Fig. 1. Estimated \mathbf{g}_{002} DFTEM image contrast computed as the ratio of the diffracted intensity at the layer and at the GaSb (GaAs) reference, respectively.

Ga(Sb,Bi) epilayers and Ga(Sb,Bi)/GaSb quantum wells (QWs) grown by molecular beam epitaxy (MBE), which formed the basis for the successful realization of the first mid-infrared QW laser with room temperature operation [O. Delorme et al., Appl. Phys. Lett. **110**, 222106 (2017)].

In general, chemically sensitive \mathbf{g}_{002} DFTEM is a powerful and direct method to determine the element distribution in III-V semiconductors with zinc-blende structure. Furthermore, \mathbf{g}_{002} DFTEM imaging is a very valuable technique for the investigation of compositional inhomogeneities in Ga(As,Bi) [E. Luna et al., Nanotechnol. **27**, 325603 (2016)], allowing the detection of small variations (around 0.5%) in Bi content. Theoretical estimations of the diffracted intensity for the 002 reflection in Ga(Sb,Bi) predict, however, that the intensity contrast to GaSb is extremely low, with $I_{002\text{-GaSbBi}}/I_{002\text{-GaSb}} = 1.19$ for Ga(Sb,Bi) with 14% Bi, which is in marked difference to Ga(As,Bi) where $I_{002\text{-GaAsBi}}/I_{002\text{-GaAs}} = 4.7$ for Ga(As,Bi) with 14% Bi, as represented in Fig. 1. Thus, in order to estimate the Bi content in Ga(Sb,Bi) and, in particular, its

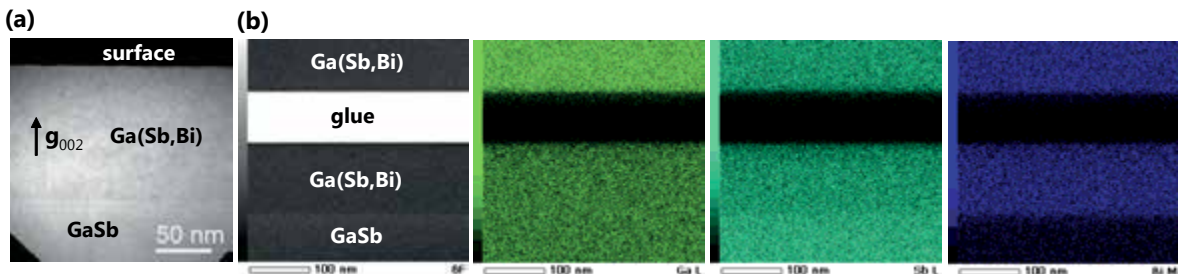


Fig. 2. (a) Chemically sensitive \mathbf{g}_{002} DFTEM micrograph and (b) bright-field STEM image and EDS compositional map of the pseudomorphic Ga(Sb,Bi) epilayer with 14% Bi.

spatial distribution (i.e. homogeneity), it is therefore necessary to correlate the results of \mathbf{g}_{002} DFTEM with local energy dispersive x-ray spectrometry (EDS) measurements, RBS estimations of [Bi], as well as macroscopic XRD studies. Note that due to the low contrast and, in general, the low signal of Ga(Sb,Bi) at (S)TEM, the measurements are very sensitive to strain, thin-foil surface relaxation and bending, hence the successful (S)TEM investigation of Ga(Sb,Bi) demands extremely high quality specimens.

Figure 2(a) displays a \mathbf{g}_{002} DFTEM micrograph of a Ga(Sb,Bi) epilayer with 14% Bi, the maximum Bi concentration incorporated into GaSb so far. No extended defects or clusters are detected in the pseudomorphic layer. Local quantitative chemical determination from the analysis of the \mathbf{g}_{002} diffracted intensity yields an average Bi content $[Bi] = (14.2 \pm 0.8)\%$, which is in good agreement with $[Bi]_{XRD} = 14\%$ and $[Bi]_{RBS} = 14\%$. The error bar refers to the standard deviation of the TEM data. On the other hand, the low contrast in \mathbf{g}_{002} DFTEM imaging of Ga(Sb,Bi) renders the detection of composition modulations (CMs) an arduous task. It is reported that the amplitude of lateral CMs in Ga(As,Bi) is about $\Delta[Bi]/[Bi] = 30\%$ [E. Luna *et al.*]. In Ga(As,Bi) with an average Bi content of 5%, the presence of a 30% modulation induces a contrast of about 16%, which is readily detectable (we estimate 3–3.6% contrast is the lower limit of detection that we achieve using \mathbf{g}_{002} DFTEM). Regarding Ga(Sb,Bi), little (if nothing) is known about

the existence, character and/or magnitude of CMs in this material system. Assuming the amplitude of CMs in Ga(Sb,Bi) is as large as that in Ga(As,Bi), then a 30% modulation in Ga(Sb,Bi) with an average Bi content of 14% would induce a contrast of about 5.7%, which is significantly smaller than in Ga(As,Bi) but still detectable. Yet a modulation of 20% in Ga(Sb,Bi) with 14% Bi would be at our limit of detection, with a 3.4% contrast. CMs below 20% would, however, be very challenging to detect using \mathbf{g}_{002} DFTEM since they do not produce enough contrast. EDS measurements of the local composition complement the information provided by \mathbf{g}_{002} DFTEM. As shown in Fig. 2(b), EDS maps of the chemical composition also evidence a homogeneous layer, at least at this level of detection, where the Ga(Sb,Bi) layer is well-delimited from the adjacent GaSb, as indicated by the decrease in the L peak Sb signal and the concomitant increase in the intensity of the Bi M peak. High angle annular dark-field (HAADF) micrographs (not shown) provide similar information to \mathbf{g}_{002} DFTEM and EDS: a homogeneous layer, where no clusters and CMs are detected. Hence, from the combined information of \mathbf{g}_{002} DFTEM, EDS and HAADF we conclude that we deal with homogeneous Ga(Sb,Bi) epilayers where CMs (if any) are below 20%.

The high structural quality of the material also reflects in the Ga(Sb,Bi)/GaSb QWs comprising reference samples as well as the laser active zone. Again, no extended

defects, clustering or CMs are detected. In addition, the QWs exhibit regular and homogeneous morphologies including smooth interfaces, as shown in Fig. 3(a). In general there is no apparent difference in the morphology of the QWs in the reference structure and in the laser, which demonstrates that in spite of the growth challenges the degree of reproducibility is remarkable further encouraging the use of Ga(Sb,Bi) for future optoelectronics devices. Preliminary quantitative determination of the Bi content from the analysis of chemically sensitive \mathbf{g}_{002} DFTEM micrographs yields $[Bi] = (11.8 \pm 1.4)\%$, which is in good agreement with the average composition deduced from XRD, $[Bi]_{XRD} = 11.5\text{--}12\%$. A first evaluation of the Ga(Sb,Bi)-on-GaSb interface width in the laser structure yields about 2.2 nm (defined by 10%–90% criterion), which is on the same order as the chemical width in other III-V heterointerfaces [e.g. 2.1 nm for (Al,Ga)As/GaAs]. Furthermore, the interfaces are strikingly well defined by a sigmoidal function describing the intrinsic broadening at semiconductor heterointerfaces [E. Luna *et al.*, Phys. Lett. Rev. **109**, 126101 (2012)], as demonstrated in Figure 3(b) which displays the experimental profile and the fitting to the sigmoidal function. Finally, the abrupt interfaces indicate that the in-situ annealing during MBE growth of the top cladding and contact layers at an increased temperature seems not to have a detrimental effect on the layers, at least in terms of interface quality, which reinforces the positive perspectives for the future use of Ga(Sb,Bi) in optoelectronic applications.

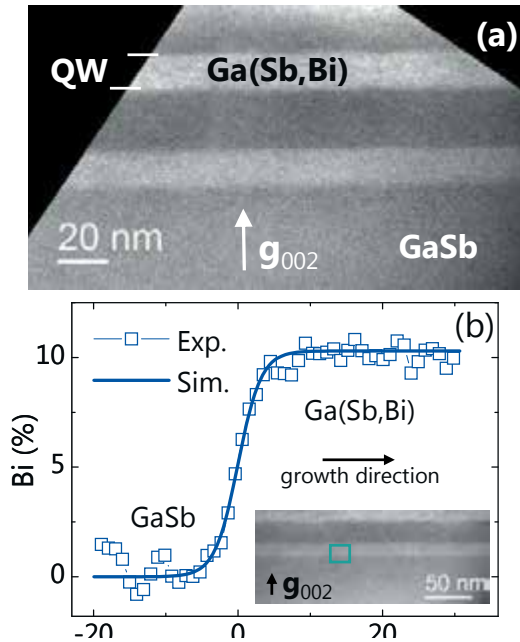


Fig. 3. (a) Chemically sensitive \mathbf{g}_{002} DFTEM micrograph of the QWs in a reference structure and (b) Bi distribution profile at the Ga(Sb,Bi)-on-GaSb interface at QWs in the laser structure, extracted from the analysis of the \mathbf{g}_{002} DFTEM diffracted intensity. The experimental data are fitted to a sigmoidal function.

In-situ growth mode analysis of homoepitaxial grown (100)-oriented β -Ga₂O₃

Z. Cheng, M. Hanke, Z. Galazka, and A. Trampert

In this study, we will report on the structural analysis of (100)-oriented β -Ga₂O₃ homoepitaxially grown by molecular beam epitaxy (MBE). The focus of this study is on the determination of the growth mode and the characterization of the structure defects within the films. *In-situ* reflection high energy electron diffraction (RHEED) and synchrotron based high resolution x-ray diffraction (HRXRD) as well as *ex-situ* transmission electron microscopy (TEM) and atomic force microscopy (AFM) were employed. The *in-situ* experiments were carried out at the PHARAO beamline U125/2-KMC at BESSY II (Helmholtz-Zentrum Berlin). This facility combines a plasma-assisted MBE system with two *in-situ* diffraction methods, namely RHEED and HRXRD. At the sample position the x-ray beam size is approximately $300 \times 500 \mu\text{m}^2$.

The MBE system uses an effusion cell to provide Ga flux and a radio-frequency plas-

ma cell to supply radical oxygen for the deposition of Ga₂O₃. During the growth, the substrate was kept at 700°C; the gallium cell and hot-plate were set to 700°C and 850°C, respectively. The plasma cell was adjusted to 400W with a constant oxygen flux of 0.6 sccm. The pressure in the growth chamber was around 6×10^{-6} mbar. Based on these parameters, the growth was maintained at an oxygen-rich condition. Finally, the micro-structure properties were analyzed by cross-section TEM (JEOL 2100 F operated at 200 kV) and the (100) surface morphologies by AFM.

The $5 \times 5 \text{ mm}^2$ high quality (100)-oriented β -Ga₂O₃ substrates used in this experiment were grown by the Czochralski process at Leibniz Institute for Crystal Growth (IKZ). After cleaning with acetone and isopropanol solvents, the substrates were properly splitted at the non-polar (100) surface termination. Then these splitted pieces were

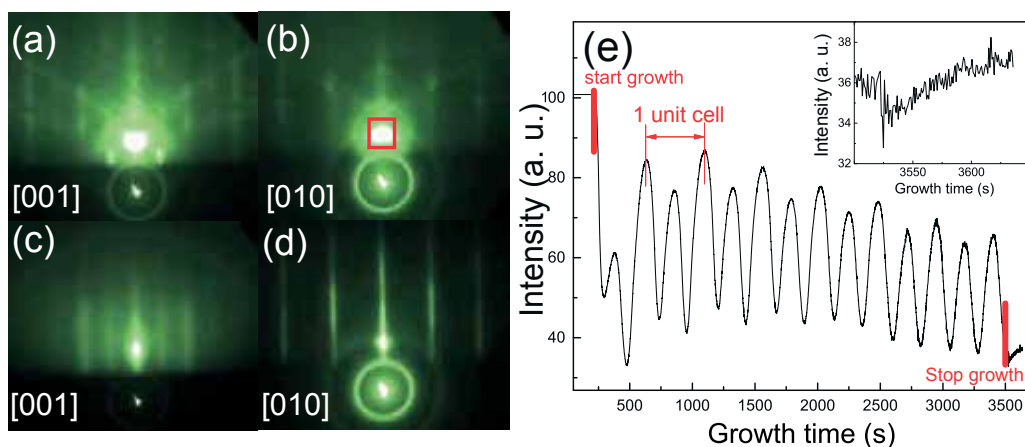


Fig. 1. RHEED patterns before (a,b) and after (c,d) the growth in two directions: [001] and [010]. The time evolution of the specular intensity was monitored at the red rectangle frame during the growth (e).

¹ Leibniz Institute for Crystal Growth, Max-Born-Str. 2, 12489 Berlin, Germany

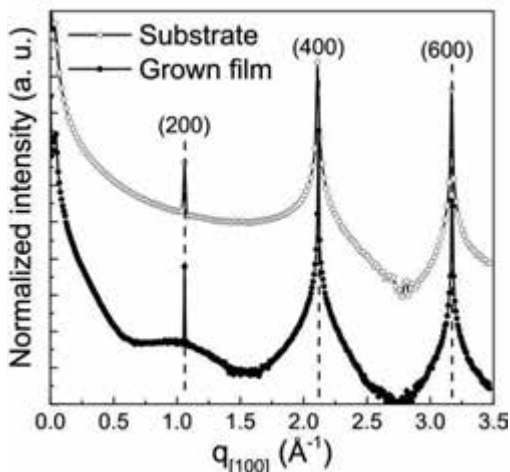


Fig. 2. *In-situ* out-of-plane HRXRD before and after growth.

mounted on the substrate holders by indium bonding with the fresh side up. The indium bonding served to increase the thermal conductivity to the substrates and to avoid external stress induced by the thermal expansion. Before transferred into the growth chamber, the substrates were degassed in the load lock chamber at 200°C for 30 min.

Figure 1 shows RHEED patterns before (a, b) and after (c, d) the homoepitaxial growth of Ga_2O_3 along the [001] and [010] azimuth, respectively. After the growth, the RHEED patterns in Fig. 1 (c) and (d) clearly revealed streaks in vertical direction, indicating an atomically flat growth surface. On the other hand, there is no streak formed after the growth, except for the ones following the bulk diffraction patterns, suggesting the growth underwent a flattening of the surface accompanied by the formation of a (1×1) surface reconstruction. During the growth, the intensity of the specular beam spot, as a function of the surface coverage, was continuously monitored and showed periodic oscillations [Fig. 1(e)]. This oscillating behavior reflects the surface nucleation and complete coalescence cycles of the $\beta\text{-Ga}_2\text{O}_3$ suggesting that the deposition can be characterized as a two-dimensional (2D) growth

mode. The period between two maxima in Fig. 1(e) implies the amount of time to grow a complete monolayer (ML) with an average rate of around 223 seconds/ML. It should be emphasized that here one ML represents half a unit cell, which will be discussed later based on the HRTEM results. After 14 periods, the growth was stopped by shutting the Ga effusion cell, whereby doing the annealing treatment, where the oxygen plasma was kept on at a constant substrate temperature, the transient intensity recovered slowly again [cf. inset in Fig. 1(e)].

Figure 2 shows the *in-situ* out-of-plane HRXRD curves of the substrates and after the homoepitaxial growth. The (h00) peak positions do not change and the full width at half maximum (FWHM) of the (400) and (600) Bragg diffraction peaks of about 0.02° stayed almost constant during the growth. The variation in the reflectivity region might be related to the change in the surface morphology expecting a broad diffuse scattering background around the (200) reflection that arises from a terrace-like surface morphology. Based on the AFM measurement, the average terrace width is around 6 nm.

The HRTEM image in Fig. 3(a) shows the cross-section of this (100)-oriented homoepitaxial layer with the electron beam along b -axis. The bright dots in the phase contrast image exhibit half of one unit cell with a height of 5.93 \AA . The image clearly presents a high density of stacking faults and formation of twin domains. The stacking faults are marked by the blue lines and the twins are indicated by the green ones. The twin can be described by a $c/2$ glide reflection of the lattice. Comparing the selected area electron diffraction pattern of the layer with that of the substrate [Fig. 3(c) and (b)], there are extra diffraction spots, marked by the red circles, showing up in the layer pattern [Fig. 3(c)]. These spots probably originate from the twin

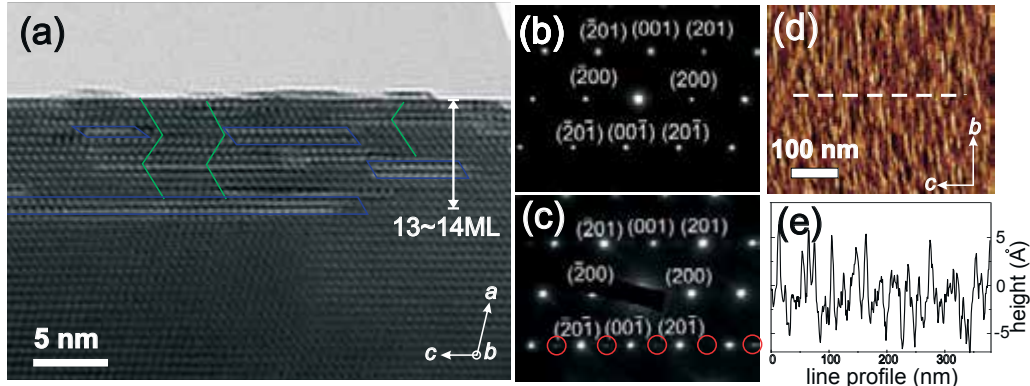


Fig. 3. HRTEM (a) shows that the homoepitaxial film consists of 13–14 monolayers with twin domains (green) and a lot of stacking faults (blue). The electron diffraction patterns at the pure substrate (b) and the grown film (c) confirm the presence of the twin domains. AFM images of the grown samples (d). The line profile along [001] direction marked as the dashed line in (d) is plotted in (e).

domains, since the patterns exhibit a good agreement with the twin domain diffraction simulation.

Due to the large amount of stacking faults, the homoepitaxial layer is highly distinguishable. The thickness of the epilayer amounts to 83 Å corresponding to a stacking of 7 unit cells. Correlated with the RHEED oscillation in Fig. 1(e), it is obvious that one oscillation period is equivalent to one complete layer deposition of half a unit cell, namely one monolayer (5.93 Å). The surface morphology as probed by AFM is shown in Fig. 3(d). The 2D nuclei have an average height of about 6 Å, as plotted in Fig. 3(e), and are strongly elongated along the *b*-direction. This height is very close to the thickness of one ML and is accordant with measurements from both RHEED and HRTEM. The elongated islands suggest that the reactive molecules may have higher mobility along *b*-axis rather than other along in-plane directions. The width of the islands also corresponds well with the average size of the nano-twins in the HRTEM, which suggests that the twins probably formed from the surface islands.

In conclusion, we have performed *in-situ* and *ex-situ* analytics on the homoepitaxial (100)-oriented $\beta\text{-Ga}_2\text{O}_3$ grown by MBE.

The formed films are grown coherently with the substrates, however, the films reveal twin domains and a high density of planar stacking faults, in contrast to the substrate which does not show this type of defects. The conspicuous RHEED specular beam oscillating feature clearly proved a layer-by-layer growth mode. Here, the RHEED, HRTEM and AFM results are very consistent in such that the growth mode is 2D layer-by-layer and one layer, or to say one ML, is just half a unit cell high in *a*-direction.

Gaussian beam electron optics with quantum point contacts

J. Freudenfeld, S. Platonov, M. Geier¹, P. Brouwer¹, V. Umansky², and S. Ludwig

Precise control of ballistic electrons on the nanoscale would be a major step towards the realization of integrated electronic quantum circuits. Quantum point contacts (QPCs), narrow one-dimensional constrictions in a two-dimensional electron system (2DES), are fundamental building blocks of nanoscale circuits, i.e., they can serve as emitters for ballistic electrons. Aiming at the coherent coupling of distant nanostructures, we consider a circuit containing two QPCs coupled via an electrostatic lens by focusing electrons moving ballistically between the QPCs.

We define the QPCs in the 2DES of a GaAs/(Al,Ga)As heterostructure by applying negative voltages V_1 and V_2 to the pairs of split gates as shown in Fig. 1(a). In our experiments, we apply a negative source drain voltage V at the contact of one of the QPCs and measure the resulting current I into the grounded contact at the back of the second QPC, while the central region of the 2DES is also electrically grounded. Figure 1(b) shows pinch-off curves measured separately for each QPC. As the gate voltages are lowered, the conductance decreases stepwise with plateaus at $G = N 2e^2/h$ with $N = 1, 2, 3, \dots$, e denoting the elementary charge and h Planck's constant. Smooth transitions between plateaus indicate parabolic barriers in the current direction [x direction in Fig. 1(a)]. Almost perfectly equidistant plateaus as a function of voltage are a fingerprint of parabolic confinement in the transverse direction (y direction). Fitting the data [dots in Fig. 1(b)] to a saddle point potential transmission function (lines) [M. Büttiker, Phys. Rev. B **41**, 7906(R) (1990)] including an anharmonic transverse

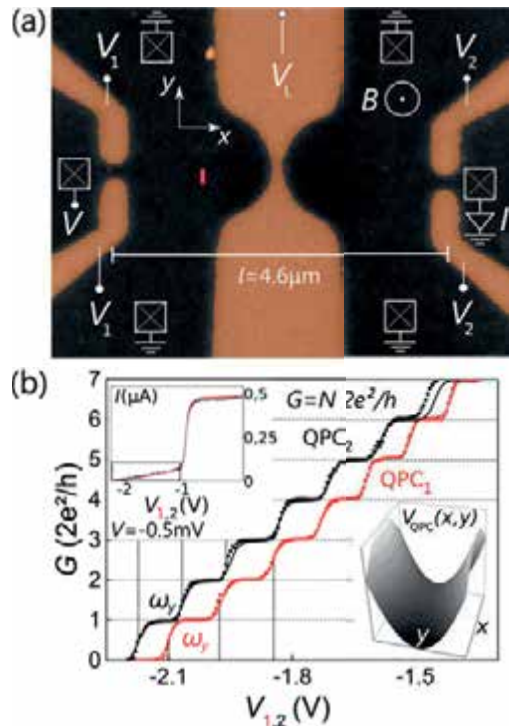


Fig. 1. (a) Atomic-force microscope image of the investigated sample. Bright areas indicate metallic gates evaporated on the dark GaAs surface. Negative voltages V_1 , V_2 , and V_L (partially) deplete the 2DES 110 nm below the surface, thereby defining QPC₁, QPC₂, and the lens. Red rectangle: position of the model defect as described in the text. (b) Pinch-off curves of the two QPCs: dots indicate measured data and lines simulated curves. Top left inset: Full pinch-off curves. Bottom right inset: Parabolic saddle point potential.

potential component, we find an anharmonicity of only 3 %. Hence, our QPCs represent almost perfect parabolic saddle point potentials as depicted in the bottom right inset of Fig. 1(b). Due to the confinement potential, electrons emitted from a QPC span a finite aperture angle so that most carriers are scattered to the grounded-side

¹Dahlem Center for Complex Quantum Systems and Institut für Theoretische Physik, Freie Universität Berlin, Germany

²Weizmann Institute of Science, Israel

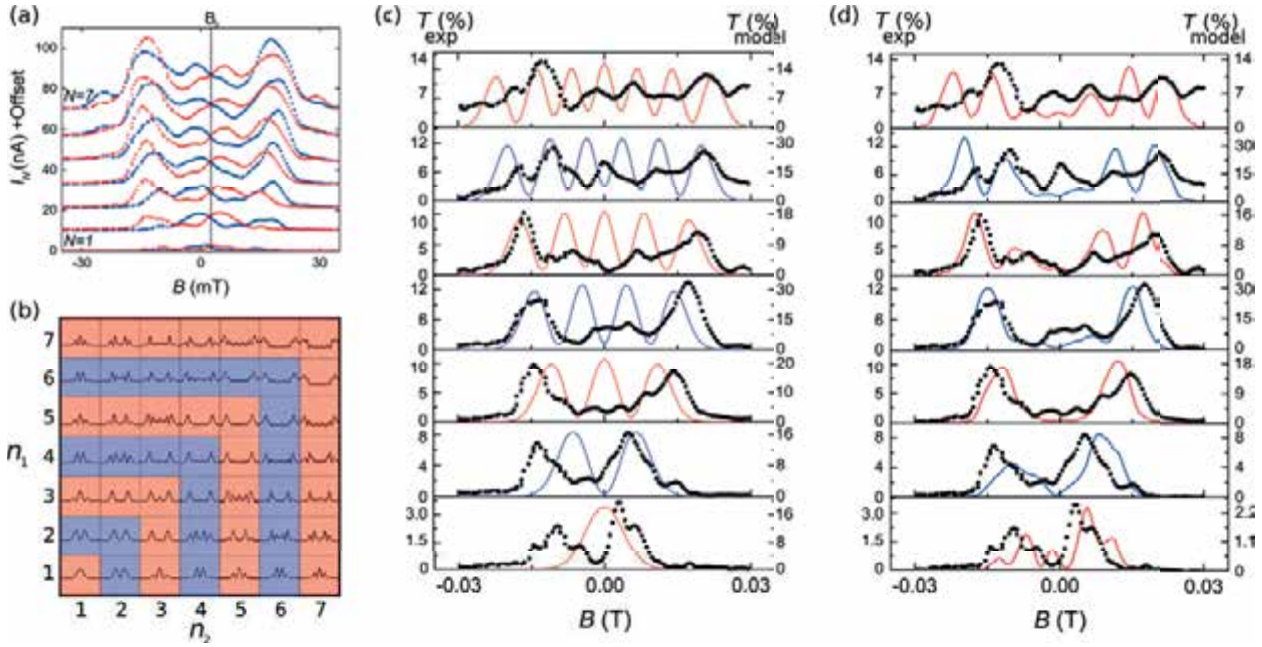


Fig. 2. (a) Ballistic current I through two QPCs in series tuned to the center of the conductance plateaus N in Fig. 1(a) as a function of the perpendicular magnetic field B . Red: V applied at left contact in Fig. 1(a) (emitter QPC₁), blue: V at right contact (emitter QPC₂). (b) Calculated transmission matrix $T_{n_1, n_2}(B)$ from sublevel n_1 of QPC₁ through n_2 of QPC₂. (c) Black dots: experimental transmissions $T_N - T_{N-1}$ calculated from measurements I_N shown in panel (a). Lines: theoretical $T_N - T_{N-1} = \sum_{i=1}^N (T_{i,N} + T_{N,i})$ from calculated T_{n_1, n_2} in (b). (d) Same experimental data as in (c), but calculations including a single defect [red rectangle in Fig. 1(a)].

contacts, and only a small portion moves ballistically through the second QPC. This greatly reduces the transmission through two QPCs in series. To probe the angular distribution of the carriers emitted from a QPC, we bend the electron trajectories by applying a perpendicular magnetic field B using the Lorentz force. For this magnetic deflection experiment, we do not use a lens, i.e. $V_L = 0$. In Fig. 2(a), we present the ballistic current flowing through both QPCs in series $I(B)$, while both QPCs are tuned to the respective centers of identical conductance plateaus for $N = 1, 2, \dots, 7$. The two colors correspond to opposite current directions. The observed mirror symmetry regarding the current direction confirms the fundamental Onsager relations for a multi-terminal measurement. As we increase N , we observe the current maxima at larger values of B corresponding to larger aperture angles. In addition, the number of oscillations in $I(B)$ increases with N , reflecting the increasing number of nodes in the wavefunction with N . We developed a

model to describe our data based on the Landauer-Büttiker approach [M. Büttiker, Phys. Rev. Lett. **38**, 9375 (1988)] and solving the Schrödinger equation for the wavefunctions of the electrons as they move between the two QPCs. Our model further implements adiabatic coupling between the QPCs and the 2DES. Since we model the QPCs as parabolic saddle point potentials, their eigenstates are Hermite functions that give rise to an electron beam profile similar to the one derived from the Gaussian beam optics model. With both QPCs tuned to the N^{th} conductance plateau, the Landauer-Büttiker approach results in a $N \times N$ transmission matrix, where the elements $T_{n_1, n_2}(B)$ describe all combinations of transmission between the occupied eigenstates $n_1, n_2 = 1, 2, \dots, N$ of the two QPCs. The overall transmission is then given by $T_N = \sum_{n_1, n_2 = 1}^N T_{n_1, n_2}$. In Fig. 2(b), we illustrate $T_{n_1, n_2}(B)$ including all matrix elements up to $N = 7$. To compare the results of our model to our experimental results in Figs. 2(c) and (d), we show the differ-

ence between neighboring transmission curves in Fig. 2(a) [black dots] in comparison to the calculated curves, $T_N - T_{N-1} = \sum_{i=1}^N (T_{i,N} + T_{N,i})$ [sum over stripes of matrix elements in Fig. 2(b)] result in lines of identical color in Fig. 2(c)]. Both experiment and theory show structures in comparable magnetic field ranges and patterns with an increasing number of features for increasing N . However, our experiments are subject to breaking the $T(B)$ symmetry. A possible origin of the deviations between the experimental results and the results of the model is electron scattering caused by disorder. To test this hypothesis, we included a single one-dimensional hard-wall scatterer indicated as a red rectangle in Fig. 1(a) into our model calculations. The resulting curves substantially improve the agreement between theory and experiment as shown in Fig. 2(d).

Next, we activate the electrostatic lens gate as indicated in Fig. 1(a) with the aim of focusing electrons between the two QPCs at $B = 0$. By applying a moderate voltage V_L , we partially deplete the 2DES below the lens gate, thereby reducing the Fermi velocity and the lens refractive index. To probe the effect of the electrostatic lens on the emission profiles discussed above, we study $I(B, V_L)$, which is displayed in Fig. 3(a) for both QPCs tuned to $N = 7$. For $V_L = 0$ V, the current distribution is identical to the top blue curve in Fig. 2(a), indicating a beam profile similar to the calculated one shown in Fig. 3(b). By decreasing V_L , we find that the outer current maxima bend towards $B = 0$, while the central maximum grows. At $V_L = -0.65$ V, all branches merge into one strongly enhanced current maximum at $B = 0$, indicating electrostatic focusing of all three maxima [see Fig. 3(c)].

In summary, we have observed electrostatic focusing of ballistic electrons emitted and detected by QPCs representing parabolic saddle point potentials. Our magnetic deflection experiments confirm that

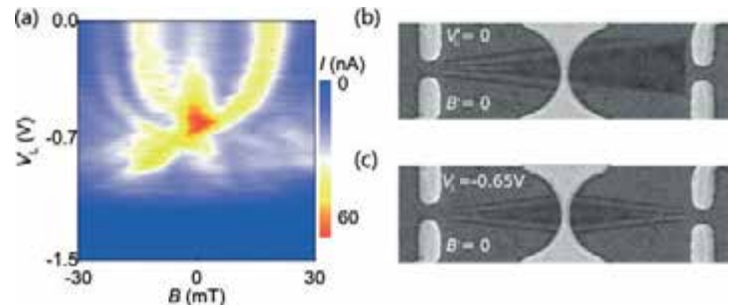


Fig. 3. (a) Current $I(B, V_L)$ as a function of both, perpendicular magnetic field B and lens voltage V_L with both QPCs tuned to $N = 7$. (b) Calculated beam profile emitted from a QPC at $N = 7$ for $B = 0$ T and $V_L = 0$ V. (c) Electrostatic focusing $I(B = 0, V_L = -0.65$ V).

the angular distribution of electrons is described by Hermite functions. We attribute deviations between the experimental and theoretical results to defect scattering and show that implementing a single defect into our model calculation strongly changes the ballistic dynamics in a mesoscopic system. Our observations favor electron dynamics according to a Gaussian beam optics model based on Hermite functions rather than frequently used plane electron wave models.

Coupled dipolar excitons in (Al,Ga)As multilayers

C. Hubert, Y. Baruchi, Y. Harpaz¹, K. Cohen¹, K. Biermann, R. Rapaport¹, and P. V. Santos

Spatially indirect (or dipolar) excitons (IXs) are coupled electron-hole pairs formed in double quantum well (DQW) structures consisting of two semiconductor quantum wells (QWs) separated by a thin barrier cf. Fig. 1(a). The barrier thickness is smaller than the exciton Bohr radius. The application of a vertical electric field F_z drives the electron and hole constituents to different QWs while maintaining the Coulomb correlation between them. F_z controls both the IX energy and lifetime via the quantum-confined Stark effect, which can reach the μs range, thus making IXs quasi-equilibrium opto-electronic excitations. While the total charge of an IX is neutral, the charge separation by F_z induces a permanent electric dipole moment \mathbf{p} , which gives rise to strong dipolar interactions between single IXs . This attractive interaction can be used to trap dipoles formed in a DQW structure through a mutual interaction energy, resulting in coaxial dipoles forming in the DQWs.

In this work, we explore the interaction of remote IXs via the dipolar interaction, which is normally the main interaction mechanism for uncharged particles. Specifically, we are focusing on near-field interactions of the dipoles so that the dipole size, which is nominally half the width of the DQW, is less than $2L$ as indicated in Fig. 1(b). The experiments were carried out in an (Al,Ga)As layer structure containing two closely spaced DQWs (DQW_L and DQW_H as shown in Fig. 1(a)). The barrier layer between the DQWs prevents carrier tunneling and bi-exciton formation. The DQWs consist of wells with different widths to enable the selective excitation of IXs in each DQW. Two laser beams, tuned to their respective di-

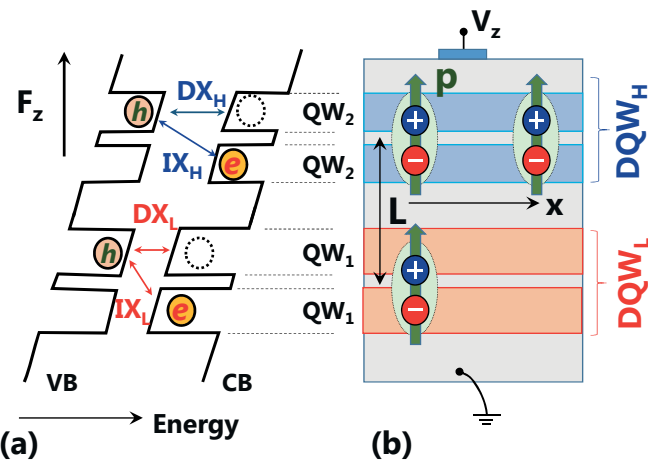


Fig. 1. (a) Interactions between indirect excitons (IX_i , i_L, H) in a sample with coupled double quantum wells (DQW_i). (a) Energy diagram showing the direct (DX) and indirect exciton transitions and (b) layer structure of the (Al,Ga)As sample. An electric field F_z applied perpendicularly to the DQWs bends the conduction (CB) and valence bands (VB) and creates IX with an electric dipole moment \mathbf{p} .

rect exciton (DX) transitions [cf. Fig. 1(a)], are used to decouple the IX_H and IX_L populations. The dipolar interaction between dipoles has the special property of being non-monotonic, unlike the Coulomb potential. The sign of the dipolar interaction depends on the ratio between the lateral (x) and vertical (L) separation between the IXs . The interactions between coplanar IXs , where $x/L = \infty$ [cf. Fig. 1(a)], is always repulsive. Between IXs in different DQWs, the potential changes from attractive at short lateral distance ratios $x/L < \sqrt{3}$ to repulsive at longer ratios [cf. Fig. 1(b)].

The interactions between IXs in the DQWs detected by using spatially resolved photoluminescence (PL) to map IX clouds excited by two laser beams with different energies and spatial profiles depicted in Fig. 2(a).

¹Hebrew University of Jerusalem, Jerusalem, Israel.

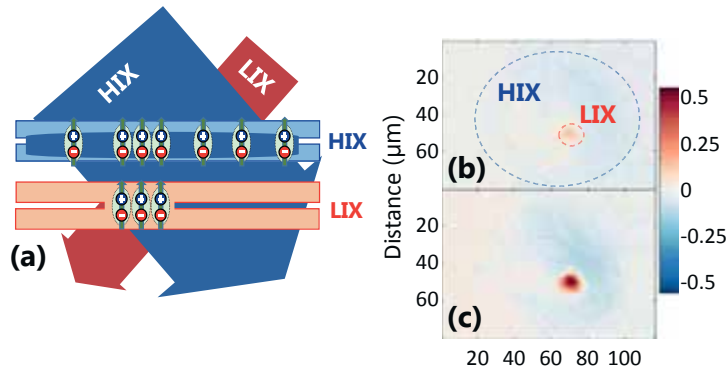


Fig. 2. (a) Optical detection of inter-DQW interactions. (a) A large laser spot L_H tuned to the DX_H energy of the upper DQW selectively generates IX_{HS} , while a smaller laser spot (L_L) tuned to DX_L creates a narrow pool of IX_{LS} . The attractive dipolar interaction between the two IX clouds changes the spatial distribution of IX s in DQW_H , which is detected by spatially resolved photoluminescence. Maps of the relative changes δI_{PL} induced by IX_L densities of (b) $2.1 \times 10^{10} \text{ cm}^{-2}$ and (c) $4.6 \times 10^{10} \text{ cm}^{-2}$.

A wide laser spot tuned to the DX transition of DQW_H creates a wide (diameter $\varphi \approx 60 \mu\text{m}$) cloud of IX_H 's with a PL intensity distribution $I_{PL,0}(x, y)$. IX_L 's are then selectively excited within a small area ($\varphi \approx 15 \mu\text{m}$) within the wide IX_H cloud using a second laser beam tuned to DQW_L . The effects of this second cloud on the IX_H distribution is then detected by measuring PL intensity profiles $I_{PL}(x, y)$ and determining the relative changes $\delta I_{PL}(x, y) = \frac{I_{PL}(x, y) - I_{PL,0}(x, y)}{I_{PL,0}(x, y)}$. In addition, since the second laser beam does not excite IX_H 's, their population remains unchanged so that any detected change in density must be caused by IX_H - IX_L coupling.

Figures 2(b) and 2(c) display PL maps recorded for a constant excitation density of IX_{HS} and increasing power of the laser exciting the IX_L cloud. The emission from IX_H s enhances in the presence of IX_L cloud, thus indicating an increased density. The magnitude of the effect increases with the initial IX_H density. These results thus clearly prove the existence of an attractive interaction between the two remote excitonic clouds. Note that the attractive nature is by no means obvious since the inter-DQW interaction changes with the spacing ratio x/L

(cf. Fig. 1) from attractive to repulsive. The spectral shift associated with the attraction of coaxial IX - IX s is also not detectable under standard measurement configurations. For the present experimental conditions, the IX_H species are effectively pushed together by the IX_L cloud as sketched in Fig. 2(b).

In conclusion, the experimental results presented here provide experimental evidence for the dipolar attraction of remote IX clouds, thus demonstrating the feasibility of IX control via dipolar interactions, which is a necessary requirement for the realization of IX - IX gates..

Quantum confinement of exciton-polaritons by microscopic potentials in a patterned (Al,Ga)As microcavity

A. S. Kuznetsov, K. Biermann, P. L. J. Helgers, E. A. Cerdá-Méndez, and P. V. Santos

The strong coupling of resonant photons and quantum-well (QW) excitons in a planar semiconductor microcavity (MC) results in the exciton-polariton quasi-particles (simply, microcavity polaritons, MPs). MPs display a wide range of attractive properties arising from their two-fold light-matter nature.

Specifically, the low effective mass of polaritons (typically on the order of 10^{-5} – 10^{-4} of the free electron mass) and, consequently, their μm -sized thermal de Broglie wavelength (on the order of a few μm at 4 K) favor the observation of quantum-confinement effects under μm -sized potentials. Applications-wise, the MPs offer a bridge between conventional micro-electronics and quantum technologies in an all-semiconductor platform. In order to achieve quantum functionalities, e.g., qubits, topological circuits, and quantum simulators, polariton confinement potentials and engineered lattices supporting polariton-interactions as well as coherent control down to the single-polariton level are required. Here, we use microcavity structuring to create polariton modulation potentials. In our MC structures, the spacer layer in-between the distributed Bragg reflectors (DBRs) is laterally structured by shallow etching before the overgrowth of the upper DBR as shown in Fig. 1. The approach is particularly beneficial, because the etching takes place above the QWs, hence keeping the latter intact. The patterning creates regions with different optical-resonance energies. Thus, the two-dimensional (2D) polariton gases have different energies in the etched and non-etched regions. We have taken advan-

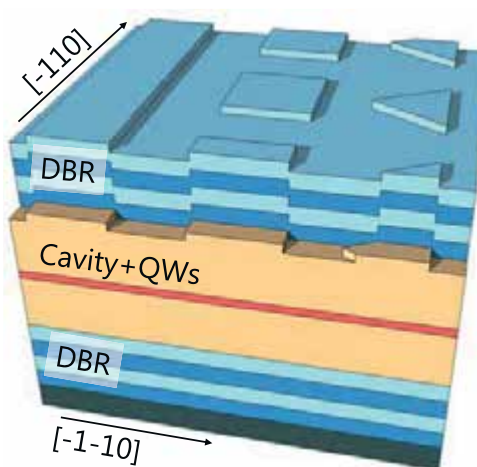


Fig. 1. A sketch of the patterned polariton (Al,Ga)As microcavity investigated in this work. The MC was grown on a 2-inch GaAs (001) substrate by molecular beam epitaxy (MBE). The cavity active region, containing 6 GaAs QWs of 15 nm thickness, was grown on top of the lower DBR. The sample was taken out of the MBE chamber and then patterned by means of photolithography and wet chemical etching to create mesas of different shapes with a nominal height of 12 nm. The etching results in a 9 meV (4.5 nm) blue-shift of the cavity mode. Finally, the sample was put back into the MBE system and overgrown with the upper DBR.

tage of this property to demonstrate traps of arbitrary shape for the one- and zero-dimensional confinement of MPs states.

Fabrication results in the MC surface profiles shown in Figs. 2(a), 2(b), and 2(c) for wire, square, and triangle traps, respectively. For large mesa sizes [cf. Figs. 2(a) and 2(c)], the shape of the surface mesa corresponds to the one photolithographically defined in the spacer region. However, for smaller mesa sizes, the surface structures

¹ Instituto de Física Av. Manuel Nava 6, Zona Universitaria San Luis Potosí, SLP 78290 México.

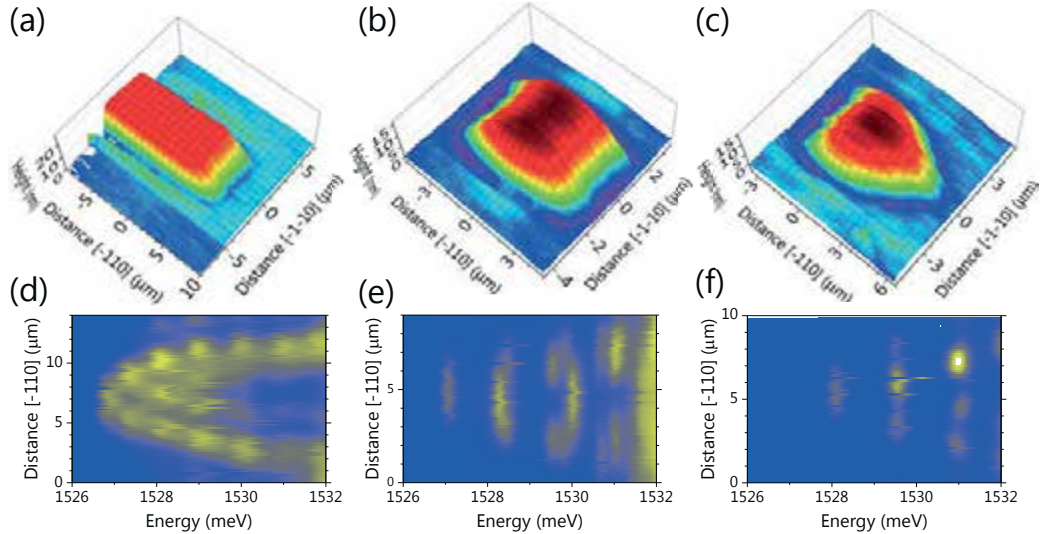


Fig. 2. Typical atomic force microscopy (AFM) images showing the surface profile of (a) 5 μm wide wire, (b) nominally $4 \times 4 \mu\text{m}^2$ square trap, and (c) a triangle trap with a nominal side length of 5 μm . Panels (d)–(e) show PL spectra, typical of the shapes in (a), (b), and (c), resolved both in energy and real space according to the horizontal and vertical axes, respectively. The energy range corresponds to the low-polariton branch. The yellow color represents emission.

retain their shape along the $[\bar{1}\bar{1}0]$ surface direction, but become elongated in the $[\bar{1}10]$ direction as shown in Fig. 2(b). The shape anisotropy, which appears due to the overgrowth of the top DBRs after etching, becomes especially pronounced in the small structures defined within the spacer. As a result, small square mesas turn into rectangular mesas at the sample surface.

The achieved potential barriers of approximately 5 meV allow us to observe clear signatures of the quantum confinement in photoluminescence (PL) spectra: discrete energy levels and spatial localization of the wave functions of MPs in the traps as shown in Figs. 2(d), 2(e), and 2(f). Well-defined confined states have been observed for trap sizes down to 1 μm , thus demonstrating that the process can produce small polariton confinement dimensions. Using the images akin to the ones in Figs. 2(d)–(f), we reconstructed the confinement potential shape. One interesting finding is that the potential energy shape changes from an approximately square-like potential for wide wires (pitch exceeding 5 μm) to a rounded-shaped one (quasi-parabolic) for narrower structures. On the one hand, this leads to the tighter confinement of the

lowest excited states within the physical dimensions of a trap. On the other hand, the finite width (exceeding 1 μm) of the lateral interfaces results in the upper energy levels being substantially extended into the barrier. This extended character of the confined MPs states results in the coupling of the electronic states in arrays of traps. As an example, we consider a 5×5 square array of $1.6 \times 1.6 \mu\text{m}^2$ traps and a lattice constant of 4.8 μm .

Figure 3(a) shows the spectrally and spatially resolved PL image of a line of traps within the array obtained under optical excitation by a laser beam with a rather large diameter of approximately 50 μm with an excitation power of 30 mW. Due to the small lattice period and traps size, the lowest levels of the individual traps hybridize to form states with bonding (s-character with energy E_{0s}) and anti-bonding (p-character with energy E_{1p}) properties. While in the former the electronic wave function concentrates on the trap sites, the wave function of the p-like states peaks in the region between traps. We attribute the energy variation of the s-states along the spatial axis to the repulsive interactions due to different polariton populations in

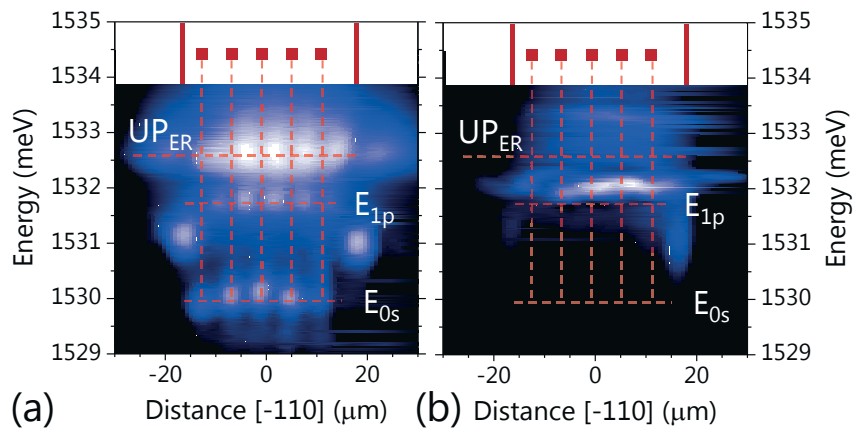


Fig. 3. PL images of a line of traps within the array recorded for laser excitations (a) below (laser power of 30 mW) and (b) above the condensation threshold (420 mW). The solid lines and squares in the top-region of the figure represent the traps and show their spatial position. The levels E_{0s} and E_{1p} (in (a)) have bonding and antibonding symmetries, respectively. Under condensation (b) that takes place in the E_{1p} states, the emission intensity increases by orders of magnitude, and the emission lines narrow. In addition, the lines blueshift due to strong repulsive polariton-polariton interactions.

each trap induced by the Gaussian intensity profile of the exciting laser beam. Note that the variation is much smaller for the p-states, because due to the stronger coupling to neighboring lattice sites the polaritons can redistribute laterally. Figure 3(b) displays a PL map of the same area recorded by increasing the laser flux by a factor of 15. In this case, the stimulated scattering of photoexcited polaritons to state E_{1p} leads to the preferential population of these states and to the formation of a Bose-Einstein-like condensate of polaritons spatially extended over all the traps. The latter is characterized by an exponential increase in emission intensity and reduction in line width. Due to its single-lattice addressability, single-level confinement and polariton-polariton interactions via hybridization, the demonstrated system may be suitable for polariton-based quantum simulators.

P. L. J. Helgers acknowledges the funding from the European Unions Horizon 2020 research and innovation programme under the Marie Skłodowska-Curie grant agreement No 642688.

Diameter evolution of selective area grown Ga-assisted GaAs nanowires

H. Küpers, R. B. Lewis, A. Tahraoui, M. Matalla¹, O. Krüger¹, F. Bastiman, H. Riechert, and L. Geelhaar

In the Ga-assisted vapour-liquid-solid (VLS) growth of GaAs nanowires (NWs), a Ga droplet acts as a collector for Ga and As and no external catalyst material is necessary. However, the dynamics of the Ga droplet during NW growth can easily lead to a diameter variation of the forming NW, resulting in either positively or negatively (inversely) tapered NWs. In addition to VLS growth at the droplet, direct vapour-solid (VS) growth on the side facets is regularly observed, which also influences the NW diameter. The goal of this study is a comprehensive description of these phenomena.

GaAs NWs were grown by molecular beam epitaxy on Si(111) substrates covered by an oxide mask which was patterned by electron beam lithography. This so-called selective area growth (SAG) enables a precise control over the location of NWs on the substrate. For SAG of Ga-assisted GaAs

NWs it was shown previously that low V/III ratios are necessary for a high vertical yield. Such conditions lead to locally Ga-rich conditions enabling the VLS growth of NWs. Figure 1(a) shows a sample that was grown under a low V/III ratio of 2.2. The NW diameter is 160 nm at the top and tapering is pronounced, due to an enlargement of the droplet. Consequently, to decrease the NW diameter the V/III ratio needs to be increased.

The different requirements for vertical growth and thin diameters imply that both features cannot be achieved with a single set of growth conditions. Therefore, we developed a growth approach with two sets of growth parameters for the different phases of growth: The first step provides growth conditions necessary to achieve a high vertical yield. These are a pre-deposition phase for Ga droplet formation, and

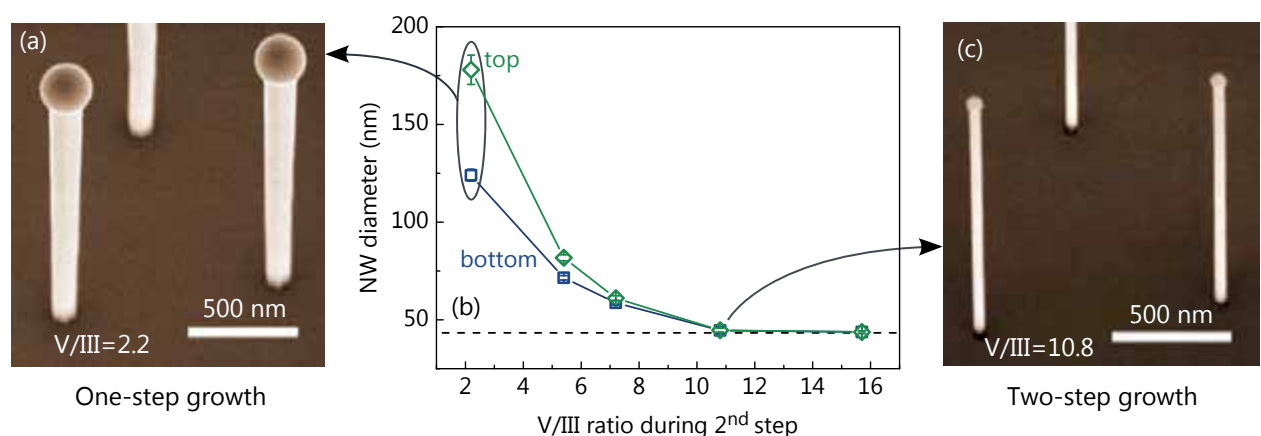


Fig. 1. (a) Micrograph of NWs grown with a constant V/III flux ratio of 2.2 for 30 min. The sample is tilted by 25° from the substrate normal. (b) NW diameter at top (green diamonds) and bottom (blue squares) for different V/III flux ratios during the second growth step. (c) Micrograph of NWs grown with a two-step growth approach under a second-step V/III flux ratio of 10.8, exemplifying the efficacy of the growth approach. The sample is tilted by 25°.

¹Ferdinand-Braun-Institut, Leibniz-Institut für Höchstfrequenztechnik, Gustav-Kirchhoff-Strasse 4, 12489 Berlin, Germany

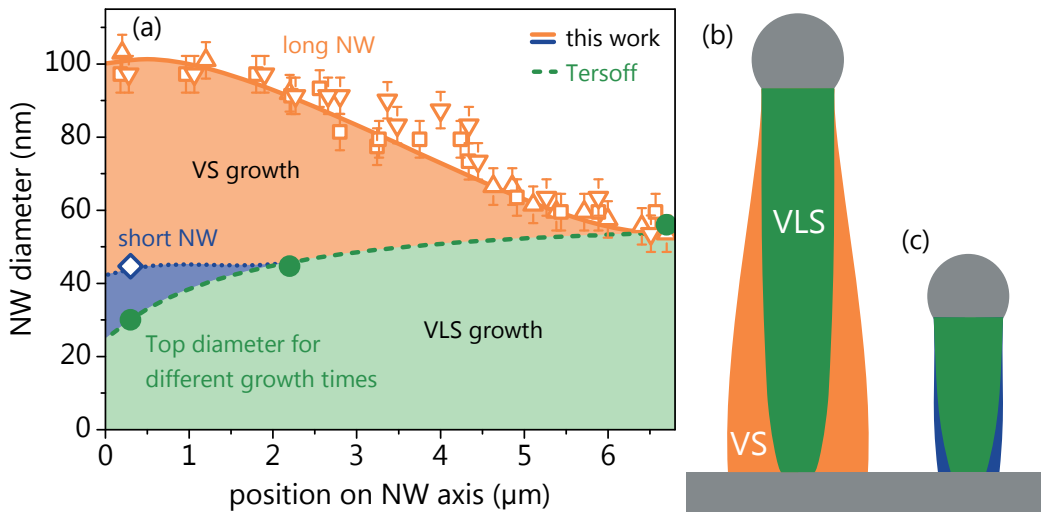


Fig. 2. (a) NW diameter as a function of position along the NW axis for NWs grown for 5, 30 and 88 min. The full green circles show the top diameter for three different lengths. The dashed green line is a fit of Tersoff's model describing droplet dynamics. The open orange triangles and squares represent the diameter at different points of three long NWs. The diameter as calculated by our combined model is shown as the orange line. The dotted blue line shows the calculated values for the short NWs and is in agreement with the experimental value at the NW bottom shown as open blue diamond. The calculated shapes of the long and short NWs are shown schematically in (b) and (c), respectively.

subsequently GaAs growth with a low V/III ratio of 2.2. In the second step the V/III ratio is increased by decreasing the Ga flux. Figure 1(b) presents the diameter at the top (green diamonds) and bottom (blue squares) of the NWs for varying V/III ratios during the second step. Both diameters decrease monotonically with increasing V/III ratio, becoming constant at a value of 45 nm for V/III ratios above 10.8.

Figure 1(c) shows a micrograph of the sample grown with a V/III ratio of 10.8 during the second step. This micrograph illustrates a thin and untapered morphology that has not been shown previously for SAG GaAs NWs of this length. Furthermore, the sample exhibits a vertical yield of 55%, which is comparable to our optimized one-step yield. This result demonstrates the efficacy of the two-step approach, which provides the optimal V/III ratio both for nucleation and NW morphology.

In this study, all two-step samples start from a similar NW base which is grown

within the first step. Thus, the diameter at the bottom of the NWs at the beginning of the second step is the same for all samples (30 nm) and it is unaffected by the droplet dynamics during the second step. Therefore, the variation of the bottom diameter in Fig. 1(b) can only be caused by direct VS growth on the side facets, which allows a quantification of this growth pathway.

To understand radial growth by both droplet dynamics and direct VS growth we need to disentangle both processes. To this end, we consider additional experimental data. The orange triangles and squares in Fig. 2(a) show the diameter along the length of NWs grown for longer time (88 min) where VS growth is even more pronounced. Also, the green circles in Fig. 2(a) show the top diameter of three samples grown for different times with the same growth conditions, plotted as a function of length. The latter diameters would be maintained if VS growth was not present and therefore represent a shape only due to droplet dynamics. Tersoff built a mod-

el for the self-assisted VLS NW growth to explain this tapering [J. Tersoff, *Nano Lett.* **15** (2015) 6609–6613]. The dashed green line represents a fit of Tersoff's model to the experimental data, describing the NW shape only due to droplet dynamics.

In order to take direct VS growth into account we developed a model which is consistent with VLS axial growth. A central factor of VLS growth of NWs is a large diffusion length on the NW sidefacets. Ga atoms that impinge on the NW sidefacet diffuse along the NW axis to reach the Ga droplet where they incorporate into the lattice at the liquid-solid interface. However, this supply by diffusion takes place mostly within one diffusion length from the droplet. For long NWs the bottom might be too far away for Ga atoms to reach the droplet. All Ga atoms that do not contribute to the diffusion supply must incorporate into the NW sidewall. By solving the one-dimensional diffusion equation we can calculate the adatom density on the NW sidewall, which we use to derive an equation for the VS growth rate on the NW sidewall based on the data for the bottom diameter in Fig. 1(b).

To describe the complete shape of NWs we simply add the contributions for VLS growth and VS growth, as radial growth due to droplet dynamics and VS growth are independent of each other. The result of the combined model is shown as the orange line in Fig. 2(a), which is in good agreement with the experimental data. At the bottom a rather flat part is present in both the model and the experimental data. Here, the droplet dynamics lead to strong negative tapering, as seen in the green curve. This effect is compensated by the VS growth, yielding a flat bottom part. The upper part of the NW exhibits a positive tapering as it is dominated by VS growth. A visualization of the calculated NW shape with the parts due to VLS and VS growth is shown in Fig. 2(b).

Finally, we employ our comprehensive model with the same parameters as used before to describe the shape of the short NWs, which is shown as the blue line in Fig. 2(a). In agreement with our experimental results, the shape is essentially untapered. Our model reveals that the untapered morphology as shown in Fig. 2(c) is a consequence of the droplet dynamics and the VS growth compensating each other. Thus, by balancing droplet dynamics and VS growth, straight NWs can be achieved but only for a certain range of NW lengths.

Polarity-induced selective area epitaxy of GaN nanowires

G. Calabrese¹, Z. S. Schiaber^{1,2}, X. Kong, A. Trampert, B. Jenichen, J. Humberto Dias da Silva³, L. Geelhaar, O. Brandt, and S. Fernández-Garrido

Single-crystalline GaN nanowires (NWs) can be synthesized by plasma-assisted molecular beam epitaxy (PA-MBE) using the self-assembled growth approach on a wide variety of dissimilar substrates. Individual GaN NWs can be as thin as 15–20 nm and are typically free of threading dislocations and strain. However, well-developed NW ensembles are characterized by a non-negligible degree of coalescence which increases the effective NW diameter and introduces structural defects as well as inhomogeneous strain. The detrimental impact of coalescence on the structural perfection of dense nanowire ensembles may thus prevent these nanostructures to realize their full potential for applications. Here, we

present a conceptually novel selective area epitaxy (SAE) approach suitable to control the NW number density and prevent their coalescence without using *ex situ* pre-patterned substrates.

Our approach exploits the fact that GaN NWs do not form on structurally and chemically uniform cation-polar substrates. In this context, by depositing Si on a Ga-polar GaN layer, we locally reverse the polarity and thus induce the SAE of N-polar GaN NWs. The influence of the amount of deposited Si on the formation of GaN NWs is investigated by scanning electron microscopy. Figures 1(a)–1(h) present bird's eye scanning electron micrographs

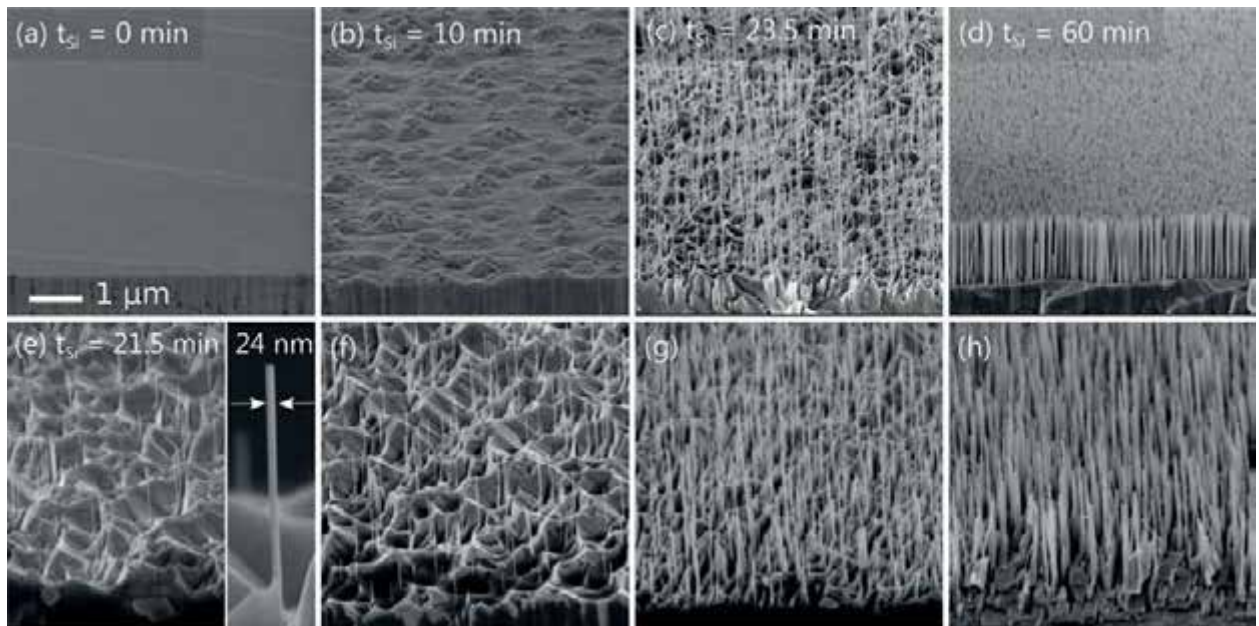


Fig. 1. (a)–(d) Bird's eye view scanning electron micrographs of samples prepared using different Si pre-deposition times, t_{Si} , as indicated in the images. The GaN growth time upon Si nitridation for all these samples was 180 min. (e)–(h) Bird's eye view scanning electron micrographs illustrating the continuous variation of the morphology across the wafer for $t_{Si} = 21.5$ min. As result of the lack of substrate rotation, the effective amount of pre-deposited Si increases from (e) to (h). The inset in (e) presents a highly magnified cross-sectional view of a GaN NW. The GaN growth time for this sample was 360 min. All the images but the inset shown in (e) were acquired using the same magnification.

¹Authors equally contributed to this work.

²Laboratório de Filmes Semicondutores Universidade Estadual Paulista Bauru, 17033-360 São Paulo, Brazil.

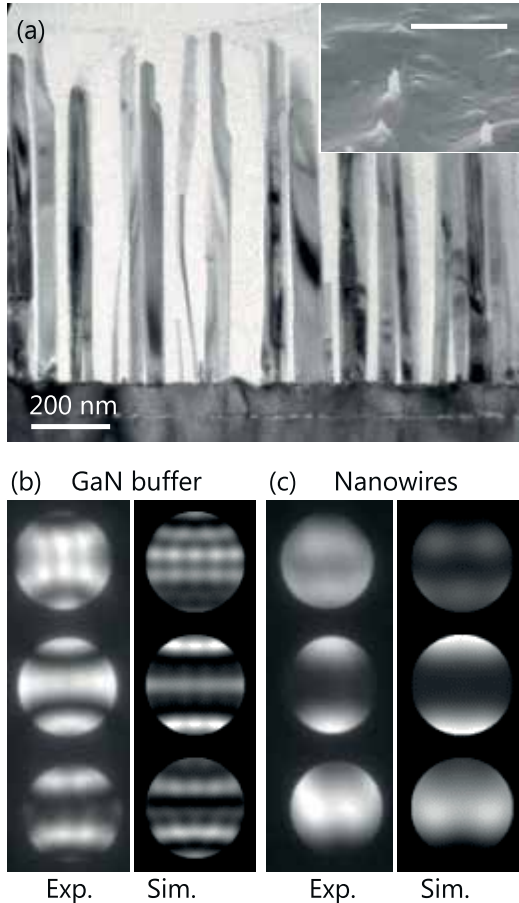


Fig. 2. (a) Cross-sectional transmission electron micrograph of the sample with a Si pre-deposition time of 60 min. The inset shows a bird's eye view scanning electron micrograph acquired after exposing the sample to KOH (scale bar 1 m). Experimental and simulated CBED patterns of (b) the GaN buffer layer and (c) a GaN NW for the 0002, 0000, and 000̄2 disks (from bottom to top). The specimen thicknesses assumed for the simulations in (b) and (c) are 131 and 52 nm, respectively.

of samples prepared using different Si deposition times t_{Si} from 0 to 60 min [the Si deposition rate is 0.9×10^{-3} monolayers (ML)/s]. For all samples, after the deposition of Si, GaN is grown at 790°C using a Ga flux of 0.3 ML/s and a N flux of 0.5 ML/s. The total GaN growth time after Si deposition is 180 min for the samples shown in Figs. 1(a)–1(d) and 360 min for the one shown in Figs. 1(e)–1(h). The micrographs in Figs. 1(e)–1(h) correspond all to the

same sample but are taken at different positions across the wafer to illustrate the influence of a continuous variation in the amount of deposited Si (the substrate is not rotated during Si deposition).

In the absence of Si deposition [Fig. 1(a)], we observe the formation of a GaN layer. For a Si deposition time of 10 min [Fig. 1(b)], the surface becomes rough but GaN NWs still do not form. However, for $t_{\text{Si}} \geq 21.5$ min we observe the formation of GaN NWs [see Figs. 1(c)–1(h)]. The NWs intersperse a faceted layer and their number density increases with the amount of deposited Si from 1.7×10^7 (for $t_{\text{Si}} = 21.5$ min) to $6.2 \times 10^9 \text{ cm}^{-2}$ (for $t_{\text{Si}} = 60$ min). Figures 1(c), 1(e) and 1(f) demonstrate that, for an optimized amount of deposited Si, ensembles of completely uncoalesced GaN NWs can be obtained. These NWs exhibit small diameters (below 30 nm), smooth sidewalls, and flat top facets [see the inset in Fig. 1(e)].

Figure 2(a) presents a transmission electron micrograph of the sample with a Si pre-deposition time of 60 min. Several GaN NWs are evident as well as the interface between the $\text{GaN}/\text{Al}_2\text{O}_3(0001)$ substrate and a 100 nm thick GaN buffer layer grown by PA-MBE prior to Si deposition. Figures 2(b) and 2(c) show the experimental and simulated convergent-beam electron diffraction (CBED) patterns of the GaN buffer layer and an exemplary GaN NW, respectively. The CBED patterns confirm that the GaN layer is Ga polar and reveal that the GaN NWs grown on top are N polar, as further demonstrated by their fast etching in a 5 M KOH solution [see the inset of Fig. 2(a)]. Hence, as intended, the polarity is reversed at the interface between the buffer layer and the GaN NWs due to Si deposition.

Figure 3(a) shows a highly-magnified bright-field TEM micrograph taken at the interface between the buffer layer and the

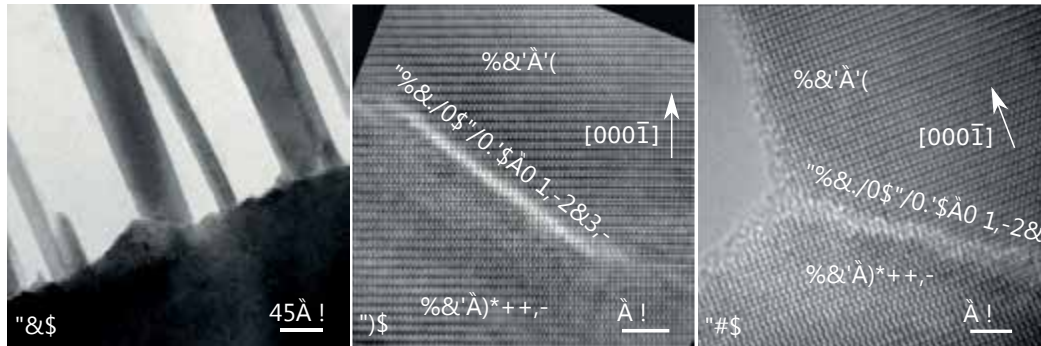


Fig. 3. (a) Representative cross-sectional TEM micrograph of GaN NWs emerging from a faceted GaN buffer layer. (b) and (c) High-resolution micrographs of the interface region for two different NWs recorded along the $(11\bar{2}0)$ zone axis.

GaN NWs of the sample with a Si pre-deposition time of 60 min, showing that the GaN NWs emanate from a faceted layer. To elucidate the origin of the observed polarity inversion, we investigate the interface between the NWs and the faceted layer underneath by high-resolution TEM [Figs. 3(b) and 3(c)]. At this interface, we clearly observe the presence of a 1–2 ML thick interlayer, which is either perfectly crystalline [Fig. 3(b)] or disordered and close to amorphous [Fig. 3(c)], depending on the location. The strong contrast variation across the interlayer implies a substantial concentration of substitutionally incorporated Si atoms giving rise to high local strain. By exposing the GaN(0001) surface to the Si flux at 790°C , we thus locally form a (Ga,
Si)(Si,N) interlayer. The formation of such a compound can be understood by taking into account the amphoteric nature of Si in GaN as well as the fact that Si can also crystallize in a tetrahedrally bonded hexagonal modification. Within this scenario, the inversion of crystal polarity might be caused by the insertion of a locally non-polar material which possesses the point- and space-group of Lonsdaleite (hexagonal diamond). The important result here is that we observe the formation of a coherent and crystalline (Ga,Si)(Si,N) interlayer that induces the polarity inversion and allows the formation of GaN NWs.

The findings reported here may not only be relevant for the growth of group-III nitride NWs, but potentially also for the SAE of other polar semiconductor compounds. A prominent candidate is ZnO, another material that regardless of the substrate exhibits a pronounced tendency to form NWs with a unique and well defined polarity.

Molecular beam epitaxy of GaN nanowires on epitaxial graphene

S. Fernández-Garrido, M. Ramsteiner, G. Gao, L. A. Galves, B. Sharma, P. Corfdir, G. Calabrese, Z. de S. Schiaber, C. Pfüller, A. Trampert, J. M. J. Lopes, O. Brandt, and L. Geelhaar

Graphene offers new opportunities to improve the performance and functionalities of optoelectronic devices based on III-V compound semiconductors. The transparency and high in-plane electrical conductivity of graphene and few-layer graphene films is of interest for the fabrication of contact layers in light-emitting diodes (LEDs), solar cells, and photodetectors, especially in the deep-UV spectral region where standard indium tin oxide contacts are not transparent. Furthermore, provided that III-V compounds can be synthesized with high structural perfection on graphene, the flexibility of this material as well as the possibility to grow or transfer it onto different substrates may enable the integration of III-V based devices with otherwise incompatible material systems. Here, we explore the synthesis of GaN nanowires (NWs) by plasma-assisted molecular beam epitaxy (PA-MBE) on different types of epitaxial graphene layer structures fabricated on SiC substrates.

Figures 1(a)–(c) show schematic illustrations of the three types of epitaxial graphene layer structures used in this work for the growth of GaN NWs. The type I graphene layer structure (GLS I) is characterized by the presence of flat terraces covered with single-layer graphene (SLG) [Fig. 1(a)]. Graphene lies in this case on the top of the so-called buffer layer, which is a C layer covalently bonded to the substrate. The sample also contains bi- to few-layer thick graphene stripes at the step edges. The type II graphene layer structure (GLS II) contains bilayer graphene (BLG) films on the flat terraces [Fig. 1(b)]. A slightly larger number of graphene layers is expected near the step edges [probably trilayer graphene, (TLG)]. The type III graphene layer structure (GLS III) contains (75 ± 15) weakly

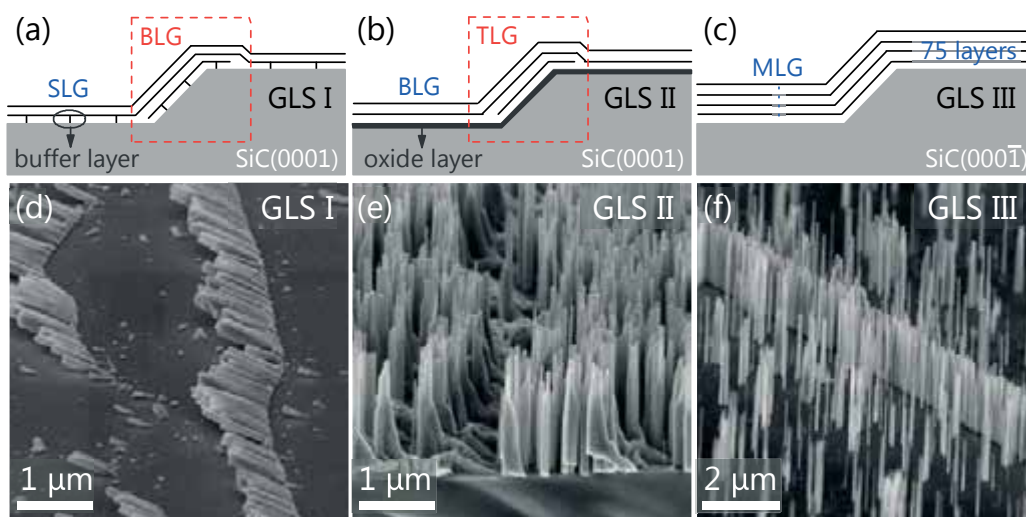


Fig. 1. Sketches of the (a) type I, (b) II, and (c) III epitaxial graphene layer structures prepared on 6H-SiC substrates. (d–f) Bird's eye view scanning electron micrographs of the GaN NW ensembles prepared on the three different types of graphene layer structures, as indicated in the images.

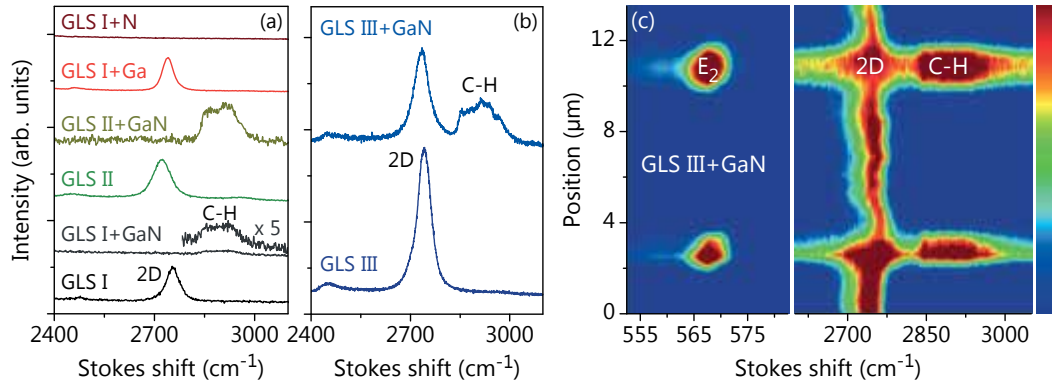


Fig. 2. Raman spectra from ensembles of GaN NWs prepared on the GLS I (GLS I + GaN) and II (GLS II + GaN). The spectra from the pristine GLS I and II as well as that of the GLS I after being exposed to either Ga (GLS I + Ga) or N (GLS I + N) at 790°C are shown for comparison. (b) Raman spectra of the GLS III prior to and after GaN growth. The Raman spectra in (a) and (b) are vertically shifted for clarity. (c) Raman linescan for the sample containing GaN NWs on the GLS III (GLS III + GaN). The color-coded scale bar on the right indicates the intensity on a linear scale. The maximum intensities of the E_2 , 2D, and C–H peaks are saturated in this figure.

interacting layers of graphene [Fig. 1(c)]. We refer to such a structure as multilayer graphene (MLG).

As a first step, we analyzed the formation of GaN NWs by PA-MBE on the GLS I. All GaN NW ensembles presented in this study were grown using identical growth conditions. The Ga and N fluxes were 0.5 and 0.8 monolayers (MLs)/s, respectively, the substrate temperature $\approx 790^\circ\text{C}$, and the growth time 6 h. For these growth conditions, NWs only formed along the step edges [Fig. 1(d)]. Next, we investigated the growth of GaN NWs on the GLS II. In contrast to the previous type of substrate, NWs nucleate everywhere but at the step edges [Fig. 1(e)]. To analyze the impact of the PA-MBE growth process on the original GLS I and II, we employed μ -Raman spectroscopy. The Raman spectra before and after the growth of GaN NWs are shown in Fig. 2(a) for the spectral range of the characteristic graphene 2D peak. The spectra of the pristine GLS I and II exhibit the expected spectral positions and lineshapes of the 2D peaks for SLG and BLG, respectively. Upon GaN growth, however, the Raman modes that reflect the existence of graphene are not detected anymore. Instead, a new Raman peak emerges in the spectral range

between 2850 and 2950 cm^{-1} in which C–H vibrational modes of hydrocarbons are commonly observed (caused by sample contamination after growth).

In order to elucidate the underlying reason for the degradation of the type I and II graphene layer structures during GaN growth, we performed two control experiments where GLS I was exposed either to Ga or active N at 790°C during 6 h. The results of the analysis of these samples by μ -Raman spectroscopy [also included in Fig. 2(a)] demonstrate that graphene is stable against Ga but is completely removed or chemically modified upon continuous exposure to active N. Provided that the underlying reason for the degradation of graphene during N irradiation is the removal of C atoms by the impinging active N species, the use of substrates containing a larger number of graphene layers might alleviate or even solve the problem. Such a scenario motivated us to investigate the growth of GaN NWs on the GLS III shown in Fig. 1(c), where a SiC(0001) substrate is covered with MLG. We found that in this case NWs nucleate preferentially at step edges and structural defects [Fig. 1(f)]. As for the previous substrates, the GLS III prior to and after GaN growth was ana-

lyzed by μ -Raman spectroscopy. As shown in Fig. 2(b), the graphene 2D peak persists upon GaN growth and exhibits only slight changes with respect to the pristine GLS III. To elucidate whether there is MLG below and in between NWs, we recorded a spectral map from the MLG and GaN Raman signals along a linescan that crosses one complete terrace and two steps of the SiC substrate [Fig. 2(c)]. A strong GaN Raman signal (the E_2 phonon line of wurtzite GaN at 568cm^{-1}) is detected at the steps reflecting the large density of NWs at these positions (3 and 11 μm). The observation of the graphene 2D peak along the whole linescan provides evidence for the presence of a continuous MLG film.

The remaining MLG structure after GaN growth was further analyzed by transmission electron microscopy (TEM). A representative high-resolution transmission electron micrograph of the graphene layers of regions below the NWs is shown in Fig. 3. In this micrograph, we detect the presence of a MLG film. The micrograph also reveals the absence of any additional compound on the surface as well as a significant reduction in the thickness of the MLG structure as compared to its original one. The remaining graphene layers are partly distorted underneath the NWs [Fig. 3] and perfectly smooth and continuous in between them (not shown here). The results derived from the analysis of the samples by TEM allow us to conclude that the exposure of graphene to active N does not result in the formation of a different compound but in an etching of graphene.

After demonstrating here the synthesis of GaN NWs on epitaxial MLG films, it would be highly interesting to analyze the electrical properties of the GaN/graphene interface as a next step. Such a study could then be used to conclusively evaluate the actual potential of using epitaxial graphene as a built-in bottom contact for the fabrication of NW-based devices by PA-MBE.

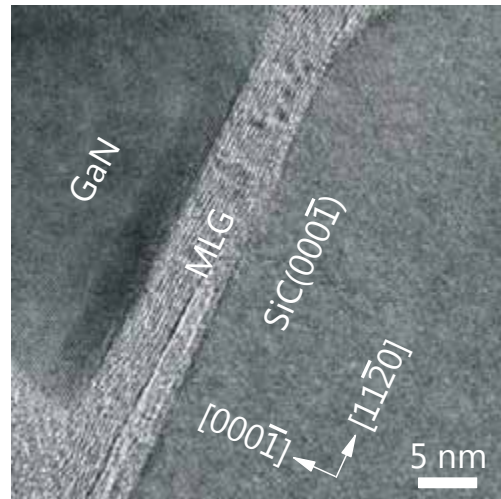


Fig. 3. High-resolution transmission electron micrograph acquired at the bottom part of a NW grown on the GLS III. The thickness of the remaining MLG film is ≈ 15 layers.

Self-assembled formation of long, thin, and uncoalesced GaN nanowires on crystalline TiN films

D. van Treeck, C. Calabrese, J. Goertz, V. M. Kaganer, O. Brandt, S. Fernández-Garrido, and L. Geelhaar

The self-assembled growth of GaN nanowires (NWs) by molecular beam epitaxy (MBE) has been established for almost two decades. However, on most of the commonly used substrates, such as Si, well developed NW ensembles usually exhibit high NW number densities, leading in turn to a massive coalescence of the NWs by bundling and imposing restrictions on their structural and optical quality. Furthermore, the high NW densities do not allow the growth on the NW side facets due to the shadowing of the impinging molecular beams by existing NWs. However, the growth of core-shell structures on the non-polar side facets may not only dramatically increase the total area of the active region but also lead to an improved luminescence efficiency of III-N-based NW light-emitting devices. Hence, it is desirable to find growth approaches that result in a lower number density and coalescence degree. Here, we demonstrate the growth of well-developed and uncoalesced GaN NW ensembles directly on a metal, TiN, with a density suitable for shell growth on the non-polar side facets. By analyzing the nature of coalescence and the nucleation processes, we elucidate the mechanisms enabling the formation of these unique NW ensembles.

As a first step towards well-developed GaN NW ensemble on TiN, we investigated the NW morphology as a function of the substrate temperature. The scanning electron (SE) micrograph in Fig. 1(a) shows an exemplary GaN NW ensemble of about 1.5 μm length grown at the optimum growth temperature of around 800°C. The NWs appear to be uncoalesced and typically have a mean diameter of around 40nm and a

number density of $1\text{--}2 \times 10^9 \text{ cm}^{-2}$. In order to elucidate the origin of these beneficial characteristics, we study in the following the evolution of the morphology at the optimum substrate temperature for different NW lengths. Figure 1(b)–1(g) shows micrographs of the NW ensembles of sample L1, L2, and L3 with mean NW lengths of about 120 nm, 1.5 μm , and 4.7 μm , respectively. With about 7%, the coalescence degree of the well-developed NW ensemble L2 is by about a factor ten lower than what has been reported for NW ensembles of the same length grown on Si. For sample L1 the coalescence degree is less than 1%. In contrast, for NWs of several μm in length as in sample L3, we observe that most NWs are coalesced and form large aggregates also on TiN. For this sample a coalescence degree of around 77% was determined, similar to the situation on Si for a length of about 1 μm . The analysis of samples L1, L2, and L3 shows that for a certain NW number density, the coalescence degree depends mainly on how long the NWs are grown. By a close inspection of various aggregates as the one shown in Fig. 1(h), we found that the height h_c at which the GaN NWs on TiN merge together can be well described by the model of Ref. [1], which initially was developed to describe coalescence on Si. Hence, we conclude that, in general, the coalescence of GaN NWs on TiN seems to be governed by the same mechanism as on Si, i.e. the bundling of NWs is driven by a reduction of the total surface energy at the expense of the elastic energy of bending.

The graphs in Fig. 2 illustrate the critical NW length H_c in dependence of the NW diameter, above which coalescence sets

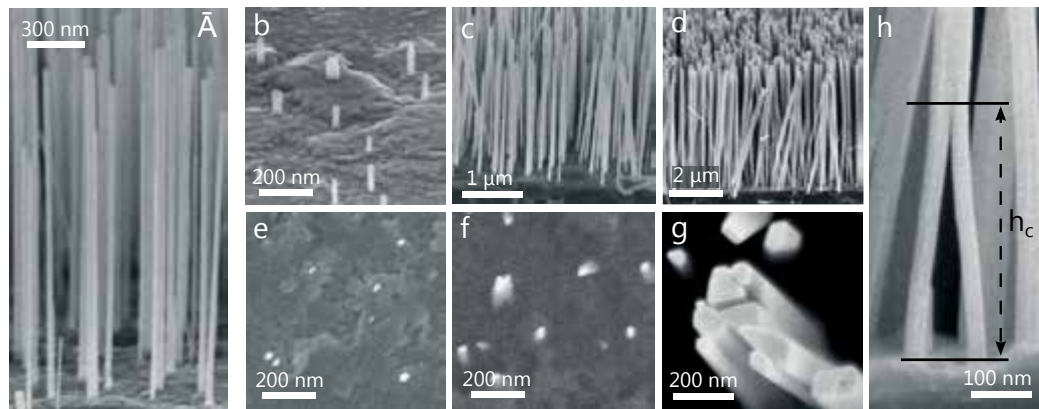


Fig. 1. a) Scanning electron micrograph of a typical, well-developed NW ensemble on TiN. Bird's eye [(b)–(d)] and top view [(e)–(g)] micrographs of NW ensembles L1 [(b) and (e)], L2 [(c) and (f)], and L3 [(d) and (g)] grown with mean NW lengths of about 120 nm, 1.5 μm , and 4.7 μm , respectively, at the optimum substrate temperature of around 800°C. Micrograph (h) illustrates the coalescence of two NWs in sample L3 at a height h_c of 415 nm.

in for a certain NW number density of the ensemble. For an optimized NW ensemble on TiN with a number density of about $1 \times 10^9 \text{ cm}^{-2}$ and a mean diameter of about 40 nm, coalescence only occurs for NWs longer than around 1.3 μm . In comparison, for typical NW ensembles on Si, during the early growth stage the NW density rises to more than $1 \times 10^{10} \text{ cm}^{-2}$, resulting in coalescence already for very short NWs of only a few hundred nm length. Hence, the key factor for the growth of long and well-developed NW ensembles with low coalescence degree is the low NW number density that can be achieved for the self-assembled formation of GaN NWs on TiN.

The above consideration raises the question about the origin of the low NW number density on TiN. In order to answer this question, we now focus on the nucleation of GaN NWs on TiN since it is this process that determines the NW number density. We carried out a statistical analysis of the nearest neighbor (NN) distances between single NWs, and the result for sample L2 is shown in Fig. 3. It is instructive to compare this experimental distribution with the distributions expected for perfect spatial order and complete disorder for the same NW number density. If the NWs nucleated in a perfectly ordered array at an equal distance from each other,

the NN distance for each NW would be 340 nm (vertical green line). In contrast, if the NWs nucleated independently from each other, the NN distance distribution would follow the Poisson probability density distribution (dark blue curve). Obviously, neither of these two opposite extremes describes the case of NW ensembles grown on TiN. Nevertheless, the shift of the NN distance distribution towards higher values with respect to the Poisson distribution is a clear indication that NWs do not form completely independently on the surface. Such a non-random nucleation behavior is a natural consequence of a diffusion-induced repulsion of neighboring NWs. In this scenario, once a NW nucleates, the adatoms diffuse towards the nucleus and the adatom concentration in the surrounding area decreases. As a result, the probability for further nucleation close to this NW is reduced. Taking this repulsive effect into account, we were able to simulate the NN distribution of sample L2 in a Monte Carlo approach for a diffusion length of 120 nm (light blue curve). This analysis shows that the Ga adatom diffusion length on the surface has an important influence on the ordering and hence on the number density of the NWs, and seems to be mainly responsible for the nucleation behavior on TiN.

As a perspective, the properties of the NW ensembles shown in the present work are an excellent basis for the fabrication of more complex structures. Due to the absence of coalescence and the low NW density, the NW ensembles on TiN are promising templates for the realization of well-defined and homogeneous multi-shell heterostructures whose properties may prove useful for applications.

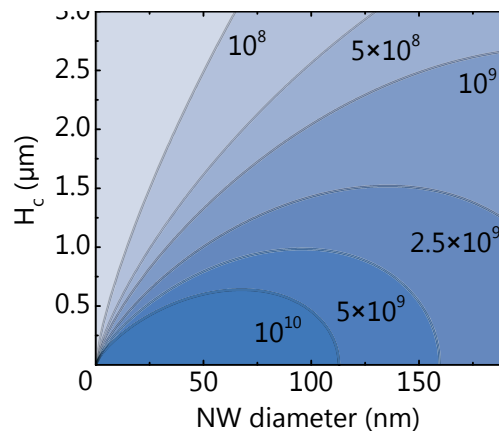


Fig. 2. Critical NW length $H_c = 4h_c/3$ derived in Ref. [1] as a function of diameter for NW ensembles with number densities from 10^8 to 10^{10} cm^{-2} . Note that here all NWs in the ensemble are assumed to have the same diameter, the same length and to be arranged in a hexagonal lattice at equal distances.

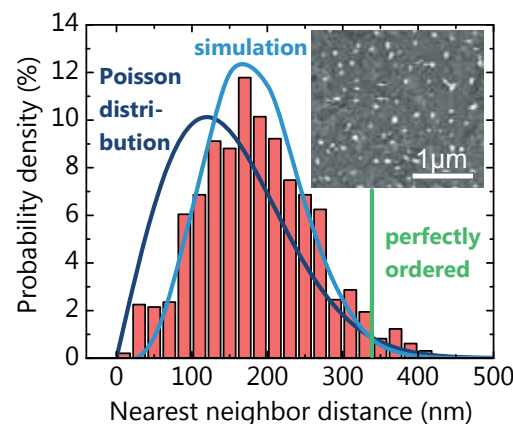


Fig. 3. Analysis of NN distances (red histogram) of sample L2. The vertical green line indicates the NW spacing that would occur in a perfectly ordered NW array, the dark blue curve corresponds to the Poisson distribution and the light blue curve shows the NN distance distribution of a simulated NW ensemble. The inset depicts a top-view micrograph of sample L2.

N-polar (In,Ga)N quantum disks in GaN nanowires vs. Ga-polar (In,Ga)N/GaN quantum wells: Comparative analysis of carrier recombination, diffusion, and radiative efficiency

F. Feix, T. Flissikowski, K. K. Sabelfeld¹, V. M. Kaganer, M. Wölz, L. Geelhaar, H. T. Grahn, and O. Brandt

(In,Ga)N/GaN(0001) quantum wells (QWs) enable solid-state lighting and Blu-ray™ technology. However, the recombination dynamics that gives rise to the intense light emission of this material is complex, and its understanding is still immature. In particular, the emission is characterized by a highly nonexponential decay of its intensity after pulsed excitation. In early studies, this observation was attributed to compositional fluctuations in the ternary alloy (In,Ga)N, creating In-rich regions resembling "quantum dots" that confine excitons with different energies and, consequently, different lifetimes, resulting in a stretched exponential decay. More recently, however, photoluminescence (PL) transients of (In,Ga)N/GaN(0001) QWs recorded over six decades in intensity demonstrated that only the initial decay follows a stretched exponential. For longer times, the decay asymptotically approaches a power law, signifying that recombination actually takes place between spatially separated, individually localized electrons and holes. This situation is analogous to amorphous semiconductors, where recombination between electron-hole pairs occurs either by tunneling or diffusion. In the case of (In,Ga)N/GaN QWs, only purely radiative tunneling recombination was considered in the past for interpreting the PL transients, but, for a full understanding of the recombination dynamics and the resulting internal quantum efficiency (IQE), it is essential to take into account diffusion as well as nonradiative processes.

In this work, we analyze the PL transients of two different samples: first, a device-grade (In,Ga)N/GaN(0001) QW structure synthesized by metal-organic vapor phase epitaxy emitting at 445 nm, and second, an ensemble of GaN(0001) nanowires with inserted (In,Ga)N quantum disks (QDs) prepared by molecular beam epitaxy emitting at 535 nm. While the first sample represents the current state-of-the-art in the blue spectral range, the second is currently considered to be a promising alternative to planar structures for long-wavelength (green and red) emission.

Figures 1(a) and 1(b) show exemplary experimental transients of the PL intensity I_{PL} for our two samples at temperatures of 10 and 250 K over a time range of 30 s. Several important observations can be made directly. First, the PL intensity decays asymptotically according to a power law for both samples and both low and high temperatures. Note the pronounced slowdown of the decay for the planar sample after about 400 ns, which occurs only at 10 K. Second, the temporally integrated PL intensity decreases from 10 to 250 K for both samples, reflecting the presence of nonradiative recombination. Despite this fact, the decay does not become exponential and is still taking place on a μs timescale. For the planar sample, the decay for times longer than 1 μs is significantly faster at 250 than at 10 K, while the shape of the PL decay of the nanowire sample hardly changes at all between 10 and 250 K.

¹ Institute of Computational Mathematics and Mathematical Geophysics, Russian Academy of Sciences, Lavrentiev Prosp. 6, 630090 Novosibirsk, Russian Federation

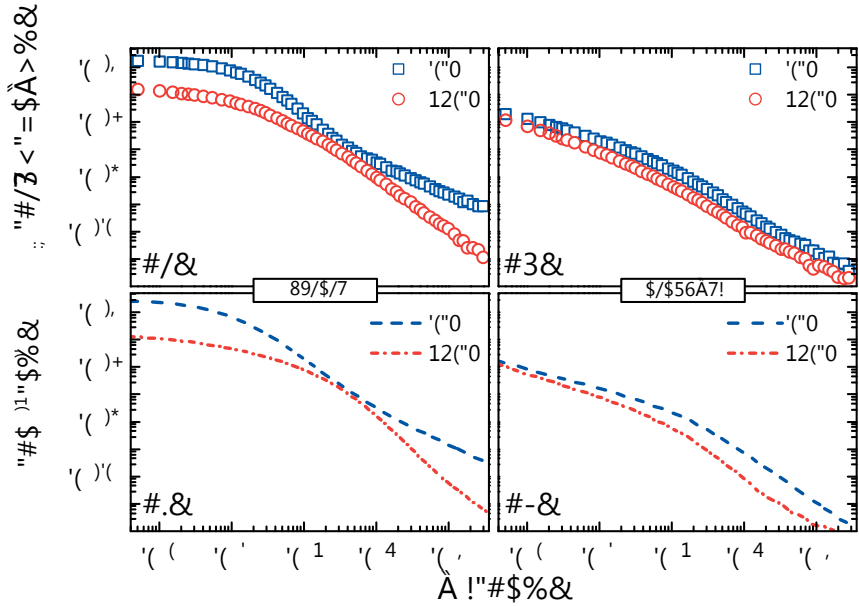


Fig. 1. Double-logarithmic representation of experimental PL transients over a time range of $30 \mu\text{s}$ recorded at the PL peak energy of the (a) planar and (b) nanowire sample at 10 and 250 K by time-correlated single-photon counting. The intensity has been scaled by the same factor to facilitate a direct comparison with the calculations. (c) and (d) Corresponding simulated photon flux transients ϕ .

For a quantitative understanding of these transients, we generalize the classical diffusion-recombination equations of semiconductor physics, treating bimolecular radiative recombination, Shockley-Read-Hall recombination, and carrier diffusion by incorporating the stochastic nature of the recombination and diffusion coefficients (i.e., the random dependence on position or distance of the respective process). The resulting integro-differential equations are solved using a Monte Carlo approach.

Figures 1(c) and 1(d) show simulated transients in comparison to the experimental ones displayed in Figs. 1(a) and 1(b), respectively. For the planar sample at 10 K, the simulation matches the experimental transient with its pronounced slowdown at 400 ns only when setting both the diffusivity and the nonradiative rate to zero, i.e., the simulated transient corresponds to the purely radiative recombination of localized electrons and holes. As discussed in more detail below, the peculiar slowdown of the decay is indeed a fingerprint for an IQE of unity. At 250 K, the simultaneous loss in in-

tensity and the acceleration of the decay are obtained by decreasing the radiative rate and enabling both electron diffusion and nonradiative recombination. Note that the power-law decay is preserved despite the nonradiative process, but the slowdown at 400 ns is eliminated as also observed experimentally.

The transients of the nanowire sample can only be reproduced by a dominant nonradiative process assuming capture coefficients that are more than two orders of magnitude larger than those of the planar sample, while the density of the centers is similar. The almost rigid downshift of the transient recorded at 250 K in Fig. 1(b) is obtained by a further increase of the capture rate, while the radiative recombination rate does not change at all. The radiative rate is smaller than that observed for the planar sample. Furthermore, diffusion is almost absent even at 250 K, reflecting that carrier localization is significantly stronger in the N-polar $(\text{In},\text{Ga})\text{N}/\text{GaN}$ QDs as compared to the planar Ga-polar $(\text{In},\text{Ga})\text{N}/\text{GaN}$ QWs. Still, due to the high-

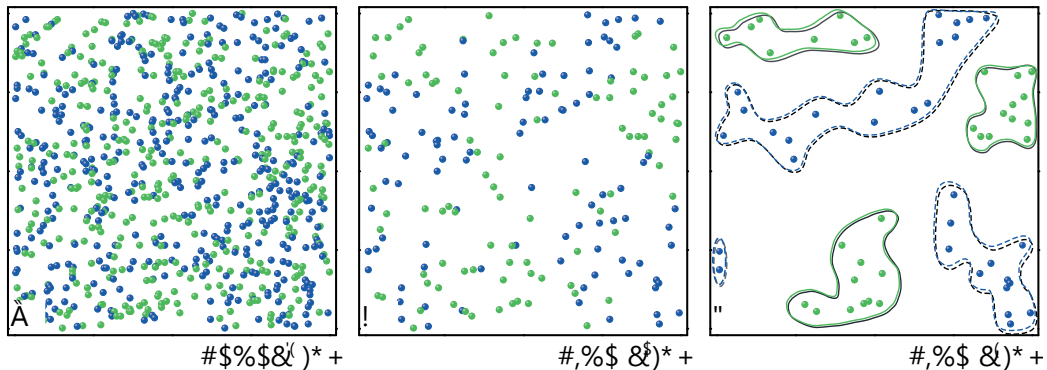


Fig. 2. Snapshots of the distribution of electrons (green) and holes (blue) during the simulated decay of the PL intensity of the planar sample at 10 K. The snapshots are $400 \times 400 \text{ nm}^2$ in size and were taken (a) right after excitation, (b) at 40 ns, and (c) at 400 ns, after which the decay slows down significantly. In (c), the emerging clusters of electrons and holes are encircled by solid and dashed lines, respectively.

ly efficient nonradiative centers in the nanowire sample, its IQE amounts to only 0.2% at 300 K as compared to 40% for the planar sample. This low IQE seems to be inherent to N-polar ($\text{In}_x\text{Ga}_{1-x}\text{N}$)/GaN quantum structures, making them unsuitable for future long-wavelength emitters.

Finally, we examine the origin of the slowdown of recombination observed for the planar sample at 10 K. Figure 2 shows simulated snapshots of the spatial distribution of electrons and holes during their radiative recombination resulting in the PL transient at 10 K as shown in Fig. 1(c). Immediately after their excitation, electrons and holes are distributed randomly [cf. Fig. 2(a)]. Obviously, the electrons and holes most likely to recombine first are those with the minimal spatial separation. Hence, electrons in close vicinity to holes will disappear and vice versa. As a consequence, clusters of each individual species emerge from the initial random distribution, as is indeed seen in the snapshot shown in Fig. 2(b). These clusters become entirely spatially separated with continuing recombination [cf. Fig. 2(c)], and it is at this point where

subsequent recombination slows down. This segregation phenomenon, resulting in the observed slowdown of the PL decay, only occurs in the absence of nonradiative recombination and diffusion.

Absence of quantum-confined Stark effect in GaN/(Al,Ga)N nanowires grown by molecular beam epitaxy

C. Sinito, P. Corfdir, C. Pfüller, S. Kölling, A. Rodil Doblado, G. Gao, J. Bartolomé Vilchez, U. Jahn, J. Lähnemann, T. Auzelle, J. K. Zettler, T. Flissikowski, P. Koenraad, H. T. Grahn, L. Geelhaar, S. Fernández-Garrido, and O. Brandt

(Al,Ga)N is the materials system of choice for the fabrication of solid-state deep ultraviolet emitters. However, due to the lack of commercial AlN substrates, planar GaN/(Al,Ga)N heterostructures suffer from high densities of threading dislocations and cracks. GaN/(Al,Ga)N nanowires (NWs) that spontaneously form in molecular beam epitaxy on for example Si do not suffer from these defects, resulting in structures of high crystal quality. The efficient strain relief at the NW sidewalls leads to reduced polarization fields as compared to planar layers. Also, the large surface-to-volume ratio of NWs facilitates efficient light extraction.

In the present work, we investigate the carrier recombination in three (Al,Ga)N NW ensembles with a single embedded GaN quantum disk (QD) of different thickness ranging from 1.8 to 6.3 nm. A sketch of the nominal nanowire structure as fabricated by plasma-assisted molecular beam epitaxy (PAMBE) is depicted in Fig. 1(a). Room temperature photoluminescence (PL) spectra of the three NW ensembles and of an ensemble of bare (Al,Ga)N nanowires are shown in Fig. 1(b). The bands at low and high energies are attributed to emission from the QDs and the (Al,Ga)N segments, respectively. This assignment is confirmed by the combined scanning electron micrographs and monochromatic cathodoluminescence (CL) maps for the ensemble with the thickest QD shown in Figs. 1(c) and 1(d). Surprisingly, the PL energy of the QDs is higher than the band gap energy of GaN and depends only weakly on the QD thickness, in contrast to the expected strong

quantum-confined Stark effect (QCSE) for QDs with a thickness larger than the GaN exciton Bohr radius ($a_B = 2.8$ nm). In addition, the PL band of the (Al,Ga)N section peaks at an unexpectedly low energy, corresponding to an Al content of 0.15 rather than to the nominal one of 0.3.

To clarify these discrepancies, we investigate the microstructure and composition of selected NWs from the ensemble with the 6.3 nm thick QD. Figure 1(e) shows a representative high-angle annular dark-field scanning transmission electron microscopy (HAADF-STEM) image of a single NW of this sample. The micrograph reveals a QD at the expected position with a thickness of 6 nm, close to the nominal value and ruling out that the high PL energy of the QDs is due to quantum confinement. Interestingly, the contrast observed in the (Al,Ga)N segments suggests the presence of a core/shell structure with an Al-poor inner core (bright) and an Al-rich outer shell (dark). In fact, radial profiles of a single NW from this sample acquired by atom probe tomography (APT) close to the QD confirm this finding and reveal an Al content of 10% for the inner core and a continuously varying Al content up to 40% in the shell (not shown here). The presence of the Al-deficient core explains the comparatively low energy observed along the entire (Al,Ga)N segment [cf. Fig. 1(c)].

To go further, we performed energy-dispersive x-ray spectroscopy (EDX) on several single NWs from the ensemble with the 6.3 nm thick QD. Linescans along the growth direction of the nanowires reveal an axial gradient in the Al content (not shown here). Com-

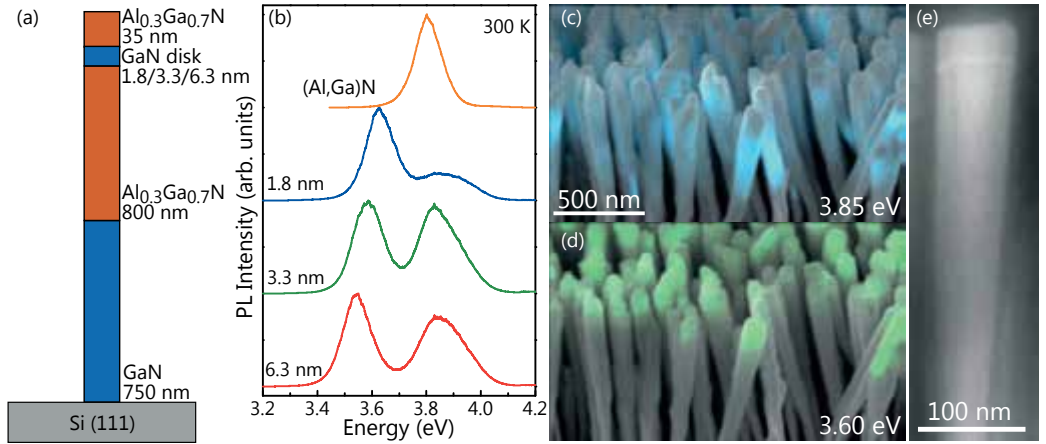


Fig. 1. (a) Sketch of the nominal nanowire structure (not to scale). (b) Room temperature PL spectra of the three GaN/(Al,Ga)N NW ensembles with an embedded GaN QD compared to the spectrum of an ensemble of bare (Al,Ga)N NWs. (c) and (d) Superposition of monochromatized CL images at low temperature with the corresponding bird's eye view scanning electron micrograph of the ensemble with the 6.3 nm thick QD. The energies selected for detection are indicated in the figures. (e) HAADF-STEM image of a single NW of the NW ensemble with the 6.3 nm thick QD.

bining the results of APT and EDX, we find that the Al content in the shell decreases from essentially 100% at the bottom of the (Al,Ga)N segment to about 40% close to the position of the QD at the top. This unintended gradient along the growth direction creates a three-dimensional (3D) electron gas in the shell owing to the spontaneous polarization of (Al,Ga)N (the so-called polarization doping). These electrons transfer into the core, having a lower band gap, and from there to the QD. The resulting high electron density inside the QDs screens the internal electrostatic field. Figure 2(a) compares the experimental transition energies for our three samples (green triangles) with those obtained by one-dimensional (1D) Schrödinger-Poisson calculations for undoped GaN/ $\text{Al}_{0.1}\text{Ga}_{0.9}\text{N}$ QDs (red squares) and for GaN/ $\text{Al}_{0.1}\text{Ga}_{0.9}\text{N}$ QDs with an electron density of $5 \times 10^{18} \text{ cm}^{-3}$ (blue circles), the value obtained in an independent 1D simulation considering the axial gradient derived above by combining APT and EDX. Considering the simplicity of our 1D model, the agreement is quite satisfactory.

For an electron density of this magnitude, the GaN QD becomes degenerate. The metallic nature of the electron system is expected to strongly affect the recombination dynamics. In fact, while the spontaneous emission rate of a nondegenerate two-dimensional (2D) electron-hole system decreases linearly with temperature, that of a highly degenerate system is constant. To obtain quantitative insights, we perform time-resolved PL spectroscopy on the NW ensemble with the 6.3 nm thick QD between 5 and 300 K. The spectrally and temporally resolved emission of the ensemble (not shown here) is characterized by a red-shift of the emission with time together with a non-exponential decay of the PL intensity. This behavior is not expected for a constant electron density, but can be understood by a NW-to-NW variation of the electron densities in the QDs, since high electron densities result in both short radiative lifetimes and high transition energies and vice versa. The red-shifted, long-living signal in our measurements thus originates from QDs with comparatively low electron density. The variation in electron

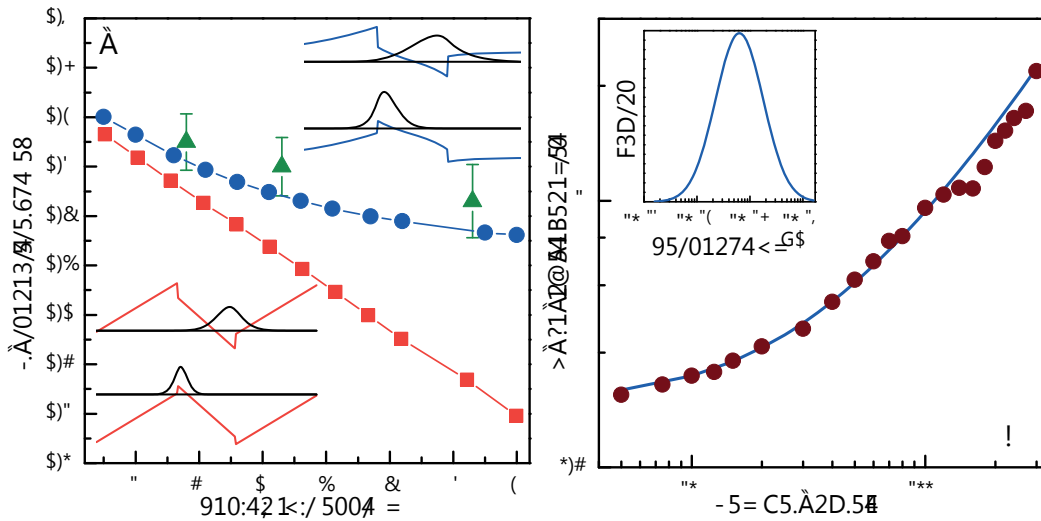


Fig. 2. (a) Transition energy as a function of the QD thickness for an electron density of 0 (red squares) and $5 \times 10^{18} \text{ cm}^{-3}$ (blue circles). The experimental points are represented by green triangles with the error bars representing the linewidth of the respective PL bands. The insets show the band profiles and the charge carrier wave functions obtained for the two cases. (b) Temperature dependence of the radiative lifetime of electron-hole pairs in the QD for the sample with a QD thickness of 6.3 nm (symbols). The solid blue line corresponds to the radiative lifetime calculated for a NW ensemble with a mean electron density of $3 \times 10^{18} \text{ cm}^{-3}$ in the QDs, but a significant NW-to-NW variation (see inset).

density can be quantified by examining the temperature dependence of the radiative lifetime for the QDs as shown in Fig. 2(b). The calculated curve is obtained by assuming the distribution of electron densities as depicted in the inset of Fig. 2(b) and is in excellent agreement with the measured values.

Our study reveals that, during the growth of (Al,Ga)N NWs by PAMBE, complex axial and radial gradients of the NW composition form spontaneously. The former results in a high electron density in embedded GaN QDs due to polarization doping. This phenomenon induces a screening of the internal electrostatic fields in the QDs and simultaneously fast and only weakly temperature-dependent recombination between photoexcited holes and the degenerate 2D electron gas in the QD.

Continuous tuning of two-section, single-mode terahertz quantum-cascade lasers by fiber-coupled, near-infrared illumination

M. Hempel, B. Röben, M. Niehle, L. Schrottke, A. Trampert, and H. T. Grahn

Frequency tuning is an important prerequisite for state-of-the-art spectroscopy, e. g. for modulation spectroscopy. In addition to intrinsic frequency tuning mechanisms for terahertz (THz) quantum-cascade lasers (QCLs) via current and temperature changes, several concepts such as external cavity setups, mechanically tuned cavities, coupled cavities, material condensation, and three-terminal configurations have been reported in the literature. Recently, a fast and continuous tuning of THz QCLs by illuminating their rear facet with a near-infrared diode laser has been demonstrated for Fabry-Pérot resonators, which typically exhibit a multi-mode spectrum. In order to achieve single-mode operation, which is desired for a variety of spectroscopic applications, we employ here a two-section cavity instead of a distributed-feedback grating. The frequency tuning behavior of this two-section resonator is investigated using a fiber optics-based illumination scheme.

As shown in Fig. 1(a), the rear facet of the THz QCL is illuminated using a diode laser (DL) by coupling the light through an optical fiber so that the excess heat due to the operation of the DL is kept outside the cryocooler, which is necessary to operate the THz QCL. In addition, the illumination beam geometry remains rather flexible. The two-section cavities were fabricated following H. Li *et al.* [Appl. Phys. Lett. **104**, 241102 (2014)]. The QCL laser cavity is separated into two parts by focused-ion beam (FIB) processing of an already mounted and characterized QCL. The employed FIB system (JEOL IB4501 dual-beam microscope) uses Ga ions with an acceleration voltage of 30 kV. The FIB cut has a length of 145 μm , a width of 8 μm , and a depth of 14 μm , preventing an electrical shortcut

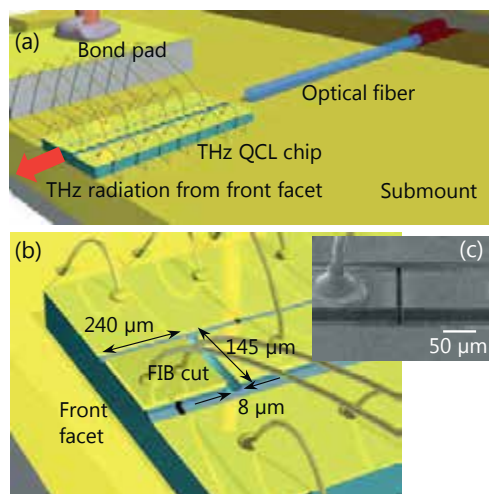


Fig. 1. (a) Schematic of the fiber-coupled DL illuminating the rear facet of the THz QCL. (b) Schematic of the FIB cut applied to the ridge of a THz QCL. (c) Side-view of the actual FIB cut recorded with a scanning electron microscope.

by burying the used Ga ions in the semi-insulating substrate under the 11- μm -thick epitaxial layer. For the QCL under investigation, which emits in continuous-wave (cw) operation at about 3.1 THz with about 10 mW for 400 A/cm² at 10 K, the 120- μm -wide laser ridge was divided into an 810- μm - and a 240- μm -long section. A schematic and a scanning electron microscopy image of the cut are shown in Figs. 1(b) and 1(c), respectively.

The spectra were recorded using a high-resolution Fourier transform spectrometer (Bruker IFS 120HR) with a spectral resolution of $\Delta\tilde{\nu} = 0.01 \text{ cm}^{-1}$. Figure 2(a) shows the spectra of the original QCL and Fig. 2(b) of the QCL after it has been cut by FIB for various currents I_{QCL} with the QCL employed in pulsed operation at 35 K.

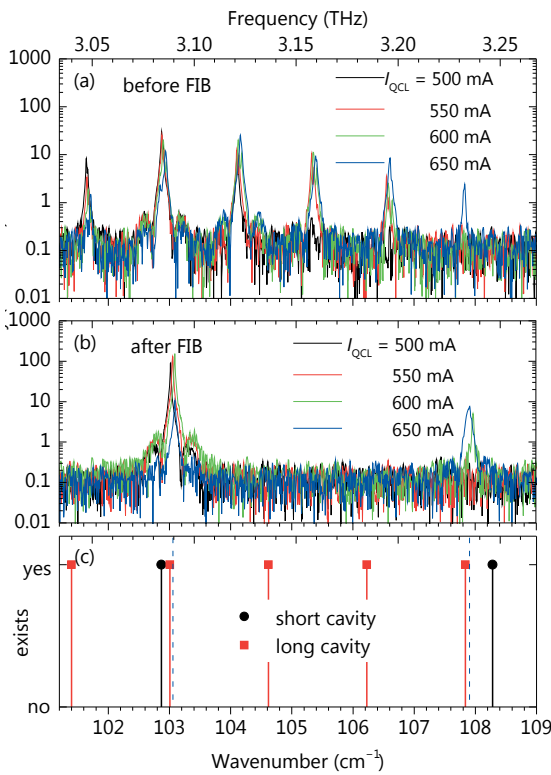


Fig. 2. (a) Lasing spectra of the original QCL before applying the FIB cut for different current levels in pulsed operation with 500-ns pulses at a repetition rate of 5 kHz for a heat sink temperature of 35 K. (b) Lasing spectra after applying the FIB cut using the same operating parameters as in (a). (c) Calculated position of the cavity modes using a refractive group index of 3.84 for the long and short section of the cavity (solid lines). The dashed lines indicate the position of the modes observed in the experiment.

The original QCL exhibits 5 to 6 spectral modes, while after the FIB cut only one prominent mode at about 3.09 THz and, for elevated currents above $I_{QCL} = 550$ mA, a second weaker mode at 3.23 THz appear. The single-mode operation of the two-section cavity laser can be modeled by calculating the Fabry-Pérot modes of the two individual cavities. For the two-section QCL, only modes are allowed which exist in both cavities at almost identical frequencies. The calculated modes for the two sections of the QCL are displayed in Fig. 2(c). For the two frequencies 3.09 and 3.24 THz, the calculated modes of the short and long cavity are sufficiently close together so that

the two-section cavity laser is expected to lase only at these two frequencies. The output power of all modes in multi-mode operation before the FIB cut is transferred into the mode at 3.09 THz after the FIB cut. The application of the FIB cut to an already processed and characterized laser has the advantage that a certain frequency can be selected within the gain region of the QCL by choosing a particular ratio of the lengths of the two sub-cavities.

Figure 3(a) shows the spectra under pulsed operation with increasing DL illumination power. The DL is always employed in cw operation. Due to the dynamic variation of the temperature and current in the QCL under pulsed operation, the spectral peaks are broadened, and the line shape becomes more complex as compared to cw operation. The increase of the DL illumination power clearly results in a blue shift of the lasing frequency. The largest frequency shift is achieved at the highest possible DL power. A further blue shift is expected for even larger illumination powers, but the application of these powers is limited by the damage threshold of the rear facet due to the heating induced by the absorption of the near-infrared light or by the limited cooling capacity of the cryocooler.

Under cw operation, both lasers are in thermal equilibrium with the heat sink. Then, their frequencies become stable, and the QCL line width is much narrower. Figure 3(b) shows the results of the QCL under cw operation for various DL driving currents. A clear blue shift of the QCL frequency is visible above $I_{DL,th}$, while below $I_{DL,th}$ a very small red shift takes place. The maximally applied DL power under cw operation is limited by the cooling capacity of the cryocooler, since the absorbed near-infrared radiation at the QCL rear facet causes an additional heating. Over the entire tuning range, the device maintains single-mode operation. Figure 3(c) shows the peak position of the lasing modes for

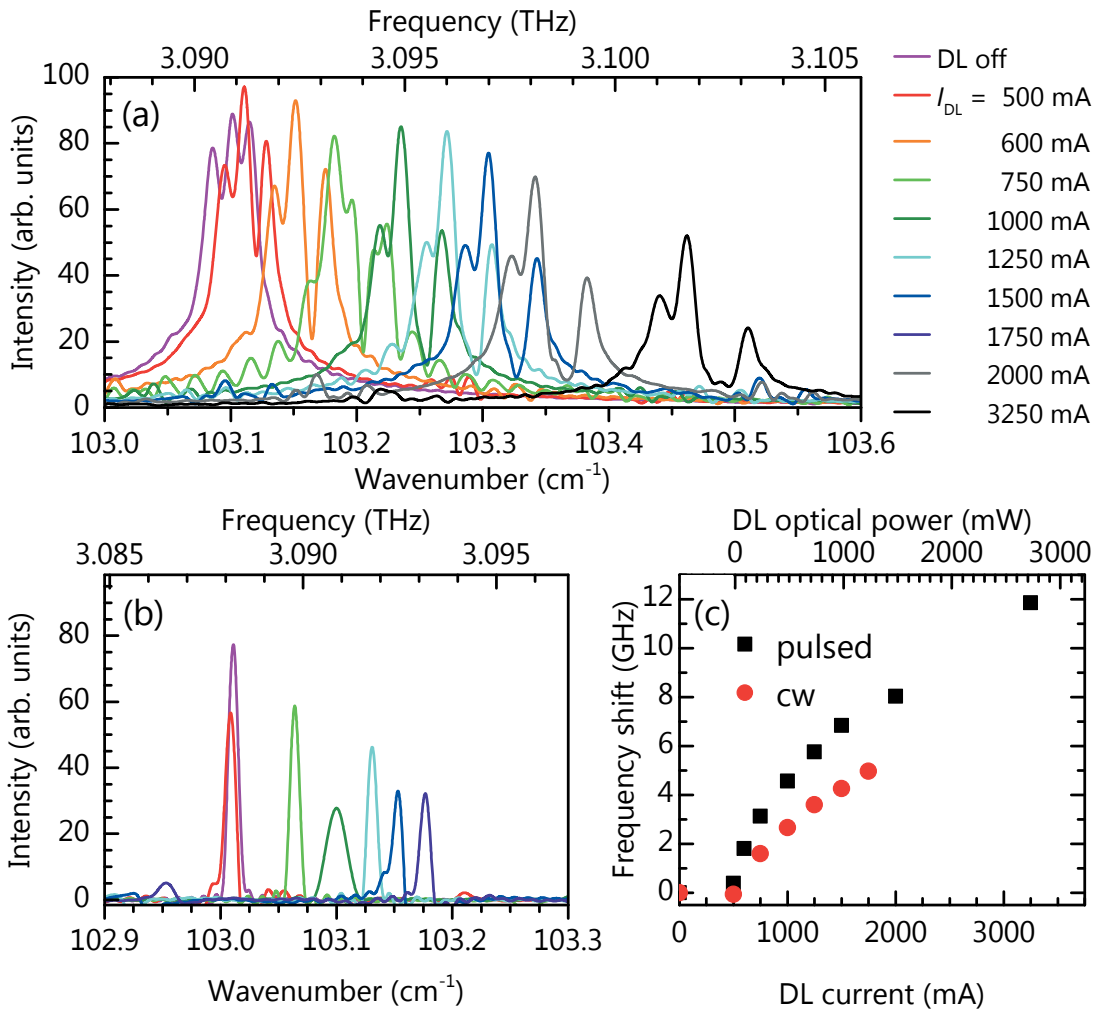


Fig. 3. (a) Frequency tuning of the two-section QCL for pulsed operation at 500 mA and 45 K for different DL driving currents. (b) Frequency tuning of the same QCL as in (a) under cw operation at 450 mA and 50 K for different DL driving currents. The legend in (a) is also valid for (b). (c) Frequency shift extracted from the peak positions in (a) and (b).

pulsed and cw operation extracted from Figs. 3(a) and 3(b), respectively. The maximal tuning range in single-mode operation of the THz QCL achieved at 2.70 W DL optical power during pulsed operation of the QCL is 11.9 GHz. A maximal tuning range of 5.0 GHz can be achieved for cw operation. While the maximal tuning range in the pulsed case is limited by the maximally employed optical power of the DL system, the tuning range for cw operation is limited by the cooling capacity of the cryocooler.

Terahertz quantum-cascade lasers as high-power and wideband, gapless sources for spectroscopy

B. Röben, X. Lü, M. Hempel, K. Biermann, L. Schrottke, and H. T. Grahn

We report on the application of multi-mode terahertz (THz) quantum-cascade lasers (QCLs) as a high-power replacement for conventional THz wideband sources used for Fourier transform infrared (FTIR) spectroscopy. Our approach is based on the intrinsic tuning of the laser modes by varying the injection current.

Figure 1(a) shows a sketch of a typical spectrum of a QCL with a Fabry-Pérot (FP) resonator consisting of several equally spaced modes. If the collective shift exceeds the mode spacing, the overall continuously covered frequency range approaches the total width of the gain profile as indicated in Figs. 1(b) and 1(c). The QCL is tuned in a short time interval Δt , while the signal of the detector of the FTIR spectrometer (FTIRS) is averaged over Δt as sketched in Fig. 1(d). When Δt is substantially smaller than the acquisition time of the FTIRS, the emission spectrum appears to be continuous due to the averaging, which we refer to as gapless,

time-averaged wideband (G-TAWB) operation. Figure 1(e) depicts the experimental setup using a QCL in G-TAWB operation as a source for an FTIRS. The employed QCL is operated at 10 K, which is placed in front of the external emission port of the FTIRS purged with nitrogen. The time averaging is realized by employing a slow pyroelectric detector for the FTIRS, and the highest resolution of the FTIRS (Bruker IFS 120HR) is 0.105 GHz. We achieve a gapless coverage over a range of 72 GHz at about 4.7 THz using G-TAWB operation. To compare the properties of the THz QCL in G-TAWB operation with those of a conventional thermal source, a heated SiC rod is employed as the source in the FTIR.

Figure 2(a) shows the emission spectrum of a GaAs/AlAs QCL in G-TAWB operation recorded with the highest resolution of the FTIRS, exhibiting a continuous coverage of 72 GHz over the range from 4.686 to 4.758 THz. The spectrum is not

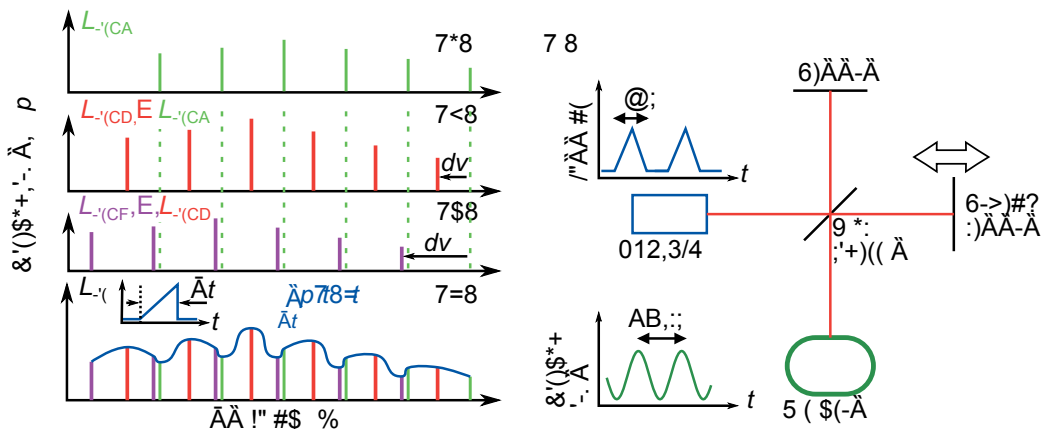


Fig. 1. (a)–(c) Schematic emission spectra of QCLs with FP resonators for increasing optical path lengths L_{opt} . The modes in (b) and (c) are collectively red-shifted by dv , which can be larger than the mode spacing as shown in (c). (d) If L_{opt} is continuously increased over a time Δt and the spectral power p is averaged over Δt , a gapless, time-averaged wideband spectrum may be generated. (e) Setup for an FTIRS with a QCL under G-TAWB operation.

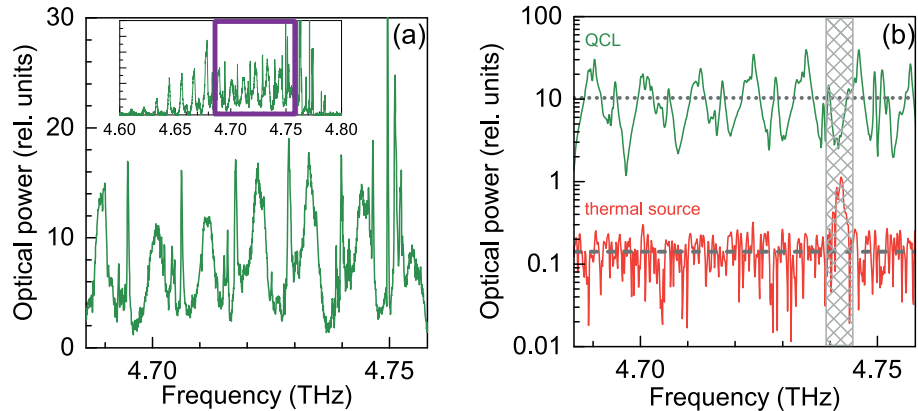


Fig. 2. (a) Spectral power in relative units of the QCL in G-TAWB operation for a frequency range of 72 GHz (4.686 to 4.758 THz) recorded with a resolution of 0.105 GHz. (b) Spectral power of the thermal source compared with the QCL in G-TAWB operation as measured with an FTIRS using a spectral resolution of 0.3 GHz. The dotted and dashed lines mark the average power of 10.4 for the QCL and 0.14 for the thermal source, respectively.

smooth, since not only the position of the FP modes, but also their power and number are a function of the injection current. Figure 2(b) shows the emission spectra of the QCL in G-TAWB operation and of the thermal source (SiC rod) with a lower resolution than in Fig. 2(a). In comparison to the thermal source, the QCL exhibits one to two orders of magnitude higher powers. Note that the hatched rectangle in Fig. 2(b) marks a peak which we attribute to a pickup of the power line frequency in the detector circuitry that can be neglected in the analysis.

Figure 3(a) shows the signal-to-noise ratio (SNR) of the QCL and the thermal source calculated from 10 consecutive measurements. Over the complete frequency range, the SNR of the QCL is significantly higher than that of the thermal source. While the average power of the QCL in Fig. 2(b) is a factor of about 75 larger than that of the thermal source, the average SNR of the QCL is only a factor of about 20 higher than that of the thermal source. In order to demonstrate that the frequency dependence of the emission power of the QCL in G-TAWB operation does not hamper the reliability of a measurement, we recorded a transmission spectrum of a 10-cm-long gas cell filled with water-saturated air at atmospheric pressure. Figure 3(b) shows

the transmission spectra of air with 100% humidity in the gas cell recorded with the QCL in G-TAWB operation as well as with the thermal source. While the measurement with the QCL clearly shows the slowly varying transmission spectrum in agreement with the simulated spectrum, the emission power of the thermal source is too low for a meaningful measurement. Figure 3(c) shows the transmission spectra recorded with a lower resolution of 1.5 GHz and with a mirror speed, which was reduced from 7.5 to 2.2 kHz. In this case, the spectra recorded with the thermal source also show reasonable results. In the spectra recorded with the thermal source, however, there is a quickly varying modulation due to noise. In contrast, the spectra using the QCL are very smooth and well reproducible. Therefore, QCLs in G-TAWB operation may pave the way for versatile high-sensitivity and high-resolution spectroscopy at THz frequencies.

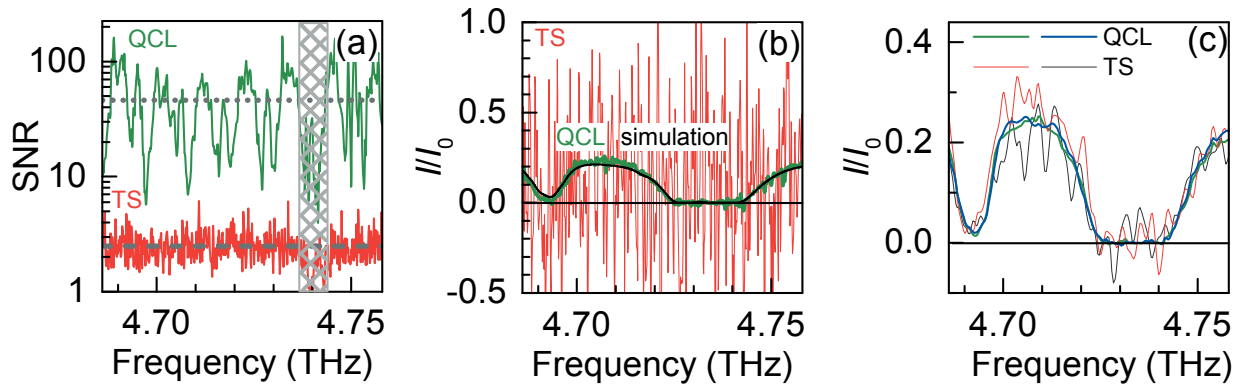


Fig. 3. (a) SNR as a function of frequency for the QCL and the thermal source (TS). The dotted and dashed lines mark the average SNR of 46 for the QCL and 2.5 for the TS, respectively. (b) Transmission spectrum of air with 100% humidity in a 10-cm-long gas cell recorded with the QCL in G-TAWB operation and the TS using a resolution of 0.3 GHz. The black curve displays a simulated transmission spectrum. (c) Transmission spectra of the same gas cell as in (b) recorded with a lower resolution of 1.5 GHz.



Departments Abteilungen

Epitaxy Epitaxie	133
Semiconductor Spectroscopy Halbleiterspektroskopie	137
Microstructure Mikrostruktur	143
Technology and Transfer Technologie und Transfer	149

Department of Epitaxy

Abteilung für Epitaxie

Head of Department: Dr. Lutz Geelhaar, geelhaar@pdi-berlin.de

The overall competence of this research department is the growth of crystalline thin films and nanostructures with extremely well-defined properties by epitaxy. Epitaxy is a process in which one crystal, the adsorbate, is grown on another crystal, the substrate, in such a way that there is a unique relation between the orientations of the two crystal lattices. Typically, the adsorbate is at most a few micrometers thick. Compared to the growth of bulk crystals, epitaxy offers several advantages: First, epitaxy allows the synthesis of materials that are only metastable and cannot be grown as bulk crystals at all. Thus, materials can be grown with specific and tailored properties that could not be obtained in any other way. Second, during epitaxy the composition of the growing crystal can be changed very abruptly—on the atomic scale—so that heterostructures consisting of different materials can be fabricated. In such heterostructures quantum phenomena can be observed, and by tailoring the heterostructures quantum phenomena can be manipulated and new functionalities can be achieved. Therefore, epitaxy is a means to realize nanostructured materials as well as artificial low-dimensional semiconductor systems and to tune their mechanical, optical, electronic, and magnetic properties.

The research activities in the epitaxy department are directed at two complementary tasks. On the one hand, our experimental contribution to the overall research of the institute is the fabrication of custom-designed nanostructured samples. On the other hand, the underlying growth mechanisms themselves are investigated, both for their own scientific sake and in or-

Die Kernkompetenz dieser Abteilung ist die Züchtung kristalliner Schichten und Nanostrukturen mit äußerst präzise definierten Eigenschaften mittels Epitaxie. Mit Epitaxie bezeichnet man den Prozess, in dem ein Kristall – das Adsorbat – auf einem anderen Kristall – dem Substrat – mit einer eindeutigen Beziehung zwischen den Kristallorientierungen gezüchtet wird. Dabei ist das Adsorbat typischerweise nicht dicker als einige Mikrometer. Epitaxie weist einige Vorteile im Vergleich zu der Züchtung von Volumenkristallen auf. So lassen sich mittels Epitaxie auch Materialien herstellen, die nur metastabil und als Volumenkristall gar nicht zu züchten sind. Auf diese Weise können besondere Materialien mit spezifischen, maßgeschneiderten Eigenschaften hergestellt werden. Der zweite wichtige Vorteil der Epitaxie liegt in der Möglichkeit, während des epitaktischen Wachstums die Zusammensetzung des Kristalls sehr abrupt – auf atomarer Skala – zu ändern, so dass sogenannte Heterostrukturen erzeugt werden können, die aus unterschiedlichen Materialien bestehen. In solchen Heterostrukturen können Quantenphänomene beobachtet und durch definiertes Einstellen der Strukturparameter manipuliert werden. Dies ermöglicht die Realisierung und Untersuchung neuer Funktionalitäten, die für Anwendungen interessant sein können. Epitaxie ist somit ein Werkzeug, mit dem nanostrukturierte Materialien wie auch künstliche niedrigdimensionale Halbleiter-systeme mit einstellbaren mechanischen, optischen, elektronischen und magnetischen Eigenschaften hergestellt werden können.



der to optimize properties that are investigated in the core research areas. Often, experiments are complemented by ab-initio calculations. Our comprehensive expertise is based on the long tradition for the fabrication of two-dimensional heterostructures comprising III-V semiconductors, but in addition we work on more and more other materials. Furthermore, research on the vertical growth of III-V nanowires has become a major activity of this research department.

The technique for crystal growth that we employ at PDI is molecular beam epitaxy (MBE). In MBE, growth takes place under extremely pure conditions in ultra-high vacuum. Crystal growth is fed by beams of neutral atoms or molecules that are typically obtained by evaporating source material in effusion cells. Due to the low pressure, these atoms or molecules do not scatter or interact with each other before they reach the substrate. In order to modify the kinetics of crystal growth, the substrate temperature is adjusted. In general, MBE offers a very high level of control over the growth conditions, and growth can be monitored *in situ* by several characterization techniques.

Arguably the most mature class of compound semiconductors is formed by the group-III arsenides GaAs, AlAs, InAs, and their alloys. Very complex heterostructures can be realized in this material system with impressive precision and reproducibility. Such samples are fabricated for investigation in the core research areas *Intersubband Emitters: GaAs-based Quantum-Cascade Lasers and Control of Elementary Excitations by Acoustic Fields*.

The performance and functionality of future semiconductor devices will be enhanced by making use of three-dimensional nanostructures. Our efforts in this direction concentrate on the creation of such structures directly by growth, i.e. in a bot-

Die Forschungsaktivitäten in der Epitaxie-Abteilung konzentrieren sich auf zwei komplementäre Linien. Auf der einen Seite werden für ein breites Spektrum an weiterführenden Forschungsaktivitäten am Institut maßgeschneiderte nanostrukturierte Proben hergestellt. Auf der anderen Seite werden die Wachstumsmechanismen selbst untersucht – aus wissenschaftlichem Interesse an den zugrundeliegenden Prozessen und um die Materialeigenschaften, die in den Forschungsschwerpunkten untersucht werden, zu optimieren. Oft werden Experimente durch ab-initio Rechnungen begleitet. Unsere umfassende Expertise basiert auf einer langen Tradition der Herstellung zweidimensionaler Heterostrukturen, die aus III-V-Halbleitern bestehen. Mittlerweile arbeiten wir aber auch intensiv an weiteren Materialsystemen. Zudem hat sich das senkrechte Wachstum von III-V-Nanodrähten zu einer Kernaktivität der Abteilung entwickelt.

Am PDI setzen wir als Methode für Kristallzüchtung die Molekularstrahlepitaxie (MBE für englisch molecular beam epitaxy) ein. Bei diesem Verfahren findet das Wachstum unter äußerst reinen Bedingungen im Ultrahochvakuum statt. Das Kristallwachstum wird durch Atom- oder Molekülstrahlen versorgt, die typischerweise durch das Verdampfen von Quellmaterial in Effusionszellen erzeugt werden. Aufgrund des niedrigen Drucks in der Wachstumskammer streuen die Atome bzw. Moleküle nicht und erfahren auch keine Wechselwirkung untereinander, bis sie auf das Substrat treffen. Um die Kinetik des Kristallwachstums zu modifizieren, wird die Substrattemperatur geregelt. Generell bietet MBE ein sehr hohes Maß an Kontrolle über Wachstumsbedingungen, und das Wachstum kann *in situ* mittels mehrerer Charakterisierungstechniken überwacht werden.

Die wohl am weitesten entwickelte Klasse von Verbindungshalbleitern wird von den Gruppe-III-Arseniden GaAs, AlAs, InAs und deren Legierungen gebildet. In diesem Ma-

tom-up approach with the help of self-organization mechanisms. In particular, we grow both group-III arsenides and nitrides not only as planar layers but also in the form of nanowires. Nanowires are structures with an extremely high aspect ratio and a diameter of the order of 100 nm. Their formation, properties, and applications are the subject of the core research area *III-V Nanowires for Optoelectronics*.

Research activities with the focus on the synthesis of materials are carried out in the core research area *Nanofabrication*. At present, the epitaxy of group-III arsenides, group-III nitrides, ferromagnetic Heusler alloys like Co_2FeSi in hybrid structures with group-III arsenide heterostructures and MgO , transparent semiconducting oxides (Ga_2O_3 and In_2O_3), phase-change alloys in the material system Ge-Sb-Te, graphene (the two-dimensional allotrope of carbon), and hexagonal BN is investigated. This research takes place in close collaboration with the core research area *Nanoanalytics* in which the emphasis of the research is on materials properties.

In practice, the key features of MBE described before can only be achieved by combining a considerable number of different technical components, and hence MBE systems are fairly complex. The core component of such systems is a chamber made from stainless steel in which ultra-high vacuum is maintained and the actual crystal growth takes place. In order to preserve ultra-purity and avoid cross-contamination, each material system requires its own, dedicated MBE chamber. For the two main material systems of PDI, group-III arsenides and group-III nitrides, we can pursue the multitude of research projects only by operating more than one MBE chamber each. In total, there are at present eleven MBE systems in use. For the fabrication of hybrid structures comprising different materials, growth on the same sample has to take place subsequently in more than

terialsystem lassen sich sehr komplexe Heterostrukturen mit beeindruckender Präzision und Reproduzierbarkeit herstellen. Solche Proben werden für weitere Untersuchungen in den Forschungsschwerpunkten *Intersubband-Emitter: GaAs-basierte Quantenkaskadenlaser und Kontrolle von Elementaranregungen durch akustische Felder* hergestellt.

Die Leistung und Funktionalität zukünftiger Halbleiter-Bauelemente wird durch die Verwendung von dreidimensionalen Nanostrukturen verbessert werden. Unsere Bemühungen in diesem Zusammenhang konzentrieren sich auf die Ausbildung solcher Strukturen direkt während des Wachstums, d.h. durch Ausnutzung von Selbstorganisationsphänomenen. Insbesondere züchten wir sowohl Gruppe-III-Arsenide als auch -Nitride nicht mehr nur als planare Schichten, sondern auch als Nanodrähte. Nanodrähte sind Strukturen, die ein äußerst hohes Aspektverhältnis und einen Durchmesser in der Größenordnung von 100 nm aufweisen. Die Bildung, die Eigenschaften und die Anwendungen von Nanodrähten sind Untersuchungsgegenstand des Forschungsschwerpunkts *III-V-Nanodrähte für Optoelektronik*.

Die Synthese von Materialien steht hingenommen im Fokus des Forschungsschwerpunkts *Nanofabrikation*. Gegenwärtig werden hier die Epitaxie von Gruppe-III-Arseniden und -Nitriden, ferromagnetischen Heusler-Legierungen wie Co_2FeSi in Hybridstrukturen mit Gruppe-III-Arsenid-Heterostrukturen und MgO , transparenten halbleitenden Oxiden (Ga_2O_3 und In_2O_3), Phasenwechsel-Materialien des Systems Ge-Sb-Te, Graphen (das zweidimensionale Allotrop von Kohlenstoff) und hexagonalem BN untersucht. Diese Forschung wird in enger Zusammenarbeit mit dem Forschungsschwerpunkt *Nanoanalytik* durchgeführt.

In der Praxis lassen sich die beschriebenen Schlüsselmerkmale von MBE nur erreichen, wenn eine beträchtliche Anzahl unterschiedlicher technischer Komponenten kombiniert

one MBE chamber. In order to avoid contamination of the interface between two materials, such samples have to be transported from one MBE chamber to the other under ultra-high vacuum conditions. Thus, some of our MBE chambers are connected as cluster systems. As an alternative, mobile ultra-high vacuum shuttle chambers are also employed to transfer samples between MBE systems.

As a distinctive experimental feature, PDI owns three special MBE chambers that allow the in-situ, real-time analysis of growth processes by x-ray diffraction. To this end, these chambers can be connected to our own beamline at the synchrotron BESSY II (Helmholtz-Zentrum Berlin für Materialien und Energie). The successful operation of such a setup critically depends on the continuous stationary operation of the MBE system at the synchrotron, since a high quality of the epitaxial layers and interfaces is imperative for a reliable quantitative analysis. Consequently, at least one of these special MBE chambers is always located at the synchrotron. Currently, a system equipped for the study of semiconducting oxides is installed there.

wird. Daher sind MBE-Anlagen recht komplex. Die Kernkomponente eines solchen Systems ist eine Kammer, die aus Edelstahl gefertigt wird. Hier findet das eigentliche Kristallwachstum statt. Um die extreme Reinheit zu erhalten und wechselseitige Verunreinigungen zu vermeiden, braucht jedes Materialsystem seine eigene, dedizierte Wachstumskammer. Für die zwei zentralen Materialsysteme des PDI, Gruppe-III-Arsenide und -Nitride, lässt sich die Vielfalt der Forschungsprojekte nur durchführen, wenn jeweils mehr als eine Kammer zur Verfügung steht. Insgesamt sind am Institut zur Zeit elf MBE-Anlagen in Betrieb. Wenn hybride Strukturen aus unterschiedlichen Materialien hergestellt werden sollen, muss das Wachstum an derselben Probe nach einander in mehr als einer MBE-Kammer stattfinden. Um eine Verunreinigung der Grenzfläche zwischen zwei Materialien zu vermeiden, müssen diese Proben zwischen MBE-Kammern unter Ultrahochvakuumbedingungen transportiert werden. Deshalb sind einige unserer MBE-Anlagen als Cluster-Systeme konzipiert. Alternativ verwenden wir kleine mobile Ultrahochvakuumkammern, um den Probentransfer zwischen MBE-Kammern zu gewährleisten.

Als experimentelle Besonderheit stehen dem PDI drei spezielle MBE-Anlagen zur Verfügung, die In-situ-Studien der Wachstumsprozesse mittels Röntgenbeugung in Echtzeit ermöglichen. Hierfür können die Kammern mit unserem eigenen Strahlrohr am Synchrotron BESSY II (Helmholtz-Zentrum Berlin für Materialien und Energie) verbunden werden. Der erfolgreiche Betrieb eines derartigen Aufbaus hängt wesentlich vom kontinuierlichen, stationären Einsatz der MBE-Anlage am Synchrotron ab. Infolgedessen befindet sich mindestens eine dieser speziellen MBE-Anlagen stets am Synchrotron. Zur Zeit wird dort eine MBE-Anlage betrieben, die für die Analyse halbleitender Oxide eingerichtet ist.

Department of Semiconductor Spectroscopy

Abteilung für Halbleiterspektroskopie

Head of Department: Prof. Dr. Holger T. Grahn, htgrahn@pdi-berlin.de

The overall competence of this research department lies in the physics and applications of semiconductor hetero- and nano-structures, in particular with regard to their electronic and optical characteristics. Dedicated spectroscopic and magneto-transport techniques are used to investigate their electronic, optical, and transport properties. The research topics include the investigation of elementary excitations in solids controlled by surface acoustic waves, the optical properties of III-V nanowires and heterostructures, terahertz quantum-cascade lasers, spin injection from ferromagnets into semiconductors, quantum transport in semiconductor-based nanoscale systems, and topological insulators.

Elementary excitations in solids such as photons, electrons, and spins are investigated and controlled by surface acoustic waves. These elementary excitations can be manipulated at gigahertz frequencies opening new perspectives for applications in optoelectronic devices. The optical properties of III-V nanowires and heterostructures are investigated by spatially and time-resolved photoluminescence spectroscopy as well as by cathodoluminescence spectroscopy in a scanning electron microscope. The correlation between structural defects and optical properties in III-V nanowires is of particular importance. Quantum-cascade lasers for the terahertz spectral region are designed, their optical as well as transport properties are simulated, complete lasers are realized, and their lasing properties are investigated. These lasers are compact sources, can be operated in single mode, exhibit typical optical output powers between several mW and several tens of mW, and function at temperatures, which do not require cooling with liquid helium. The injection of spins

Die übergreifende Kompetenz dieser Forschungsabteilung liegt in der Physik und den Anwendungen von Hetero- und Nanostrukturen aus Halbleitern, insbesondere bezüglich ihrer elektronischen und optischen Charakteristika. Deziidierte spektroskopische und Magnetotransport-Methoden werden zur Untersuchung der elektronischen, optischen und Transport-Eigenschaften verwendet. Die Forschungsthemen umfassen Elementaranregungen in Festkörpern kontrolliert durch akustische Oberflächenwellen, die optischen Eigenschaften von III-V-Nanodrähten und -Heterostrukturen, Terahertz-Quantenkaskadenlaser, Spininjektion aus Ferromagneten in Halbleiter, Quantentransport in auf Halbleitern basierenden nanoskaligen Systemen und topologische Isolatoren.

Elementaranregungen in Festkörpern wie Photonen, Elektronen und Spins werden spektroskopisch untersucht und durch akustische Oberflächenwellen kontrolliert. Die Möglichkeit, diese Elementaranregungen bei Gigahertz-Frequenzen zu manipulieren, eröffnet neue Perspektiven für Anwendungen in optoelektronischen Bauelementen. Die optischen Eigenschaften von III-V-Nanodrähten und -Heterostrukturen werden mit räumlich und zeitlich aufgelöster Photolumineszenz-Spektroskopie sowie Kathodolumineszenz-Spektroskopie in einem Raster-elektronenmikroskop untersucht. Die Korrelation von strukturellen Defekten mit den optischen Eigenschaften von III-V-Nanodrähten ist von besonderer Bedeutung. Quantenkaskadenlaser werden für den Terahertz-Spektralbereich entwickelt. Deren op-



from a ferromagnet into a semiconductor is studied using ferromagnet-semiconductor hybrid structures by looking at their magneto-optical and magneto-transport properties. In order to achieve spin control, all-electrical spin injection and detection are investigated using lateral spin transport devices. The electronic and spin properties of semiconductor-based nanoscale systems such as nanowires and quantum dots defined laterally in heterostructures are studied by quantum transport experiments with the aim of developing new strategies for information processing. Finally, the electronic transport properties of topological insulators, in which charges are only transported on the surface and not in the bulk, are examined by studying the weak antilocalization effect due to spin orbit coupling and the electron-electron interaction.

The facilities for optical spectroscopy include Raman spectroscopy to study the vibrational modes in semiconductor films, heterostructures, and nanowires as well as in topological insulators and graphene. Continuous-wave photoluminescence and photoluminescence excitation spectroscopy from the ultraviolet (325 nm) to the near-infrared spectral region (1.7 μm) are used to investigate III-V films, heterostructures, and nanowires. The spectroscopic techniques for the near-infrared to ultraviolet spectral regions such as Raman and photoluminescence spectroscopy can also be used with a spatial resolution down to about 0.5 μm and in magnetic fields up to 8 T. Furthermore, using cathodoluminescence spectroscopy and imaging in a scanning electron microscope, the spatial resolution can be enhanced into the range of ten nanometers. In addition, element identification is achieved by energy- and wavelength-dispersive x-ray spectroscopy, and the crystallographic orientation as well as the strain state can be determined using electron backscatter diffraction. Time-resolved photoluminescence spectroscopy on a pico- to microsecond time scale from the

tische und Transport-Eigenschaften werden berechnet sowie gemessen und es werden vollständige Bauelemente realisiert. Diese Quantenkaskadenlaser sind kompakte Quellen, erlauben Einzelmodenbetrieb, besitzen typische optische Ausgangsleistungen zwischen einigen mW und einigen zehn mW, und funktionieren bei Temperaturen, die keine Kühlung mit flüssigem Helium erfordern. Die Injektion von Spins aus einem Ferromagneten in einen Halbleiter wird an Ferromagnet-Halbleiter-Hybridstrukturen untersucht, indem ihre magneto-optischen und Magnetotransport-Eigenschaften gemessen werden. Ein Ziel ist es, Kontrolle über Spins in einem Halbleiter zu erhalten. Hierfür werden die rein elektrische Spin-injektion und -detektion mit lateralen Spin-transport-Bauelementen untersucht. Die elektronischen und Spin-Eigenschaften von auf Halbleitern basierenden nanoskaligen Systemen wie beispielsweise Nanodrähte und Quantenpunkte, die lateral in Heterostrukturen definiert sind, werden mittels Quantentransportexperimenten für die Entwicklung neuer Strategien in der Informationsverarbeitung untersucht. Schließlich werden die elektronischen Transport-eigenschaften von topologischen Isolatoren studiert, in denen Ladungsträger nur an der Oberfläche und nicht im Volumen transpor-tiert werden.

Im Bereich der spektroskopischen Messme-thoden steht uns die Ramanspektroskopie für Untersuchungen der Schwingungsmoden in Halbleiterschichten, Heterostruktu-ren, Nanodrähten, topologischen Isolatoren und Graphen zur Verfügung. Darüber hin-aus werden Halbleiterschichten, Heterostrukturen und Nanodrähte mittels Photolumineszenz- und Photolumineszenzan-regungs-Spektroskopie vom ultravioletten (325 nm) bis zum nahen infraroten (1,7 μm) Spektralbereich untersucht. Diese Metho-den können mit einer räumlichen Auflösung von bis zu 0,5 μm und in Magnetfeldern von bis zu 8 T eingesetzt werden. Kathodolu-mineszenz-Spektroskopie in Kombination mit den Abbildungsmöglichkeiten eines

ultraviolet (240 nm) to the near-infrared spectral region (1.3 μm) and pump-and-probe spectroscopy with a subpicosecond time resolution are employed to investigate the carrier and polarization dynamics in III-V films, heterostructures, and nanowires. Fourier-transform spectroscopy is used in the far-infrared spectral region to record the lasing parameters of terahertz quantum-cascade lasers and in the mid-infrared region to study vibrational modes. The magneto-transport experiments on ferromagnet-semiconductor hybrid devices, semiconductor-based nanoscale systems, and topological insulators can be performed in magnetic fields up to 16 T and at temperatures down to 50 mK.

In 2017, the electrical generation of surface acoustic waves on doped semiconductor substrates using piezoelectric ZnO films sputtered onto evaporated thin metal layers has been demonstrated. With this technique, the active layers for the surface acoustic waves can be placed close to doped layers, expanding the application range of surface acoustic waves in semiconductor devices. Acoustic transport of electrons and holes along a group-III-arsenide nanowire induced by surface acoustic waves can inject electric charges into an ensemble of quantum dot-like recombination centers that are spatially separated from the optical excitation area. The respective results are relevant for the dynamic control of single-photon emission in III-V semiconductor heterostructures.

The radiative and nonradiative recombination processes in planar (In,Ga)N/GaN(0001) quantum wells and (In,Ga)N quantum disks embedded in GaN(000 $\bar{1}$) nanowires have been investigated using photoluminescence spectroscopy under both, continuous-wave and pulsed, excitation. The results reveal that even dominant nonradiative recombination conserves the power-law decay. The luminous efficiency of ordered arrays of GaN nanowires with well-defined diameters, representing

Rasterelektronenmikroskops erreicht eine Ortsauflösung bis in den Bereich von zehn Nanometern. Hinzu kommt die Möglichkeit, chemische Elemente durch energie- und wellenlängendiffusive Röntgenspektroskopie zu identifizieren. Mit Hilfe der Elektronenrückstreuung erhalten wir Informationen über die kristallographische Orientierung sowie Verspannungen im Material. Zeitaufgelöste Photolumineszenz-Spektroskopie auf einer Zeitskala von Piko- bis Mikrosekunden vom ultravioletten (240 nm) bis zum nahen infraroten (1,3 μm) Spektralbereich und Anrege-Abtast-Spektroskopie mit einer Zeitauflösung unterhalb einer Pikosekunde werden eingesetzt, um die Ladungsträger- und Polarisationsdynamik in III-V-Schichten, -Heterostrukturen und -Nanodrähten zu untersuchen. Mittels Fouriertransform-Spektroskopie werden im ferninfraroten Spektralbereich die Emissionseigenschaften von Terahertz-Quantenkaskadenlasern und im mittleren infraroten Spektralbereich Schwingungsmoden untersucht. Die Magneto-transport-Experimente an Ferromagnet-Halbleiter-Hybrid-Bauelementen, auf Halbleitern basierenden nanoskaligen Systemen und topologischen Isolatoren können in Magnetfeldern bis zu 16 T und Temperaturen bis herunter zu 50 mK durchgeführt werden.

Im Jahr 2017 haben wir die elektrische Erzeugung von akustischen Oberflächenwellen auf dotierten Substraten unter Verwendung von piezoelektrischen ZnO-Filmen, die auf aufgedampfte dünne metallische Schichten gesputtert wurden, nachgewiesen. Mit diesem Verfahren können die aktiven Schichten von akustischen Oberflächenwellen in unmittelbarer Nähe von dotierten Schichten realisiert werden, was den Anwendungsbereich für die akustischen Oberflächenwellen in Halbleiterbauelementen erweitert. Akustischer Transport von Elektronen und Löchern entlang eines Gruppe-III-Arsenid-Nanodrahtes – angeregt durch akustische Oberflächenwellen – kann zur Injektion von elektrischen Ladungen in ein Ensemble von Quantenpunkt-artigen Rekombinationszentren, die räumlich von dem optischen An-

the building blocks for light-emitting as well as light-detecting devices integrated on Si substrates, decreases by more than one order of magnitude when the nanowire diameter is increased from 120 to 240 nm. A detailed analysis of both, steady-state and transient photoluminescence data, reveals that this quenching is not caused by a corresponding decrease of the internal quantum efficiency. By examining the coupling of light into and out of the nanowire by numerical simulations, the change in absorbance is shown to be minor in the investigated diameter range, while the extraction efficiency for thin nanowires is enhanced by an order of magnitude as compared to thick nanowires.

The photoluminescence properties of InAs quantum dots grown by molecular beam epitaxy on GaAs(110) using Bi as a surfactant reveal that the quantum dot photoluminescence intensity is linearly polarized and biexcitons with positive as well as negative binding energies are observed, two findings that we associate with the strain in the (110) plane. This strain leads to piezoelectric fields and to a strong mixing between heavy- and light-hole states. Using secondary electrons in a scanning electron microscope, crystal twinning along the axis of GaAs and GaAs/(Al,Ga)As core/shell nanowires can be imaged with a spatial resolution of 10 nm. These experiments show that, based on commonly available scanning electron microscopy methods, an overview of the structural properties along an entire nanowire and their impact on the spectral and spatial luminescence distribution can be efficiently obtained providing a quick feedback for the optimization of the growth conditions. The electronic properties of GaAs nanowires composed of both, the zincblende and wurtzite modifications, have been studied using a ten-band $k\cdot p$ model. In the wurtzite phase, two energetically close conduction bands are of importance for the confinement and the energy levels of the electron ground state. The coexistence of two conduction bands together with their

regungsbereich getrennt sind, führen. Die entsprechenden Resultate sind für die dynamische Kontrolle von Einzel-Photonen-Emission in III-V-Halbleiterheterostrukturen von Bedeutung.

Die strahlenden und nichtstrahlenden Rekombinationsprozesse in planaren $(In,Ga)N/GaN(0001)$ -Quantenfilmen und $(In,Ga)N$ -Quantenscheiben, die in $GaN(000\bar{1})$ -Nanodrähten eingebettet sind, wurden mittels Photolumineszenz-Spektroskopie sowohl unter Anregung im Dauerstrichbetrieb als auch unter gepulster Anregung untersucht. Die Resultate zeigen, dass sogar die vorherrschende nichtstrahlende Rekombination den einem Potenzgesetz folgenden Zerfall. Die Lichteffizienz von geordneten Feldern von GaN -Nanodrähten mit wohldefinierten Durchmessern, die als Bausteine sowohl für lichtemittierende als auch lichtdetektierende Bauelemente integriert auf Si-Substraten dienen können, nimmt um mehr als eine Größenordnung ab, wenn der Nanodrahtdurchmesser von 120 auf 240 nm vergrößert wird. Eine detaillierte Analyse von sowohl stationären als auch transiентen Photolumineszenzdaten zeigt, dass diese Reduktion nicht durch einen entsprechenden Rückgang der internen Quanteneffizienz hervorgerufen wird. Durch die Untersuchung der Kopplung von Licht in den und aus dem Nanodraht mit Hilfe von numerischen Simulationen konnte gezeigt werden, dass die Änderung des Absorptionsgrades in dem untersuchten Durchmesserbereich gering ist, während die Extraktionseffizienz für dünne Nanodrähte im Vergleich zu dicken Nanodrähten um eine Größenordnung erhöht ist.

Die Photolumineszenzeigenschaften von InAs-Quantenpunkten, die mittels Molekularstrahlepitaxie auf GaAs(110) unter Verwendung von Bi als Surfactant gewachsen werden, weisen eine lineare Polarisation der Quantenpunkt-Photolumineszenztensität auf. Gleichzeitig werden Biexcitonen sowohl mit positiver als auch negativer Bindungsenergie beobachtet. Beide Ergebnisse

opposite strain dependence results in rather complex electronic and optical properties of GaAs polytype nanostructures.

Single-mode emission of terahertz quantum-cascade lasers with a side-mode suppression ratio better than -25 dB has been achieved by realizing a two-section cavity laser in a post-processing step using a focused ion beam. By illuminating the rear facet of the quantum-cascade laser with a fiber-coupled light source emitting at 777 nm, the emission frequency can be tuned by 5 and 12 GHz under continuous-wave and pulsed operation, respectively. Multi-mode quantum-cascade lasers at about 4.7 THz operated with a fast ramped injection current, which leads to a collective tuning of equally-spaced Fabry-Pérot laser modes exceeding their separation, can be used for a continuous coverage of the emission spectrum over 72 GHz. This terahertz source is superior to conventional thermal sources used in Fourier-transform infrared spectroscopy in terms of signal-to-noise ratio as well as dynamic range by one to two orders of magnitude.

Axiotaxy, a new type of texture in thin films, has been observed in growing films of the thermoelectric and topological-insulator material Bi_2Te_3 on $\text{InP}(111)\text{B}$ by hot wall epitaxy. In addition to the usual epitaxial component, for which the (0001) plane of Bi_2Te_3 is parallel to the (111) plane of InP , fiber textures led by the $\text{Bi}_2\text{Te}_3(11\bar{2}0)$ plane emerge. The corresponding fiber axes are aligned to the $\langle 11\bar{1} \rangle$ and $\langle 77\bar{2} \rangle$ directions of InP . Diffuse boundary reflection of electrons in the presence of a magnetic field is demonstrated to induce a rectification effect in circular-shaped ballistic nanochannels. The unambiguous identification of the origin of the current based on the antisymmetric magnetic-field dependence reveals that the rectification effect is sensitive to the extent that extraction of electrical energy out of environmental non-equilibrium noise is achieved.

nisse werden mit der Verspannung in der (110) -Ebene in Verbindung gebracht. Diese Verspannung führt zu piezoelektrischen Feldern und zu einer starken Vermischung von Zuständen schwerer und leichter Löcher. Mit Hilfe von Sekundärelektronen in einem Rasterelektronenmikroskop ist es möglich, die Zwillingsbildung entlang der Achse von GaAs-Nanodrähten und Nanodrähten mit einem GaAs-Kern und einer $(\text{Al},\text{Ga})\text{As}$ -Schale mit einer räumlichen Auflösung von 10 nm abzubilden. Diese Experimente zeigen, dass auf der Grundlage von üblicherweise zur Verfügung stehenden raster-elektronenmikroskopischen Methoden sehr effizient ein Überblick über die strukturellen Eigenschaften entlang eines kompletten Nanodrahts und deren Auswirkung auf die spektrale und räumliche Lumineszenzverteilung unter der Voraussetzung einer schnellen Rückkopplung für die Optimierung der Wachstumsbedingungen gewonnen werden kann. Die elektronischen Eigenschaften von GaAs-Nanodrähten, die sowohl aus der Zinkblende- als auch aus der Wurtzit-Phase bestehen, wurden mittels eines Zehn-Band- $k \cdot p$ -Modells untersucht. In der Wurtzit-Phase sind zwei energetisch nahe beieinander liegende Leitungsbänder für das Confinement und die Energieniveaus des Elektronengrundzustandes von Bedeutung. Die Koexistenz zweier Leitungsbänder zusammen mit deren gegensätzlicher Verspannungsabhängigkeit führt zu recht komplexen elektronischen und optischen Eigenschaften von polytypen GaAs-Nanostrukturen.

Einzelmodenemission von Terahertz-Quantenkaskadenlasern mit einer Nebenmodenunterdrückung von mehr als -25 dB konnte durch die Realisierung eines Lasers mit zwei Sektionen, der mit Hilfe von fokussierten Ionenstrahlen nachbearbeitet wurde, erreicht werden. Durch Beleuchtung der Rückfacette des Quantenkaskadenlasers mit einer fasergekoppelten Lichtquelle, die bei 777 nm emittiert, konnte die Emissionsfrequenz über 5 bzw. 12 GHz im Dauerstrich- bzw. gepulsten Betrieb abgestimmt werden. Wenn

Mehrmoden-Quantenkaskadenlaser bei ca. 4,7 THz mit einem schnellen, linear anwachsenden Injektionsstrom betrieben werden, können die abstandsgleichen Fabry-Pérot-Lasermoden im Verbund über mehr als den Modenabstand verschoben werden, so dass eine kontinuierliche Abdeckung des Emissionsspektrums über 72 GHz erreicht werden kann. Diese Terahertzquelle ist konventionellen thermischen Quellen, die in der Fouriertransform-Infrarotspektroskopie eingesetzt werden, sowohl im Signal-Rausch-Verhältnis als auch im dynamischen Bereich um ein bis zwei Größenordnungen überlegen.

Axiotaxie, eine neue Art von Textur in dünnen Filmen, wurde in mit *hot wall epitaxy* gewachsenen Filmen aus dem thermoelektrischen und Topologischen-Isolator-Material Bi_2Te_3 auf InP(111)B beobachtet. Zusätzlich zu den üblichen epitaktischen Komponenten, für die die (0001)-Ebene von Bi_2Te_3 parallel zu der (111)-Ebene von InP ist, treten Fasertexturen, die durch die $\text{Bi}_2\text{Te}_3(\bar{1}\bar{1}20)$ -Ebene geführt werden, auf. Die entsprechenden Faserachsen sind entlang der $\langle 1\bar{1}\bar{1} \rangle$ - und $\langle 7\bar{7}\bar{2} \rangle$ -Richtungen von InP ausgerichtet. Die Reflektion von Elektronen an unscharfen Grenzflächen in Anwesenheit eines magnetischen Feldes führt zu einem Gleichrichtungseffekt in kreisförmigen ballistischen Nanokanälen. Die eindeutige Identifizierung des Ursprungs des Stromes basierend auf der antisymmetrischen Magnetfeld-Abhängigkeit zeigt, dass der Gleichrichtungseffekt eine Empfindlichkeit für die Gewinnung von elektrischer Energie aus dem umgebenden Nichtgleichgewichtsrauschen aufweist.

Department of Microstructure

Abteilung für Mikrostruktur

Head of Department: Dr. Achim Trampert, trampert@pdi-berlin.de

The major research goal of the department Microstructure is to understand material properties on the basis of detailed knowledge of their microstructure. Here the term "microstructure" in the broadest sense includes all kinds of defects, i.e. all deviations from the regular structure, and their geometry and physical configuration—regardless of length scales. The probe volume detecting these features must therefore range from the macroscopic scale to the single atom level. Consequently, advanced X-ray and electron diffraction techniques, transmission electron microscopy imaging and spectroscopy as well as scanning tunneling microscopy and spectroscopy are applied with high spatial resolution and high sensitivity to analyze quantitatively the structural, chemical and electronic properties of the wide range of material systems grown at PDI or by external collaborators. Examples are low-dimensional semiconductor systems, heterostructures, ferromagnet-semiconductor hybrid structures, and metastable materials and material combinations. Experimental results on hetero-phase interfaces and phase stability, epitaxial strain relaxation processes and the formation of extended and complex defects, and artificial nanostructures are compared with computer simulations and supported by theoretical modeling. Finite Element calculations can virtually cover any non-trivial geometry and chemical composition profile of low-dimensional structures and may thereby provide a highly realistic view of elastic strain relaxation and piezoelectric polarization fields within heteroepitaxial systems.

Transmission electron microscopy (TEM) is one of the key tools for direct imaging of the local atomic structure of materials. An

Das Ziel der Abteilung Mikrostruktur liegt darin, Materialeigenschaften auf der Basis einer detaillierten Kenntnis ihrer Mikrostruktur zu verstehen. Hierbei werden als „Mikrostruktur“ alle Arten von Defekten in Kristallen, also alle Abweichungen von der regelmäßigen Struktur, deren Geometrie und physikalischen Konfiguration unabhängig von der Längenskala verstanden. Das Volumen, innerhalb dessen die Struktur detektiert wird, muss infolgedessen den gesamten Bereich von makroskopischen Dimensionen über die Nanometerskala bis zur Ebene einzelner Atome abdecken. Dementsprechend werden Röntgen- und Elektronenbeugungstechniken, abbildende und spektroskopische Transmissionselektronenmikroskopie sowie Rastertunnelmikroskopie jeweils mit hoher räumlicher Auflösung und Empfindlichkeit eingesetzt, um die strukturellen, elektronischen und chemischen Eigenschaften einer großen Vielfalt von Materialsystemen quantitativ zu untersuchen, die am PDI oder von externen Kooperationspartnern hergestellt werden. Beispiele für untersuchte Materialien sind niedrig-dimensionale Halbleiterstrukturen, Heterostrukturen, Ferromagnet-Halbleiter Hybridstrukturen sowie metastabile Materialien und Materialkombinationen. Experimentelle Ergebnisse zu Phasengrenzflächen und zur Phasenstabilität, zu Relaxationsmechanismen der Gitterfehlانpassung und zur Entstehung ausgedehnter und komplexer Defekte, sowie zu künstlichen Nanostrukturen werden mit Computersimulationen verglichen und die Interpretationen durch theoretische Modelle untermauert. Aufgrund ihrer universellen Möglichkeiten bei der Simulation sehr realitätsnaher Modelle mit nicht-trivialer Geometrie und chemischer



important supplement is the high-angle annular dark-field (HAADF) detector in a scanning TEM, which is used for chemical sensitive Z-contrast imaging with atomic resolution. Electron energy-loss spectroscopy and the recently acquired energy dispersive x-ray spectroscopy complete the analytical performance of our microscopes in the field of chemical bonding and composition, and allow two-dimensional mappings.

As one of our strengths high-resolution and analytical TEM is used to quantitatively determine the structural roughness of semiconductor heterostructure interfaces and their chemical intermixing. In particular, we are able to analyze the composition profiles of planar interfaces up to the atomic level. Moreover, there is an attempt to correlate the interface property with the physical functionality of the heterostructure. Examples are here the investigations of ultra-thin (Al,Ga)As/GaAs interface profiles in quantum cascade laser structures or of Ga(Sb,Bi)/GaSb quantum wells in infrared laser diodes. On the other hand, the atomic configurations—atom position and type—at coherent interfaces between dissimilar materials or in nano-sized clusters are analyzed on the basis of (scanning) TEM in combination with image contrast simulations. Further examples comprise the interface character in three-dimensional core/shell or axial heterojunction nanowires and epitaxial interfaces in van der Waals heterostructures such as graphene on SiC or sapphire.

In parallel to our scientific research on specific materials issues, we continually refine and develop our experimental methods per se. In the recent years, we have implemented electron tomography, a technique for obtaining three-dimensional object reconstructions of complex structures and nano-scale materials. Essential condition for this purpose is the tomography sample preparation using the focused ion beam technique. Results on the three-dimension-

Komposition kommt der Methode der Finiten Elemente hierbei eine Schlüsselrolle zu. Als numerisches Pendant zu rein analytischen Ansätzen liefert diese quantitativ, räumlich aufgelöst Deformations- und Spannungstensoren in realen Objekten sowie, für heteroepitaktische Systeme mit fehlender Inversionssymmetrie, ein dreidimensionales Bild der piezoelektrischen Polarisierung.

Die Transmissionselektronenmikroskopie (TEM) ist eines der zentralen Werkzeuge, um die lokale atomare Struktur von Materialien abzubilden. Eine wesentliche Erweiterung im Raster-TEM-Betrieb ist der Weitwinkel-Dunkelfeld-Detektor (HAADF, high-angle annular dark-field), der eine chemisch sensitive Z-Kontrast Abbildung mit atomarer Auflösung ermöglicht. Dazu vervollständigen die Elektronen-Energieverlustspektroskopie und die kürzlich ange schaffte energiedispersive Röntgenspektroskopie die analytische Leistungsfähigkeit unserer Mikroskope im Bereich der Messung chemischer Bindungen und Zusammensetzungen, und ermöglichen zweidimensionale Mappings der Ergebnisse.

Eine unserer besonderen Stärken liegt im Einsatz von hochauflösender und analytischer TEM, um die strukturelle Grenzflächenrauhigkeit und Durchmischung von Halbleiterheteroübergängen zu bestimmen. Insbesondere das chemische Zusammensetzungsprofil über planare Grenzflächen kann bis auf die atomare Ebene quantitativ ermittelt und modelliert werden. Darüber hinaus wird versucht, die strukturelle Grenzflächeneigenschaft direkt mit der physikalischen Funktionalität der Heterostruktur zu korrelieren. Als Beispiele dienen die jüngsten Untersuchungen der Profile von ultradünnen (Al,Ga)As/GaAs Grenzflächen in Quantenkaskadenlasern oder von Ga(Sb,Bi)/GaSb Quantentöpfen in Infrarotlaserdioden. Andererseits wird die atomare Konfiguration – das heißt, die Art und Position der Atome – an kohärenten Grenzflächen zwischen stark unter-

al morphology of complex nitride-based nanowire heterostructures including their element distributions, as well as the spatial distribution and behaviour of extended defects in planar compound semiconductor heterostructures evidence the enormous potential of the method. The final goal is to study not only the structure and morphology but also its related physical and chemical properties.

The activities are part of our newly established "**Application Laboratory Electron Tomography**". The Application Laboratory is financially supported by the European Fund for Regional Development (EFRE) and by the Senate of Berlin. At the time, a specialized laboratory is just getting rebuild to install our new cutting-edge aberration corrected microscope that will drastically increase the method performance. Objective of the laboratory is the methodically development and extensions to promote materials research, to collaborate with external partners and to utilize the tomography method to industrial applications.

Moreover, a further methodical development affects our in-situ electron microscopy of dynamic processes. Heating experiments in the microscope serve to analyze defect formation and propagation, structural phase transitions and solid-state reactions with high spatial resolution. The direct observation of atoms in real-time and their correlated motion open the opportunity for basic understanding of materials properties and functionalities. So, we succeeded in observing the high temperature solid-liquid phase transition of Ge-Sb-Te alloys at 600°C. It has been shown that the velocities of interface movements are very similar during crystallization and melting, nevertheless, the underlying dynamic processes are considerably different pointing to distinctly different atomic mechanisms at the interface.

The physical properties of ultimately small structures at solid-vacuum interfaces are

schiedlichen Materialien oder in nanoskopischen Clustern mit Hilfe von (Raster-) TEM in Kombination mit Bild-Kontrastsimulationen analysiert. Weitere Beispiele umfassen die Natur von Grenzflächen in Nanosäulen mit lateraler oder axialer Heterostruktur, oder in van-der-Waalsgebundenen Schichtsystemen wie Graphen auf SiC oder Saphir.

Parallel zu unserer Forschung zu spezifischen Materialeigenschaften, bei der ein breites Spektrum mikroskopischer Techniken als Werkzeug verwendet wird, verbessern und entwickeln wir kontinuierlich die experimentellen Methoden selbst. So haben wir die Technik der Elektronentomographie eingeführt – eine Technik, mit der man dreidimensionale Rekonstruktionen komplexer nanoskaliger Strukturen und Materialien erhalten kann. Eine wesentliche Voraussetzung dazu ist die Herstellung spezieller Tomographieproben unter Nutzung fokussierter Ionenstrahlen. Ergebnisse zur dreidimensionalen Morphologie und zur Elementverteilung in komplexen Nitrid-basierten Nanosäulen sowie zur räumlichen Verteilung und Wechselwirkung von Kristalldefekten in planaren Halbleiterheterostrukturen belegen das enorme Potential der Methode für die Materialentwicklung. Ziel ist hierbei, nicht nur die Struktur und Morphologie, sondern auch die physikalischen und chemischen Eigenschaften zu studieren und miteinander zu korrelieren. Die Arbeiten sind Bestandteil des neu gegründeten **Applikationslabors Elektronentomographie**. Das Applikationslabor wird vom Berliner Senat sowie aus Mitteln des Europäischen Fonds für regionale Entwicklungen (EFRE) gefördert. Gegenwärtig wird ein besonderes Labor für die Installation des durch Fördermittel neu angeschafften und topmodernen aberrationskorrigierten Rastertransmissionselektronenmikroskops aufgebaut, das die Leistungsfähigkeit der Elektronentomographie deutlich verbessern wird. Aufgabe dieses Applikationslabors ist es, die Methode und ihre Weiterentwicklungen in der Materialforschung und Materialentwicklung voranzutreiben, mit externen Partnern zu kooperieren und die Elektronentomogra-

explored by low-temperature scanning tunneling microscopy (LTSTM) carried out in ultrahigh vacuum and at liquid-helium temperature. Our microscopes feature a highly stable "Besocke-Beetle" type scanner design allowing us to (i) manipulate single atoms and molecules adsorbed on a surface, and (ii) probe the local density of electronic states as well as elementary excitations of individual nanostructures by scanning tunneling spectroscopy. In this way, the correlation between structure and properties of semiconductor-based nanostructures can be analyzed at the atomic scale. Starting at a base temperature of 5 K, the sample temperature can be varied in-situ up to ~100 K, enabling to study, e.g., surface diffusion at the single-atom level, as well as the competition between thermally excited and current-induced dynamics of engineered nanostructures and molecular switches linked to the semiconductor surface. One of our microscopes offers the capability to detect current-induced light emitted from the tunnel junction to combine optical spectroscopy with the spatial resolution of STM.

X-ray diffraction as a non-destructive probe can penetrate fairly thick layers and therefore allows to study beside surfaces, buried interfaces and structures inside the volume of the crystal. As a diffraction technique, it combines sub-Ångstrom resolution with a large interaction volume that provides statistically reliable structural properties. Results are analyzed quantitatively on the basis of modeling and simulation of diffraction data and complemented by electron microscopy measurements. In the x-ray laboratory of our institute the basic parameters of many grown structures are quickly obtained in order to give immediate feedback for further growth experiments.

The in-situ x-ray diffraction to investigate epitaxial layers during molecular beam epitaxy (MBE) has been established in our PHARAO facility at the synchrotron BESSY II (Helmholtz-Zentrum Berlin, HZB).

phie für industrielle Anwendungen nutzbar zu machen.

Eine weitere methodische Entwicklung betrifft unsere in-situ Elektronenmikroskopie dynamischer Prozesse. Temperaturabhängige Experimente im Mikroskop nutzen wir dazu, Defektbildung und -propagationen, strukturelle Phasenübergänge und Festkörperreaktionen an Grenzflächen mit hoher räumlicher Auflösung zu studieren. Durch die direkte Beobachtung von Atomen und deren korrelierte Bewegung in Echtzeit eröffnet sich die Möglichkeit, ein grundlegendes Verständnis von Materialverhalten und -eigenschaften zu gewinnen. So ist es 2017 gelungen, den Hochtemperaturübergang zwischen fester und flüssiger Phase von Ge-Sb-Te Verbindungen bei 600°C nanometergenau zu beobachten. Es hat sich gezeigt, dass die Geschwindigkeiten der Grenzflächenbewegung während Schmelz- bzw. Kristallisationsvorgang vergleichbar sind, sich jedoch die zugrundliegenden dynamischen Prozesse deutlich unterscheiden, was auf unterschiedliche atomare Mechanismen an der fest-flüssig Grenzfläche hinweist.

Die physikalischen Eigenschaften von kleinsten Strukturen an der Grenzfläche zwischen Festkörper und Vakuum werden mit Tieftemperatur-Rastertunnelmikroskopie untersucht. Diese Experimente finden im Ultrahochvakuum und bei Temperaturen von flüssigem Helium statt. Unsere Mikroskope sind mit einem äußerst stabilen „Besocke-Beetle“-Scanner Typ ausgestattet, der es uns ermöglicht, einzelne Atome und Moleküle, die auf einer Oberfläche adsorbiert sind, abzubilden und zu manipulieren. Ortsaufgelöste Tunnelspektroskopie-Experimente erlauben uns, die lokale elektronische Zustandsdichte auszumesen und Elementaranregungen zu untersuchen, die durch inelastische Streuung der Tunnelelektronen selbst induziert werden.

Die Kombination, einerseits Halbleiter-Nanostrukturen aus einzelnen Atomen auf-

Performed in-situ, under real growth conditions, and in real-time, our research improves the understanding of fundamental growth processes during MBE. Our work focuses on the study of epitaxial growth modes, structural analysis of interfaces and layer stacks, phase transitions, and phenomena associated with the combination of very dissimilar materials. The successful operation of such a setup critically depends on the continuous stationary operation of the MBE system at the synchrotron, since a high quality of the epitaxial layers is imperative for a reliable quantitative analysis. That is why this activity is organized in joint work with the Epitaxy department.

Besides the in-situ diagnostic at BESSY II we perform complementary x-ray diffraction measurements at the synchrotron sources PETRA III in Hamburg and ESRF in Grenoble (France). Of particular interests are newly approaching techniques like diffraction with highly focused x-rays in order to study individual low-dimensional structures. Thereby we overcome the ensemble average inherent to x-ray techniques applying millimeter-sized x-ray spots.

bauen zu können, und andererseits ihre Eigenschaften lokal zu charakterisieren, ermöglicht es uns, Korrelationen zwischen Struktur und Eigenschaften auf atomarer Skala zu studieren. Der hier experimentell erreichbare Temperaturbereich zwischen 5 K und 100 K lässt uns zum Beispiel Oberflächendiffusionsprozesse mit atomarer Auflösung studieren und ermöglicht es, die Wechselwirkung zwischen thermisch angeregter und strominduzierter Dynamik von künstlichen Nanostrukturen und molekularen Schaltern auf Halbleiteroberflächen zu untersuchen. Eines unserer Mikroskope bietet die Möglichkeit, strominduziertes Licht, das im Tunnelkontakt erzeugt wird, zu detektieren, um so optische Spektroskopie mit ortsaufgelöster Rastertunnelmikroskopie zu verbinden.

Röntgenbeugung ist eine zerstörungsfreie Methode zur Strukturaufklärung mit relativ großer Eindringtiefe. Sie ermöglicht somit neben dem Studium von Oberflächen auch Untersuchungen von Grenzflächen und Strukturen innerhalb des kristallinen Materials. Als Beugungstechnik verbindet sie sub-Ångström Auflösung mit einem großen Wechselwirkungsvolumen, wodurch Materialeigenschaften mit statistischer Zuverlässigkeit zu bestimmt werden können. Ergebnisse werden mittels Modellierung und Simulation der Beugungsdaten quantitativ ausgewertet und durch elektronenmikroskopische Messungen komplettiert. In unserem Röntgenlabor können die wesentlichen strukturellen Parameter sehr schnell bestimmt werden, um so unmittelbare Rückkopplung für die Wachstumsexperimente zu geben.

In-situ Röntgenbeugung wurde an unserem PHARAO Experiment am Synchrotron BESSY II (Helmholtz Zentrum Berlin, HZB) etabliert, um epitaktische Schichten bereits während des Wachstums mittels Molekularstrahlepitaxie zu untersuchen. Da diese Experimente in-situ, bei realen Wachstumsbedingungen und in Echtzeit durchgeführt werden können, vertiefen

wir hiermit unser Verständnis der fundamentalen Wachstumsprozesse. Unsere Untersuchungen konzentrieren wir hierbei auf epitaktische Wachstumsformen, die strukturelle Analyse von Grenzflächen und Schichtstrukturen, auf Phasenübergänge und Phänomene, die bei der Kombination von stark unterschiedlichen Materialien auftreten. Der erfolgreiche Betrieb eines solch komplexen experimentellen Aufbaus hängt wesentlich vom durchgängigen, stationären Betrieb des Epitaxie-Systems am Synchrotron ab, da die hohe strukturelle Qualität der Schichten Grundvoraussetzung für die quantitative Analyse ist. Die Aktivität wird gemeinsam mit der Abteilung Epitaxie betrieben.

Unsere Untersuchungen bei BESSY werden durch Messungen an den Synchrotronquellen PETRA III in Hamburg und ESRF in Grenoble ergänzt. Insbesondere für die Untersuchungen von Nanostrukturen ist die Nutzung hochfokussierter Röntgenstrahlung interessant, um einzelne niedrig-dimensionale Strukturen zu untersuchen. Dabei ergänzen wir die bisher für die Röntgenmethoden typische Ensemblemittelung durch Anwendung extrem kleiner Röntgenspots.

Department of Technology and Transfer

Abteilung für Technologie und Transfer

Head of Department: Dr. Carsten Hucho, hucho@pdi-berlin.de

Research activities at PDI rely on a support infrastructure that ranges from services such as building equipment, appliances, utilities management and the machine shop over cleanroom operation and semiconductor technology to administration of human resources, and finances to transfer of know-how and intellectual property.

This wide range of activities is arranged in four sections, which will be described in more detail below: I Utilities Management, II Semiconductor Technology, III Administration, IV Knowledge Transfer.

I Utilities Management

PDI is tenant in a building administered by Humboldt-Universität (HU). While the central services are provided by HU, the special infrastructural needs of a materials science institute are coordinated within this department. This comprises the supply with technical gases (especially liquid Helium for temperature-dependent experiments and liquid Nitrogen as a coolant for MBE-systems), electricity, the data- and communication-infrastructure, the operation of clean-rooms and chemistry labs and air-conditioning as well as cooling systems of the research laboratories.

II Semiconductor Technology

Most materials that are grown in the epitaxy department need further processing for subsequent scientific investigations. Our technologists provide structuring on sub-micrometer scales and processes like metallization and contacting, cutting of wafers, prepatternning, cleaning and elec-

Die Forschungsaktivitäten des PDI werden durch eine Infrastruktur unterstützt, die von Haustechnik über Wartung, die feinmechanische Werkstatt und den Betrieb von Reinräumen bis zur Personalverwaltung, Einkauf und Finanzen und den Transfer von Wissen und Intellectual Property reicht.



Dieses breite Spektrum an Aktivitäten kann in vier Bereiche zusammengefasst werden: I Haustechnik, II Halbleiter-Technologie, III Verwaltung, IV Wissenstransfer.

I Haustechnik

Das PDI ist Nutzer eines Gebäudes, das von der Humboldt-Universität verwaltet wird. Während zentrale Dienste (Strom, Heizung, Wasser) durch die HU sichergestellt werden, werden die spezielleren Infrastrukturbedürfnisse eines materialwissenschaftlichen Instituts innerhalb der Abteilung Technologie und Transfer koordiniert.

Dies umfasst neben der Versorgung mit Spezialgasen (wie Helium für temperaturabhängige Experimente und flüssigem Stickstoff für MBE-Systeme), Strom, die Daten- und Kommunikations-Infrastruktur, den Betrieb der Reinräume und Chemielabore und Klima und Gerätekühlung für die Labore.

II Halbleiter-Technologie

Die meisten Materialien, die in der Abteilung Epitaxie gewachsen werden, benötigen eine weitere Prozessierung für anschließende wis-

trical characterization of processed structures. The semiconductor technology group operates clean rooms with facilities for the whole process of photolithography (mask-design, mask-writing, exposing and developing) which is employed to prepare the samples for subsequent selective metallization or overgrowth (with, e.g., piezoelectric material), wet and dry etching, sputtering and thermal evaporation. The rather limited resolution of photolithography is offset by its high flexibility and extended by electron-beam lithography. Photolithography can be used for rapid prototyping as well as for small series.

The wet chemical etching and the dry etching capabilities are optimized for the materials prepared within the epitaxy department and are constantly developed further.

III Administration

The administration of PDI relies on the backbone of the central administration of Forschungsverbund Berlin e.V. (FVB). All legally binding processes like salaries, work-contracts, purchase-orders, the administration of travel, etc. are administered at FVB. At the institute a small number of specially trained administrative staff provide an interface between research and administration, supervised by the scientific administrative coordinator.

This interfacing-approach is set up to free scientist from administrative burden as much as possible while at the same time translating their needs for the professional administration at FVB and reconciling the sometimes complex administrative needs with the reality of rapidly developing research activities, involving strategic changes, unforeseeable developments, and international staff with varying bureaucratic necessities but also the need for practical, personal support. This warrants that administration of the institute is a service to the scientists and that administration of resources is not misunderstood as administrating science.

senschaftliche Untersuchungen – zum Beispiel Vereinzen von Wafern, Strukturierungen, Metallisierung und das Überwachsen mit Schichten außerhalb der MBE, elektrische und strukturelle Charakterisierungen, etc. Unsere Technologie ermöglicht laterale Strukturierungen auf der sub-Mikrometer-Skala mittels konventioneller optischer Lithographie und Elektronenstrahllithographie und stellt Verfahren für die Metallisierung, Kontaktierung, das Vereinzen, Reinigen und einfache elektrische Charakterisierungen zur Verfügung. Die Halbleiter Technologie verfügt über einen Reinraum mit einer Prozessstrecke für Photo- und Elektronenstrahllithographie (vom Maskentwurf und -schreiben über Belichtung und Entwicklung bis zum Ätzen und Beschichten). Hierbei stehen nasschemische Ätzverfahren und Trockenätzverfahren sowie Sputteranlagen und Anlagen für das thermische Verdampfen von Metallen zur Verfügung.

Die Ätzverfahren werden auf die Materialien angepasst, die in der Abteilung Epitaxie hergestellt werden und werden ständig weiterentwickelt.

III Verwaltung

Die Verwaltung des PDI baut auf die zentrale Verwaltung des Forschungsverbund Berlin e.V. (FVB) auf, dem gemeinsamen Träger von acht Instituten. Alle rechtlich bindenden Prozesse wie die Zahlbarmachung von Gehältern, Arbeitsverträge, Beschaffungsaufträge, die Verwaltung und Abrechnung von Dienstreisen etc. werden zentral im FVB verwaltet. Diese Verwaltung wird durch eine kleine Zahl besonders geschulter administrativer Mitarbeiterinnen und Mitarbeiter und einen wissenschaftlich-administrativen Koordinator am Institut ergänzt, die eine Schnittstelle zwischen Forschung und Verwaltung darstellen.

In jedem Fall wird die Verwaltung als Dienstleistung für den Wissenschaftsbetrieb gesehen und darauf geachtet, dass

IV Knowledge Transfer

The simplistic approach to ask for proof of practicability or usability of research results—especially from institutes doing 'hard' science—is recently being substituted by a deeper understanding of the necessities of transferring knowledge into society. Rather than proving short-term applicability of our research results, our understanding of transfer ranges from informing the public about nanotechnology and materials science at large (involving public relations, developing concepts for science-communication and -visualization), providing expertise to industry, education and politics, to tracing, securing and making available intellectual property—be it in the frame of open source arrangements, licensing or marketing of patents.

The engagement of our technology transfer manager has in recent years lead to a considerable professionalization of the transfer activities. Besides the development of transfer-concepts and the definition of internal processes, the idea of technology transfer of PDI is being discussed within Leibniz-Gemeinschaft and in an increasing network of technology transfer professionals. The Head of the Technology and Transfer department is speaker of the workgroup Knowledgetransfer of Leibniz-Gemeinschaft and member of the group initiated by the president defining the guidelines for knowledge-transfer.

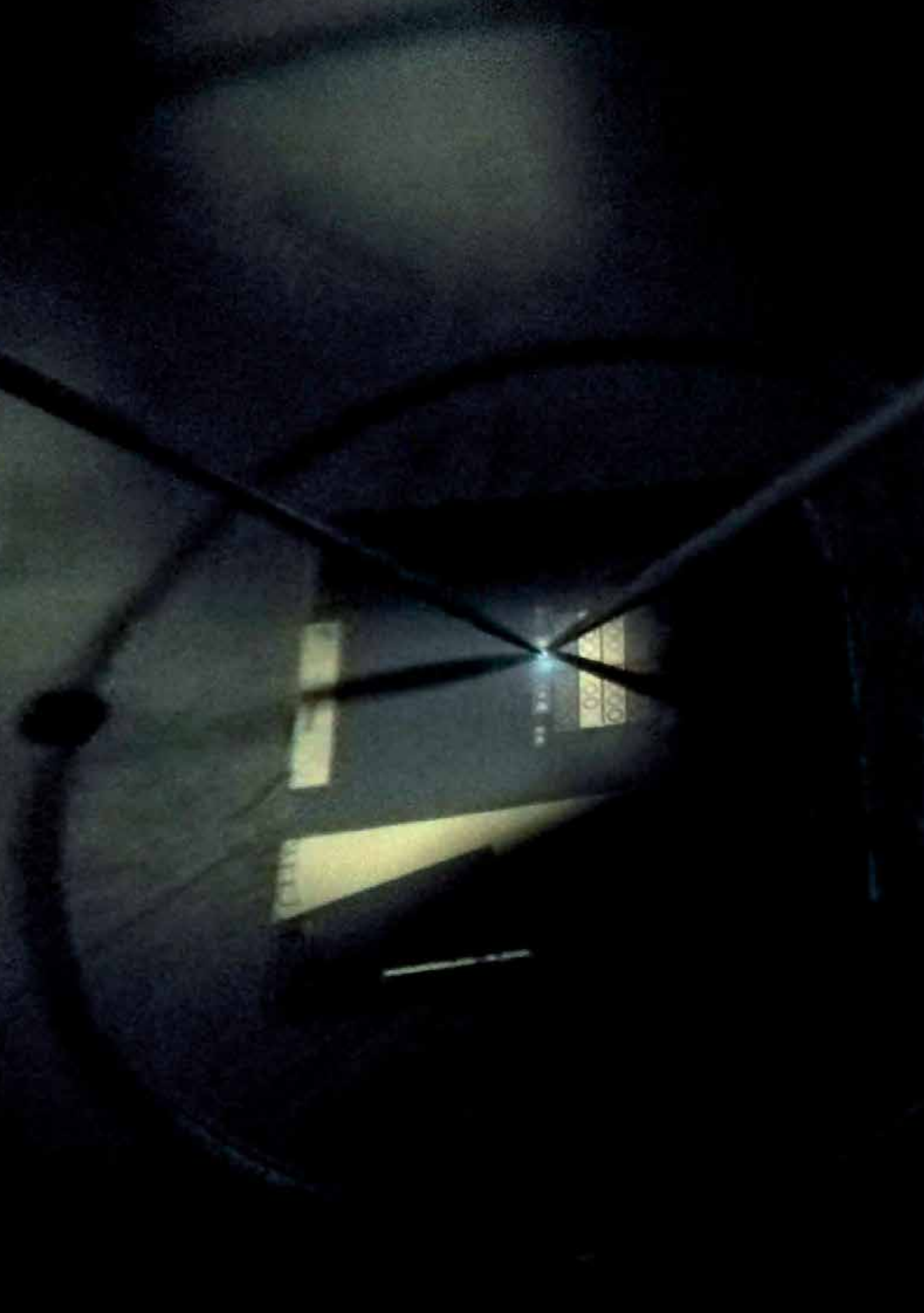
die Verwaltung von Ressourcen nicht mit der Verwaltung von Wissenschaft verwechselt wird.

IV Wissenstransfer

Wissenschaft zum Wohl der Gesellschaft zu betreiben, ist ein Kernpunkt des Selbstverständnisses der Einrichtungen der Leibniz-Gemeinschaft. Dies bedeutet, dass Leibniz-Einrichtungen die Verwendbarkeit ihrer Forschungsergebnisse fördern. Das PDI, dessen Forschung auf fundamentale Fragen der Materialwissenschaften zielt, die künftige Anwendungen beeinflussen, inspirieren oder gar erst ermöglichen, sieht eine wichtige Aufgabe darin, dieses Wissen zum gesellschaftlichen Nutzen zur Verfügung zu stellen.

In der Abteilung Technologie und Transfer werden Kompetenzen und Ressourcen für den Technologietransfer (im Technologie-transferbüro durch die Transferbeauftragte) ebenso bereitgestellt wie für den Transfer des Wissens in die Gesellschaft.

In der Leibniz-Gemeinschaft wird Transfer disziplinübergreifend verstanden. Die Disziplinspezifika werden schließlich bei der Umsetzung durch die maßgeschneiderten Transferwerkzeuge sichtbar. Das PDI stellt seit November 2014 mit dem Leiter der Abteilung Technologie und Transfer den Sprecher des Arbeitskreises Wissenstransfer der Leibniz-Gemeinschaft – dieser ist auch Mitglied der Präsidiumsgruppe zur Entwicklung des Leibniz Leitbildes für Wissenstransfer.



Facts & Figures

Zahlen & Fakten

Publications	155
Ph.D. Theses	163
Master Theses	163
Bachelor Thesis	164
Students Working on their Master Thesis	164
Conferences organized by the Institute	165
Seminar of Visitors	165
Budget Summary	167
Summary of External Funding	168
Visiting Scientists	169
Staff	171
Long-term fellows	173
Supporting Staff	173

Facts & Figures

Zahlen und Fakten

Publications

J. Aberl, P. Klenovský, J. S. Wildmann, J. Martín-Sánchez, T. Fromherz, E. Zallo, J. Humlíček, A. Rastelli, and R. Trotta,
Inversion of the exciton built-in dipole moment in In(Ga)As quantum dots via nonlinear piezoelectric effect,
Phys. Rev. B **96**, 045414, 6 pages (2017).
DOI: 10.1103/PhysRevB.96.045414

S. Assali, J. Lähnemann, T. T. T. Vu, K. D. Jöns, L. Gagliano, M. A. Verheijen, N. Akopian, E. P. A. M. Bakkers, and J. E. M. Haverkort,
Crystal phase quantum well emission with digital control,
Nano Lett. **17**, 6062–6068 (2017).
DOI: 10.1021/acs.nanolett.7b02489

N. Bachsoliani, S. Platonov, A. D. Wieck, and S. Ludwig,
Mesoscopic field-effect-induced devices in depleted two-dimensional electron systems,
Phys. Rev. Applied **8**, 064015, 8 pages (2017).
DOI: 10.1103/PhysRevApplied.8.064015

J.-B. Barakat, S. Dadgostar, K. Hestroffer, O. Bierwagen, A. Trampert, and F. Hatami,
Growth of GaP and AlGaP on GaP(111)B using gas-source molecular-beam epitaxy,
J. Cryst. Growth **477**, 91–96 (2017).
DOI: 10.1016/j.jcrysgr.2017.02.029

J. Bartolomé, M. Hanke, D. v. Treeck, and A. Trampert,
Strain driven shape evolution of stacked (In,Ga)N quantum disks embedded in GaN nanowires,
Nano Lett. **17**, 4654–4660 (2017).
DOI: 10.1021/acs.nanolett.7b01136

J. Berggren, M. Hanke, E. Luna, and A. Trampert,
Supernormal hardness increase of dilute Ga(As,N) thin films,
J. Appl. Phys. **121**, 095105, 6 pages (2017).
DOI: 10.1063/1.4978019

K. Berlin and A. Trampert,
Liquid-solid phase transition of Ge-Sb-Te alloy observed by in-situ transmission electron microscopy,
Ultramicroscopy **178**, 27–32 (2017).
DOI: 10.1016/j.ultramic.2016.10.010

J. E. Boschker, E. Tisbi, E. Placidi, J. Momand, A. Redaelli, B. J. Kooi, F. Arciprete, and R. Calarco,
Textured Sb₂Te₃ films and GeTe/Sb₂Te₃ superlattices grown on amorphous substrates by molecular beam
epitaxy,
AIP Adv. **7**, 015106, 8 pages (2017).
DOI: 10.1063/1.4974464

J. E. Boschker, R. N. Wang, and R. Calarco,
GeTe: A simple compound blessed by a plethora of properties,
CrystEngComm **19**, 5324–5335 (2017).
DOI: 10.1039/C7CE01040K

J. E. Boschker and R. Calarco,
Growth of crystalline phase change materials by physical deposition methods,
Adv. Phys.: X **2**, 675–694 (2017).
DOI: 10.1080/23746149.2017.1346483

V. Bragaglia, A. M. Mio, and R. Calarco,
Thermal annealing studies of GeTe-Sb₂Te₃ alloys with multiple interfaces,
AIP Adv. **7**, 085113, 7 pages (2017).
DOI: 10.1063/1.5000338

Facts & Figures – Publications

D. Braun, M. Schmidbauer, M. Hanke, A. Kwasniewski, and J. Schwarzkopf,
Tunable ferroelectric domain wall alignment in strained monoclinic $K_xNa_{1-x}NbO_3$ epitaxial films,
Appl. Phys. Lett. **110**, 232903, 4 pages (2017).
DOI: 10.1063/1.4985191

G. Calabrese, S. V. Pettersen, C. Pfüller, M. Ramsteiner, J. K. Grepstad, O. Brandt, L. Geelhaar,
and S. Fernández-Garrido,
Effect of surface roughness, chemical composition, and native oxide crystallinity on the orientation of
self-assembled GaN nanowires on Ti foils,
Nanotechnol. **28**, 425602, 9 pages (2017).
DOI: 10.1088/1361-6528/aa84a1

S. Cecchi, E. Zallo, J. Momand, R. N. Wang, B. J. Kooi, M. A. Verheijen, and R. Calarco,
Improved structural and electrical properties in native $Sb_2Te_3/Ge_xSb_2Te_{3+x}$ van der Waals superlattices due to
intermixing mitigation,
APL Mat. **5**, 026107, 6 pages (2017).
DOI: 10.1063/1.4976828

S. Cecchi, R. N. Wang, E. Zallo, and R. Calarco,
Unconventional strain relaxation of Sb_2Te_3 grown on a GeTe/ Sb_2Te_3 /GeTe heterostructure on Si(111),
Nanosci. Nanotechnol. Lett. **9**, 1114–1117 (2017).
DOI: 10.1166/nnl.2017.2441

E. A. Chekhovich, A. Ulhaq, E. Zallo, F. Ding, O. G. Schmidt, and M. S. Skolnick,
Measurement of the spin temperature of optically cooled nuclei and GaAs hyperfine constants in GaAs/AlGaAs
quantum dots,
Nat. Mater. **16**, 982–987 (2017).
DOI: 10.1038/nmat4959

Z. Z. Cheng, M. Hanke, P. Vogt, O. Bierwagen, and A. Trampert,
Phase formation and strain relaxation of Ga_2O_3 on c-plane and a-plane sapphire substrates as studied by
synchrotron-based x-ray diffraction,
Appl. Phys. Lett. **111**, 162104, 4 pages (2017).
DOI: 10.1063/1.4998804

C. Chèze, F. Feix, M. Anikeeva, T. Schulz, M. Albrecht, H. Riechert, O. Brandt, and R. Calarco,
In/GaN(0001)-($\sqrt{3} \times \sqrt{3}$)R30° adsorbate structure as a template for embedded (In,Ga)N/GaN monolayers and
short-period superlattices,
Appl. Phys. Lett. **110**, 072104, 4 pages (2017).
DOI: 10.1063/1.4976198

C. Chèze and R. Calarco,
Self-limited In incorporation in (In,Ga)N/GaN short-period superlattices,
Nanosci. Nanotechnol. Lett. **9**, 1118–1122 (2017).
DOI: 10.1166/nnl.2017.2442

P. Corfdir, R. B. Lewis, L. Geelhaar, and O. Brandt,
Fine structure of excitons in InAs quantum dots on GaAs(110) layers and nanowire facets,
Phys. Rev. B **96**, 045435, 7 pages (2017).
DOI: 10.1103/PhysRevB.96.045435

A. Davtyan, T. Krause, D. Kriegner, A. Al-Hassan, D. Bahrami, S. M. M. Kashani, R. B. Lewis, H. Küpers,
A. Tahraoui, L. Geelhaar, M. Hanke, S. J. Leake, O. Loffeld, and U. Pietsch,
Threefold rotational symmetry in hexagonally shaped core–shell (In,Ga)As/GaAs nanowires revealed by
coherent X-ray diffraction imaging,
J. Appl. Crystallogr. **50**, 673–680 (2017).
DOI: 10.1107/S1600576717004149

O. Delorme, L. Cerutti, E. Luna, G. Narcy, A. Trampert, E. Tournié, and J.-B. Rodriguez,
GaSbBi/GaSb quantum well laser diodes,
Appl. Phys. Lett. **110**, 222106, 5 pages (2017).
DOI: 10.1063/1.4984799

F. Feix, T. Flissikowski, K. K. Sabelfeld, V. M. Kaganer, M. Wölz, L. Geelhaar, H. T. Grahn, and O. Brandt,
Ga-polar (In,Ga)N/GaN quantum wells versus N-polar (In,Ga)N quantum disks in GaN nanowires: A
comparative analysis of carrier recombination, diffusion, and radiative efficiency,
Phys. Rev. Applied **8**, 014032, 13 pages (2017).
DOI: 10.1103/PhysRevApplied.8.014032

S. Fernández, J. Grandal, A. Trampert, and F. B. Naranjo,
 Tailoring of microstructure and optoelectronic properties of Aluminum doped Zinc Oxide changing gun tilt,
Mater. Sci. Semicond. Process. **63**, 115–121 (2017).
 DOI: 10.1016/j.mssp.2016.12.043

S. Fernández-Garrido, M. Ramsteiner, G. H. Gao, L. A. Galves, B. Sharma, P. Corfdir, G. Calabrese,
 Z. de Souza Schiaber, C. Pfüller, A. Trampert, J. M. J. Lopes, O. Brandt, and L. Geelhaar,
 Molecular beam epitaxy of GaN nanowires on epitaxial graphene,
Nano Lett. **17**, 5213–5221 (2017).
 DOI: 10.1021/acs.nanolett.7b01196

M. Foerster, F. Macià, N. Statuto, S. Finizio, A. Hernández-Mínguez, S. Lendínez, P. V. Santos, J. Fontcuberta,
 J. M. Hernández, M. Kläui, and L. Aballe,
 Direct imaging of delayed magneto dynamic modes induced by surface acoustic waves,
Nat. Commun. **8**, 407, 7 pages (2017).
 DOI: 10.1038/s41467-017-00456-0

L. A. Galves, J. M. Wofford, G. V. Soares, U. Jahn, C. Pfüller, H. Riechert, and J. M. J. Lopes,
 The effect of the SiC(0001) surface morphology on the growth of epitaxial mono-layer graphene nanoribbons,
Carbon **115**, 162–168 (2017).
 DOI: 10.1016/j.carbon.2017.01.018

S. Gaucher, B. Jenichen, J. Kalt, U. Jahn, A. Trampert, and J. Herfort,
 Growth of Fe₃Si/Ge/Fe₃Si trilayers on GaAs(001) using solid-phase epitaxy,
Appl. Phys. Lett. **110**, 102103, 5 pages (2017).
 DOI: 10.1063/1.4977833

Á. Guzmán, R. Gargallo-Caballero, X. Lü, and H. T. Grahn,
 Laterally biased structures for room temperature operation of quantum-well infrared photodetectors,
J. Cryst. Growth **477**, 272–276 (2017).
 DOI: 10.1016/j.jcrysgro.2017.04.023

Á. Guzmán, R. San-Roman, R. Gargallo-Caballero, and H. T. Grahn,
 Laterally biased quantum-well infrared photodetectors operating at room temperature with low dark currents,
IEEE J. Sel. Topics Quantum Electron. **24**, 1900206, 6 pages (2018).
 DOI: 10.1109/JSTQE.2017.2703307

T. Hagelschuer, M. Wienold, H. Richter, L. Schrottke, H. T. Grahn, and H.-W. Hübers,
 Real-time gas sensing based on optical feedback in a terahertz quantum-cascade laser,
Opt. Express **25**, 30203–30213 (2017).
 DOI: 10.1364/OE.25.030203

J. Hartmann, F. Steib, H. Zhou, J. Ledig, L. Nicolai, S. Fündling, T. Schimpke, A. Avramescu, T. Varghese,
 A. Trampert, M. Straßburg, H.-J. Lugauer, H.-H. Wehmann, and A. Waag,
 Study of 3D-growth conditions for selective area MOVPE of high aspect ratio GaN fins with non-polar vertical
 sidewalls,
J. Cryst. Growth **476**, 90–98 (2017).
 DOI: 10.1016/j.jcrysgro.2017.08.021

C. Hauswald, I. Giuntini, T. Flissikowski, T. Gotschke, R. Calarco, H. T. Grahn, L. Geelhaar, and O. Brandt,
 Luminous efficiency of ordered arrays of GaN nanowires with sub-wavelength diameters,
ACS Photonics **4**, 52–62 (2017).
 DOI: 10.1021/acsphotonics.6b00551

M. Hempel, B. Röben, M. Niehle, L. Schrottke, A. Trampert, and H. T. Grahn,
 Continuous tuning of two-section, single-mode terahertz quantum-cascade lasers by fiber-coupled,
 near-infrared illumination,
AIP Adv. **7**, 055201, 6 pages (2017).
 DOI: 10.1063/1.4983030

M. Hilse, B. Jenichen, and J. Herfort,
 GaAs-Fe₃Si semiconductor-ferromagnet core-shell nanowires for spintronics,
 in: *Novel Compound Semiconductor Nanowires: Materials, Devices and Applications*, edited by F. Ishikawa and
 I. Buyanova (Pan Stanford, 2017), pp. 221–254.
 DOI: 10.4032/9781315364407

Facts & Figures – Publications

M. Hilse, B. Jenichen, and J. Herfort,
Magnetic properties of GaAs-Fe₃Si core-shell nanowires—A comparison of ensemble and single nanowire investigation,
AIP Adv. **7**, 056305, 6 pages (2017).
DOI: 10.1063/1.4973748

V. Hortelano, H. Weidlich, W. T. Masselink, G. Mahler, and Y. Takagaki,
Demonstration of magnetic-field-induced rectification using circular ballistic channels with a rough boundary,
Semicond. Sci. Technol. **32**, 125005, 6 pages (2017).
DOI: 10.1088/1361-6641/aa90ab

H. Y. Huang, R. Trotta, Y. H. Huo, T. Lettner, J. S. Wildmann, J. Martín-Sánchez, D. Huber, M. Reindl, J. X. Zhang, E. Zallo, O. G. Schmidt, and A. Rastelli,
Electrically-pumped wavelength-tunable GaAs quantum dots interfaced with rubidium atoms,
ACS Photonics **4**, 868–872 (2017).
DOI: 10.1021/acspophotonics.6b00935

H.-W. Hübers, H. Richter, R. Eichholz, M. Wienold, K. Biermann, L. Schrottke, and H. T. Grahn,
Heterodyne spectroscopy of frequency instabilities in terahertz quantum-cascade lasers induced by optical feedback,
IEEE J. Sel. Topics Quantum Electron. **23**, 1800306, 6 pages (2017).
DOI: 10.1109/JSTQE.2017.2684078

C. Hubert, K. Biermann, A. Hernández-Mínguez, and P. V. Santos,
Indirect excitons in (111) GaAs double quantum wells,
Superlattices Microstruct. **108**, 51–56 (2017).
DOI: 10.1016/j.spmi.2017.01.023

V. M. Kaganer, T. Ulyanenkova, A. Benediktovitch, M. Myronov, and A. Ulyanenkov,
Bunches of misfit dislocations on the onset of relaxation of Si_{0.4}Ge_{0.6}/Si(001) epitaxial films revealed by high-resolution x-ray diffraction,
J. Appl. Phys. **122**, 105302, 6 pages (2017).
DOI: 10.1063/1.4990135

J. Kamimura, P. Bogdanoff, F. F. Abdi, J. Lähnemann, R. van de Krol, H. Riechert, and L. Geelhaar,
Photoelectrochemical properties of GaN photoanodes with cobalt phosphate catalyst for solar water splitting in neutral electrolyte,
J. Phys. Chem. C **121**, 12540–12545 (2017).
DOI: 10.1021/acs.jpcc.7b02253

J. Kamimura, P. Bogdanoff, M. Ramsteiner, P. Corfdit, F. Feix, L. Geelhaar, and H. Riechert,
p-type doping of GaN nanowires characterized by photoelectrochemical measurements,
Nano Lett. **17**, 1529–1537 (2017).
DOI: 10.1021/acs.nanolett.6b04560

J. Kellner, G. Bihlmayer, V. L. Deringer, M. Liebmann, C. Pauly, A. Giussani, J. E. Boschker, R. Calarco, R. Dronskowski, and M. Morgenstern,
Exploring the subsurface atomic structure of the epitaxially grown phase-change material Ge₂Sb₂Te₅,
Phys. Rev. B **96**, 245408, 11 pages (2017).
DOI: 10.1103/PhysRevB.96.245408

T. Krause, M. Hanke, L. Nicolai, Z. Z. Cheng, M. Niehle, A. Trampert, M. Kahnt, G. Falkenberg, C. G. Schroer, J. Hartmann, H. Zhou, H.-H. Wehmann, and A. Waag,
Structure and composition of isolated core-shell (In,Ga)N/GaN rods based on nanofocus x-ray diffraction and scanning transmission electron microscopy,
Phys. Rev. Applied **7**, 024033, 10 pages (2017).
DOI: 10.1103/PhysRevApplied.7.024033

M. Kumar, G. Sarau, M. Heilmann, S. Christiansen, V. Kumar, and R. Singh,
Effect of ammonification temperature on the formation of coaxial GaN/Ga₂O₃ nanowires,
J. Phys. D: Appl. Phys. **50**, 035302, 9 pages (2017).
DOI: 10.1088/1361-6463/50/3/035302

H. Küpers, A. Tahraoui, R. B. Lewis, S. Rauwerdink, M. Matalla, O. Krüger, F. Bastiman, H. Riechert, and L. Geelhaar,
 Surface preparation and patterning by nano imprint lithography for the selective area growth of GaAs nanowires on Si(111),
Semicond. Sci. Technol. **32**, 115003, 6 pages (2017).
 DOI: 10.1088/1361-6641/aa8c15

L. F. Lastras-Martínez, E. Cerdá-Méndez, N. Ulloa-Castillo, R. Herrera-Jasso, L. E. Rodríguez-Tapia, O. Ruiz-Cigarrillo, R. Castro-García, K. Biermann, and P. V. Santos,
 Microscopic optical anisotropy of exciton-polaritons in a GaAs-based semiconductor microcavity,
Phys. Rev. B **96**, 235306, 6 pages (2017).
 DOI: 10.1103/PhysRevB.96.235306

L. F. Lastras-Martínez, J. Almendarez-Rodríguez, G. Flores-Rangel, N. A. Ulloa-Castillo, O. Ruiz-Cigarrillo, C. A. Ibarra-Becerra, R. Castro-García, R. E. Balderas-Navarro, M. H. Oliveira, Jr., and J. M. J. Lopes,
 Optical detection of graphene nanoribbons synthesized on stepped SiC surfaces,
J. Appl. Phys. **122**, 035701, 7 pages (2017).
 DOI: 10.1063/1.4993453

S. Lazić, A. Hernández-Mínguez, and P. V. Santos,
 Control of single photon emitters in semiconductor nanowires by surface acoustic waves,
Semicond. Sci. Technol. **32**, 084002, 11 pages (2017).
 DOI: 10.1088/1361-6641/aa7295

R. B. Lewis, L. Nicolai, H. Küpers, M. Ramsteiner, A. Trampert, and L. Geelhaar,
 Anomalous strain relaxation in core-shell nanowires via simultaneous coherent and incoherent growth,
Nano Lett. **17**, 136–142 (2017).
 DOI: 10.1021/acs.nanolett.6b03681

R. B. Lewis, P. Corfdir, H. Li, J. Herranz, C. Pfüller, O. Brandt, and L. Geelhaar,
 Quantum dot self-assembly driven by a surfactant-induced morphological instability,
Phys. Rev. Lett. **119**, 086101, 6 pages (2017).
 DOI: 10.1103/PhysRevLett.119.086101

R. B. Lewis, P. Corfdir, J. Herranz, H. Küpers, U. Jahn, O. Brandt, and L. Geelhaar,
 Self-assembly of InAs nanostructures on the sidewalls of GaAs nanowires directed by a Bi surfactant,
Nano Lett. **17**, 4255–4260 (2017).
 DOI: 10.1021/acs.nanolett.7b01185

H. Li, C. Draxl, S. Wurster, R. Pippan, and L. Romaner,
 Impact of *d*-band filling on the dislocation properties of bcc transition metals: The case of tantalum-tungsten alloys investigated by density-functional theory,
Phys. Rev. B **95**, 094114, 8 pages (2017).
 DOI: 10.1103/PhysRevB.95.094114

C. B. Lim, A. Ajay, J. Lähnemann, C. Bougerol, and E. Monroy,
 Effect of Ge-doping on the short-wave, mid- and far-infrared intersubband transitions in GaN/AlGaN heterostructures,
Semicond. Sci. Technol. **32**, 125002, 10 pages (2017).
 DOI: 10.1088/1361-6641/aa919c

W.-H. Lin, U. Jahn, H. Küpers, E. Luna, R. B. Lewis, L. Geelhaar, and O. Brandt,
 Efficient methodology to correlate structural with optical properties of GaAs nanowires based on scanning electron microscopy,
Nanotechnol. **28**, 415703, 11 pages (2017).
 DOI: 10.1088/1361-6528/aa8394

Y.-T. Liou, A. Hernández-Mínguez, J. Herfort, J. M. J. Lopes, A. Tahraoui, and P. V. Santos,
 Acousto-electric transport in MgO/ZnO-covered graphene on SiC,
J. Phys. D: Appl. Phys. **50**, 464008, 10 pages (2017).
 DOI: 10.1088/1361-6463/aa8e8a

Facts & Figures – Publications

E. Luna, J. Puustinen, M. Wu, J. Hilska, M. Guina, and A. Trampert,
The role of epitaxial strain on the spontaneous formation of Bi-rich nanostructures in Ga(As,Bi) epilayers and
quantum wells,
Nanosci. Nanotechnol. Lett. **9**, 1132–1138 (2017).
DOI: 10.1166/nnl.2017.2448

E. Luna, R. Gargallo-Caballero, F. Ishikawa, and A. Trampert,
Morphological and chemical instabilities of nitrogen delta-doped GaAs/(Al,Ga)As quantum wells,
Appl. Phys. Lett. **110**, 201906, 5 pages (2017).
DOI: 10.1063/1.4983837

Y. Manzke, J. Herfort, and M. Ramsteiner,
Bias-dependent electrical spin generation in Fe₃Si/GaAs: Consistent behavior in nonlocal and local spin valves
and in the three-terminal configuration,
Phys. Rev. B **96**, 245308, 6 pages (2017).
DOI: 10.1103/PhysRevB.96.245308

O. Marquardt, M. Ramsteiner, P. Corfdir, L. Geelhaar, and O. Brandt,
Modeling the electronic properties of GaAs polytype nanostructures: Impact of strain on the conduction band
character,
Phys. Rev. B **95**, 245309, 8 pages (2017).
DOI: 10.1103/PhysRevB.95.245309

O. Marquardt, T. Krause, V. Kaganer, J. Martín-Sánchez, M. Hanke, and O. Brandt,
Influence of strain relaxation in axial In_xGa_{1-x}N/GaN nanowire heterostructures on their electronic properties,
Nanotechnol. **28**, 215204, 6 pages (2017).
DOI: 10.1088/1361-6528/aa6b73

O. Marquardt, V. M. Kaganer, and P. Corfdir,
Nanowires, in: *Handbook of Optoelectronic Device Modeling and Simulation: Fundamentals, Materials,
Nanostructures, LEDs, and Amplifiers*, Vol. 1, edited by J. Piprek (CRC Press, 2017), pp. 397–417.
ISBN: 9781498749466

I. Miccoli, J. Aprojanz, J. Baringhaus, T. Lichtenstein, L. A. Galves, J. M. J. Lopes, and C. Tegenkamp,
Quasi-free-standing bilayer graphene nanoribbons probed by electronic transport,
Appl. Phys. Lett. **110**, 051601, 5 pages (2017).
DOI: 10.1063/1.4975205

A. M. Mio, S. M. S. Privitera, V. Bragaglia, F. Arciprete, S. Cecchi, G. Litrico, C. Persch, R. Calarco, and E. Rimini,
Role of interfaces on the stability and electrical properties of Ge₂Sb₂Te₅ crystalline structures,
Sci. Rep. **7**, 2616, 9 pages (2017).
DOI: 10.1038/s41598-017-02710-3

A. M. Mio, S. M. S. Privitera, V. Bragaglia, F. Arciprete, C. Bongiorno, R. Calarco, and E. Rimini,
Chemical and structural arrangement of the trigonal phase in GeSbTe thin films,
Nanotechnol. **28**, 065706, 7 pages (2017).
DOI: 10.1088/1361-6528/28/6/065706

J. Momand, R. Wang, J. E. Boschker, M. A. Verheijen, R. Calarco, and B. J. Kooi,
Dynamic reconfiguration of van der Waals gaps within GeTe-Sb₂Te₃ based superlattices,
Nanoscale **9**, 8774–8780 (2017).
DOI: 10.1039/C7NR01684K

M. Musolino, A. Tahraoui, L. Geelhaar, F. Sacconi, F. Panetta, C. De Santi, M. Meneghini, and E. Zanoni,
Effect of varying three-dimensional strain on the emission properties of light-emitting diodes based on
(In,Ga)N/GaN nanowires,
Phys. Rev. Applied **7**, 044014, 11 pages (2017).
DOI: 10.1103/PhysRevApplied.7.044014

M. Niehle, A. Trampert, J.-B. Rodriguez, L. Cerutti, and E. Tournié,
Electron tomography on III-Sb heterostructures on vicinal Si(001) substrates: Anti-phase boundaries as a sink
for threading dislocations,
Scr. Mater. **132**, 5–8 (2017).
DOI: 10.1016/j.scriptamat.2017.01.018

M. Niehle, J.-B. Rodriguez, L. Cerutti, E. Tournié, and A. Trampert,
 On the origin of threading dislocations during epitaxial growth of III-Sb on Si(001): A comprehensive transmission electron tomography and microscopy study,
Acta Mater. **143**, 121–129 (2017).
 DOI: 10.1016/j.actamat.2017.09.055

Y. Pan, K. Kanisawa, N. Ishikawa, and S. Fölsch,
 Scanning tunnelling spectroscopy and manipulation of double-decker phthalocyanine molecules on a semiconductor surface,
J. Phys.: Condens. Matter **29**, 364001, 7 pages (2017).
 DOI: 10.1088/1361-648X/aa7dc4

Y. Pan, K. Kanisawa, and S. Fölsch,
 Creating and probing quantum dot molecules with the scanning tunneling microscope,
J. Vac. Sci. Technol. B **35**, 04F102, 5 pages (2017).
 DOI: 10.1116/1.4979848

A. Papadogianni, L. Kirste, and O. Bierwagen,
 Structural and electron transport properties of single-crystalline In_2O_3 films compensated by Ni acceptors,
Appl. Phys. Lett. **111**, 262103, 5 pages (2017).
 DOI: 10.1063/1.5006421

P. K. Patil, E. Luna, T. Matsuda, K. Yamada, K. Kamiya, F. Ishikawa, and S. Shimomura,
 GaAsBi/GaAs multi-quantum well LED grown by molecular beam epitaxy using a two-substrate-temperature technique,
Nanotechnol. **28**, 105702, 8 pages (2017).
 DOI: 10.1088/1361-6528/aa596c

A. Reszka, A. Wierzbicka, K. Sobczak, U. Jahn, U. Zeimer, A. V. Kuchuk, A. Pieniążek, M. Sobanska, K. Klosek, Z. R. Zytkiewicz, and B. J. Kowalski
 An influence of the local strain on cathodoluminescence of $\text{GaN}/\text{Al}_x\text{Ga}_{1-x}\text{N}$ nanowire structures
J. Appl. Phys. **120**, 194304, 7 pages (2016).
 DOI: 10.1063/1.4968004

B. Röben, X. Lü, M. Hempel, K. Biermann, L. Schrottke, and H. T. Grahn,
 Terahertz quantum-cascade lasers as high-power and wideband, gapless sources for spectroscopy,
Opt. Express **25**, 16282–16290 (2017).
 DOI: 10.1364/OE.25.016282

K. K. Sabelfeld, V. M. Kaganer, C. Pfüller, and O. Brandt,
 Dislocation contrast in cathodoluminescence and electron-beam induced current maps on $\text{GaN}(0001)$,
J. Phys. D: Appl. Phys. **50**, 405101, 11 pages (2017).
 DOI: 10.1088/1361-6463/aa85c8

M. Sawicka, A. Feduniewicz-Żmuda, M. Kryśko, H. Turski, G. Muziol, M. Siekacz, P. Wolny, and C. Skierbiszewski,
 Indium incorporation in semipolar (2021) and nonpolar (1010) InGaN grown by plasma assisted molecular beam epitaxy,
J. Cryst. Growth **459**, 129–134 (2017).
 DOI: 10.1016/j.jcrysgro.2016.11.105

M. Sawicka, P. Wolny, M. Kryśko, H. Turski, K. Szkudlarek, S. Grzanka, and C. Skierbiszewski,
 Comparative study of semipolar (2021), nonpolar (1010) and polar (0001) InGaN multi-quantum well structures grown under N- and In-excess by plasma assisted molecular beam epitaxy,
J. Cryst. Growth **465**, 43–47 (2017).
 DOI: 10.1016/j.jcrysgro.2017.02.045

M. Schmidbauer, D. Braun, T. Markurt, M. Hanke, and J. Schwarzkopf,
 Strain engineering of monoclinic domains in $\text{K}_x\text{Na}_{1-x}\text{NbO}_3$ epitaxial layers: A pathway to enhanced piezoelectric properties,
Nanotechnol. **28**, 24LT02, 7 pages (2017).
 DOI: 10.1088/1361-6528/aa715a

Facts & Figures – Publications

M. Schmidbauer, M. Hanke, A. Kwasniewski, D. Braun, L. von Helden, C. Feldt, S. J. Leake, and J. Schwarzkopf,
Scanning X-ray nanodiffraction from ferroelectric domains in strained $K_{0.75}Na_{0.25}NbO_3$ epitaxial films grown on
(110) $TbScO_3$,
J. Appl. Crystallogr. **50**, 519–524 (2017).
DOI: 10.1107/S1600576717000905

J. Schwarzkopf, D. Braun, M. Hanke, R. Uecker, and M. Schmidbauer,
Strain engineering of ferroelectric domains in $K_xNa_{1-x}NbO_3$ epitaxial layers,
Front. Mater. **4**, 26, 10 pages (2017).
DOI: 10.3389/fmats.2017.00026

B. Sharma, T. Schumann, M. H. de Oliveira, Jr., and J. M. J. Lopes,
Controlled synthesis and characterization of multilayer graphene films on the C-face of silicon carbide,
Phys. Status Solidi A **214**, 1600721, 7 pages (2017).
DOI: 10.1002/pssa.201600721

Z. de Souza Schiaber, G. Calabrese, X. Kong, A. Trampert, B. Jenichen, J. H. Dias da Silva, L. Geelhaar, O. Brandt,
and S. Fernández-Garrido,
Polarity-induced selective area epitaxy of GaN nanowires,
Nano Lett. **17**, 63–70 (2017).
DOI: 10.1021/acs.nanolett.6b03249

M. Spies, M. I. den Hertog, P. Hille, J. Schörmann, J. Polaczyński, B. Gayral, M. Eickhoff, E. Monroy, and
J. Lähnemann,
Bias-controlled spectral response in GaN/AlN single-nanowire ultraviolet photodetectors,
Nano Lett. **17**, 4231–4239 (2017).
DOI: 10.1021/acs.nanolett.7b01118

Y. Takagaki, B. Jenichen, M. Ramsteiner, and U. Jahn,
Axiotaxy of bismuth telluride films on InP(111)B by high-temperature hot wall epitaxy,
Cryst. Growth Des. **17**, 1977–1981 (2017).
DOI: 10.1021/acs.cgd.6b01899

J. Tejada, E. M. Chudnovsky, R. Zarzuela, N. Statuto, J. Calvo-de la Rosa, P. V. Santos, and
A. Hernández-Mínguez,
Switching of magnetic moments of nanoparticles by surface acoustic waves,
Europhys. Lett. **118**, 37005, 7 pages (2017).
DOI: 10.1209/0295-5075/118/37005

C. Vogel, M. Ramsteiner, R. Sekine, A. Doolette, and C. Adam,
Characterization of phosphorus compounds in soils by deep ultraviolet (DUV) Raman microspectroscopy,
J. Raman Spectrosc. **48**, 867–871 (2017).
DOI: 10.1002/jrs.5115

P. Vogt, O. Brandt, H. Riechert, J. Lähnemann, and O. Bierwagen,
Metal-exchange catalysis in the growth of sesquioxides: Towards heterostructures of transparent oxide
semiconductors,
Phys. Rev. Lett. **119**, 196001, 5 pages (2017).
DOI: 10.1103/PhysRevLett.119.196001

R. N. Wang, W. Zhang, J. Momand, I. Ronneberger, J. E. Boschker, R. Mazzarello, B. J. Kooi, H. Riechert,
M. Wuttig, and R. Calarco,
Formation of resonant bonding during growth of ultrathin GeTe films,
NPG Asia Mater. **9**, e369, 6 pages (2017).
DOI: 10.1038/am.2017.95

J. M. Wofford, S. Nakhaie, T. Krause, X. J. Liu, M. Ramsteiner, M. Hanke, H. Riechert, and J. M. J. Lopes,
A hybrid MBE-based growth method for large-area synthesis of stacked hexagonal boron nitride/graphene
heterostructures,
Sci. Rep. **7**, 43644, 10 pages (2017).
DOI: 10.1038/srep43644

Z. Z. Yin, H. Song, Y. H. Zhang, M. Ruiz-García, M. Carretero, L. L. Bonilla, K. Biermann, and H. T. Grahn,
Noise-enhanced chaos in a weakly coupled GaAs/(Al,Ga)As superlattice,
Phys. Rev. E **95**, 012218, 7 pages (2017).
DOI: 10.1103/PhysRevE.95.012218

M. Yuan, C. Hubert, S. Rauwerdink, A. Tahraoui, B. von Someren, K. Biermann, and P. V. Santos,
Generation of surface acoustic waves on doped semiconductor substrates,
J. Phys. D: Appl. Phys. **50**, 484004, 7 pages (2017).
DOI: 10.1088/1361-6463/aa92a5

E. Zallo and R. Calarco,
Crescita epitassiale van der Waals per memorie a cambiamento di fase,
Nuovo Sagg. **33**, No. 3 & 4, 31–40 (2017).

E. Zallo, S. Cecchi, J. E. Boschker, A. M. Mio, F. Arciprete, S. Privitera, and R. Calarco,
Modulation of van der Waals and classical epitaxy induced by strain at the Si step edges in GeSbTe alloys,
Sci. Rep. **7**, 1466, 7 pages (2017).
DOI: 10.1038/s41598-017-01502-z

Ph.D. Theses

Zettler, Johannes
Growth of GaN nanowire ensembles in molecular beam epitaxy: Overcoming the limitations of their
spontaneous formation
Humboldt-Universität zu Berlin, March 2017

Wang, Rui Ning
Epitaxial growth and characterization of GeTe and GeTe/Sb₂Te₃ superlattices
Humboldt-Universität zu Berlin, March 2017

Vogt, Patrick
Growth Kinetics, Thermodynamics, and Phase Formation of group-III and IV oxides during Molecular Beam
Epitaxy
Humboldt-Universität zu Berlin, June 2017

Bragaglia, Valeria
Epitaxial Growth and Ultrafast Dynamics of GeSbTe Alloys and GeTe/Sb₂Te₃ Superlattices
Humboldt-Universität zu Berlin, July 2017

Krause, Thilo
Strain-related phenomena in (In, Ga)N/GaN nanowires and rods investigated by nanofocus x-ray diffraction and
the finite element method
Humboldt-Universität zu Berlin, November 2017

Platonov, Sergey
Control of Electron Dynamics in Mesoscopic Quantum Circuits
Ludwig-Maximilians-Universität München, Dezember 2017

Master Theses

Tschammer Carsten

Growth by molecular beam epitaxy, properties, and applications of NiO

Humboldt-Universität zu Berlin, December 2016

Wimmer, Kilian

Nucleation of GaN nanowires in plasma-assisted molecular beam epitaxy

Humboldt-Universität zu Berlin, January 2017

Schultz, Markus

Quantitative Transmission Electron Microscopy on $\text{Bi}_2\text{Te}_3/\text{InP}$ Semiconductor Heterostructures

Freie Universität Berlin, January 2017

Qurat-Ul-Ain

Molecular beam growth and characterization of graphene films on SiN/Si templates

Universität Freiburg, March 2017

Papadogianni, Alexandra

The surface electron accumulation layer of Ni-doped In_2O_3 grown by molecular beam epitaxy and its application in gas-sensing

Freie Universität Berlin, April 2017

Amador Méndez, Nuño

Towards GaN nanowires based microcavities

Universidad Politécnica de Madrid, July 2017

Monge Bartolomé, Laura

Electrical characterization of single GaAs core-shell nanowires with Si n-type doped shell

Universidad Politécnica de Madrid, July 2017

Hüttenhofer, Ludwig

Electrical characterization of n-type GaAs nanowires - Optimization of ohmic contacts and quantum transport experiments (D)

Ludwig-Maximilians-Universität München, October 2017

Bachelor Thesis

Gutsche, Florian

Electrical characterization of Indium oxide layers for Seebeck gas sensors (D)

Humboldt-Universität zu Berlin, June 2017

Students Working on their Master Thesis

Hoffmann, Georg

Humboldt-Universität zu Berlin

Sabelfeld, Alexander

Technische Universität Berlin

Oliva, Miriam

Technische Universität Berlin

Winkler, Daniel

Technische Universität Berlin

Ian Correa Sampaio

Universidade Federal de Minas Gerais, Brasilien

Conferences organized by the Institute

**Leibniz-Workshop on Knowledge-Transfer,
"Jenseits des Schutzrechts – alternative wirtschaftliche Verwertungsstrategien für Forschungswissen"**

May 10, 2017

Paul-Drude-Institut für Festkörperelektronik

Leibniz-Institut für Gewässerökologie und Binnenfischerei

Workshop held at Leibniz-Zentrum für Marine Tropenökologie (ZMT), Bremen

Compound Semiconductor Week 2017

May 14–18, 2017

Paul-Drude-Institut für Festkörperelektronik

Workshop held at dbb forum Berlin

**Leibniz-Workshop on Knowledge-Transfer,
"Beratung, Vermittlung, Dialog"**

November 16, 2017

Paul-Drude-Institut für Festkörperelektronik

Leibniz-Institut für Gewässerökologie und Binnenfischerei

Workshop held at BMBF, Bonn

Seminar of Visitors

11.01.2017

Prof. Dr. José M. Calleja, Universidad Autónoma de Madrid, Spain

InGaN single photon emitters in nanowires: Properties and dynamic control

23.01.2017

Prof. Kirill Bolotin, Freie Universität Berlin, Germany

Bending, pulling, and cutting wrinkled two-dimensional materials

28.02.2017

Dr. Nicolae Barsan, Eberhard Karls Universität Tübingen, Germany

Basic understanding of gas sensing with nano-structured Semiconducting Metal OXides (SMOX): Operando studies

28.02.2017

Prof. Dr. Stefan Eisebitt, Max-Born-Institut, Berlin, Germany

Watching Spins Move

10.03.2017

Dr. Dmitriy Krizhanovskii, University of Sheffield, United Kingdom

Nonlinear polariton phenomena in semiconductor photonic structures

22.03.2017

Dr. Oliver Portugall, CNRS, Toulouse, France

Semiconductor Spectroscopy beyond 100 Tesla—The Generation and Use of Megagauss Fields

27.03.2017

Dr. Steffen Breuer, Fraunhofer IAF/HHI, Germany

Ultra-thin barrier AlN/GaN HEMTs grown by MBE and MOCVD

19.04.2017

Mrs. Gelavizh Ahmadi, Freie Universität Berlin, Germany

Magnetic fingerprints of molecules on superconductors

09.06.2017

Dr. Van Dong Pham, FAU Erlangen-Nürnberg, Germany

Tuning the electronic and dynamic properties of single molecules by tip manipulation

06.07.2017

Dr. Juanita Bocquel, University of New South Wales, Australia

Probing phosphorus nanostructures in silicon at the atomic scale

20.07.2017

Dr. Nikolai Borgardt, National Research University of Electronic Technology, Moscow, Russia

TEM studies of (i) atomic structure of pyrocarbon, (ii) defects in GaN nanowires

26.07.2017

Dr. A.V. Poshakinskiy, Ioffe Institute, St. Petersburg, Russia

Optomechanics in multiple-quantum-well structures

01.08.2017

Prof. Dr. Gloria Platero, CSIC, Cantoblanco, Madrid, Spain

Long range electron transfer and dark states in ac driven triple quantum dots

08.08.2017

Dr. Piero Mazzolini, Istituto Italiano di Tecnologia, Milano, Italy

Functional properties control of doped TiO₂ for new generation solar cell devices

14.08.2017

Prof. Luis Felipe Lastras-Martinez, Universidad Autónoma de San Luis Potosí, Mexico

Optical characterization of graphene nanoribbons

06.11.2017

Vanessa Schaller, IBM Zürich & TU München

1D Ballistic Transport Signature in InAs Nanowires

24.11.2017

Prof. Armando Rastelli, Johannes Kepler University Linz

Epitaxial quantum dots as scalable light sources for quantum technologies

04.12.2017

Prof. Christoph Koch, Humboldt-Universität zu Berlin

Mapping strain, charges, and bandgaps at sub-nm spatial resolution by transmission electron microscopy

06.12.2017

Dr. Jesús Zúñiga Pérez, Centre de Recherche sur l'Hétéro-Epitaxie et ses Applications (CRHEA), Centre National de la Recherche Scientifique (CNRS)

ZnO optical microcavities: from materials science to room-temperature polariton lasers

15.12.2017

Prof. Jonathan Finley, Walter Schottky Institut and Physik Department, TU-München

Quantum optics with semiconductor artificial atoms

Budget Summary

Fiscal year	2016 (actual amount)	2017 (actual amount)
	k€	k€
Revenues		
Allocations	9,498.2	9,633.4
Earnings	29.1	11.1
Sum	9,527.3	9,644.5
Expenditures		
Staff	5,202.7	5,757.7
Administrative expenses	2,990.3	2,954.1
Equipment investment funds	1,334.3	932.7
Sum	9,527.3	9,644.5
External funding through projects		
Granted funds	2,900.3	3,201.4
Spent funds	1,824.1	2,858.9

Summary of External Funding

Agency	Period	Title	
BMBF	01.07.2014–30.06.2017	Development, implementation and professionalization of a transfer concept at the PDI	Dr. Carsten Hucho
BMBF	01.12.2015–30.11.2018	Design principles in organic electronics: Heterogeneities in the volume and at phase boundaries – Charge and energy transfer processes at hybrid organic/inorganic semiconductor interfaces (LETOIG)	Dr. Oliver Brandt
EFRE	01.08.2016–31.07.2019	Application laboratory electron tomography	Dr. Achim Trampert
DFG	01.07.2005–30.06.2017	Collaborative Research Center 658 – Conformational changes of single molecules on semiconductor surfaces induced by inelastic electron tunnelling processes	Dr. Stefan Fölsch
DFG	01.01.2014–31.08.2017	Manipulation and spectroscopy of quantum structures on semiconductor surfaces by cryogenic scanning tunneling microscopy	Dr. Stefan Fölsch
DFG	01.04.2014–30.06.2017	Interaction of surface acoustic waves with epitaxial graphene	Dr. Alberto Hernández-Míguez
DFG	01.04.2014–31.12.2017	Correlation between structural and optical properties of single semiconductor nanowires with core-shell heterostructure	Dr. Lutz Geelhaar
DFG	01.07.2014–30.06.2017	Exciton-polariton condensates in acoustic and periodic potentials	Dr. Paulo V. Santos
DFG	01.08.2015–31.07.2017	High-resolution terahertz semiconductor spectroscopy with quantum- cascade lasers	Prof. Holger T. Grahn
DFG	01.01.2016–30.09.2017	Quantum-cascade lasers for far-infrared magneto-spectroscopy of novel semiconductor materials in megagauss magnetic fields	Prof. Holger T. Grahn
DFG	01.10.2015–31.03.2018	Interactions in mesoscopic structures in non-equilibrium	Dr. Stefan Ludwig
DFG	01.07.2016–30.06.2019	Manipulation of single electrons and single excitons by surface acoustic waves	Dr. Paulo V. Santos
DFG	01.12.2015–30.11.2018	Quantum Hall based Aharonov-Bohm spectroscopy: electron-electron interaction in non-linear magnetotransport	Dr. Stefan Ludwig
DFG	01.05.2017–30.04.2020	Nonequilibrium Phenomena and Interactions in Ultrapure III-V Nanowires	Dr. Stefan Ludwig
DFG	01.09.2017–31.08.2019	Manipulation and spectroscopy of quantum structures on semiconductor surfaces by cryogenic scanning tunneling microscopy	Dr. Stefan Fölsch
EU	01.01.2015–31.12.2018	SPRInG – short period superlattices for rational (In,Ga)N	Dr. Raffaella Calarco
EU	01.06.2015–31.05.2018	SAWtrain – dynamic electromechanical control of semiconductor nanostructures by acoustic fields	Dr. Paulo V. Santos
GIF	01.01.2015–01.04.2017	Atoms, molecules and lattices of dipolar excitons	Dr. Paulo V. Santos
WGL (SAW)	01.05.2013–30.04.2017	Direct growth of single-crystalline semiconductors on polycrystalline metallic films and foils	Dr. Lutz Geelhaar
WGL (SAW)	01.07.2015–30.06.2018	Epitaxial phase change superlattices designed for the investigation of non-thermal switching	Dr. Raffaella Calarco
WGL (SAS)	01.07.2016–30.06.2020	Growth and fundamentals of oxides for electronic applications (GraFOx)	Dr. Oliver Bierwagen

Visiting Scientists

Name	Institute	Period	Topic	Country
Koszeniewski Rolim, Guilherme	Chemistry Institute-UFRGS	03.04.2017–31.07.2017	Tailored synthesis and characterization of graphene films on dielectric substrates	Brazil
Dr. Rodriguez, Jean-Baptiste	Université de Montpellier-IES	19.05.2017–24.05.2017	Structural properties of Ga(Sb,Bi)/GaSb heterostructures	France
Delorme, Olivier	Université de Montpellier-IES	19.05.2017–24.05.2017	Transition electron microscopy studies of Ga(Sb,Bi)/GaSb heterostructures	France
Prof. Dr. Arciprete, Fabrizio	Department of Physics, Università di Roma Tor Vergata	06.02.2017–10.02.2017	Analysis of experimental results for the growth of GST-based alloys on InAs(111)	Italy
Tisbi, Elisa	Department of Physics, Università di Roma Tor Vergata	23.01.2017–18.02.2017	MBE growth of PCM alloys and superlattices	Italy
Kosuke, Yano	Graduate school of Science and Engineering, Ehime University	13.05.2017–18.05.2017	Functional Nanowire Synthesis Based on Molecular Beam Epitaxy	Japan
Prof. Dr. Ishikawa, Fumitaro	Graduate school of Science and Engineering, Ehime University	13.05.2017–18.05.2017	Functional Nanowire Synthesis Based on Molecular Beam Epitaxy	Japan
Dr. Cerdá Méndez, Edgar	Universidad Autónoma de San Luis Potosí	26.06.2017–07.07.2017	Modulation of microcavity polaritons by acoustic waves	Mexico
Prof. Dr. Lastras-Martínez, Luis Felipe	Insituto de Investigacion en Comunicacion Optica (IICO), Universidad Autonoma de San Luis Potosi (UASLP)	20.07.2017–17.08.2017	Deformaciones inducidas en superficies semiconductoras: caracterización por medio de técnicas ópticas	Mexico
Ulloa Castillo, Nicolás Antonio	Instituto de Investigacion en Comunicacion Optica, UASLP	07.11.2016–31.10.2017	Surface acoustic waves to explore coherent electron spin transport in dipolaritons condensates"	Mexico
Prof. Dr. Grepstad, Jostein K.	Norwegian Univ. of Science and Technology - Department of Electronics and Telecommunications	01.09.2016–30.06.2017	Photoemission spectroscopy and materials science of magnetic materials	Norway
Reszka, Anna	Institute of Physics, Polish Academy of Sciences	29.05.2017–03.06.2017	Cathodoluminescence of III-V nanowires	Poland
Sobanska, Marta	Institute of Physics, Polish Academy of Sciences	09.07.2017–15.07.2017	Application of line-of-sight quadrupole mass spectroscopy for in-situ monitoring of gallium incorporation during plasma-assisted molecular beam epitaxy (PAMBE) growth of GaN nanowires	Poland
Dr. Zaleski, Karol	NanoBioMedical Centre, Adam Mickiewicz University Poznan	13.11.2017–13.12.2017	Deposition of Heusler alloys thin films on on graphene substrates	Poland

Facts & Figures – Visiting Scientists

Name	Institute	Period	Topic	Country
Prof. Dr. Sabelfeld, Karl	Institute of Computational Mathematics and Mathematical Geophysics Russian Academy of Sciences	24.07.2017–11.08.2017	Monte Carlo simulations of cathodoluminescence at dislocations in GaN	Russian Federation
Fandam, Ravjeer	Universidad Politécnica de Madrid	20.11.2017–22.12.2017	Interferometry and Raman spectroscopy of SAW signals in graphene transferred on piezoelectric substrate like ZnO and LiNbO ₃	Spain
Andersson, Gustav	University of Chalmers	15.05.2017–16.06.2017	Propagating acoustic fields on semiconducting structures	Sweden
Prof. Dr. McCartney, Martha	Arizona State University	04.05.2017–07.05.2017	Transmission Electron Microscopy Study on Interfaces in Novel III-V Semiconductor Heterostructures	USA
Prof. Dr. Smith, Dave	Arizona State University	04.05.2017–07.05.2017	Transmission Electron Microscopy Study on Interfaces in Novel III-V Semiconductor Heterostructures	USA
Buck, Nathan	Kennesaw State University	29.05.2017–21.07.2017	Internship Joachim Herz Foundation	USA
Patil, Prasanna Dnyaneshwar	Southern Illinois University	11.05.2017–10.08.2017	Electrical measurements of epitaxially grown van der Waals heterostructures	USA
Matheson, Graham	University of Washington, Seattle	26.06.2017–30.11.2017	Local electrical measurements of single GaAs nanowires	USA
Prof. Dr. Msall, Madeleine	Bowdoin College	26.07.2017–30.06.2018	Multi-frequency interdigital transducers, spatial scanning of surface acoustic waves and the control of quantum electronic states"	USA

Staff

(December 31, 2017)

Scientific staff: including Ph. D. students (D) and externally funded personnel (P)

Auzelle, Thomas (P)	Charge and energy transfer at hybrid organic/inorganic semiconductor interfaces
Biermann, Klaus	Molecular beam epitaxy of GaAs-based advanced heterostructures
Bierwagen, Oliver	Molecular beam epitaxy of oxides
Brandt, Oliver	Group-III nitrides and ferromagnet/semiconductor hybrid structures
Budde, Melanie (D, P)	Molecular beam epitaxy and doping of p-type semiconducting oxides
Calabrese, Gabriele	Molecular beam epitaxy of III-N nanowires on metallic substrates
Calarco, Raffaella	Molecular beam epitaxy of group-III nitrides and phase-change materials
Cecchi, Stefano (P)	Growth and optical pump-x-ray as well as THz probe measurements of chalcogenide superlattices
Cheng, Zongzhe (D)	In-situ x-ray diffraction on group-III sesquioxides
Chèze, Caroline (P)	Molecular beam epitaxy of nitride-based short-period superlattices
Czubak, Dietmar (D)	Spin transport in ferromagnet-semiconductor hybrid structures with two-dimensional transport channels
Drube, Hardy (D)	Electron tomography of interfaces and thin films
Feldl, Johannes (D, P)	Optical spectroscopy of semiconducting oxides, in particular perovskites and sesquioxides
Fernández Garrido, Sergio	Molecular beam epitaxy of group-III nitrides
Flissikowski, Timur	Ultrafast dynamics of semiconductor structures
Fölsch, Stefan	Low-temperature scanning tunneling microscopy and spectroscopy
Freudenfeld, Jaan (D)	Interacting electronic nanostructures
Gao, Guanhui	Transmission electron microscopy of nanowire heterostructures
Gaucher, Samuel (D)	Molecular beam epitaxy of Ge-containing multiple ferromagnet/semiconductor hybrid structures
Geelhaar, Lutz	Molecular beam epitaxy and semiconductor nanowires
Grahn, Holger	Optical and electrical properties of semiconductor nanostructures
Hanke, Michael	Synchrotron x-ray diffraction
Heilmann, Martin	Molecular beam epitaxy of graphene/h-BN van der Waals heterostructures
Helgers, Paul (D, P)	Acoustically modulated gigahertz single-photon sources using coupled quantum wires and dots in microcavities
Hellermann, Jan (D)	Quantumtransport measurements at low temperatures and high frequencies
Herfort, Jens	Ferromagnet-semiconductor heterostructures
Hernández Minguez, Alberto	Spin polarization in acoustically induced moving electrons in graphene
Herranz Zamorano, Jesús	Devices based on group-III arsenide nanowires
Hubert, Colin (D)	Acoustic transport of exciton spins in (111) quantum wells
Hucho, Carsten	Technology and transfer
Jahn, Uwe	Spatially resolved optical and structural properties of heterostructures
Jenichen, Bernd	X-ray diffraction and electron microscopy

Facts & Figures – Staff

Jordão Lopes, João Marcelo	Graphene and h-BN epitaxy
Kaganer, Vladimir	Theories of molecular-beam-epitaxial growth and x-ray scattering
Küpers, Hanno (D)	Growth and luminescence properties of GaAs/(In,Ga)As core-shell nanowires
Kuşdemir, Erdi (D, P)	Influence of Mg on the growth of (In,Ga)N/GaN short period superlattices
Kuznetsov, Alexander	Microcavity exciton-polaritons in artificial potential landscapes
Lähnemann, Jonas	Spatially resolved optical spectroscopy and structural and chemical analysis of nanostructures
Li, Hong	Theoretical studies of semiconductor nanostructures
Liou, Yi-Ting (D, P)	Acousto-electric modulation of few-layer epitaxial graphene.
Lü, Xiang	Terahertz cascade and quantum-cascade lasers
Ludwig, Stefan	Quantum transport in nanoelectronic systems
Luna Garcia de la Infanta, Esperanza	Transmission electron microscopy of heterointerfaces
Mazzolini, Piero	Growth kinetics and doping of (Ga,Al) ₂ O ₃
Nicolai, Lars (D, P)	Spectroscopic electron tomography and microscopy of nanomaterials Electron tomography of semiconductor heterostructures
Niehle, Michael (P)	(In _{1-x} Ga _x) ₂ O ₃ based gas sensors
Pham, Van Dong (P)	Atom manipulation on III-V semiconductors by low-temperature scanning tunneling microscopy
Ramsteiner, Manfred	Electronic, vibrational, and magnetic properties of semiconductors
Riechert, Henning	Director
Röben, Benjamin (D)	Terahertz quantum-cascade-lasers with gratings for feedback and coupling
Santos, Paulo Ventura	Acoustic, optic, and magnetic properties of nanostructures
Schrottke, Lutz	Quantum-cascade lasers and optical properties of heterostructures
Schultz, Markus (D)	In-situ transmission electron microscopy on semiconductor interfaces and defect structures
Sinito, Chiara	Optical spectroscopy of organic/inorganic hybrid systems
Tahraoui, Abbes	Comprehensive semiconductor technology
Takagaki, Yukihiko	Electric properties of nanometer-scale materials
Trampert, Achim	Microstructure and electron microscopy
van Treeck, David (D)	Molecular beam epitaxy of axial and radial group-III nitride nanowire heterostructures
Vogt, Patrick	Molecular beam epitaxy of semiconducting oxides
Wolny, Paweł (D, P)	Growth of (In,Ga)N short-period superlattices: Surface manipulation by supply of active species
Yin, Yefei (D, P)	Quantum Hall effect and quantum transport
Yuan, Mingyun (P)	Manipulation of single excitons by surface acoustic waves
Zallo, Eugenio (P)	Growth and optical pump-optical probe measurements of chalcogenide superlattices

Long-term fellows

Aranha Galves, Lauren (CSF)	Growth and characterization of graphene nanoribbons on SiC substrates
Lewis, Ryan (AvH)	Molecular beam epitaxy of (In,Ga,Al)As nanowires with Bi

Supporting Staff

Anders, Walid	Technology
Arnhold, Kerstin	Finances / Purchasing and Equal Opportunities Officer
Behnke, Steffen	Technician
Bluhm, Anne-Kathrin	Technician
Dormeyer, Dagmar	Library
Ferber, Thomas	Workshop
Frank, Katrin (P)	Technician
Hablizel, Kai (P)	European and National Grant Management
Hartung, Andreas	Human Resources and Travel Management
Heinitz, Sebastian	Electrician
Henschke, Falko	Workshop
Herrmann, Claudia	Technician
Holldack, Anja	Personal Assistant to Prof. Riechert / Third Party Funding
Hörlicke, Michael	Technician
Krauß, Sabine	Technician and Chairwoman Works Council
Krawczyk, Irene	Graphic and Web Design
Litschauer, Maximilian (P)	Student Assistant
Matk, Susanne	Personal Assistant to Dr. Hucho / Third Party Funding
Matzeck, Margarita (P)	Technician
Meister, Sebastian	Technology
Pakulat, Bernd	Head of IT and Data Protection Officer
Pfeiffer, Astrid	Technician
Pfeiffer, Jörg	Head of Workshop
Rauwerdink, Sander	Technology
Reischel, Mercedes	Transfer Management
Riedel, Angela	Technician
Schönherr, Hans-Peter	Technician
Seidel, Werner	Technology
Sieg, Michael	Workshop
Steffen, Doreen	Technician
Stemmler, Carsten	Technician
Venohr, Thomas	Workshop
Wirsig, Arno	Technology
Wirt, Andreas	IT

U-Bhf Hausvogteiplatz



Contact
Kontakt

DIRECTORATE

Prof. Dr. Henning Riechert

Director

phone: +49 30 20377-365

fax: +49 30 20377-201

riechert@pdi-berlin.de

Anja Holldack

Office

phone: +49 30 20377-352

holldack@pdi-berlin.de

Dr. Carsten Hucho

Scientific-Administrative Coordinator

phone: +49 30 20377-234

hucho@pdi-berlin.de

Susanne Matk

Office

phone: +49 30 20377-481

matk@pdi-berlin.de

TRANSFER

Dr. Carsten Hucho

phone: +49 30 20377-234

fax: +49 30 20377-515

hucho@pdi-berlin.de

Mercedes Reischel

Technology Transfer Manager

phone: +49 30 20377-289

fax: +49 30 20377-515

reischel@pdi-berlin.de

ADMINISTRATION

Andreas Hartung

Human Resources

phone: +49 30 20377-475

hartung@pdi-berlin.de

Kerstin Arnhold

Purchasing/Finances

phone: +49 30 20377-358

fax: +49 30 20377-425

arnhold@pdi-berlin.de

PUBLIC RELATIONS

Dr. Carsten Hucho

phone: +49 30 20377-234

fax: +49 30 20377-515

hucho@pdi-berlin.de

DEPARTMENTS

Dr. Lutz Geelhaar

Head of Department Epitaxy
phone: +49 30 20377-359
fax: +49 30 20377-201
geelhaar@pdi-berlin.de

Dr. Achim Trampert

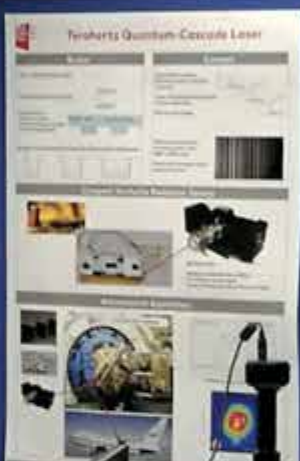
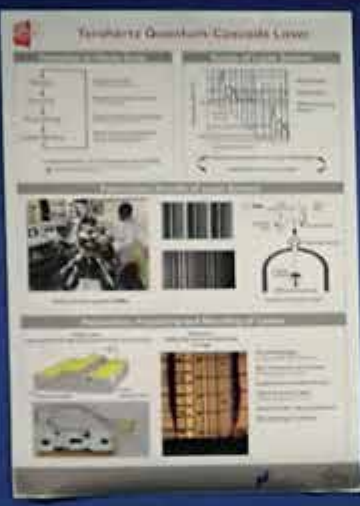
Head of Department Microstructure
phone: +49 30 20377-280
fax: +49 30 20377-201
trampert@pdi-berlin.de

Prof. Dr. Holger T. Grahn

Head of Department Semiconductor Spectroscopy
phone: +49 30 20377-318
fax: +49 30 20377-301
htgrahn@pdi-berlin.de

Dr. Carsten Hucho

Head of Department Technology and Transfer
phone: +49 30 20377-234
fax: +49 30 20377-515
hucho@pdi-berlin.de





Imprint Impressum

Paul-Drude-Institut für Festkörperelektronik,
Leibniz-Institut im Forschungsverbund Berlin e.V.

Hausvogteiplatz 5-7
10117 Berlin
Germany

Tel. +49 30 20377-481
Fax +49 30 20377-515

info@pdi-berlin.de

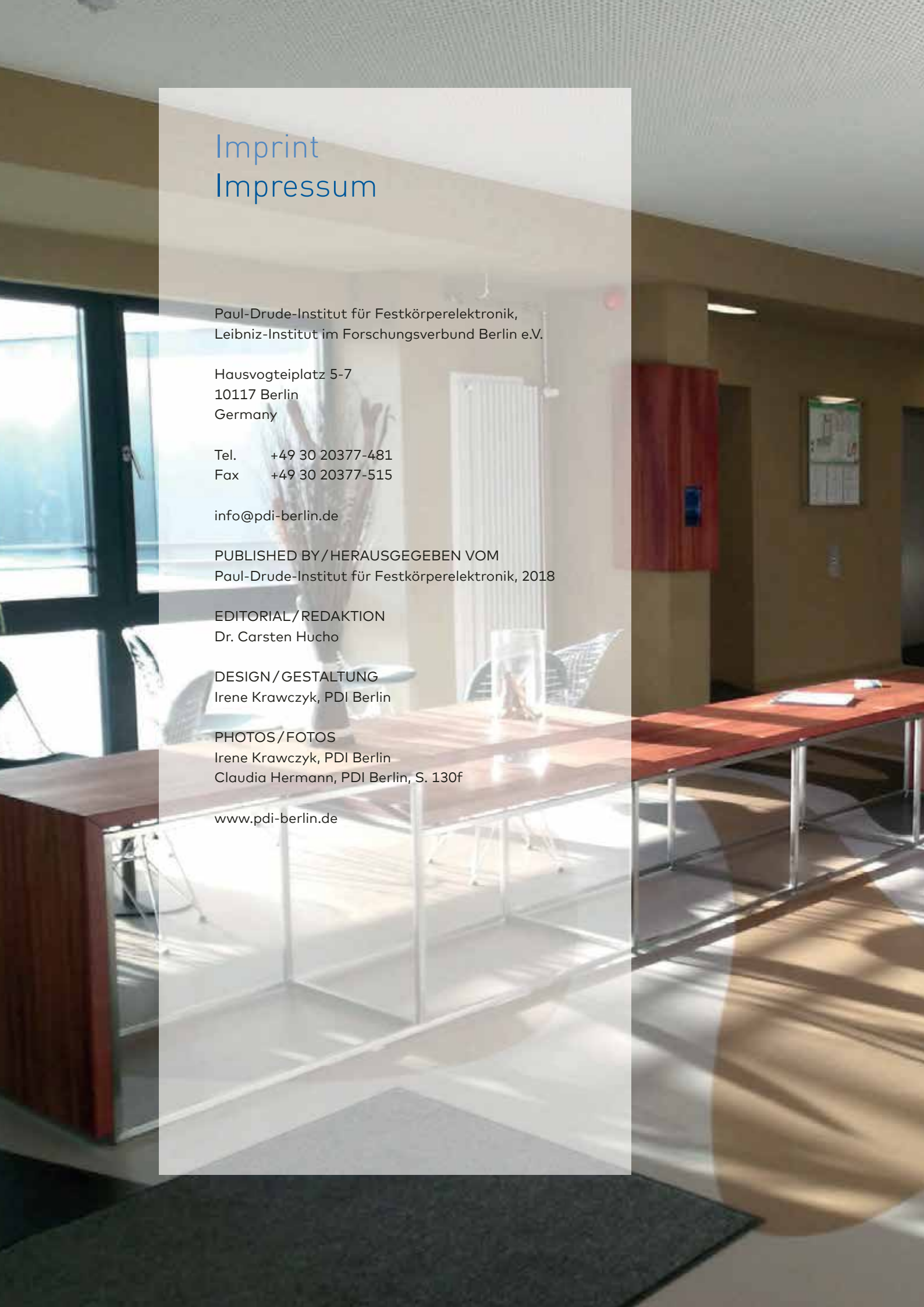
PUBLISHED BY/HERAUSGEgeben VOM
Paul-Drude-Institut für Festkörperelektronik, 2018

EDITORIAL/REDAKTION
Dr. Carsten Hucho

DESIGN/GESTALTUNG
Irene Krawczyk, PDI Berlin

PHOTOS/FOTOS
Irene Krawczyk, PDI Berlin
Claudia Hermann, PDI Berlin, S. 130f

www.pdi-berlin.de







Scientists and administrative staff experience phases of extreme stress at their workplace. The final stage of a dissertation, preparations for large conferences, or development of proposals for scholarship programs, leave little or no time for life outside the office or the lab. The employees' enormous personal engagement arises from their strong identification with the research they are involved in. While such identification can be very positive, leading to profound satisfaction with one's professional activity, it can also result in pressure and tensions in the family environment.

We at PDI place great importance on promoting work-life balance and support our employees in this respect through individual solutions. Our measures are continuously developed within an external audit process. On August 30, 2012 PDI was certified by berufundfamilie gGmbH for its engagement in pursuing a family-friendly human resources policy.

Alle Wissenschaftlerinnen und Wissenschaftler und die Wissenschaft unterstützenden Mitarbeiterinnen und Mitarbeiter kennen Phasen extremer zeitlicher Belastungen bei ihrer Arbeit. Während der Endphase einer Doktorarbeit, im Umfeld großer Tagungen oder in der Antragsphase für ein Stipendienprogramm ist oft kaum noch Platz für ein Leben außerhalb des Büros und Labors. Das enorme persönliche Engagement der Mitarbeiterinnen und Mitarbeiter speist sich aus der starken Identifikation mit der Forschung. Im positiven Fall bedeutet diese Identifikation große Zufriedenheit mit der beruflichen Tätigkeit – sie kann aber auch zu Belastungen und Einschränkungen im familiären Umfeld führen.

Wir legen am PDI großen Wert auf die Vereinbarkeit von Beruf und Familie und unterstützen unsere Mitarbeiterinnen und Mitarbeiter hierbei durch individuelle Maßnahmen. Im Rahmen eines externen Auditierungsprozesses werden unsere Maßnahmen weiterentwickelt. Das PDI wurde am 30.8.2012 für sein Engagement für eine familienbewusste Personalpolitik durch die berufundfamilie gGmbH zertifiziert.



Paul-Drude-Institut für Festkörperelektronik,
Leibniz-Institut im Forschungsverbund Berlin e.V.

Hausvogteiplatz 5-7
10117 Berlin
Germany

www.pdi-berlin.de

